Search for New Physics in Tau-pair Events in ATLAS at the LHC

Doctoral Dissertation by

Zofia Czyczuła

Experimental High Energy Physics Group
Niels Bohr Institute
The Graduate School of Science
Faculty of Science
University of Copenhagen
Denmark

June 2009

PREFACE

ATLAS is one of the main four particle detector experiments constructed at the Large Hadron Collide (LHC), a new world-largest particle accelerator situated at CERN in Switzerland. Being designed as a general-purpose detector, ATLAS is intended to search for new phenomena which involve highly massive particles whose detection was beyond the reach of past, lower-energy experiments. Amongst its main goals are investigations of the electroweak symmetry breaking mechanism encompassing searches for the missing piece of the Standard Model, the Higgs boson or alternatively technicolors. As the Standard Model (SM) is believed not to be an ultimate theory of nature, it is also anticipated that ATLAS will shed light on new, more fundamental theories.

In this thesis the outcome of my research conduced in ATLAS between June 2006 and May 2009 is summarised. The work has followed the progress of the experiment, which during the years 2006-2008 was in its final preparation stage. The ATLAS detector was finally assembled in June 2008 and successfully registered the first particles from the LHC on 10 September 2008. A great disappointment came on the 19 September 2008 when the operation had to be stopped due to an accident in the LHC tunnel caused by malfunctioning of the accelerator's magnet system. The work presented in this thesis includes therefore studies performed exclusively on the simulated data. The LHC is scheduled to be brought to operation again in September 2009.

This thesis is dedicated to searches for a new heavy neutral particle decaying into a pair of tau leptons. As a reference for the signal, an extra gauge boson (Z') from the Sequential Standard Model (SSM) has been used. Since, however, experimental consequences of the existence of a new heavy resonance are similar regardless of its theoretical origin, the studies can be viewed as a generic search in the two tau leptons final state. The tau-pair signature is important as it is sensitive to particles which couple preferentially to the third generation fermions. Furthermore it offers potential for measuring of polarisation asymmetry which provides important constraints on the nature of the observed resonance.

Outline

The thesis is organised in two parts. Part I consists of three chapters. In Chapter I general theoretical aspects of this work are discussed. Chapter II provides description of the experiment. In Chapter III my own research conduced in ATLAS are summarised followed by conclusions. Part II consists of the four ATLAS Notes[1], detailing my studies:

A. Z.Czyczula et.al, “Searching for New Physics using High-P_T Tau Pairs in ATLAS”, ATL-PHYS-INT-2008-038.

B. Z.Czyczula, M.Dam, “Electron veto in the tau identification package TAU1P3P”, ATL-PHYS-INT-2008-007.

C. Z.Czyczula, M.Dam, “Cut-based electron veto algorithm for the track-seeded part of tauRec”, ATL-PHYS-INT-2009-023.

D. Z.Czyczula, M.Dam, “Prospects of Measuring the Tau Polarisation in $Z' \to \tau^+\tau^-$ events in ATLAS”, ATL-PHYS-INT-2009-049.

They will be referred to in the thesis with the respective capital letters. Notes A and D are related to searches for new physics in tau-pair events while B and C are dedicated to improvements in the tau lepton reconstruction and identification. They are placed in the chronological order to reflect the improvements in the ATLAS simulation and reconstruction algorithms.

Acknowledgements

I would like to express my gratitude to Mogens Dam for his excellent supervision, for giving me freedom to develop my own ideas and directing me with the right questions. I am thankful to him for always having time for discussions, for sharing his impressive knowledge and experience and for always honest and constructive criticism.

---

[1] Declarations, signed by corresponding co-authors, stating that I am the first author of the Notes have been submitted together with the thesis.

During the three years at the Niels Bohr Institute (NBI) I had the pleasure to share the office with Stefania Xella. I admire her passion and involvement in work in ATLAS. I would like to thank her for cheerful and stimulating atmosphere in the office and for her continuous support for my research. In general, I am grateful to all High Energy Physics group at NBI for creating such a friendly and motivating place to work.

I wish to thank all colleagues from the ATLAS experiment. In particular I am grateful to Trevor Vickey for fruitful and inspiring collaboration as well as to Elzbieta Richter-Was, Olya Igonkina and Anna Kaczmarska for numerous interesting discussions.

I am sincerely thankful to my boyfriend Øystein and my family: my mother, my brother Lubczyk and my sister-in-law Ula for their invaluable support and for giving me the strength needed to finish the thesis. Last but not least, I would like to thank Øystein and all my friends for many enjoyable social events.

CONTENTS

PART I

NEW PHYSICS AND THE ATLAS EXPERIMENT

1 WHY SEARCH FOR NEW PHYSICS IN TAU-PAIR EVENTS?

In this chapter the motivation for searches for an extra heavy neutral particle decaying into tau pairs is discussed.

The chapter is organised as follows: In Sect. 1.1, basic concepts and the Lagrangian of the Standard Model are discussed based on [1, 2, 3]. The focus is on the electroweak part of the theory which is important for further discussion of the various extensions of this sector. The section closes with a list of shortcomings of the SM. As a next step, theories Beyond the Standard Model (BSM) are discussed in Sect. 1.2. After a short review of various models in Sect. 1.2.1, the discussion focuses on a new heavy neutral particle which is a generic feature of many BSM theories. An emphasis is put on new extra gauge bosons, arising as a manifestation of an extended gauge symmetry group. Their theoretical origins are outlined in Sect. 1.2.2, while the present constraints on their masses are presented in Sect. 1.2.3. Other sources of heavy neutral particles are briefly summarised in Sect. 1.2.4. An overview of phenomenology of an extra gauge boson is given in Sect 1.3, where various observables, such as the cross section, the forward-backward and the polarisation asymmetries, invariant mass spectrum and the width are discussed. Since the thesis concentrates on searches for a heavy resonance decaying into tau pairs, Sect. 1.4 outlines the main characteristics of the tau lepton. The general properties of taus are summarised in Sect 1.4.1 while their sensitivity to the polarisation is discussed in Sect. 1.4.2.

1.1 The Standard Model

1.1.1 Introduction

It is currently accepted that the fundamental blocks of matter are three families of quarks and three families of leptons. Studies of the symmetries they exhibit lead to establish the Standard Model, a theory which describes electromagnetic, weak and strong interactions of the elementary particles. So far all attempts to encompass the last type of known interactions, gravity, has been unsuccessful. In the Standard Model, forces between quarks and leptons are mediated by force carrying particles called gauge bosons. Electromagnetic interactions are mediated by photons, weak interactions by weak bosons and strong interactions by gluons. The symmetry underlying the Standard Model is assumed to be spontaneously broken at some scale in order for the elementary particles to acquire mass. Existence of the Higgs boson, a neutral particle introduced to break the symmetry, has not yet been experimentally confirmed. Fig.1.1 shows the Standard Model particles.

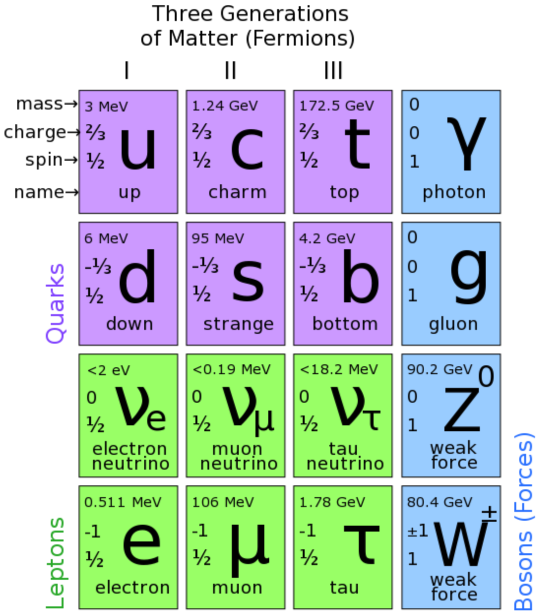

Figure 1.1: The Standard Model particles.

1.1.2 Principles of the Standard Model

The importance of symmetries in nature was first emphasised by Emma Noether, who showed in 1918, that there is a symmetry associated with every conservation law. The invariance under spacetime transformations such as space translation, time displacement and rotation leads to the conservation of momentum, energy and angular momentum, respectively. Similarly the requirement of charge conservation (electron charge or color charge) follows from invariance under a global phase (gauge) transformation.

The structure of fundamental interactions, embedded in the Standard Model, are connected to the local gauge invariance. The idea being that by promoting the global symmetry to local, the originally free particle theory transforms into the theory of interacting particle fields. The requirement of local gauge invariance is accomplished by introducing new vector boson fields, the so-called gauge fields. The number of introduced vector fields corresponds to the number of independent generators of a chosen symmetry group. Therefore by a proper specification of the symmetry group one can describe the particle system with the number of vector field which is expected from experiments.

The gauge symmetry group of the Standard Model is SU(3)×SU(2)×U(1). There are no particular reasons for this choice, except that it successfully describes the experimental data and it is the simplest group that reproduces the currently known features of particles interactions. The SU(2)×U(1) group was chosen, in the sixties, by Glashow to unify electromagnetic and weak interactions. It predicted the existence of four massless gauge fields. Later, Weinberg and Salam showed that the weak bosons can acquire mass via spontaneous breaking of the SU(2)×U(1) gauge symmetry. This theory is known as the Glashow-Weinberg-Salam model [4]. The SU(3) symmetry group, on the other hand, is associated with the local color symmetry of quarks. It underlies the theory of Quantum Chromo Dynamics (QCD), established in sixties and seventies, which describes the interaction of quarks inside hadrons.

The Standard Model, at that time, suffered from serious conceptual and technical deficiencies. The only known way of extracting any information from the fundamental equations was to expand in a power series in the coupling constants. Such an expansion is called perturbation theory. It turns out that each term in the perturbation series, except for the leading order contribution, is affected by ultraviolet divergences. The theory was therefore not accepted until the early seventies, when G.'t Hooft demonstrated that the SM is a renormalisable theory. This means that the prediction of physical observables such as the masses or the cross sections can be calculated to an arbitrary precision [1].

1.1.3 The Standard Model Lagrangian

Within the Standard Model, the quarks and leptons are represented by fermion fields. Since the electroweak interactions are chiral[2], the left- and the right-handed components

---

[1] Renormalisation procedure removes singularities from perturbation theory at the expense of introducing a (finite) number of arbitrary constants whose values need to be measured by experiment.

[2] There is no theoretical explanation why nature chose the basic electroweak interactions to be chiral.

are assigned to different representations of the SU(2) group, i.e. the left-handed fields transform as SU(2)-doublets and the right-handed fermions transform as singlets. The fundamental fermions can therefore be grouped as:

$$\left.\begin{matrix} \binom{\nu_e}{e^-}_L & \binom{\nu_\mu}{\mu^-}_L & \binom{\nu_\tau}{\tau^-}_L \\ \binom{u}{d'}_L & \binom{c}{s'}_L & \binom{t}{b'}_L \end{matrix}\right\} \begin{matrix}\text{Left-handed fermions} \\ \text{SU(2)-doublets}\end{matrix}$$

$$\left.\begin{matrix} e^-_R & \mu^-_R & \tau^-_R \\ u_R & c_R & t_R \\ d_R & s_R & b_R \end{matrix}\right\} \begin{matrix}\text{Right-handed fermions} \\ \text{SU(2)-singlets}\end{matrix}$$

and they transform as:

$$\Psi_L = \frac{1}{2}(1-\gamma_5)\Psi \longrightarrow e^{iY\beta(x)+iI_j\alpha^j(x)}\Psi_L \tag{1.1}$$

$$\Psi_R = \frac{1}{2}(1+\gamma_5)\Psi \longrightarrow e^{iY\beta(x)}\Psi_R \tag{1.2}$$

where I_j, j=1,2,3 are the three generators of the SU(2) group and Y is the generator of the U(1) group, often referred to as the weak isospin and the weak hypercharge, respectively. The respective charges of the weak isospin and weak hypercharge need to be conserved due to gauge invariance. Unification of weak and electromagnetic interactions yields the Gell-Mann-Nishijima relation for the electromagnetic charge: $Q = \frac{Y}{2} + I_3$ with I_3 being the third component of the weak isospin.

In the following, the focus is on the electroweak part of the theory. For overview of the QCD Lagrangian the reader is referred to [5]. The fundamental electroweak Lagrangian can be written as a sum of three contributions:

$$\mathscr{L} = \mathscr{L}_G + \mathscr{L}_H + \mathscr{L}_Y \tag{1.3}$$

where:

$\mathscr{L}_G$: the gauge part, describing kinetic energy of fermions, their interactions with the gauge fields, as well as gauge fields and their self interactions,

$\mathscr{L}_H$: the part describing Higgs potential and Higgs-gauge Boson interactions,

$\mathscr{L}_Y$: the part describing Higgs-fermion (Yukawa) interactions.

The first term, $\mathscr{L}_G$ is given by:

$$\mathscr{L}_G = \sum_f i\left\{\bar{f}_L\gamma^\mu(D_L)_\mu f_L + \bar{f}_R\gamma^\mu(D_R)_\mu f_R\right\} - \frac{1}{4}B_{\mu\nu}B^{\mu\nu} - \frac{1}{4}W^i_{\mu\nu}W^{\mu\nu}_i \tag{1.4}$$

where the sum is over all left- and right-handed fermion fields, denoted by f_L and f_R respectively, and the covariant derivatives for the left- and the right-handed fields are given by:

$$(D_L)_\mu = \partial_\mu + igI_iW^i_\mu + ig'\frac{Y}{2}B_\mu, \tag{1.5}$$

$$(D_R)_\mu = \partial_\mu + ig'\frac{Y}{2}B_\mu, \tag{1.6}$$

where W^i_μ, i=1,2,3 and B_μ are respectively the SU(2) and U(1) gauge fields, with field strength tensors given by:

$$W^i_{\mu\nu} = \partial_\mu W^i_\nu - \partial_\nu W^i_\mu + g\epsilon^{ijk}W^j_\mu W^k_\nu, \tag{1.7}$$

$$B_{\mu\nu} = \partial_\mu B_\nu - \partial_\nu B_\mu. \tag{1.8}$$

The SU(2) coupling constant g and the weak hypercharge coupling constant g' are related to the electromagnetic coupling constant e through the Weinberg angle θ_W as $g = e/\sin\theta_W$ and $g' = e/\cos\theta_W$. The first two terms in eq. 1.4 describe the kinetic energy of the fermions and the interaction of the gauge fields with the left- and the right-handed fermions, respectively. The remaining two terms are the kinetic energy and self coupling of the W_μ fields and the kinetic energy of the B_μ field. The term bilinear in $W_{\mu\nu}$ generates quadratic and cubic self interactions which are characteristic for non-Abelian gauge theories.

The second term, $\mathscr{L}_H$, has the form:

$$\mathscr{L}_H = ((D_L)_\mu H)^\dagger((D_L)^\mu H) - V(H, H^\dagger). \tag{1.9}$$

Here four scalar (Higgs) fields, H, are introduced. They are arranged in a complex SU(2)$_L$ isospin doublet with weak hypercharge $Y = 1$. The self-interaction term between the Higgs fields, which has the famous "mexican hat" shape, $V(H)$, is given by:

$$V(H) = -\mu^2H^\dagger H + \lambda^2(H^\dagger H)^2, \quad \lambda^2 > 0. \tag{1.10}$$

Provided that μ^2 is positive, the potential is at its minimum when $H^\dagger H = \frac{\mu^2}{2\lambda} = \frac{v^2}{2}$.

Since electric charge is a conserved quantity, the gauge group associated with electromagnetic interactions, U$(1)_{em}$, needs to remain a true symmetry of the vacuum. This is accomplished by letting the neutral component of the Higgs doublet have the vacuum expectation value (VEV):

$$\langle H \rangle = \frac{1}{\sqrt{2}} \begin{pmatrix} 0 \\ v \end{pmatrix}. \tag{1.11}$$

After a suitable gauge transformation, we can parametrise H around its minimum as:

$$H = \frac{1}{\sqrt{2}} \begin{pmatrix} 0 \\ v+h \end{pmatrix}. \tag{1.12}$$

The neutral field h is usually referred to as the Higgs field. The Standard Model symmetry group, SU$(3)_c\times$SU$(2)_L\times$U$(1)_Y$, is spontaneously broken and the remaining symmetry is SU$(3)_c\times$U$(1)_{em}$.

This mechanism, called the Higgs mechanism, gives rise to masses for the gauge fields, $W_\mu^\pm$ and Z_μ, and leaves the photon field, A_μ, massless. The physical gauge fields are defined as:

$$W_\mu^\pm = \frac{W_\mu^1 \mp W_\mu^2}{\sqrt{2}}, \qquad Z_\mu = \frac{gW_\mu^3 - g' B_\mu}{\sqrt{g'^2+g^2}}, \qquad A_\mu = \frac{g' W_\mu^3 + gB_\mu}{\sqrt{g'^2+g^2}} \tag{1.13}$$

of which the first two acquire masses:

$$M_W^2 = \frac{g^2v^2}{4}, \qquad M_Z^2 = \frac{M_W^2(g^2+g'^2)}{g^2} = \frac{M_W^2}{cos^2\theta_W}. \tag{1.14}$$

The value for the $\sin^2\theta_W$ is 0.23 and the masses for the W and the Z boson are 80.4 and 91.2 GeV/c^2 respectively. The measured values for the couplings then yield v=246 GeV.

The last term in the Lagrangian, $\mathscr{L}_Y$ describes the interaction between fermions and the Higgs doublet. It has the form:

$$\mathscr{L}_Y = -\sum_f g_f(\bar{\Psi}_L^f H)\Psi_R^f + h.c. \tag{1.15}$$

The Yukawa couplings, g_f are arbitrary values, determined from experiments. To generate masses one substitutes eq. 1.11 for H and we can express the fermionic masses as: $m_f = \frac{v}{\sqrt{2}}g_f$.

We can express the fermion-gauge boson interaction part, introduced in $\mathscr{L}_G$ via covariant derivatives, in the following form:

$$\mathscr{L}_G^{int} = -\left\{\frac{g}{\sqrt{2}}(J_{cc}^\mu W_\mu^+ + J_{cc}^{\mu\dagger} W_\mu^-) + g\sin\theta_W J_{em}^\mu A_\mu + \sqrt{g'^2+g^2}J_{nc}^\mu Z_\mu\right\}. \tag{1.16}$$

and identify the physical currents as:

$$J^{\mu}_{cc} = \bar{\Psi}_L \gamma^{\mu} I^{+} \Psi_L, \quad J^{\mu}_{em} = \bar{\Psi} \gamma^{\mu} Q \Psi, \quad J^{\mu}_{nc} = \bar{\Psi} \gamma^{\mu} \left\{ \frac{1}{2}(1-\gamma_5) I_3 - Q \sin^2 \theta_W \right\} \Psi \tag{1.17}$$

where I^{+} and I^{-} are the isospin raising and lowering operators. The coupling of the photon is chirally symmetric. The Z_{μ} field, like the A_{μ} field, couples to both left- and the right-handed fermions, however due to I_3 dependence it couples with different strengths. It is responsible for the neutral current (NC) type of interactions. The $W^{\pm}_{\mu}$ fields only couple to the left-handed fields and change the flavor of the quark within a given isospin doublet. The down-type quark mass eigenstates (d,s,b) are connected to the down-type quark gauge eigenstates (d',s',b') through the Cabbibo-Kobayashi-Maskawa (CKM) matrix. Therefore the weak charged current interactions may shift between all types of flavour. Flavour changing neutral current transitions such as $d \rightarrow s$ are prohibited at tree level [3].

1.1.4 Experimental status of the Standard Model

After its establishment in the seventies, the Standard Model has undergone a large number of stringent experimental tests.

To gauge the agreement of the theory with data, Fig.1.2 shows a comparison of indirectly (theoretically inferred) and directly measured values of various electroweak observables. All deviations are inside 3σ and therefore are consistent with being statistical fluctuations.

1.1.5 Shortcomings of the Standard Model

Although the Standard Model is a very successful theory, it is believed not to be an ultimate theory of nature. Reasons for that are twofold. First of all, there are a number of phenomena, which are not explained within the Standard Model framework. They are as follows.

Origin of mass of neutrinos. Various measurements of atmospheric and solar neutrinos have provided evidence for neutrino oscillations and therefore for neutrino masses and mixing [7]. The SM assumes the neutrinos to be massless particles.

Source of the Dark Matter and the Dark Energy Cosmological observations, such as the cosmic microwave background and the structure and movements of galaxies

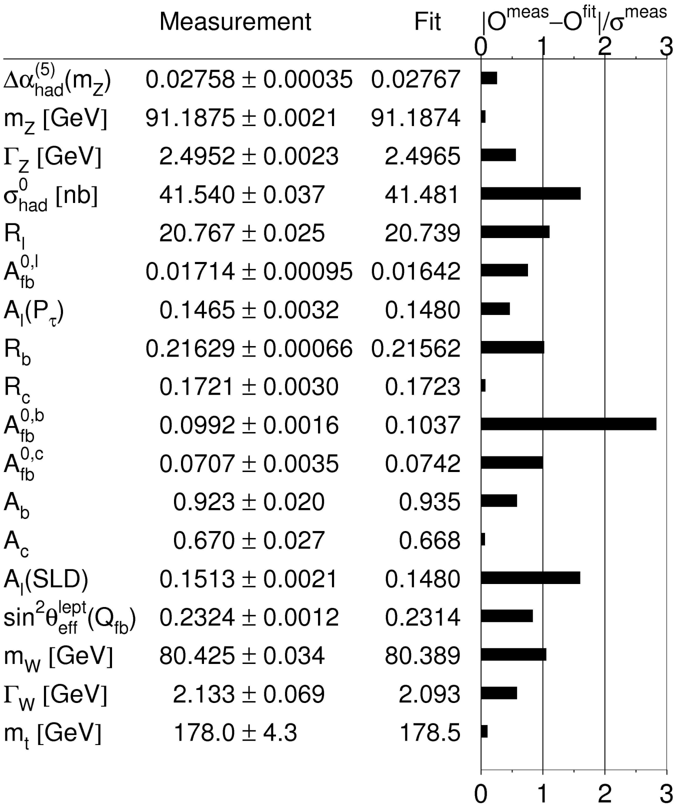

	Measurement	Fit
$\Delta\alpha^{(5)}_{had}(m_Z)$	0.02758 ± 0.00035	0.02767
m_Z [GeV]	91.1875 ± 0.0021	91.1874
Γ_Z [GeV]	2.4952 ± 0.0023	2.4965
σ^0_{had} [nb]	41.540 ± 0.037	41.481
R_l	20.767 ± 0.025	20.739
$A^{0,l}_{fb}$	0.01714 ± 0.00095	0.01642
$A_l(P_\tau)$	0.1465 ± 0.0032	0.1480
R_b	0.21629 ± 0.00066	0.21562
R_c	0.1721 ± 0.0030	0.1723
$A^{0,b}_{fb}$	0.0992 ± 0.0016	0.1037
$A^{0,c}_{fb}$	0.0707 ± 0.0035	0.0742
A_b	0.923 ± 0.020	0.935
A_c	0.670 ± 0.027	0.668
A_l(SLD)	0.1513 ± 0.0021	0.1480
$\sin^2\theta^{lept}_{eff}(Q_{fb})$	0.2324 ± 0.0012	0.2314
m_W [GeV]	80.425 ± 0.034	80.389
Γ_W [GeV]	2.133 ± 0.069	2.093
m_t [GeV]	178.0 ± 4.3	178.5

Figure 1.2: For various electroweak observables, comparison of the measurements with their SM fitted values [6].

show that the energy content of universe consists of roughly 5% baryonic matter, 25 % dark matter and 70 % dark energy [8]. The SM describes only the baryonic matter.

Gravity The fourth type of interaction, gravity, is not incorporated in the SM. At the electroweak scale, gravity is so weak as to be negligible. The scale at which effects of quantum gravity are expected to become important is of the order of 10^{19} GeV and is referred to as the Planck scale, M_p.

Baryogenesis The baryon anti-baryon asymmetry observed in the universe is not explained by the SM.

Furthermore, there is a number of problems which either remain unsolved or the solutions incorporated in the Standard Model do not have any fundamental justifications, such as:

The Higgs mechanism and the fine-tuning problem. The Higgs field and the shape of the Higgs potential has been introduced ad hoc. If the Higgs scalar field has indeed a VEV to give a right mass to the $W^{\pm}$ and the Z boson, m_h^2 should be of the order of [100 GeV]^2. Assuming validity of the SM up to some scale, Λ, the Higgs boson mass will receive radiative correction coming from vacuum polarisation diagrams (predominantly top quark loops) of the same order as the scale. It is natural to assume Λ to be the Grand Unification Theory (GUT) scale which is $\sim 10^{16}$ GeV. The natural value for the Higgs mass squared is, therefore, 10^{32} GeV^2, a factor of 10^{28} higher than the experimentally constrained value. This difference, between the experimental value of the Higgs mass and its theoretical 'natural' value, is often referred to as the hierarchy problem. A precise adjustment (fine-tuning) of the SM parameters to fix the hierarchy problem is not very satisfying.

The unification problem. The SM gauge group SU(3)$_C\times$ SU(2)$_L\times$ U(1)$_Y$ consists of three different subgroups each having its coupling constant. The couplings run with the scale and it would be natural if they converge toward a common value at some scale. This scale is referred to as the GUT scale. However, precision measurements have shown, that the three coupling constants do not exactly meet in a single point [9].

The masses and the flavor problem. The SM does not explain why there are exactly three generations of quarks and leptons, the last two being heavier version of the first. Furthermore, the masses of the fermions span over many order of magnitude, as summarised in Fig. 1.1. The reason for this is unknown.

1.2 Models Beyond the Standard Model

1.2.1 A General Overview

Several extension of the Standard Model have been postulated to address the problems outlined in Sect. 1.1.5. General concepts involve:

Imposing supersymmetry. Supersymmetry (SUSY) [10] is a theory which postulates the existence of a symmetry between fermions and bosons. It predicts that for every SM particle, there exist a supersymmetric partner with the same mass but with the spin differing by 1/2. Since the particles have not yet been discovered, the symmetry must be broken at some scale. Supersymmetry is an appealing extension of the SM because it provides solutions both to the hierarchy (through cancellation of the fermion and boson loops) and to the unification problems. In R-parity conserving models, the Lightest SUSY Particle (LSP) is stable and can therefore account for the Dark Matter. The most popular model is the Minimal Supersymmetric Standard Model (MSSM) [11].

Imposing Unification of Gauge Interactions. The Grand Unification Theories [12] predict that at some large scale, $\sim 10^{16}$ GeV, the electromagnetic, weak and strong interactions are unified. This is accomplished by embedding the SM symmetry group $SU(3)_c \times SU(2)_L \times U(1)_Y$ into a larger group, such as SO(10), with only one gauge coupling constant. In most of these models the electroweak symmetry is broken by introducing the Higgs field. Supersymmetry is often required since it provides a solution to the hierarchy problem.

Allowing extra space-time dimensions. The idea being that the four-dimensional world we live in, is embedded in the higher dimensional space. Since the extra dimensions have not been detected so far, they have to be either compactified as in the N.Arkani-Hamed, S.Dimopoulos, and G.Dvali (ADD) [13] and Universal Extra Dimension (UED) models or have a strong curvature, which makes it hard to escape into them as in the Randall-Sundrum (RS) model [14]. In these models, gravity can propagate in the extra dimensions and therefore the Standard Model particles experience only a small fraction of total gravitational force. In this way, the hierarchy problem is solved because the fundamental scale of gravity (and therefore the ultimate limit up to which the SM is valid) lies around the TeV region. In scenarios, where the SM particles are allowed to propagate in the extra dimensions (such as in the UED model) for every SM particle there is a series of particles, the so-called Kaluza-Klein (KK) excitations. The lightest of these KK modes is stable and is therefore a good candidate for Dark Matter [8].

Dynamical symmetry breaking. The dynamic approach to electroweak symmetry breaking has been developed in order to eliminate the somewhat unnatural elementary Higgs boson. The idea was motivated by the premise that every fundamental energy scale should have a dynamical origin and thus the weak scale should reflect the characteristic energy of a new strong interaction called technicolor. Technicolor (TC) and Extended Technicolor (ETC) models are asymptotically free, gauge theories of fermions with no elementary scalars. The electroweak symmetry is dynamically broken through the new, technicolor interaction [15].

Modification of existing particles and their interactions. An example is the String Theory, which assumes particles to be string-like and interactions to be extended, rather then point-like. This theory naturally incorporates Gravity. Supersymmetry and other extra symmetries are also required in these models. Another example is provided by composite models in which quarks and leptons are built of more fundamental constituents.

The goal of experimental physics is to verify the correctness of the models, alternatively to put constraints on the Beyond the Standard Model (BSM) theories. Many hundreds of models, however, can be constructed in the way that they pass the electroweak precision tests. One can vary the number, the size and the shape of the extra dimension, alter the rank of an extra gauge group, impose sypersymmetry or add explicitly extra particles.

A generic feature of most of the SM extensions is the existence of a neutral heavy particle which can decay into two leptons of opposite charge.

1.2.2 Extra Gauge Bosons

A large group of models predict the existence of one or more extra spin-1 gauge boson, commonly called Z'. The Z' particles can be classified into two broad categories depending on whether they arise in GUT scenarios or not [17]. The few examples given in this section are meant to illustrate the various possibilities rather then to provide an exhaustive, fully exclusive list of models. For a detailed review of the models the reader is referred to [17, 18, 19].

The SU(5), SO(10) and E_6 GUT models

The first GUT model was proposed by Georgi and Glashow in 1974 [12]. In this model the SM gauge group $SU(3)_c \times SU(2)_L \times U(1)_Y$ is embedded in a simple group SU(5). The unified group, SU(5), is then thought to be spontaneously broken to the SM group at the GUT scale. The model yields a mechanism for proton decay, predicting its lifetime to be much shorter than experimentally observed. Besides, the experimental measurement of the Weinberg mixing angle ($\sin^2\theta_W$=0.23) contradicts prediction of this model ($\sin^2\theta_W$=0.375). Despite its deficiencies, it created the foundation for more complex models, which are passing experimental constraints. Many of these models involve supersymmetry or superstrings. Here we treat them as originating purely from GUT.

The two most popular GUT scenarios are based on a SO(10) and an E_6 symmetry groups [17].

In SO(10) models, the symmetry can be broken according to the following pattern:

$$\mathrm{SO}(10) \longrightarrow \mathrm{SU}(3)_C \times \mathrm{SU}(2)_L \times \mathrm{U}(1)_Y \times \mathrm{U}(1)_\chi.$$

The extra $\mathrm{U}(1)_\chi$ group leads to existence of the extra neutral gauge boson, commonly denoted Z'_χ. Another interesting possibility is the Left-Right Model which arises from the following intermediate symmetries:

$$\mathrm{SO}(10) \longrightarrow \mathrm{SU}(3)_C \times \mathrm{SU}(2)_L \times \mathrm{SU}(2)_R \times \mathrm{U}(1)_{\mathrm{B-L}}.$$

The $\mathrm{U}(1)_{\mathrm{B-L}}$ is a global gauge symmetry associated to conservation of baryon minus lepton (B-L) number. The presence of the extra $\mathrm{SU}(2)_R$ group can be interpreted as a manifestation of the left-right symmetry of the gauge interactions. The LRM predicts, besides the Z', existence of new charged $W'^{,\pm}$ bosons which couple only to right-handed currents. In SO(10) models one new fermion with the quantum number of the right-handed neutrino is added to complete the SM particle multiplet.

In the E_6 case, the symmetry group can break according to the following pattern:

$$\begin{aligned} E_6 &\longrightarrow \mathrm{SO}(10) \times \mathrm{U}(1)_\Psi \longrightarrow \mathrm{SU}(5) \times \mathrm{U}(1)_\chi \times \mathrm{U}(1)_\Psi \\ &\longrightarrow \mathrm{SU}(3)_C \times \mathrm{SU}(2)_L \times \mathrm{U}(1)_Y \times \mathrm{U}(1)_\chi \times \mathrm{U}(1)_\Psi, \end{aligned}$$

where $\mathrm{U}(1)_\chi$ and $\mathrm{U}(1)_\Psi$ are additional symmetries. The two new Z' bosons will be linear combinations, parametrised by the mixing angle α, of the Z'_χ and Z'_Ψ arising from the two U(1) groups. The Z' given by [18]:

$$Z'(\alpha) = Z'_\chi \cos\alpha + Z'_\Psi \sin\alpha, \tag{1.18}$$

is often assumed to have mass at the TeV scale while the orthogonal state is very heavy and therefore beyond the reach of the LHC.

Special cases of interests are the models where: (i) α=0^o, corresponding to the extra Z'_χ of SO(10), (ii) α=90^o, corresponding to the extra Z'_Ψ of E$_6$ and (iii) α=sin^{-1}($\sqrt{3/8}$) $\sim$ 37.76^o leading to the Z'_η motivated by superstring theories. The E$_6$ model, besides the extra gauge bosons, predicts a large number of exotic fermions. The couplings of these fermions to gauge bosons are fixed in the GUT but the masses are not constrained by the theory.

Models with Extended Weak or Hypercharge Interactions.

Extra gauge bosons arising in models with additional gauge interactions which single out the third generation of fermions provide an interesting non-GUT example [20]. These models involve a dynamical gauge symmetry breaking instead of the usual Higgs field. They can also be string-inspired [21].

A general idea is that one (or more) of the Standard Model groups SU(N) is extended into an SU(N)×SU(N) gauge structure. Fermions of the third generation transform under one SU(N) group and those of the first and second generation transform under the other one as discussed in [20]. The SU(N)×SU(N) group breaks to its diagonal subgroup leading to a set of massive SU(N) gauge bosons which couple with different strengths to fermions of different generations. Examples are theories with an extended SU(2)×SU(2) structure for the weak interactions, such as non-commuting extended technicolor (NCETC) models [22] and topflavor models [23]. Another possibilities are models with an extended hypercharge gauge group, as for instance topcolor-assisted technicolor [24].

The Sequential Standard Model

The Sequential Standard Model (SSM) is not a real model as it breaks the gauge invariance principle. However, due to its simplicity, it is very commonly used in experimental physics as a benchmark scenario. In the SSM scenario, the Z' (Z'_{SSM}) is a heavier copy of the Z boson. Its couplings to fermions are identical to those of the SM Z boson.

1.2.3 Experimental Limits on the Extra Gauge Bosons

Most of the theories, which postulate existence of the extra gauge boson as a manifestation of an extended symmetry group, do not predict the masses of these particles. Several collider experiments have, however, put constraints on their masses.

To extract limits from data, one selects observables O_i and compares with the predictions $O_i((\mathrm{SM}) + Z')$ from a model including a Z'. This allows to exclude or confirm the theory at a given Confidence Level (CL). The limits can be derived from direct production of the Z' or can be based on indirect measurements of various SM signatures below the Z' resonance.

Limits on Z' bosons with universal couplings to fermions

For a few representative models described in Sect. 1.2.2, Tab. 1.1 summarises lower limits on the Z' boson masses derived at 95% CL. *Direct* searches have been performed by the D0 and CDF experiments at Tevatron, 1.96 TeV $p\bar{p}$ Collider. The indirect limits come from various precision *electroweak* data and from measurements of *interference* effects in the process $e^+e^- \to f\bar{f}$ at center-of-mass energy between 130-209 GeV at the Large Electron-Positron (LEP) Collider.

Z' model	*Direct* ($p\bar{p}$)	*Electroweak* (e^+e^-)	*Interference* (e^+e^-)
Z'_{SSM}	923	1500	1305
Z'_{LRM}	630	860	600
Z'_{χ}	822	-	781
Z'_{ψ}	822	-	475
Z'_{η}	891	619	515

Table 1.1: Lower limits, in GeV/c^2, on various Z' models at 95 % CL [25].

Since Z' bosons in these models have universal couplings to all lepton species, the direct searches were undertaken in e^+e^- or $\mu^+\mu^-$ final states as they provide the cleanest signatures. Sensitivity for searches using $\tau^+\tau^-$ invariant mass is considerably lower as illustrated in Fig. 1.3 [26]. In this channel, the SSM Z' can be ruled out only when having a mass below 399 GeV/c^2.

Limits on Z' bosons with enhanced coupling to third generation fermions

In scenarios where a Z' couples preferentially to third generation fermions, direct searches in leptonic final states can only be performed in the two tau channel. One would therefore expect the limit for the Z' mass to be lower than in case of a Z' boson with universal couplings. It turns out, however, that the indirect searches conducted at LEP impose rather severe constraints on such models. The idea being that one can approximate the contribution of the Z' to fermion-fermion scattering as contact interactions, which have

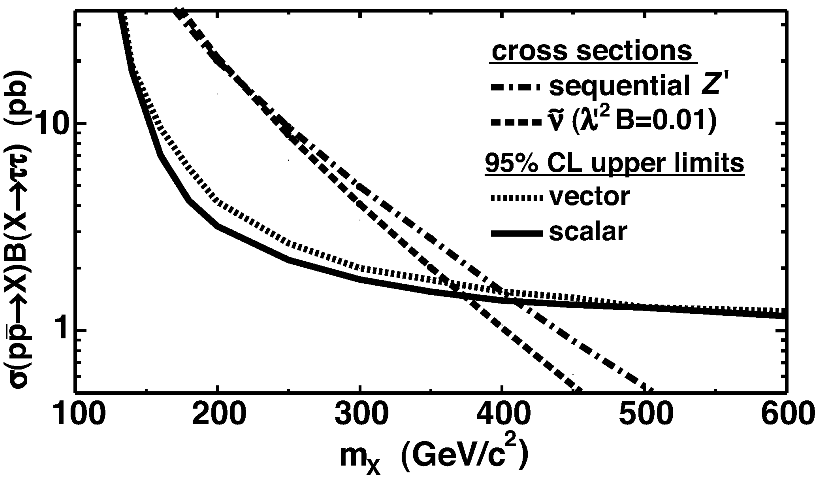

Figure 1.3: Upper limits at 95% CL on the production cross section times branching ratio to tau pairs of scalar and vector particles, as a function of particle mass. The cross section times tau pair branching ratio for the SSM Z' is superimposed [26].

scale set by the mass of the Z' boson. The limits on contact interactions yield a lowest lower limit on the Z' mass of 1090 GeV/c^2 at 95% CL [27].

1.2.4 Other Extra Bosons and Technihadrons

Physics beyond the SM can manifest itself in the existence of one or several new non-gauge heavy neutral particles decaying into a pair of leptons, such as:

The Higgs boson Two heavy (H,A) and one light (h) neutral spin-0 particles are predicted in the Minimal Supersymmetric Standard Model (MSSM) [11] as a consequence of the introduction of two Higgs doublets. The masses of these particles are typically expressed in terms of two parameters, the mass of the CP-odd Higgs boson (m_A) and the ratio between the vacuum expectation values of the two Higgs doublets ($\tan\beta$). They are in general unconstrained by the theory [11]. The lower limit on the mass of m_A was set by LEP experiment to be 93.4 GeV/c^2 [25]. Yukawa couplings of the Higgs bosons are proportional to the mass of the fermions and therefore non-universal for the three families of leptons. The couplings of the Higgs bosons to the down-type fermions, and therefore to the tau leptons, are strongly enhanced for a large region of the MSSM parameter space (large values of $\tan\beta$).

RS graviton The Randal-Sundrum model [14, 28] predicts the existence of a tower of Kaluza Klein (KK) excitation of the graviton. The graviton-fermion couplings are in general universal for all lepton species. The current limits are set by the CDF and D0 collaborations. They depend on the parameters of the model and range from several hundred GeV/c^2 to one TeV/c^2 [25].

KK excitation of the SM Z boson In some models with flat extra dimensions, the gauge bosons, Z, W and γ, are allowed to propagate in the bulk[3] [28]. These theories predicts existence of Kaluza Klein excitations of the SM fields. The first excited state of the Z boson (often denoted Z'), can have a mass of the order of TeV/c^2 and therefore could be produced and observed at the LHC [28].

Technihadrons The existence of a vector meson such as techni-ρ (ρ_{TC}) or techni-ω (ω_{TC}) is postulated in technicolor theories [15, 16]. In general, they are predicted to couple universally to the three generation leptons. The strongest limits come from searches undertaken by the CDF collaboration, which rule out ρ_{TC} and ω_{TC} with masses below 280 GeV/c^2 for a particular model and choice of parameters [29].

1.3 Extra Gauge Bosons and the Large Hadron Collider

Some part of the formalism introduced in this section follows [30].

1.3.1 The $pp \to \gamma/Z/Z' \to f\bar{f}$ process.

The idea to describe the $pp \to \gamma/Z/Z' \to f\bar{f}$ process based on the parton model [31], originally developed for the process of an electron-proton deep inelastic scattering (DIS), was first proposed by Drell and Yan [32, 33]. Given the properties of asymptotic freedom of QCD, the idea is that partons which form the protons interact freely during collisions. The hadronic cross section is hence obtained by summing independent contributions of each parton, weighted by the Parton Density Functions (PDF) in the proton. Furthermore, the factorisation theorem states that one can separate a (short distance) hard process from long distance phenomena and express the inclusive cross section as:

$$\sigma_{pp\to f\bar{f}} = \sum_{q,\bar{q}} \int\int dx_1 dx_2 f_q(x_1,\mu_F^2) f_{\bar{q}}(x_2,\mu_F^2) \hat{\sigma}_{q\bar{q}\to f\bar{f}}(x_1,x_2,\mu_F^2), \tag{1.19}$$

where x_1 and x_2 are the momentum fractions of the protons taken by partons, μ_F^2 is the factorisation scale and $\hat{\sigma}_{q\bar{q}\to f\bar{f}}$ is the cross section for the hard process: $q\bar{q} \to f\bar{f}$.

---

[3] The term 'bulk' denotes the the overall space with number of dimensions greater then four.

Regardless of the theoretical origin of an extra gauge boson, the phenomenological description of its production and decay is analogous to that of the SM Drell-Yan process $q\bar{q} \to \gamma/Z \to f\bar{f}$ as illustrated in Fig. 1.4.

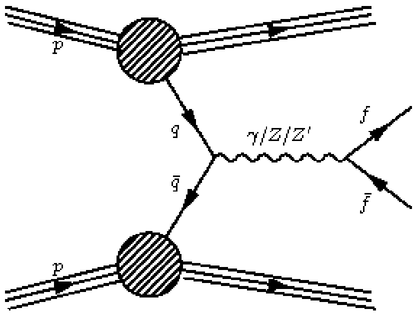

Figure 1.4: The Feynman diagram for $pp(q\bar{q}) \to \gamma/Z/Z' \to f\bar{f}$ process.

1.3.2 The $q\bar{q} \to \gamma/Z/Z' \to f\bar{f}$ process.

At high energies, in the massless fermion limit, helicity conservation ensures that the extra gauge bosons couple to pairs of fermions with opposite helicities. The only non-zero contributions to the $q\bar{q} \to \gamma/Z/Z' \to f\bar{f}$ process are therefore: $q_L\bar{q}_R \to f_L\bar{f}_R$, $q_L\bar{q}_R \to f_R\bar{f}_L$, $q_R\bar{q}_L \to f_L\bar{f}_R$ and $q_R\bar{q}_L \to f_R\bar{f}_L$. The four configurations give rise, at the lowest order[4], to a differential cross section of the form[5] [30]:

$$\frac{\mathrm{d}\hat{\sigma}^{qf}}{\mathrm{d}\cos\theta}(\hat{s}) = \sum_{B,B'} \frac{\mathrm{d}\hat{\sigma}^{qf}_{BB'}}{\mathrm{d}\cos\theta}(\hat{s}) = \sum_{B,B'} \hat{\sigma}^{qf}_{BB'}(\hat{s}) \times \{\frac{3}{8}(1+\cos^2\theta) + \frac{3}{4}\frac{C^{qf}_{BB'}}{D^{qf}_{BB'}}\cos\theta\}, \tag{1.20}$$

where θ is the angle between the initial state quark and the final state fermion and B, B' stand for the gauge bosons γ, Z and Z'. The factor $\hat{\sigma}^{qf}_{BB'}(\hat{s})$ can be expressed as [30]:

$$\hat{\sigma}^{qf}_{BB'}(\hat{s}) = \frac{\hat{s}N^q_c}{12\pi} g^2_B g^2_{B'} D^{qf}_{BB'} \frac{(\hat{s}-M^2_B)(\hat{s}-M^2_{B'}) + M_B\Gamma_B M_{B'}\Gamma_{B'}}{[(\hat{s}-M^2_B)^2 + M^2_B\Gamma^2_B][(\hat{s}-M^2_{B'})^2 + M^2_{B'}\Gamma^2_{B'}]}. \tag{1.21}$$

In the above relation, N^q_c =3 stands for the number of colors, M_B and Γ_B are the mass and the width of the bosons B. The g_B is the coupling strength of the electromagnetic, weak or extra gauge interactions for B being γ, Z or Z' respectively.

The coefficients $C^{qf}_{BB'}$ and $D^{qf}_{BB'}$ are the following combination of the vector (g_V) and axial-vector (g_A) effective couplings [30]:

$$\begin{aligned} C^{qf}_{BB'} &= g_V^{B,q} g_V^{B,f} g_A^{B',q} g_A^{B',f} + g_V^{B,q} g_A^{B,f} g_A^{B',q} g_V^{B',f} + g_A^{B,q} g_V^{B,f} g_V^{B',q} g_A^{B',f} + g_A^{B,q} g_A^{B,f} g_V^{B',q} g_V^{B',f} \\ D^{qf}_{BB'} &= g_V^{B,q} g_V^{B,f} g_V^{B',q} g_V^{B',f} + g_V^{B,q} g_A^{B,f} g_V^{B',q} g_A^{B',f} + g_A^{B,q} g_V^{B,f} g_A^{B',q} g_V^{B',f} + g_A^{B,q} g_A^{B,f} g_A^{B',q} g_A^{B',f}. \end{aligned} \tag{1.22}$$

---

[4] Higher order effects are discussed, for example, in Ref [18].

[5] The Feynman rules and basic steps to derive this formula can be found in Appendix.

Note that since the electromagnetic interactions are chirally symmetric, the axial couplings of photon are zero (g_A^{γ} =0 in the above relations). The couplings $g_V^{Z'}$, $g_A^{Z'}$and therefore $g_{Z'}$ depend on the particular Z' model.

Various measurable observables are constructed in the way that they are sensitive to the angular dependence of the cross section. They are of great importance in determination of the properties of the extra gauge interactions, such as its chiral structure.

1.3.3 Asymmetries at the Z' pole

At parton level, the forward-backward asymmetry is related to the $C_{BB'}^{qf}$ and $D_{BB'}^{qf}$ coefficients via:

$$\hat{A}_{FB} = \frac{\hat{\sigma}^{qf}(\cos\theta > 0) - \hat{\sigma}^{qf}(\cos\theta < 0)}{\hat{\sigma}^{qf}(\cos\theta > 0) + \hat{\sigma}^{qf}(\cos\theta < 0)} = \frac{3}{4}\frac{C_{BB'}^{qf}}{D_{BB'}^{qf}} \tag{1.23}$$

At the Z' peak, neglecting the small contributions from γ and Z exchange, this asymmetry can be expressed as:

$$\hat{A}_{FB} = \frac{3}{4} \underbrace{\frac{(g_L^q)^2 - (g_R^q)^2}{(g_L^q)^2 + (g_R^q)^2}}_{A_q} \underbrace{\frac{(g_L^f)^2 - (g_R^f)^2}{(g_L^f)^2 + (g_R^f)^2}}_{A_f}, \tag{1.24}$$

where g_L and g_R are the neutral current chiral couplings, related to the vector and axial-vector couplings through the relations $g_L = g_V + g_A$ and $g_R = g_V - g_A$. The A_q and A_f are hence called the initial-state and the final state fermions polarisation (chiral) asymmetries.

At hadronic colliders the forward-backward asymmetry, A_{FB}, depends on the initial state quarks momenta. The $\hat{A}_{FB}$ needs to be, therefore, convoluted with the parton density functions as explained in Sect. 1.3.1. The asymmetry A_{FB} is, thus, a complicated function of the couplings of the Z' to both leptons and quarks and of the structure functions of the proton. Furthermore for the A_{FB} to be a measurable quantity at symmetric proton-proton collisions, one needs to assume that the quarks (since being harder then $\bar{q}$) are travelling in the same direction as the Z' [34]. The measurable asymmetry is therefore somewhat washed out.

Additional information is available for decay channels in which the helicities of the final state fermions are experimentally accessible. At the Z' peak, the polarisation asymmetry A_f and the longitudinal polarisation, P_f, of fermion f are connected through the relation:

$$A_f = \frac{(g_L^f)^2 - (g_R^f)^2}{(g_L^f)^2 + (g_R^f)^2} = -P_f \tag{1.25}$$

Measurement of A_f, which depends only on couplings to the finale state fermions, does not involve knowledge of the proton structure function.

In theories, where more than one extra gauge boson is predicted, a single measurement of its cross section is not enough to determine its coupling strength to fermions. In the E_6 scenario, for example, the Z' couplings depend on a mixing angle α (see eq. 1.18), which is a free parameter of the theory. This parameter can be determined by measuring the forward - backward or the polarisation asymmetry (in the $Z' \rightarrow \tau\tau$ events) as illustrated in Fig. 1.5. Note, that A_f is a much steeper function of α for most of the range of the mixing angle and therefore a measurement of A_f will result in a better determination of α than would an equally precise measurement of A_{FB} [35].

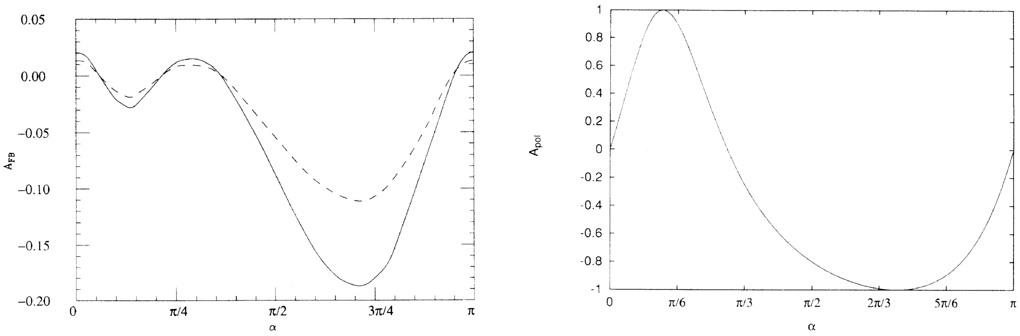

(a) (b)

Figure 1.5: The forward - backward asymmetry (a) and the polarisation asymmetry (b) as a function of the mixing angle α defined in Sect. 1.2.2. In plot (b) A_{pol} stands for A_f. The dashed and the solid lines in (a) correspond to a lepton rapidity cut $|\eta|$ <2.5 and $|\eta|$ <5.0 respectively. The plots were made assuming the Z' to be produced at 40 TeV (center-of-mass energy) pp collider [35].

1.3.4 The Invariant Mass spectrum

Spectra of the invariant mass of the $q\bar{q} \rightarrow \gamma/Z/Z' \rightarrow f\bar{f}$, can be obtained by integrating the angular distribution given in eq. 1.20 over the angle θ and by setting the centre of mass energy $\sqrt{\hat{s}}$ to be $m_{f\bar{f}}$. Restricting a search to $m_{f\bar{f}} > 200$ GeV/c^2 region, one can neglect the Z peak. The two fermion invariant mass can therefore be expressed as [30]:

$$\hat{\sigma}(m_{f\bar{f}}^2) = \frac{N_c^q}{12\pi}(g_\gamma^4 D_{\gamma\gamma}^{qf} + g_Z^4 D_{ZZ}^{qf} + 2g_\gamma^2 g_Z^2 D_{\gamma z}^{qf})\frac{1}{m_{f\bar{f}}^2}$$

$$+\frac{N_c^q}{12\pi}g_{Z'}^4 D_{Z'Z'}^{qf}\frac{m_{f\bar{f}}^2}{(m_{f\bar{f}}^2-M_{Z'}^2)^2+M_{Z'}^2\Gamma_{Z'}^2} \tag{1.26}$$

$$+\frac{N_c^q}{12\pi}(g_\gamma^2 g_{Z'}^2 D_{\gamma Z'}^{qf}+g_Z^2 g_{Z'}^2 D_{ZZ'}^{qf})\frac{m_{f\bar{f}}^2-M_{Z'}^2}{(m_{f\bar{f}}^2-M_{Z'}^2)^2+M_{Z'}^2\Gamma_{Z'}^2}.$$

The first term in this expression corresponds to the SM DY spectra $q\bar{q}\to\gamma/Z\to f\bar{f}$ where the Z peak has been neglected. The second part characterises the Z' resonance, which has the Breit - Wiegner shape, while the last describes the interference of the Z' with the Z and γ bosons. The smaller are the Z' couplings (as compared to those of the Z and γ) the more dominant the interference term is with respect to the Z' peak.

1.3.5 The Z' Width and decay channels

In the absence of any exotic decay channels, the total decay width of the Z' is given by the sum of the partial decay widths to neutrino, leptons and quarks of all three generations. Decays such as $Z'\to W^+W^-$ are expected to be rare [36] and therefore neglected in the current discussion. The partial width of the Z' decaying into a pair of fermions is given (at the lowest order assuming the fermions to be massless) by [30]:

$$\Gamma_{Z'}=\frac{1}{12\pi}M_{Z'}g_{Z'}^2 N_c^q[(g_V^f)^2+(g_A^f)^2]. \tag{1.27}$$

The Z' width is typically of the order of three percent of the mass of the resonance. If exotic decay modes are kinematically allowed, the Z' width becomes larger and, more significantly, the branching rations to conventional fermions smaller.

Considering only decays into known particles, observation of extra gauge bosons in a proton-proton collider may be possible in the following channels:

e^+e^- or $\mu^+\mu^-$ channel. The $Z'\to e^+e^-$ and $Z'\to\mu^+\mu^-$ decays have the highest sensitivity, due to the lowest backgrounds. A high mass resolution in the two electron channel enable measurement of the Z' width [37].

$\tau^+\tau^-$ channel. The $\tau^+\tau^-$ channel has considerably larger background than the e^+e^- or $\mu^+\mu^-$ final states. It also yields significantly worse invariant mass resolution. However, it enables extracting further information by measuring the polarisation asymmetry A_f. Moreover, this channel enables observation of a Z' with enhanced couplings to third generation fermions.

$t\bar{t}$ or $b\bar{b}$ channel. Studies of the heavy flavor decay modes $Z' \rightarrow t\bar{t}$ and $Z' \rightarrow b\bar{b}$ have shown low sensitivity due to the overwhelming QCD background [38].

$q\bar{q}$ channel. The QCD backgrounds are far too large to allow observation of a Z' decaying into light quark pairs.

1.4 Tau Leptons and the Large Hadron Collider

1.4.1 Properties of the Tau Lepton

The tau lepton, τ^-, is the first-discovered member of the third quark-lepton family [39] [6]. It is identical in all respects to its lighter generation counterparts, the electron and the muon, expect for the mass. The tau lepton is unstable. It has a lifetime, τ, of 290.6 fs [25] and $c\tau$ of about 87 μm. With the mass of 1.777 GeV/c^2, it is the only lepton whose decays into hadrons are kinematically allowed.

Decay of the tau lepton can be described via exchange of a virtual W boson as illustrated in Fig. 1.6. The W couples to the first and the second family leptons as well as to the first family quark doublet, consisting of the u quark and the Cabbibo-rotated d' quark fields.

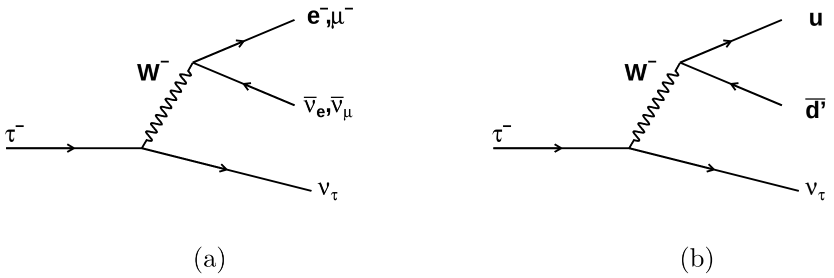

Figure 1.6: The Feynman diagram for (a) leptonic and (b) hadronic τ^- decay.

Leptonic decay modes are well described theoretically. Measurements of tau leptonic branching fractions and lifetime enable precise tests of lepton universality - the fundamental assumption of the SM.

Hadronic decay modes lack theoretical description based on first principles as there is no theory of strong interactions in the limit of low momentum transfer. The

---

[6] For its discovery in mid-seventies M. Perl was awarded the 1995 Nobel Prize in physics.

quark and antiquark do not emerge individually. Hadronisation of the quark pairs, $\bar{u}d$ and $\bar{u}s$, is dominated by resonance production. The meson may be a pseudoscalar, vector or axial-vector particle such as π^-,ρ^-,a_1^- or K^-,K^{*-},K_1^-.

The main tau branching fractions are summarised in Tab. 1.2.

τ^- decay mode	BR %
$\tau^- \rightarrow e^- \bar{\nu}_e \nu_\tau$	17.85
$\tau^- \rightarrow \mu^- \bar{\nu}_\mu \nu_\tau$	17.36
$\tau^- \rightarrow \pi^- \nu_\tau$	10.91
$\tau^- \rightarrow K^- \nu_\tau$	0.67
$\tau^- \rightarrow \rho^- \nu_\tau$	25.95
$\tau^- \rightarrow K^{*-} \nu_\tau$	1.43
$\tau^- \rightarrow h^- 2\pi^0 \nu_\tau$	9.49
$\tau^- \rightarrow h^- 3\pi^0 \nu_\tau$	1.18
$\tau^- \rightarrow h^- h^- h^+ \nu_\tau$	9.80
$\tau^- \rightarrow h^- h^- h^+ \pi^0 \nu_\tau$	5.38

Table 1.2: The main branching ratio (BR) of τ^- [25]. $h^\pm$ stands for $\pi^\pm$ or $K^\pm$. The τ^+ modes are obtained by charge conjugation of the τ^- decays.

1.4.2 Tau Leptons as Polarisation Analysers

Since parity is maximally violated in the charge current weak interactions, the tau is associated with a purely left-handed weak isodoublet partner ν_τ. Due to angular momentum conservation, the angular distributions of the tau decay products depend strongly on the spin orientation of the tau. The idea is illustrated in Fig. 1.7 for the two body $\tau^- \rightarrow \pi^- \nu$ decay mode.

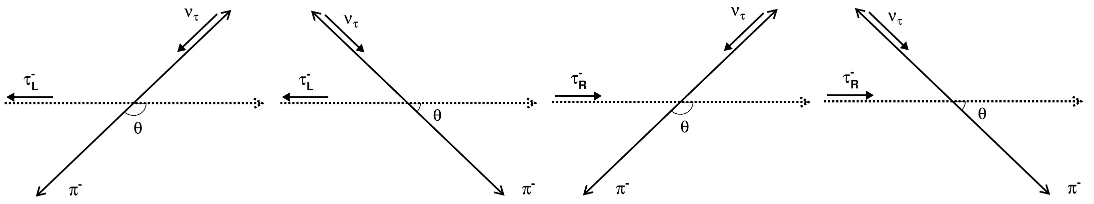

(a) (b) (c) (d)

Figure 1.7: Decay of the left- and the right-handed τ^- into $\pi^-\nu$ in the tau rest frame. The dashed arrows indicate the direction of the τ in the laboratory frame, while the small arrows denote the spin orientation of the fermions. Due to helicity conservation decays (a) and (d) are favoured while decays (b) and (c) are suppressed.

The discussion below of the formalism relating tau longitudinal polarisation, P_τ, to the momentum of its decay particles follows [40].

Hadronic tau decays

The main observable being sensitive to the tau polarisation is the angle, θ, in the tau rest frame between the tau line of flight and the direction of the visible decay products. The decay distribution of τ^- in the $\pi^-\nu$ channel[7] is given by:

$$\frac{1}{\Gamma_\pi}\frac{\mathrm{d}\Gamma_\pi}{\mathrm{d}\cos\theta} = \frac{1}{2}\left[1 + P_\tau \cos\theta\right]. \tag{1.28}$$

For decays involving vector mesons (ρ^-, a_1^-, $K^{*,-}$), the hadronic system can be either transversely (T) or longitudinally (L) polarised. The two possibilities give rise to the two decay distributions

$$\frac{1}{\Gamma_v}\frac{\mathrm{d}\Gamma_v^{\mathrm{L}}}{\mathrm{d}\cos\theta} = \frac{\frac{1}{2}m_\tau^2}{m_\tau^2 + 2m_v^2}\left[1 + P_\tau \cos\theta\right], \tag{1.29}$$

and

$$\frac{1}{\Gamma_v}\frac{\mathrm{d}\Gamma_v^{\mathrm{T}}}{\mathrm{d}\cos\theta} = \frac{m_v^2}{m_\tau^2 + 2m_v^2}\left[1 - P_\tau \cos\theta\right], \tag{1.30}$$

respectively, where v indicates the vector meson state.

Relations given in eq. 1.28-1.30 follow from angular momentum conservation. Decays $\tau^-_{L(R)} \rightarrow \nu_L \pi^-$ and $\tau^-_{L(R)} \rightarrow \nu_L v^-_L$ favour backward (forward) emission of the pion or the longitudinally polarised vector meson, while inverse is true for transversely polarised vector meson emission $\tau^-_{L(R)} \rightarrow \nu_L v^-_T$.

Since the neutrino is not observed, the tau direction and thus the decay angle θ cannot be directly measured. After transformation to the laboratory frame, the decay distributions (1.29-1.30), in the collinear approximation limit ($m_\tau \ll E_\tau$), take the form:

$$\begin{aligned}\frac{1}{\Gamma_v}\frac{\mathrm{d}\Gamma_v^{\mathrm{L}}}{\mathrm{d}\cos\theta} &= \frac{m_\tau^2 m_v^2}{(m_\tau^2 - m_v^2)(m_\tau^2 + 2m_v^2)} \\ &\times \left[\frac{m_\tau^2}{m_v^2}\cos^2\omega + \sin^2\omega + P_\tau\cos\theta \times (\frac{m_\tau^2}{m_v^2}\cos^2\omega + \frac{m_\tau}{m_v}\sin 2\omega\tan\theta - \sin^2\omega)\right],\end{aligned} \tag{1.31}$$

$$\begin{aligned}\frac{1}{\Gamma_v}\frac{\mathrm{d}\Gamma_v^{\mathrm{T}}}{\mathrm{d}\cos\theta} &= \frac{m_\tau^2 m_v^2}{(m_\tau^2 - m_v^2)(m_\tau^2 + 2m_v^2)} \\ &\times \left[\frac{m_\tau^2}{m_v^2}\sin^2\omega + 1 + \cos^2\omega + P_\tau\cos\theta \times (\frac{m_\tau^2}{m_v^2}\sin^2\omega - \frac{m_\tau}{m_v}\sin 2\omega\tan\theta - 1 - \cos^2\omega)\right],\end{aligned} \tag{1.32}$$

---

[7] For τ^+ decays, due to CP invariance, the P_τ changes sign.

In the above relations, ω is the angle between the vector meson quantisation axis in the laboratory and the tau rest frame. It is given by:

$$\cos\omega = \frac{(m_\tau^2 - m_v^2) + (m_\tau^2 + m_v^2)\cos\theta}{(m_\tau^2 + m_v^2) + (m_\tau^2 - m_v^2)\cos\theta} \tag{1.33}$$

The fraction of the tau energy carried by the hadronic system, $x_h = E_h/E_\tau$, is related to the angle θ by:

$$\cos\theta = \frac{2x_h - 1 - m_h^2/m_\tau^2}{1 - m_h^2/m_\tau^2}, \tag{1.34}$$

where m_h is the mass of the hadronic system.

Fig. 1.8a shows the left- and the right-handed taus' decay distributions in the $\tau^- \to \pi^-\nu$ channel. A clear difference is seen. For decays via vector mesons, there appears a strong enhancement of hard longitudinal ρ for P_τ =+1 and soft transverse ρ states for P_τ=-1, as shown in Fig. 1.8b-1.8c. However if no attempt is made to analyse the polarisation of the hadronic systems, one must average over eq. 1.29-1.30 (eq. 1.31-1.32). As a result, the sensitivity to P_τ is reduced by a factor $\alpha_h = \frac{m_\tau^2 - 2m_h^2}{m_\tau^2 + 2m_h^2}$, which is $\sim 1/2$ for the decay involving ρ and almost vanishes in the case of a_1 state.

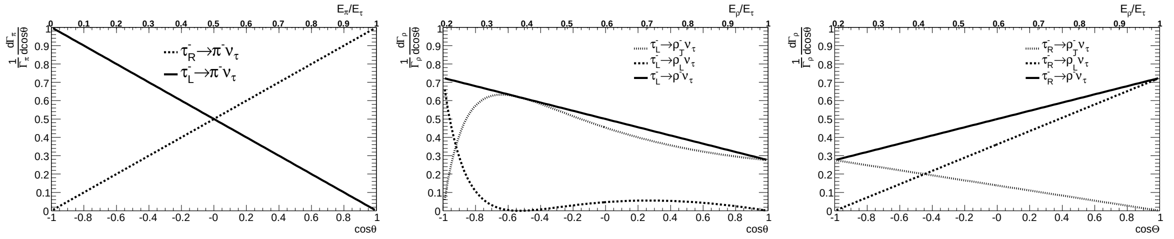

(a) (b) (c)

Figure 1.8: The angular decay distribution in the laboratory frame of (a) $\tau^- \to \pi^-\nu$ (b) $\tau_L^- \to \rho^-\nu$ and (c) $\tau_R^- \to \rho^-\nu$.

For the $\rho^-\nu \to \pi^-\pi^0\nu$ final state, the decay angle ψ in the ρ^- rest frame between the ρ^- and the π^- directions is sensitive to the polarisation of the hadronic state. In terms of laboratory observables, ψ is given by

$$\cos\psi = \frac{m_v}{\sqrt{m_v^2 - 4m_\pi^2}} \, \frac{E_{\pi^-} - E_{\pi^0}}{|\mathbf{p}_{\pi^-} + \mathbf{p}_{\pi^0}|}, \tag{1.35}$$

where E_{π^-} and E_{π^0} ($\mathbf{p}_{\pi^-}$ and $\mathbf{p}_{\pi^0}$) are the energies (momenta) of the charged and neutral pions, respectively. The decay distributions of the ρ indicate that transversely polarised ρ favour equal slitting of the ρ energy between the two pions, while longitudinally polarised states lead to a large asymmetry between the pion energies. The complete information of the tau polarisation in the $\rho^-\nu \to \pi^-\pi^0\nu$ final state is contained in the double decay angular distribution shown in Fig. 1.9.

Tau decays via a_1 vector meson lead to three pions in the final state. To extract full information of the parent tau helicity in those decays, up to six kinematical variables are involved. Furthermore this procedure requires an assumption of a model for the a_1 decay [41, 42].

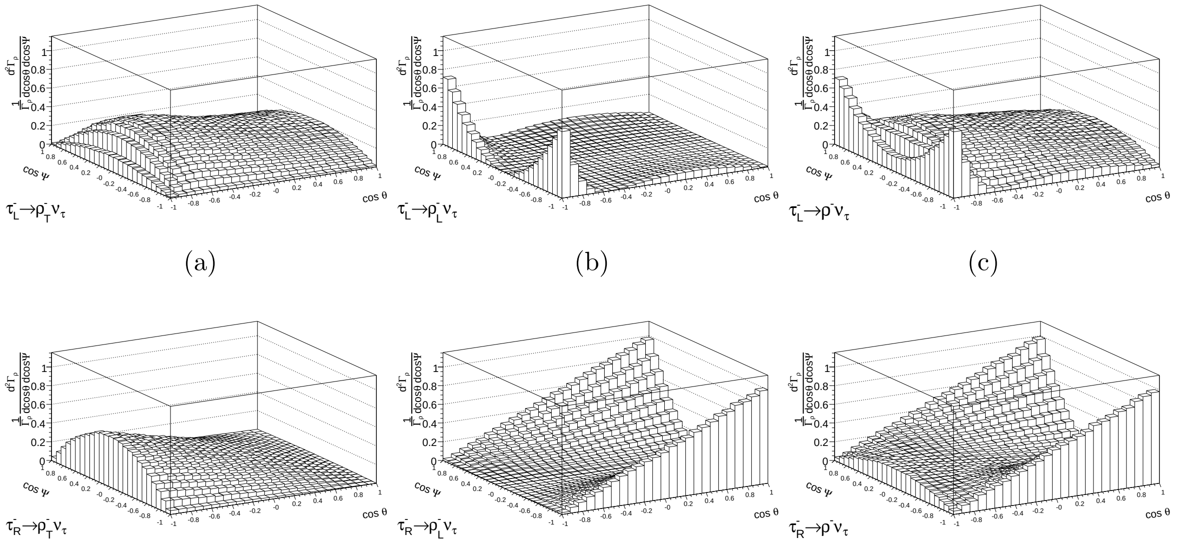

(a) (b) (c)

(d) (e) (f)

Figure 1.9: The decay distributions $\frac{1}{\Gamma_\rho}\frac{d^2\Gamma_\rho}{\mathrm{d}\cos\theta\mathrm{d}\cos\Psi}$ for $\tau_L \to \rho\nu$ (a),(b),(c) and $\tau_R \to \rho\nu$ (d),(e),(f) proceeding via transversely (a),(d) and longitudinally polarised (b),(e) ρ states as well as the sum of the two contributions (c),(f).

Leptonic tau decays

For the leptonic tau decays, there are two neutrinos in the final state. The laboratory frame distribution for the $\tau^- \to l^-\bar{\nu}_l\nu_\tau$ channel takes the form:

$$\frac{1}{\Gamma_l}\frac{\mathrm{d}\Gamma_l}{\mathrm{d}x_l} = \frac{1}{3}(1-x_l)\left[(5+5x_l-4x_l^2)+P_\tau(1+x_l-8x_l^2)\right], \tag{1.36}$$

with $x_l = E_l/E_\tau$, which yields relatively weak dependence of the lepton spectrum on P_τ.

Sensitivity

For each tau decay channel, using the symbol $\mathbf{z}$ to designate the set of n observables used for extraction of the tau longitudinal polarisation, the decay distribution can be written in the generic form [42]:

$$W(\mathbf{z}) = f(\mathbf{z}) + P_\tau g(\mathbf{z}), \tag{1.37}$$

where the f and g functions satisfy the normalisation and positivity conditions:

$$\int f(\mathbf{z}) d^n\mathbf{z} = 1, \quad \int g(\mathbf{z}) d^n\mathbf{z} = 0, \quad f \geq 0, \quad |g| \leq f. \tag{1.38}$$

To quantify the analysing power of each of the different tau decay channels, the sensitivity S can be calculated as [42]:

$$S^2 = \int \frac{g^2}{f + P_\tau g} d^n\mathbf{z}. \tag{1.39}$$

Each channel contributes to the P_τ measurement with a weight w being the product of the sensitivity squared, S^2, times the branching fraction B for a particular mode: $w = S^2 B$. Tab. 1.3 summarises the sensitivities for the main tau decay channels in the ideal case, that is when detector effects are neglected. In the case of the $\tau \rightarrow \pi\nu$, the decay kinematics are fully reconstructed, and therefore S takes its maximal value of 0.58. Since, however, the $\tau \rightarrow \rho\nu$ channel has twice higher branching fraction, this mode has a higher weight to the total measurement then the $\tau \rightarrow \pi\nu$ channel.

Channel	Number of observables		
Sensitivity	$\cos\theta$	$\cos\theta$ and $\cos\psi$	all
$\tau \rightarrow \pi\nu_\tau$	0.58	-	0.58
$\tau \rightarrow \rho\nu_\tau$	0.26	0.49	0.49
$\tau \rightarrow a_1\nu_\tau$	0.10	0.23	0.45
$\tau \rightarrow l\bar{\nu}_l\nu_\tau$	0.22	-	0.22

Table 1.3: Sensitivities of the τ decay channels assuming P_τ=-0.15 [42].

Measurement of tau polarisation in the $Z' \rightarrow \tau^+\tau^-$ events

There are two important aspects related to the measurement of the tau polarisation in $Z' \rightarrow \tau^+\tau^-$ events.

First of all, due to angular momentum conservation, fermions produced in Z′ decays have opposite helicities: $\mathrm{Z}' \rightarrow \tau^+_{\mathrm{L}}\tau^-_{\mathrm{R}}$ or $\mathrm{Z}' \rightarrow \tau^+_{\mathrm{R}}\tau^-_{\mathrm{L}}$. Since, however, also the helicities of the ν_τ and $\bar{\nu}_\tau$ are opposite, the angular distributions in τ^- and τ^+ decays have the same P_τ dependence:

$$W(\mathbf{z})_{\tau^\pm} = f(\mathbf{z}) + P_\tau g(\mathbf{z}), \tag{1.40}$$

As a consequence, the decay distributions of the τ^- and τ^+ can be simply added up in the P_τ measurement without discrimination between the charges.

Secondly, the $\cos\theta$ variable depends on the fraction of the tau energy carried by the hadronic system, $x_h = E_h/E_\tau$. The measurement therefore relies on knowledge of the tau energy. Since energy is carried away by neutrinos, this is experimentally accessible only via the collinear approximation in which the visible decay products are assumed to emerge along the directions of the parent tau-leptons and the total missing momentum in the event is assumed to arise from the neutrinos from the tau decays. In this limit, the two unknown visible momentum fractions x_1 and x_2 are constrained by:

$$\begin{aligned} \frac{p_{x,1}}{x_1} + \frac{p_{x,2}}{x_2} &= p_{x,1} + p_{x,2} + p_{x,miss} \\ \frac{p_{y,1}}{x_1} + \frac{p_{y,2}}{x_2} &= p_{y,1} + p_{y,2} + p_{y,miss}, \end{aligned} \tag{1.41}$$

where p_x ($p_{x,miss}$) and p_y ($p_{x,miss}$) denote the x and y components of the transverse momentum of the visible decay products (neutrinos). The collinear approximation reaches its limit when the two tau decays are back-to-back. Thus, for a heavy Z', it leads to a considerable loss of statistics with an acceptance only at 10 % level. A method suited for tau polarisation measurement in the $Z' \rightarrow \tau^-\tau^+$ events at the LHC is discussed in Note D.

2 EXPERIMENTAL SETUP

The Large Hadron Collider (LHC) at CERN will provide collisions of particles at unprecedented high energies, which existed a fraction of nano-second after the Big Bang. Under these extreme conditions, never reached before in a laboratory, new particles may be produced and measured in the detectors providing signs of new physics. This chapter describes the overall experiment with the emphasis put on those aspects which are important for triggering, reconstruction and identification of τ leptons. It is organised as follows. In Sect. 2.1, a short overview of the LHC is given. First, physics goals are outlined and subsequently the LHC accelerator is briefly described. Next the layout of the ATLAS (A Toroidal LHC ApparatuS) detector is presented in Sect. 2.2 based on [44]. Physics requirements imposed on the design of ATLAS and its main components are reviewed. In Sect. 2.3 the ATLAS trigger system is shortly outlined. The chapter closes with Sect. 2.4 where the full simulation of events in ATLAS is described and the main aspects related to reconstruction of τ leptons are reviewed.

2.1 The Large Hadron Collider

2.1.1 Goals

The LHC is intended to provide proton-proton collisions[1], with a centre of mass energy of 14 TeV at a designed luminosity of $10^{34}\text{cm}^{-2}\text{s}^{-1}$. This high luminosity and resulting interaction rate are needed because of the small cross-section expected for many interesting new physics processes such as a production of heavy neutral bosons as shown in Fig. 2.1. Collisions will happen every 25 ns and will yield approximately 23 collisions per bunch crossing. The multiple interactions per bunch crossing are commonly refereed to as *pile-up* events. The LHC will also collide heavy ions, such as lead nuclei, at 5.5 TeV per nucleon pair at a designed luminosity $10^{27}\text{cm}^{-2}\text{s}^{-1}$.

---

[1] The choice of protons as beam constituents ensures that the energy losses in the form of synchrotron radiation are small.

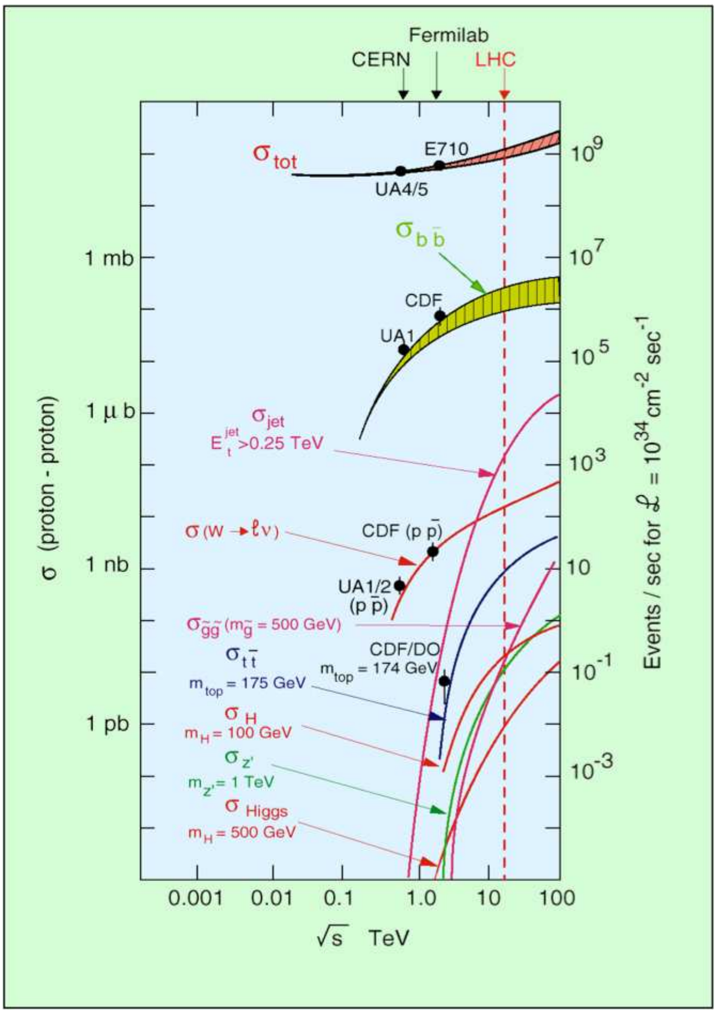

Figure 2.1: The cross section and interaction rates for various physics processes as a function of a centre of mass energy of the protons [45].

2.1.2 Design

The Large Hadron Collider has been installed in a 27 kilometre circumference tunnel, which is approximately 100 meters underground and was used in the previous Large Electron Positron experiment. The equal charge of the two proton beams requires two separate beam lines. The accelerator consists therefore of two interleaved synchrotron rings, which share the same mechanical structure and cryostat. The main elements of the magnet system are 1232 superconducting niobium-titanium dipole and 392 quadrupole magnets operating in super-fluid helium in temperature of 1.9 Kelvin. The dipole magnets are used steer the particles along the ring while the quadrupole magnets are focusing the beams. The dipole magnet strength is 8.3 T.

A system of smaller accelerators prepare the proton beams to be injected into the LHC. The system consists of the 50 MeV Linac, the 1 GeV booster, the 26 GeV Proton

Synchrotron (PS) and the 450 GeV Super Proton Synchrotron (SPS). The protons are then accelerated in the LHC ring to 7 TeV. The two beams are made to collide at four points where the main detectors are built. ATLAS and CMS [46] are general purpose detectors. Although they share the same physics goals they involve different technical solutions and magnet system. ALICE [47] is optimised to study the quark-gluon plasma in collision of heavy nuclei, while LHCb [48] is designed to investigate CP violation in the b-quark sector.

2.1.3 Coordinate System

The interaction point defines the origin of the coordinate system. The beam direction defines the z-axis, the x-axis is defined as pointing from interaction point to the centre of the LHC and the positive y-axis points upwards. The polar angle to the z-axis is called θ and the azimuthal angle ϕ is measured around the beam axis. Positions are usually given in terms of pseudorapidity η, defined as $\eta = -\ln \tan \theta/2$.

2.2 The ATLAS Detector

2.2.1 Performance goals and layout structure

The goal of ATLAS is to cover the largest possible range of physics, such as searches for new heavy bosons (in particular the Higgs boson), supersymmetric particles or any other phenomena indicating new physics at energies up to a few TeV. The masses of the new particles are, in general, unconstrained by theory and their branching fractions into different final states vary as a function of their masses. The detector has to be, therefore, sensitive in a large number of possible decay channels. It needs to be capable of measuring particle's momentum and position with high resolution and provide an excellent particle identification. Due to the very high interaction rate, the detectors require fast and radiation-hard electronics.

Since the QCD dijet production dominates by many orders of magnitude over the production of new particles, ATLAS has to enable identification of experimental features characteristic to the rare processes. A typical signature of many new physics events is the presence of non-interacting particles, such as the SM neutrinos or SUSY neutralinos. Their observation is possible through detection of the momentum imbalance in the transverse plane often referred to as the missing momentum, P_T^{miss}. For the reconstruction of P_T^{miss} it is important that the ATLAS calorimeter system has a coverage as close to 4π as possible. Many new physics events, such as Higgs boson production and decay, are characterised by the presence of b quarks in the final state. The ATLAS detector has therefore been designed to enable reconstruction of secondary vertices which are of great importance in identification of b-jets.

To accomplish its task, ATLAS combines several sub-detectors. The layout structure, with inner detectors, calorimeters and muon spectrometer is shown in Fig. 2.2.

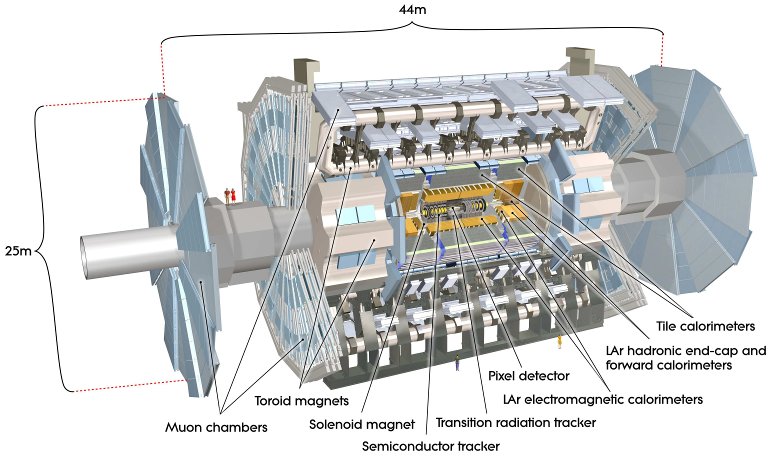

Figure 2.2: Overview of the ATLAS detector [44].

2.2.2 The Inner Detector

Approximately 1000 particles will emerge at the interaction point every 25 ns creating a very large track density in the Inner Detector (ID). To achieve the high momentum and vertex resolution as well as a robust pattern recognition, the ID is built using a typical layer structure. It consists of three fine granularity sub-detectors, which involve different technologies. The Pixel Detector (PD) is located closest to the interaction point, the Semi-Conductor Tracker (SCT) is in the middle, while the Transition Radiation Tracker (TRT) is placed at outer radii. The expected resolution of the track momentum measurement is $\sigma_{p_T}/p_T = 0.05\% p_T \oplus 1\%$, with p_T given in GeV/c. Each sub-detector consist of a barrel and two end-caps as illustrated in Fig. 2.3.

Pixel Detector and Semiconductor Tracker

The PD is designed to provide precision measurements closest to the interaction point. The pixels are built of silicon. They are arranged in three precision layers, at average

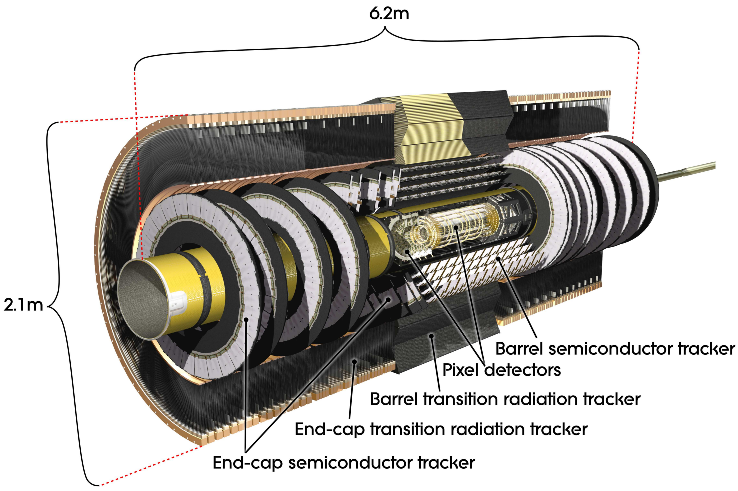

Figure 2.3: Overview of the ATLAS Inner Detector [44].

radii, R, of 5.1, 8.9 and 12.3 cm, typically crossed by each track. The intrinsic accuracies are 10 μm in the $R\phi$ direction and 115 μm in the z direction. The SCT consists of four semiconducting double-sided layers at average radii of 29.9, 37.1, 44.3 and 51.4 cm and provides eight precision measurements for each track. The resolution is 17 μm in the $R\phi$ direction and 580 μm in the beam direction. Both precision tracking detectors (PD and SCT) cover the region $|\eta|$ <2.5. The barrel-end-cap transition occurs at $|\eta| \sim 1.7$ in the PD and at $|\eta| \sim 1.4$ in the SCT detector. The semiconducting trackers allow impact parameter measurements and reconstruction of secondary vertices for short-lived particles such as τ-lepton. The innermost layer of pixels, called B-layer, is especially important as it enhances the performance of the secondary vertex measurement.

Transition Radiation Tracker

At the larger radii between 55.4 and 108.2 cm, straw tubes are used for tracking. The straws have a wire of tungsten in the middle and are filled with xenon-based gas mixture. A particle which crosses a straw causes the gas to ionise, and the ionisation electrons drift to the anode wire. The straw hits contribute significantly to the momentum measurement. The TRT only provides $R\phi$ information, for which it has an intrinsic accuracy of 130 μm per straw. The lower precision per point compared to the silicon is compensated by the large number of measurements. The TRT enables track following up to $|\eta| = 2.0$ with the barrel-end-cap transition occurring at $|\eta| = 0.7$.

Besides its tracking function, TRT is also designed to provide particle identification.

The idea is exploiting the Transition Radiation (TR) which occurs when a charged ultra-relativistic particle traverse a boundary (interface) between two media with different dielectric constants. The effect depends on the media and the distance between boundaries. The straws are, therefore, interleaved with radiator material to enhance the emission of TR. The probability that a charged particle emits TR increases with the Lorentz boost factor γ. Thus, at a given momentum, a lighter particle has a higher probability to emit TR then a heavier particle. This effect therefore enables efficient discrimination between electrons and pions. Since transition radiation gives a higher signal amplitude in comparison to the one coming from ionisation, the dual function of the TRT is accomplished by having two thresholds: a low threshold for ionisation, and a high threshold for TR hits.

2.2.3 Calorimeters

The ATLAS calorimeters are located outside the solenoidal magnets which surround the inner detector. The layout structure of the ATLAS calorimeters, with electromagnetic and hadronic components, is illustrated in Fig. 2.4a.

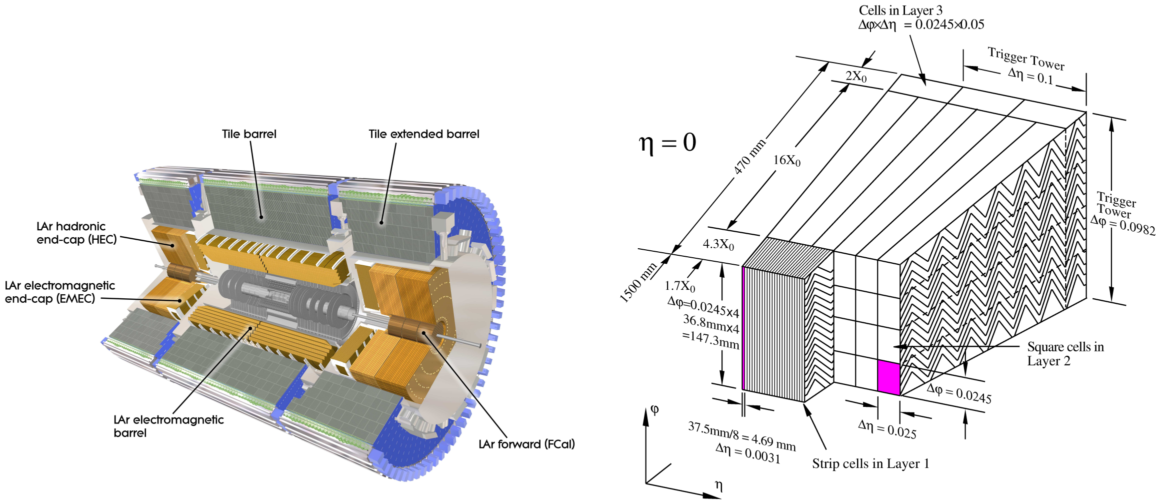

(a) (b)

Figure 2.4: Overview of the ATLAS calorimeters (a), structure of LAr calorimeter in the barrel region (b) [44].

LAr electromagnetic calorimeter

The electromagnetic (EM) calorimeter is a lead-LAr (LAr for Liquid Argon) detector with accordion-shaped electrodes, lead absorber plates and LAr active medium. The use of LAr necessitates the operation at low temperatures, and therefore the calorimeter is immersed inside a cryostat. The choice of accordion geometry ensures complete ϕ symmetry without azimuthal cracks. The EM calorimeter is divided into a barrel part ($|\eta|$ <1.475) and two end-cap components (1.375< $|\eta|$ <3.2). The detector covers the region up to the radius of 2.25 meter, corresponding to more then 22(24) radiation lengths (X_0) in the barrel (end-cap) region.

The EM calorimeter is designed to provide precision measurement of electrons and photons. The energy resolution is $\sigma_E/E = 10\%/\sqrt{E} \oplus 0.7\%$. In the region devoted to precision physics ($|\eta|$ <2.5) the EM calorimeter is segmented into three longitudinal fine granularity sections as shown in Fig. 2.4b. In the region of $|\eta|$ <1.8, a presampler detector is used to correct for energy losses of particles traversing through the inner detector, the magnet coil and the cryostat. The coarser granularity of the rest of the calorimeter is sufficient to satisfy the physics requirements for jet reconstruction and the missing transverse energy (E_T^{miss}) measurements.

Hadronic calorimeters

The hadronic calorimeter surrounds the EM calorimeter. Radially, the detector extends from an inner radius of 2.28 meters to an outer radius of 4.25 meters. It consists of a barrel Tile calorimeter ($|\eta|$ <1.7) and two end-cap calorimeters (1.5< $|\eta|$ <4.9). The Tile calorimeter uses steel as the absorber and scintillating tiles as the active material. The central barrel ($|\eta|$ <1) is longitudinally segmented into three layers, while the extended barrels (0.8< $|\eta|$ <1.7), are divided into two layers. The end-cap calorimeter consist of the Hadronic End-cap Calorimeter (HEC), covering the region 1.5< $|\eta|$ <3.2 and the high-density Forward Calorimeter (FCal), covering the region 3.1< $|\eta|$ <4.9. The HEC uses LAr as the active material, interleaved with copper as absorber and is segmented into four layers. The FCal consists of three sections, and uses tungsten instead of cooper.

The large η coverage of the calorimeters ensures a good missing transverse energy measurements, which is important for many physics signatures, such as those involving τ leptons and supersymmetric particles. The granularity of these detectors, although coarser than in case of EM calorimeters, is sufficient for jet reconstruction and E_T^{miss} measurements. The energy resolution is $\sigma_E/E = 50\%/\sqrt{E} \oplus 3\%$ for the Tile and HEC and $\sigma_E/E = 100\%/\sqrt{E} \oplus 10\%$ for the FCal respectively. Transition in technology between the barrel and the end-cap calorimeters was necessary to reduce the effects of radiation in the forward region, where the particle multiplicity is the largest.

2.2.4 The Muon System

The muon spectrometer is used for identification and high precision measurements of muons. Its layout structure is shown in Fig. 2.5.

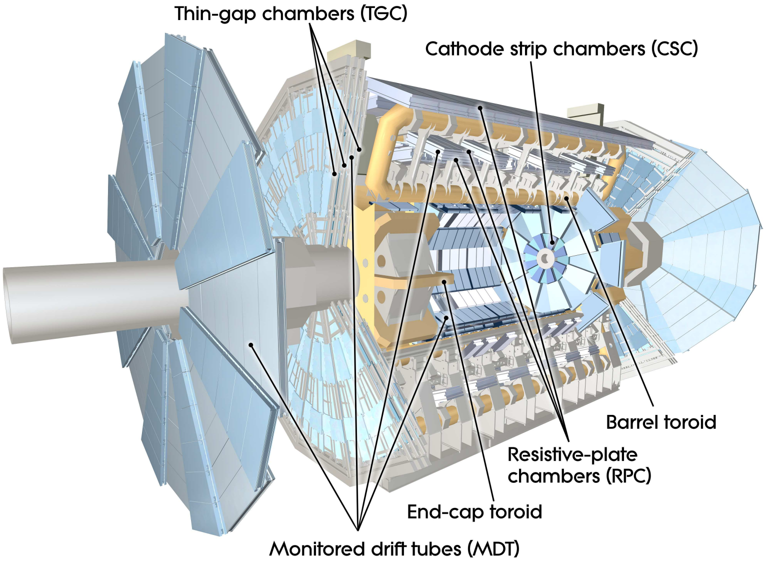

Figure 2.5: Overview of the ALTAS muon spectrometer [44].

The measurements of muon momenta is based on the magnetic deflection of muon tracks in the magnetic field. The field is provided by the barrel toroid, which is placed within $|\eta|$ <1.4, and by two end-cap magnets, which are situated between 1.6 and 2.7 in $|\eta|$. In order to accomplish various physics requirements and to cover a large geometrical region, four different chamber technologies are involved. The Monitor Drift Tubes (MDT's) are designed for precision measurements of track coordinates over a large η-range ($|\eta|$ <2.7). At large rapidities, 2.0< $|\eta|$ <2.7, in the innermost layer Cathode Strip Chambers (CSC's) are exploited instead of MDT's. The remaining two chambers: Resistive Plate Chambers (RPC's) in the barrel and Thin Gap Chambers (TGC's) in the end-cap region, have faster drift times and are therefore used for triggering.

2.3 The ATLAS Trigger System

The nature of proton-proton collisions at the LHC has another non-trivial consequence. The interaction rate at the design luminosity is approximately one GHz, while the present capabilities of storage and data handling limit the data recording to about 200 Hz. A highly sophisticated trigger system is therefore a prerequisite to achieve the acceptable event rate and at the same time ensure that all possible signals of new physics are selected with high efficiency. Most of the bandwidth is assigned to triggers which rely on a single, or a combination of, specific feature of an event, such as the presence of a lepton, photon, a high p_T jet or large transverse missing energy. These signatures are generic enough to cover the wide range of physics processes predicted by both the Standard Model and its various extensions.

The ATLAS trigger system achieves the large required rejection factor against backgrounds by using a multi-level design where the event selection decision is split into different stages (Trigger Level) of increasing complexity and processing time. A schematic overview of the system is shown in Fig. 2.6.

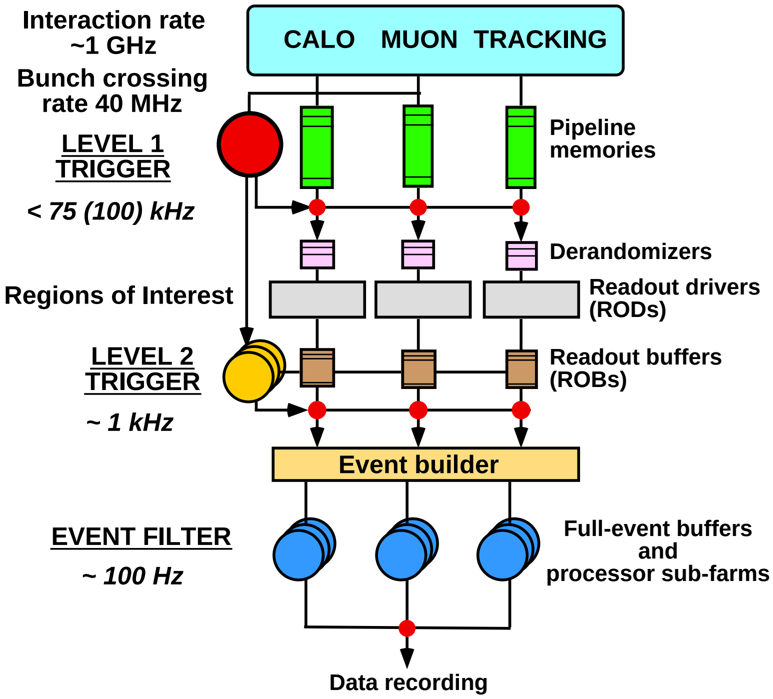

Figure 2.6: Overview of the ALTAS trigger system [49].

The level one (L1) trigger is hardware based and uses the information from the muon trigger chambers as well as reduced-granularity towers from calorimeters. Any sufficiently high p_T object regardless of its type (electron/photon, muon, tau lepton, jet or E_T^{miss}), causes a positive trigger decision. Regions in ϕ and η in the detector, where these objects have been found are called Regions-of-Interests (RoI's). At L1, within 2.5μs only, the data rate is reduced to approximately 75 kHz.

The RoI data includes information on the type of feature identified and the criteria passed, such as a p_T threshold. This information is subsequently used by the High-Level Triggers (HLT): the Level two (L2) and the Event Filter (EF). The L2 selection is seeded by RoI and uses, at full granularity, all the available detector data within the RoI's. It is designed to reduce the rate to approximately 3.5kHz with an event processing time of about 40 ms. The final stage of the event selection is carried by the EF, which uses optimised version of the standard offline ATLAS reconstruction software. It reduces the event rate roughly to 200 Hz. Details about the ATLAS trigger system can be found in [44, 50].

2.4 Monte Carlo Simulation and Reconstruction of Physics Events

Given the complexity of the ATLAS experiment, precise simulations of events are necessary to understand the measured outcome of the collisions. The simulated data enable one to study the discovery potential of the detector and to understand signatures of interesting processes. This knowledge is then used to design the trigger system as well as to develop and optimise the algorithms for the offline events reconstruction.

2.4.1 General framework

Monte Carlo simulation and reconstruction of events are performed within `ATHENA` [52], the ATLAS offline software framework. It consists of several steps which are briefly described below.

Event generation. There are two general purpose Monte Carlo (MC) generators: `PYTHIA` [53] and `HERWIG` [54] which provide a framework for events generation at the LHC. Both generators cover a wide range of physics processes implemented with overall leading order accuracy. They represent, however, different approaches to the 'parton shower', hadronisation and simulation of the underlying event (the remnants of the protons). In the absence of real data it is not possible to judge which of the two generators provide more realistic event description.

There are also other MC programs, which are dedicated to simulation of a specific part of an event and can be interfaced to the general purpose generators. Examples are the `MC@NLO` [55] package which implements, for a limited number of processes, a next-to-leading order matrix element for hard scattering, or the `TAUOLA` [56] library which is used to simulate decays of polarised taus.

The information of the generated particles, their types and kinematics, is stored in the `HepMC` [51] event record.

Detector Simulation and Digitalisation. The generated final state particles are subsequently passed through the ATLAS detector. Their interaction with traversed material is simulated within the `GEANT4` [57] framework. Detailed information on the detector geometry and the magnetic field is used when simulating particles' propagation. At this step, the decay of long lived particles is handled.

To enable comparison with the detector output, the simulated events are digitised. The output format is called the Raw Data Object (RDO).

Reconstruction. As a first step, tracks and calorimeter clusters are reconstructed by the use of complex pattern recognition methods specific for different subdetetctors. This information is subsequently used to create physics objects such as: electrons, muons, photons, tau leptons, jets and missing transverse energy. Each object is reconstructed by the use of a dedicated algorithm.

The results are stored in various formats with different amount of information and event size. The Event Summary Data (ESD) contain, besides the physics objects, the complete information about the energy deposits in the calorimeter cells and about the reconstructed tracks and clusters. The Analysis Object Data (AOD) have reduced size and content while Athena Aware Ntuple (AAN) are dedicated for physics analysis and provide only necessary information on the reconstructed physics quantities.

2.4.2 Tau Lepton Reconstruction and Identification

The tau lepton decays hadronically 65% of all cases, and the remaining fraction of decays are to lighter leptons. Since it will not be possible in the ATLAS detector to discriminate between prompt light leptons and leptons from tau decays, the leptonic modes are not used as the signature of tau production. Identification of hadronically decaying taus is a challenging task, mainly due to the overwhelming background from QCD dijet production.

The hadronic tau decays consist mainly of one or three charged hadrons accompanied with neutrinos and possibly neutral pions. Its reconstruction is restricted to the hadronic components while the neutrinos give rise to the transverse missing energy. Tau decays produce a jet-like cluster in the calorimeter. Such a jet is further characterised by the number of associated tracks reconstructed in the Inner Detector, typically one (one-prong decays) or three (three-prong decays). However due to detector effects, both upwards and downwards migration in the track multiplicity relative to the true number of tracks is observed.

Reconstruction and identification of hadronically decaying taus in ATLAS is performed within the so-called `tauRec` package. In this section only very few relevant aspects are mentioned. An extensive description of the `tauRec` package can be found in [58, 59]. There are two algorithms implemented in the package:

Calorimeter-seeded (historically called `tauRec`) is a generic algorithm and provides a robust tau identification over a wide energy range from 10 GeV up to one TeV. It starts from a calorimeter cluster and then searches for associated tracks within a narrow cone of $\Delta R < 0.3$[2] seeded by the cluster direction. The tracks are required to have p_T above 2 GeV/c and pass loose quality criteria. The energy of the tau is determined by the seed cluster reconstructed in the calorimeters.

Track-seeded (historically called `tau1p3p`) is more specialised, as it is optimised for identification of low energy taus mainly from W and Z boson decays. It starts by selecting a good quality track with p_T above 6 GeV/c and associates the other tracks to the seed track in a narrow cone of $\Delta R < 0.2$. The algorithm requires that there are no tracks in the isolation ring $0.2 < \Delta R < 0.4$. Subsequently the

---

[2] The distance ΔR in the pseudorapidity-azimuthal angle space is defined as $\Delta R = \sqrt{\Delta\eta^2 + \Delta\phi^2}$.

calorimeter energy, deposited in a fixed cone seeded by the track at the vertex, is collected. The tau energy is determined using the energy flow algorithm [60]. This method uses the measured track momentum to improve the overall measurement of the energy in the calorimeters. It provides improvements in the low energy range between 20 and 60 GeV.

The two approaches are illustrated in Fig. 2.7.

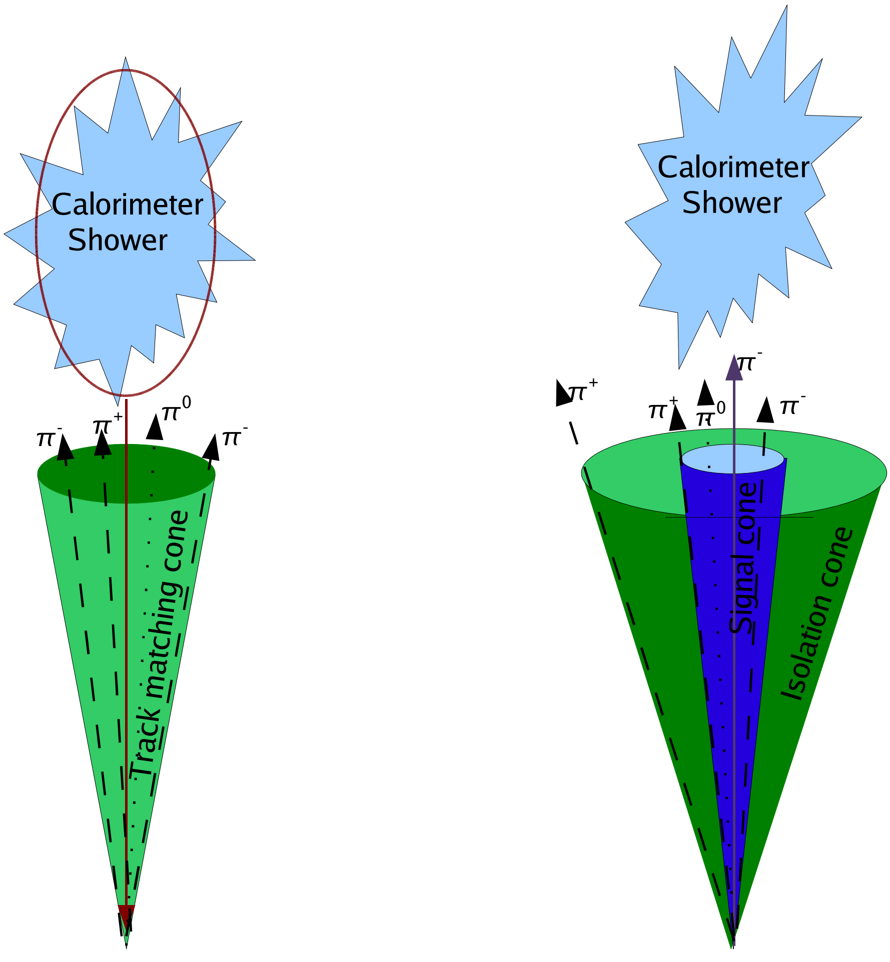

(a) (b)

Figure 2.7: An illustration of the calorimeter-seeded (a) and the track-seeded (b) algorithms for tau reconstruction and identification.

Due to the relatively small mass of the tau lepton, a tau-jet is well collimated. The narrowness of the shower in the calorimeter and low track multiplicity make it possible to distinguish the tau lepton from the QCD jet. The identification, in both algorithms, is based on the combined information from the inner detector and the calorimeters. In both cases, a traditional cut based selection method as well as multi-variate discrimination techniques have been implemented. Their performance for the low and intermediate energy range is discussed in details in [58, 59]. The identification of taus in the high energy region is documented in Note A of this thesis.

The tau identification methods, optimised for rejection of QCD jets, intrinsically provides no rejection against electrons. In the `tauRec` package, suppression of electrons is provided by dedicated tools and is discussed in details in Notes B and C.

Recently[3], the track-seeded and the calorimeter-seeded algorithms run in a merged configuration so it is possible to have reconstructed taus with both a track-seed and a calorimeter-seed, with variables from both `tau1p3p` and `tauRec` algorithms available for tau identification.

---

[3] Since Athena version 14.

3 SUMMARY OF THE THESIS CONTRIBUTION TO ATLAS

This chapter is meant to provide a general overview of the thesis contribution to ATLAS. The work is further detailed in the four Notes included in Part II.

3.1 Searches for a new heavy resonance with tau-pair signature

The existence of an extra gauge boson is a generic feature of many extensions of the SM as discussed in Chapter 1. It can be detected in ATLAS via its decays to two leptons of opposite charge. While studies of heavy resonances decaying into a pair of electrons or muons have been widely conducted in ATLAS [37], the work presented in this thesis shows the first attempt to include searches in the two tau lepton final state.

3.1.1 Discovery potential

The potential of ATLAS to discover a high-mass resonance decaying into two tau leptons is studied in detail in Note A. As a reference for the signal a Z' in the SSM model has been used with masses between 600 and 2000 GeV/c^2. A possible discovery has been studied in a realistic scenario where all detector effects were included and relevant trigger requirements fulfilled. The studies show that despite the large QCD background, the Z' could be discovered in the low mass region already with a few hundred pb^{-1} of integrated luminosity. In order to find the Z' with masses between 1200 and 2000 GeV/c^2, one has to collect more data as illustrated in Fig. 3.1a.

To gauge the discovery range, Fig. 3.1b shows the cross-section needed for a 3σ and a 5σ discovery as a function of a true mass of the Z' assuming one fb^{-1} of data. The 5σ limit can be reached for the Z' mass up to almost 1200 GeV/c^2. For comparison, searches in the e^+e^- or $\mu^+\mu^-$ final states would be able to discover the Z' with a mass up to about 2000 GeV/c^2 [37].

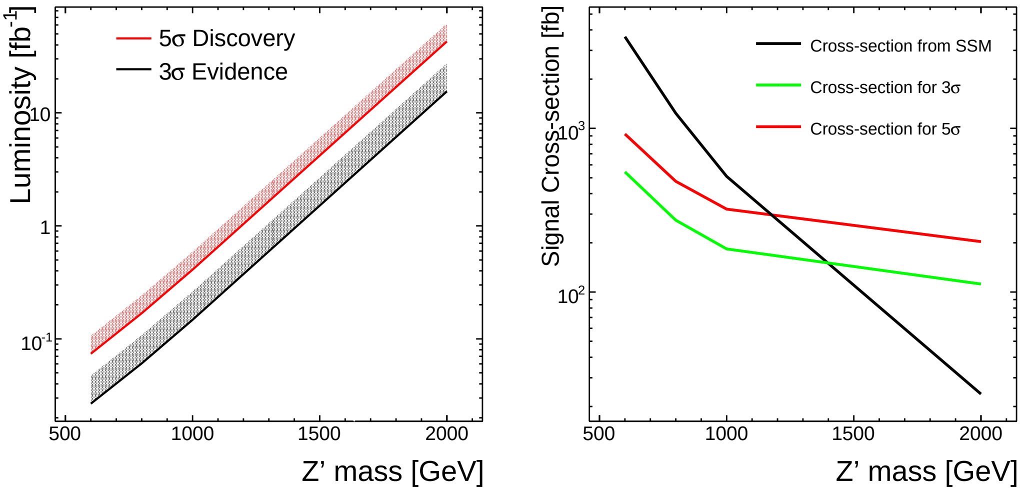

(a) (b)

Figure 3.1: For the $pp \rightarrow Z' \rightarrow \tau^+\tau^-$ process: (a) the luminosity required for 3σ evidence and a 5σ discovery as a function of the true SSM Z' mass and (b) the cross-section required for 3σ evidence and a 5σ discovery as a function of the true Z' mass assuming 1 fb^{-1} of data. The cross-section from the SSM, as a function of Z' mass, is superimposed.

Beyond the SSM model

Although a specific model has been chosen to simulate the signal, the result presented in Fig. 3.1b holds to a large extent for other Z' models. The brief discussion below, of the validity of a model independent search, follows detailed studies performed in [61].

The efficiency of reconstructing an extra gauge boson in the two lepton final state is related to the Z' mass and the coupling constants to quarks. The latter depends on the underlying model. Given that the parton distribution functions of u and d quarks in the proton are different and that leptons in ATLAS can be precisely measured only within pseudorapidity of 2.5 there will be a different fraction of lepton-pairs accepted in the processes: $u\bar{u} \rightarrow Z'$ and $d\bar{d} \rightarrow Z'$, respectively. The difference in reconstruction efficiency for the two extreme scenarios, is of the order of 10% for a Z' with mass of 500 GeV/c^2 and decreases as a function of mass. In most existing models, the Z' couples to a combination of up type and down type quark pairs and therefore the effect will be less stringent.

The effect of tau polarisation and its correlations

It should be emphasised that at the time the samples used for the studies presented in Note A were produced, the `TAUOLA` library was not adopted to simulate tau polarisation and its correlations in the $Z' \to \tau\tau$ process. However the acceptance for event selection, developed in Note A, depends on the kinematics of the two final state tau leptons and therefore on their spin configurations, as discussed in Note D (Sect 4.3). It has been studied that negligence of the spin effects results in an underestimation of the cross section by approximately 6% for the SSM Z' with 600 GeV/c^2 mass. The effect is expected to be less profound for the higher mass points, since the distributions of the event selection variables (such as p_T of the taus or the transverse missing energy) lie further away from the cut values. Had nature produced a Z' of 600/c^2 GeV which couples exclusively to left-handed (right-handed) taus, the required cross section for the discovery would have to be 26 % (13%) higher (lower) than the one shown in Fig. 3.1b.

Discovery of other bosons

In the first approximation, the studies presented in Note A, also illustrate the sensitivity of ATLAS to discover non-gauge bosons, such as a Higgs boson or a Graviton, in the two tau channel. The following effects need to be, however, taken into account. First of all, the spin correlations of the taus coming from decays of a spin-zero Higgs, a spin-one Z' or a spin-two Graviton will be different leading to a difference in the acceptance for the event selection. Secondly, since the production mechanisms of the three bosons differ, they will have different rapidity distributions. Furthermore the pseudorapidity distributions of the final state tau leptons will depend on the spin of the parent resonance. Both effects will influence the acceptance for selection of two taus within $|\eta| <2.5$. Last, the cross section for production of a Higgs or a Graviton is considerably lower than that of a Z' for most models. Therefore it might be necessary to explore extra signatures in these events to accomplish a more efficient separation between signal and backgrounds. For instance in case of the associated production of a Higgs, the sensitivity could be improved by combining the analysis with the requirement of additional identified b-jets in the final state.

3.1.2 Polarisation Measurement

In the event of discovery of a new particle, a natural question emerges regarding the exact nature of the resonance. Interesting constraints on its couplings can be derived by measuring the longitudinal polarisation of the final state tau leptons as discussed in Sect. 1.3.3. Prospects for such measurement have been explored and documented in Note D. The studies were performed based on fully simulated data samples of the SSM Z' with 600 GeV/c^2 mass and both taus decaying hadronically. The proposed method made use of the inclusive sample of one-prong decays with one or more π^0s, corresponding to more than one third of all tau decays. The polarisation was extracted using the Υ variable, which relies on the energy sharing between the charged and the neutral pions, and thus does not require knowledge of the energy of the decaying tau. The result of the fit to the Υ variable is presented in Fig. 3.3. It has been concluded that within the chosen scenario and assuming 30 fb^{-1} of data the tau polarisation could be determined with combined statistical and systematic uncertainties of about 0.12.

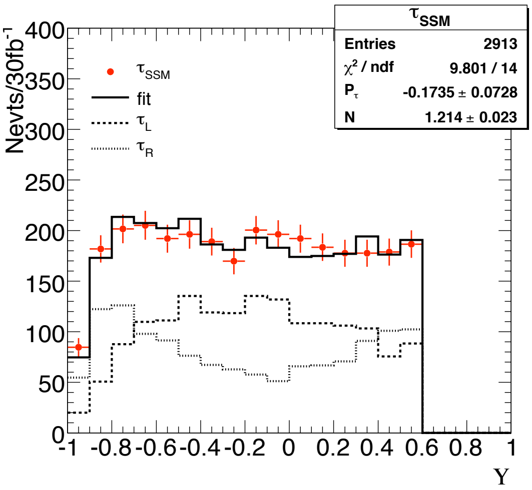

Figure 3.2: Results of the fit to the tau polarisation observable Υ, for taus from the SSM Z' of 600 GeV/c^2 mass. The true tau polarisation (P_τ) equals -0.15.

3.2 Improvements of the tau lepton reconstruction and identification

Searches for new physics in channels involving taus require an excellent understanding of tau leptons' signatures in the ATLAS detector. It can be achieved by observing taus originating from the Standard Model $t\bar{t}$, W and Z decays. These processes will be used as control channels and will be important for tau energy calibration and background normalisation for searches for new physics.

Efficient and robust reconstruction and identification of hadronically decaying taus is provided by the `tauRec` package which was introduced in Sect. 2.4.2. Its development was a team work of many people in ATLAS. In Notes B and C two improvements to the package are discussed: optimisation of criteria for track selection and suppression of backgrounds coming from isolated electrons. Despite the considerable overlap between the two notes inclusion of both illustrates the development of the algorithm.

Selection of tracks from charged hadrons originating from tau decays is a key element of tau reconstruction within the track-seeded approach. Initially, the algorithm used the track quality criteria developed in the context of b-quark tagging. Such selection enabled to efficiently eliminate tracks with hadronic interactions within the Inner Detector (which is important for energy-flow algorithm) as well as to suppress the fraction of taus with misidentified charge. These criteria have been revisited and optimised to accomplish requirements specific for reconstruction of tau leptons such as a high purity in determination of number of prongs. New selection criteria, which considerably diminish migration between one- and three-prong events and at the same time improve the overall tau reconstruction efficiency, have been developed and implemented as default in the track-seeded algorithm. For details the reader is referred to Note B.

The other improvement to the track-based tau reconstruction and identification concerns development and implementation of a dedicated algorithm for suppression of electrons. The method is cut based and uses information form both tracking and calorimetry. Initially the tool was optimised to provide electron rejection in the low energy region up to 80 GeV, which is relevant for tau identification within the track-based approach.

Following the development of the `tauRec` package, the algorithm was adopted to perform on a merged collection of taus reconstructed by both the track- and the calorimeter-seeded approach. The discrimination variables have been reviewed and optimised to cover the energy range from 10 to 1000 GeV. To satisfy requirements of various physics analysis the method was extended to provide three flags: `LOOSE`, `MEDIUM` and `TIGHT` corresponding to different levels of electron suppression. Its performance as a function of calorimeter-seeded transverse energy and pseudorapidity is shown in Figures 3.3a and

3.3b respectively.

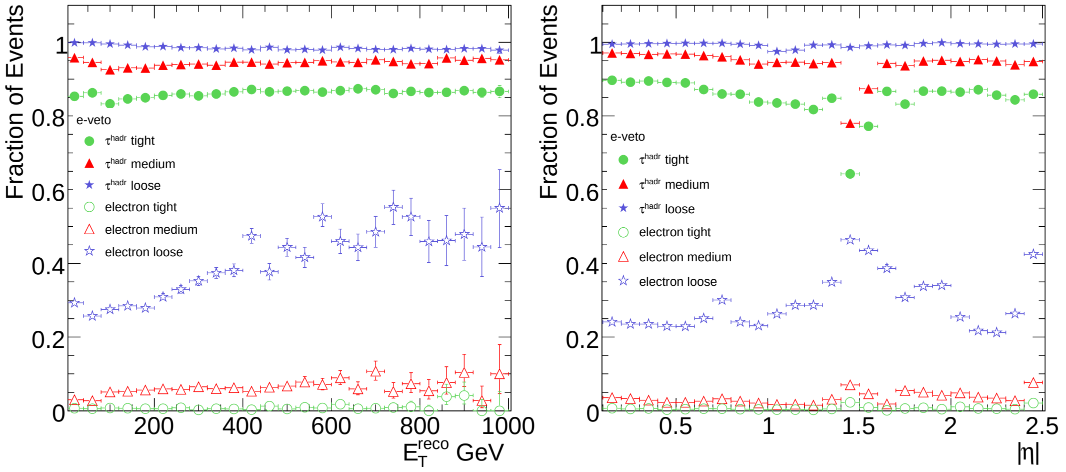

(a)

(b)

Figure 3.3: Selection efficiency for hadronic taus and electrons as a function of (a) E_T and (b) $|\eta|$.

Another related change which appeared in the `tauRec` package concerned the quality criteria applied on the seed track. Since the cut on the fraction of TRT hits exceeding high threshold was designed to veto tracks coming from electrons, this requirement was moved to the dedicated electron veto tool. As a next step in the merging procedure of `tauRec`, it is planned to adopt the algorithm to provide electron suppression for all reconstructed taus, that is also those which do not have the track seed.

3.3 Conclusions

With the start-up of the Large Hadron Collider in the near future an exciting period in particle physics research will begin. In this thesis, the potential for ATLAS to discover a new particle using tau-pair signature has been discussed based on fully simulated data samples. Such particle could be discovered in this channel already with a few fb^{-1} of integrated luminosity. After collecting more data, measurement of tau polarisation would provide an interesting constraint on the nature of the resonance. Now it is time to get data!

BIBLIOGRAPHY

[1] M.Peskin and D.Schroeder, *An Introduction to Quantum Field Theory*, Persus Books, Cambridge, 1995.

[2] A.Pich, *The Standard Model of Electroweak Interactions*, `hep-ph/0502010`.

[3] P.Langacker, *Introduction to the Standard Model and Electroweak Physics*, `arXiv:0901.0241v1`.

[4] S.L.Glashow, *Partial Symmetries of Weak Interactions*, Nucl. Phys. 22 (1961) 579-588.
S.Weinberg, *A Model of Leptons*, Phys. Rev. Lett. 19 (1967) 1264 - 1266.
A.Salam In *Elementary Particle Theory*, ed.N.Svartholm (Almquist and Wiksells, Stockholm 1969), 367-377.

[5] G.Ecker, *Quantum Chromodynamics*, `hep-ph/0604165v1`.

[6] The ALEPH Collaboration, The DELPHI Collaboration, The L3 Collaboration, The OPAL Collaboration, The SLD Collaboration, The LEP Electroweak Working Group and The SLD Electroweak and Heavy Flavour Groups, *Precision electroweak measurements on the Z resonance*, Phys. Rep. 427 (2006) 257-454.

[7] P.Langacker, J.Erler, E.Peinado, *Neutrino Physics*, J. Phys. Conf. 18 (2005) 154-187.

[8] M.Kamionkowski, *Dark Matter and Dark Energy*, `arXiv:0706.2986v1`.

[9] U.Amaldi, W.de Boer, H. Furstenau, *Comparison of grand unified theories with electroweak and strong coupling constants measured at LEP*, Phys. Lett. 260 (1991) 447-455.

[10] H.Nilles, *Supersymmetry, Supergravity and Particle Physics*, Phys. Rept. 110 (1984) 1-162.

[11] S. Martin, *A Supersymmetry Primer*, `arXiv:hep-ph/9709356v5`.

[12] H. Georgi, S. Glashow, *Unity of All Elementary-Particle Forces*, Phys. Rev. Lett. 32 (1974) 438.

[13] N.Arjani-Hamed, S.Dimipoulos, G.Dvali, *The hierarchy problem and new dimensions at a millimeter*, Phys. Lett. B429 (1998) 263-272.

[14] L.Randall and R.Sundrum, *An alternative to compactification*, Phys. Rev. Lett. 83 (1999) 4690-4693.

[15] K.Lane, *An Introduction to technicolor*, `hep-ph/9401324`. K.Lane, *Technicolor 2000*, `hep-ph/0007304`.

[16] C. Hill, E. Simmons, *Strong Dynamics and Electroweak Symmetry Breaking*, Phys. Rept. 381 (2003) 235-402.

[17] T.G. Rizzo, *Z' phenomenology and the LHC*, `hep-ph/0610104v1`.

[18] A.Leike, *The Phenomenology of Extra Neutral Gauge Bosons*, Phys. Rept. 317 (1999) 143-250.

[19] P. Langacker, *The Physics Of Heavy Z' Gauge Bosons*, `arXiv:0801.1345`.

[20] K. Lynch, S. Mrenna, M.Narain and E. Simmons, *Finding Z' bosons coupled preferentially to the third family at CERN LEP and the Fermilab Tevatron*, Phys. Rev. D63 (2000) 035006.

[21] G.Cleaver *et al.*, *Physics implications of flat directions in free fermionic superstring models. I. Mass spectrum and couplings*, Phys. Rev. D59 055005.

[22] R.S.Chivukula, E.H.Simmons, and. J.Terning, *Limits on Non-Commuting Extended Technicolor*, Phys. Rev. D53 (1996) 5258.

[23] D.J.Muller and S.Nandi, *Topflavor: A Separate SU(2) for the Third Family*, Phys. Lett. B383 (1996) 345.

[24] C.T. Hill, *Topcolor Assisted Technicolor*, Phys. Lett. B345 (1995) 483-489.

[25] C.Amsler *et al.*, *Review of Particle Physics*, Phys. Lett. B667 (2008) 1 and 2009 partial update for the 2010 edition.

[26] D. Acosta *et al.*, *Search for New Physics Using High-Mass Tau Pairs from 1.96 TeV $p\bar{p}$ Collisions*, Phys. Rev. Lett. 95 (2005) 131801.

[27] R.S.Chivukula, E.H.Simmons, *Electroweak Limits on Non-Universal Z' Bosons*, Phys. Rev. D 66 (2002) 015006.

[28] G.F.Giudice, D.J.Wells, *Extra Dimentions*, in C.Amsler *et al.*, *Review of Particle Physics*, Phys. Lett. B667 (2008) 1 and 2009 partial update for the 2010 edition.

[29] The CDF Collaboration, A. Abulencia *et al.*, *Search for New High Mass Particles Decaying to Lepton Pairs in $p\bar{p}$ Collisions at $\sqrt{s}$=1.96 TeV*, Phys. Rev. Lett 95 (2005) 252001.

[30] J.Morel, *New resonance (Z') search in the electron channel with ATLAS detector*, CERN-THESIS-2009-024.

[31] J.D.Bjorken, E.A.Paschos, *Inelastic Electron Proton and gamma Proton Scattering, and the Structure of the Nucleon*, Phys. Rev. 185 (1969) 1975-1982.

[32] S.D.Drell and T.M.Yan, *Massive Lepton Pair Production in Hadron-Hadron Collisions at High-Eneries*, Phys. Rev. Lett. 25 (1970) 316-320.

[33] S.D.Drell and T.M.Yan, *Partons and their applications at high energies*, Ann. Phys. 66 (1971) 578.

[34] M.Schafer, F.Ledroit, B.Trocme, *$Z' \to e^+e^-$ studies in full simulation (DC1)*, ATL-PHYS-PUB-2005-010.

[35] J.D. Anderson, M.H. Austern, R.N. Cahn, *Measurement of Z' couplings at future hadron colliders through decays to τ leptons*, Phys. Rev. D46 (1992) 290-302.

[36] V.Barger, K.Whisnant, *Heavy-Z-boson decays to two bosons in E_6 superstring models*, Phys. Rev. D36 (1987) 3429.
M.Cvetic, P.Langacker, *Rare decays as diagnostics for Z' gauge couplings at hadron colliders*, Phys. Rev. D 46 (1992) R14-R18.

[37] The ATLAS Collaboration, *Exotic Processes* in *Expected Performance of the ATLAS Experiment, Detector, Trigger and Physics*, CERN-OPEN-2008-020, `arXiv:0901.0512`.

[38] S. Gonzalez de la Hoz, L. March, E. Ros, *Search for hadronic decays of* Z_H *and* W_H *in the Little Higgs model*, ATL-PHYS-PUB-2006-003.

[39] M.Perl *et al.*, *Evidence for Anomalous Lepton Production in* e^+e^- *Annihilation*, Phys. Rev. Lett. 35 1489.

[40] K.Hagiwara, A.D.Martin and D.Zeppenfeld, τ *Polarization measurement at LEP and SLC*, Phys. Lett. B235 (1990) 198-202.

[41] A.Rouge, *Polarization observables in the* $3\pi\nu$ *decay mode of the* τ, Z. Phys. C48 (1990) 75-77.

[42] M.Davier, L.Duflot, F.Le Diberder and A.Rouge, *The optimal method for the measurement of tau polarization*, Phys. Lett. B306 (1993) 411-417.

[43] A.Rouge, *Tau decays as polarization analysers*, Proceedings of the First Workshop on Tau Lepton Physics, Orsay, 1990.

[44] The ATLAS Collaboration, *The ATLAS experiment at the CERN Large Hadron Collider*, J. Instrum. 3 (2008) S08003.

[45] G.Flugge, *Future Research in High Energy Physics*, 1993 European School of High Energy Physics, Yellow reports, CERN 94-04.

[46] The CMS Collaboration, *Technical Design Report*, CERN-LHCC-2006-001.

[47] The ALICE Collaboration, *ALICE Technical proposal for a Large Ion collider Experiment at the CERN LHC*, CERN-LHCC-95-71.

[48] The LHCb Collaboration, *LHCb Technical Design Report. Reoptimized detector design and performance*, CERN-LHCC-2003-030.

[49] The ATLAS Collaboration, *ATLAS Detector and Physics Performance. Technical Design Report Vol.2*, CERN-LHCC-99-15.

[50] The ATLAS Collaboration, *Trigger* in *Expected Performance of the ATLAS Experiment, Detector, Trigger and Physics*, CERN-OPEN-2008-020, `arXiv:0901.0512`.

[51] M. Dobbs and J.B. Hansen, *The HepMC C++ Monte Carlo Event Record for High Energy Physic*, ATL-SOFT-2000-001, Comput.Phys.Commun.134 (2001) 41-46.

[52] ATLAS Computing group, ATLAS Computing, Technical Design Report, CERN-LHCC-2005-22, 2005.

[53] T. Sjöstrand *et al.*, *High-energy-physics event generation with Pythia 6.1*, Comp. Phys. Comm. 135 (2001) 238; T. Sjöstrand *et al.*, *PYTHIA 6.4 physics and manual*, J. High Energy Phys. JHEP05 (2006) 026.

[54] G. Corcella, I.G. Knowles, G. Marchesini, S. Moretti, K. Odagiri, P. Richardson, M.H. Seymour and B.R. Webber, *HERWIG 6. An Event generator for hadron emission reactions with interfering gluons (including supersymmetric processes)*, JHEP 0101 (2001) 010.

[55] S. Frixione and B.R. Webber, *Matching NLO QCD computations and parton shower simulations*, JHEP 0206 (2002) 029.

[56] S. Jadach, Z. Was, R. Decker and, J.H. Kühn, *The τ decay library TAUOLA, version 2.4*, Comp. Phys. Comm. 76 (1993) 361.

[57] S. Agostinelli *et al.*, GEANT4 Collaboration, *GEANT4: A simulation toolkit*, Nucl. Instrum. Meth. A506 (2003) 250303.

[58] The ATLAS Collaboration, *Tau Leptons* in *Expected Performance of the ATLAS Experiment, Detector, Trigger and Physics*, CERN-OPEN-2008-020, `arXiv:0901.0512`.

[59] A.Christov *et al.*, *Performance of the tau reconstruction and identification algorithm with release 14.2.10*, ATL-COM-PHYS-2009-229, public version in preparation.

[60] E.Richter-Was, H.Przysiezniak, F.Tarrade, *Exploring hadronic tau identification with DC1 datat samples: a track based approach*, ATL-PHYS-2004-030.

[61] F.Ledroit, J.Morel, B.Trocme, *Z' at LHC*, ATL-PHYS-PUB-2006-024.

Appendix

Calculation of cross section for the $q\bar{q} \to \gamma/Z/Z' \to f\bar{f}$ process

Interaction of a Z' boson with the SM fermions can be written as:

$$\mathscr{L} = g_{Z'}\bar{f}\gamma^{\mu}\left\{\frac{g_L^{Z'}+g_R^{Z'}}{2} - \frac{g_L^{Z'}-g_R^{Z'}}{2}\gamma^5\right\} f Z'_{\mu} = g_{Z'}\bar{f}\gamma^{\mu}\left\{g_V^{Z'} - g_A^{Z'}\gamma^5\right\} f Z'_{\mu}, \tag{3.1}$$

where the couplings $g_{Z'}$, $g_V^{Z'}$ and $g_A^{Z'}$ depend on the particular Z' model.

The differential cross section for the $q\bar{q} \to f\bar{f}$ process, with f produced into a solid angle $d\Omega$ can be written as [1]:

$$\frac{d\hat{\sigma}}{d\Omega} = \frac{1}{64\pi^2\hat{s}}|M|^2. \tag{3.2}$$

In the above formula $\hat{s}$ is the center of mass energy squared, M is the quantum-mechnical amplitude for the process to occur.

According to the Feynman rules, contributions to the amplitude can be represented by diagrams. The amplitude for the $q\bar{q} \to \gamma/Z/Z' \to f\bar{f}$ process[1], is given by a sum of a three diagrams, corresponding the the exchange of the γ, Z and Z' as illustrated in Fig.3.4.

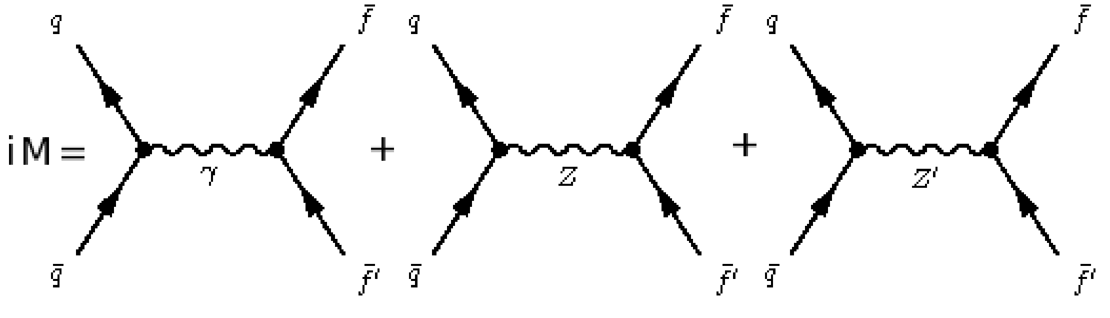

Figure 3.4: The three Feynman diagrams contributing in the lowest order to the amplitude for the $q\bar{q} \to \gamma/Z/Z' \to f\bar{f}$ process.

The amplitude squarred $|M|^2$ can then be written as:

$$\frac{d\hat{\sigma}}{d\Omega} = \frac{1}{64\pi^2\hat{s}}\sum_{B,B'} Re[M_B M^*_{B'}] = \sum_{B,B'}\frac{d\hat{\sigma_{B,B'}}}{d\Omega}, \tag{3.3}$$

---

[1] To the lowest order in the perturbation series.

B boson	Propagator ($P_{B_{\mu\nu}}(k)$	Vertex ($I_B^{f\mu}$)
γ	$-ig_{\mu\nu}/k^2$	$-ig_\gamma \gamma^\mu g_V^{\gamma f}$
Z	$-i\frac{g_{\mu\nu}-k_\mu k_\nu/M_Z^2}{k^2-M_Z^2+iM_Z\Gamma_Z}$	$-ig_Z\gamma^\mu(g_V^{Zf}-g_A^{Zf}\gamma^5)$
Z'	$-i\frac{g_{\mu\nu}-k_\mu k_\nu/M_{Z'}^2}{k^2-M_{Z'}^2+iM_{Z'}\Gamma_{Z'}}$	$-ig_{Z'}\gamma^\mu(g_V^{Z'f}-g_A^{Z'f}\gamma^5)$

Table 3.1: Feynman rules for the $q\bar{q} \to \gamma/Z/Z' \to f\bar{f}$ process.

where M_B is the amplitude for a single diagram corresponding to an exchange of a boson B being the photon γ, the electroweak gauge boson Z or the extra gauge boson Z'. Total amplitude squared is a sum of contributions from pure exchange of the γ, Z or Z' ($B = B'$) as well as from the interference terms between the bosons ($B \neq B'$).

Each diagram is made up from the following components: i) external lines representing the four incoming and outgoing particles, ii) internal lines (propagators) denoting an exchange of the corresponding boson $B = \gamma$,Z or Z' and iii) vertices representing interactions of the correponding boson with fermions. The amplitude associated with a single diagram $q\bar{q} \to B \to f\bar{f}$ can be expressed in terms of the Feynman rules as:

$$-iM_B = \bar{v}_{\bar{q}} I_B^{q\mu} u_q \times P_{B_{\mu\nu}}(k) \times \bar{u}_f I_B^{q\mu} v_{\bar{f}} \tag{3.4}$$

where I_B denotes the $B \to f\bar{f}$ vertex, $P_{B_{\mu\nu}}(k)$ the propagator of boson B and k is the four momentum transfer constraint by the momentum conservation at each vertex. The u, v, $\bar{u}$ and $\bar{u}$ are spinors representing the initial and the final state fermions. The Feynman rules for the vertices and the propagators are summarised in Tab.3.3.

Information on the initial and the final spin states is carried by the four spinors: u, $\bar{u}$, v, $\bar{v}$. Calculation of unpolarised cross-sections involves averaging over the initial and summing over the final spin states. This sum can be performed using the following relations [1]:

$$\sum_s u^s(p)\bar{u}^s = p^\mu\gamma_\mu + m \qquad \sum_s v^s(p)\bar{v}^s = p^\mu\gamma_\mu - m \tag{3.5}$$

Expressions in eq.3.3 of the form $Re[M_B M_{B'}^*]$, can then be evaluated using the Feynman trace technology.

Part II

Included ATLAS Notes

A

Z. Czyczula, T. Vickey, M. Dam, S. Xella, B. Mellado, S.L. Wu

Searching for New Physics using High-P_T Tau Pairs in ATLAS

Searching for New Physics using High-P_T Tau Pairs in ATLAS

Z. Czyczula,[1] M. Dam, S. Xella
Niels Bohr Institute, University of Copenhagen,
DK-2100 Copenhagen, Blegdamsvej 17, Denmark

B. Mellado, T. Vickey,[1] Sau Lan Wu
Department of Physics, University of Wisconsin,
Madison, Wisconsin, USA

Abstract

A number of non-Standard-Model physics processes can lead to events in ATLAS with tau lepton pairs in the final state. In this note we discuss the potential for ATLAS to observe high-mass resonances which decay into two oppositely-charged taus. All three di-tau final states are considered in the study presented here: lepton-lepton, lepton-hadron and hadron-hadron. Using the official ATLAS offline reconstruction software, we consider a Z' with masses between 600 and 2000 GeV. The application of this study to Graviton and heavy MSSM Higgs boson searches is also discussed.

---

[1] Corresponding authors: Zofia.Czyczula@cern.ch and Trevor.Vickey@cern.ch

Contents

1 Introduction

At the LHC, a number of non-Standard-Model physics processes can lead to events with tau lepton pairs in the final state. Examples include the production of extra gauge bosons predicted by Grand Unified Theories (GUT), Extra Dimensions (ED), Superstring theories, Little Higgs as well as Strong Dynamics models [1, 2, 3]. These theories predict the existence of the Z', a new massive and electrically neutral particle which couples equally to all fermion generations [4]. There are however a few models which extend the SU(N) group of the Standard Model to an SU(N)×SU(N) gauge structure in such a way that coupling to the third generation is enhanced [5, 6]. Fermions from the third generation transform under one special unitary group, while those of the first and the second generations transform under a different SU(N). When the SU(N)×SU(N) spontaneously breaks into its diagonal subgroup, the broken generators correspond to the set of massive SU(N) gauge bosons that couple to fermions with different strengths. Examples are non-commuting extended technicolors (NCETC) and a top-flavour model which extends SU(2)×SU(2) structure for the weak interactions as well as top-colour assisted technicolor and flavour-universal top-color assisted technicolor models which include the extended U(1)×U(1) group [7, 8, 9]. In this note we discuss the potential to observe a high-mass resonance which decays into two oppositely-charged taus[1]. All studies presented in this paper refer to proton-proton collisions at a 14 TeV centre-of-mass energy. This note is organized as follows: In Sec. 2, we discuss kinematical quantities of the signal events based on Monte Carlo (MC) truth information. Subsequently, in Sec. 3, we focus on optimizing the rejection of jets coming from QCD di-jet production while providing an efficient identification of high p_T taus. In Sec. 4, various trigger possibilities for each final state (lepton-lepton, lepton-hadron and hadron-hadron) are discussed. Next, in Sec. 5, for each final state (lepton-lepton, lepton-hadron and hadron-hadron) we discuss the individual event selection and significance. Finally we conclude with Sec. 6, where a discussion of the results is presented together with the outlook for further studies. Appendix A provides all details related to the MC samples used in this analysis. Appendix B includes some extra figures related to Sec. 3.

2 Signal Events

In this note we focus on a Standard-Model-like Z' boson produced in the Drell-Yan process via $q\bar{q} \rightarrow \gamma/Z/Z'$. The Feynman diagram for this process is shown in Fig. 1a. At the level of the matrix element calculation, the interference with γ and Z cannot be neglected, therefore in order to not be dominated by $q\bar{q} \rightarrow \gamma/Z$ production, a cut at half of the invariant mass ($\sqrt{\hat{s}}/2$) of the Z' boson has been applied. As a reference for these studies, we assume the simple extension to the Standard Model (SSM). Events were generated in `PYTHIA` [10] which is a general purpose MC generator for high-energy physics events. The production cross-section times branching ratio into a tau-pair as a function of the Z' boson mass is shown in Fig. 1b. The theoretical cross-section is obtained through a convolution of the leading order (LO) matrix element (ME) and the parton distribution functions for protons with the parton shower algorithm accounting for higher order corrections (i.e., soft and collinear enhancements) due to initial state radiation (ISR). More details on generation of the Z' boson can be found in Ref. [10]. It

---

[1] Throughout this paper the charges of the leptons are inferred to be of opposite sign.

should be noted that tau leptons are decayed inside of `PYTHIA` [2], and hence information on the spin correlations of the τ-lepton decay products is not provided.

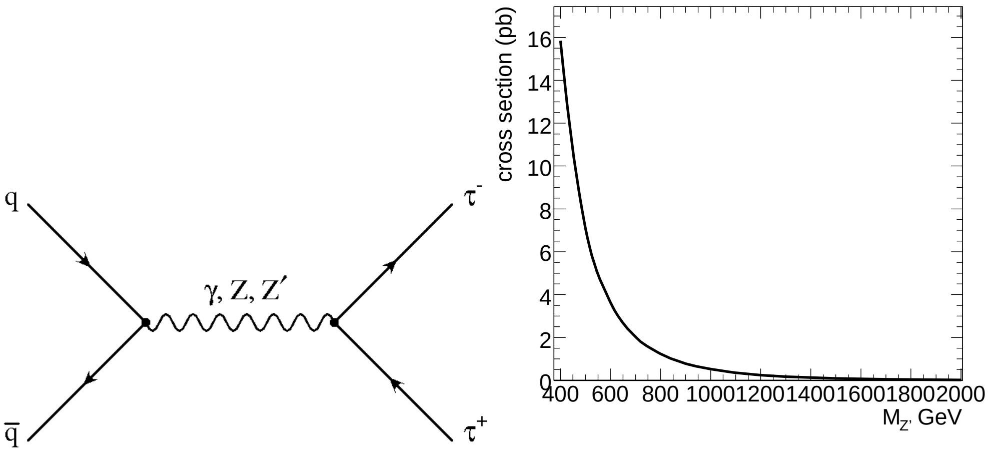

(a) (b)

Figure 1: (a) Feynman Diagram for the Drell-Yan production of $Z' \rightarrow \tau\tau$ and (b) cross-section for $Z' \rightarrow \tau\tau$ production in the SSM as a function of mass.

Current experimental upper limits on the mass of the SSM Z' boson are derived from searches using high-mass tau pairs at the Tevatron experiments and are set to 400 GeV [12]. To study the potential for observing a Z' over a large mass range we consider four different samples of an SSM Z' with masses equal to 600, 800, 1000 and 2000 GeV. Figure 2a shows the mass of the Z' boson from MC generator-level truth for each of the four generated mass points. The intrinsic width obtained from a Gaussian fit in the range of two RMS values around the mean is on the order of $\sim 2\%$ of the gauge boson mass. It should be stressed that the width of the resonance is not an intrinsic feature of the Z' boson but is directly related to the model chosen which predicts the existence of such a gauge boson.

Since the production mechanism is a $2 \rightarrow 1$ process, a non-zero transverse momentum originates from ISR in the case where the Z' recoils against one or more QCD jets. Figures 2b and 2c show the p_T[3] and η distributions of the Z' bosons, respectively. The Z' is produced predominantly in the forward region of the detector with relatively low transverse momentum (p_T/M is on the order of 0.11 and 0.05 for masses of 600 and 2000 GeV, respectively).

In Fig. 3a the transverse momentum distribution of the un-decayed taus coming from the four Z' bosons and sharp Jacobian peak around half of each Z' boson mass can be observed. Figure 3b shows the integrated cosine distribution of the angle between the two tau-lepton visible decay products. Most of the events are produced back-to-back due to the relatively low transverse momentum of the Z'. Experimentally, it is impossible to resolve the neutrino system for such a configuration, therefore those events will not contribute to the invariant mass reconstruction, as discussed later on in Sec. 5. Another feature of $Z' \rightarrow \tau\tau$ events is the relatively large missing transverse

---

[2] Given that the `TAUOLA` package [11] has not been adapted for physics with extra gauge bosons, it has not been used for generation of the signal events.

[3] If not stated otherwise, for all objects but hadronic taus p_T denotes the transverse momentum. In later case p_T stands for the transverse momentum of the visible decay products.

energy (E_T^{miss}) coming from neutrinos from the tau-lepton decays as shown in Fig. 3c. The plots in Fig. 4 show for each Z' mass kinematical quantities, the p_T and η distributions of leptonic and hadronic taus visible decay products. In Tab. 1 the cross-section, intrinsic width and average p_T of the Z' boson as well as an average p_T of tau-leptons, of the hadronic system and of leptons from tau decay are summarized for the four Z' mass points.

	Z' Mass			
MC truth	600 GeV	800 GeV	1000 GeV	2000 GeV
Cross-section fb (Z')	3639.0	1240.0	509.0	24.0
Γ (Z')	13.2	17.6	21.9	43.4
Mean p_T GeV (Z')	63.9	70.5	77.7	94.8
Mean p_T GeV (Un-decayed τ)	216.2	286.1	352.7	678.7
Mean p_T GeV (Hadr. τ)	141.6	187.3	230.3	444.4
Mean p_T GeV (Lep- e, μ)	75.2	99.4	123.2	235.5

Table 1: For four different Z' mass points the cross-section, intrinsic width and average p_T of the Z' bosons are given. The average p_T of the un-decayed tau-leptons, of the hadronically-decaying taus and the average p_T of the leptonic daughters (e and μ) from leptonically-decaying taus are also given.

3 High p_T tau performance

3.1 Tau Reconstruction

Tau jets are well-collimated low-multiplicity jets with hadronic and electromagnetic energy depositions. Two algorithms are implemented in ATLAS for the reconstruction of hadronic τ decays: The calorimeter-seeded `tauRec` algorithm [13], and the track-seeded `tau1p3p` algorithm [14]. The former begins with a calorimeter cluster and builds identification variables based on information from the electromagnetic (ECAL) and hadronic (HCAL) calorimeters as well as from the Inner Detector (ID). The latter starts from a reconstructed track and collects the energy deposited around the track impact point in the calorimeter. In `tau1p3p`, the energy of the visible decay products of the hadronically decaying taus is reconstructed using an energy flow algorithm [15] and has been tuned for the low and intermediate p_T ranges of the hadronic tau ($20 \lesssim p_T \lesssim 80$ GeV/c). This approach however, strongly underestimates the energy in the high p_T region hence, due to the high p_T nature of taus from a heavy Z', the reconstruction of hadronic τ-candidates in the study that we present here was done using `tauRec`.

The `tauRec` algorithm starts from a reconstructed cluster with $E_T > 15$ GeV and, for the purposes of performance studies, this cluster is labeled a reconstructed τ if a true τ-jet was found in a cone of $\Delta \mathrm{R} = \sqrt{\Delta\eta^2 + \Delta\phi^2} < 0.3$. In the version of the ATLAS software used for this analysis [4], the package does not provide any discrimination against electrons or muons either at the reconstruction or the identification level, therefore a significant fraction of true electrons and some true muons (92% and 8%, respectively[5]) are reconstructed as hadronic taus. In order to avoid "double-counting",

---

[4] For details on ATLAS software version see Appendix A.

[5] These numbers were evaluated inclusively on the four Z' samples.

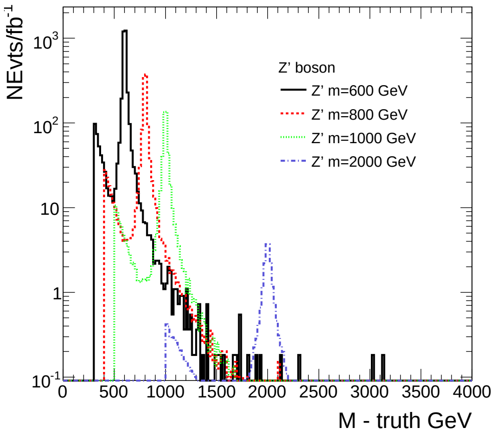

(a)

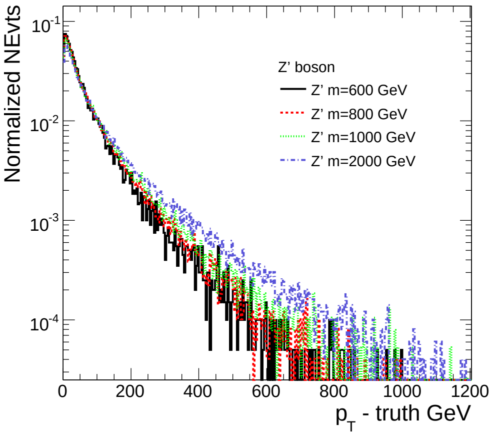

(b)

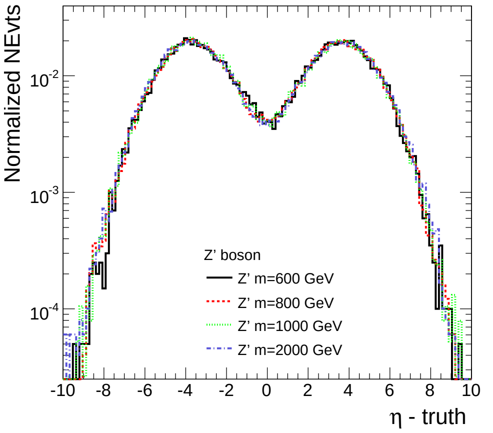

(c)

Figure 2: For various Z' masses (a) the distribution of the true mass, (b) the p_T distribution and (c) the η distribution are shown.

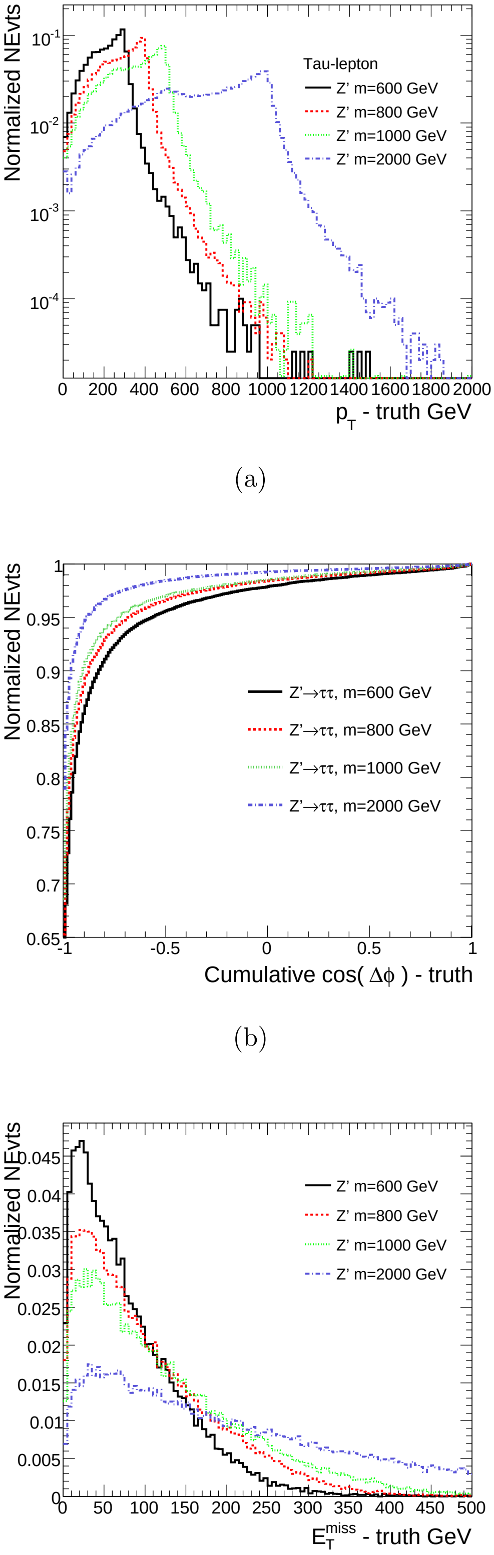

(a)

(b)

(c)

Figure 3: For various Z' masses (a) the p_T distribution of the tau-leptons, (b) the integrated cosine distribution of the angle between the two tau decay products and (c) the missing transverse energy.

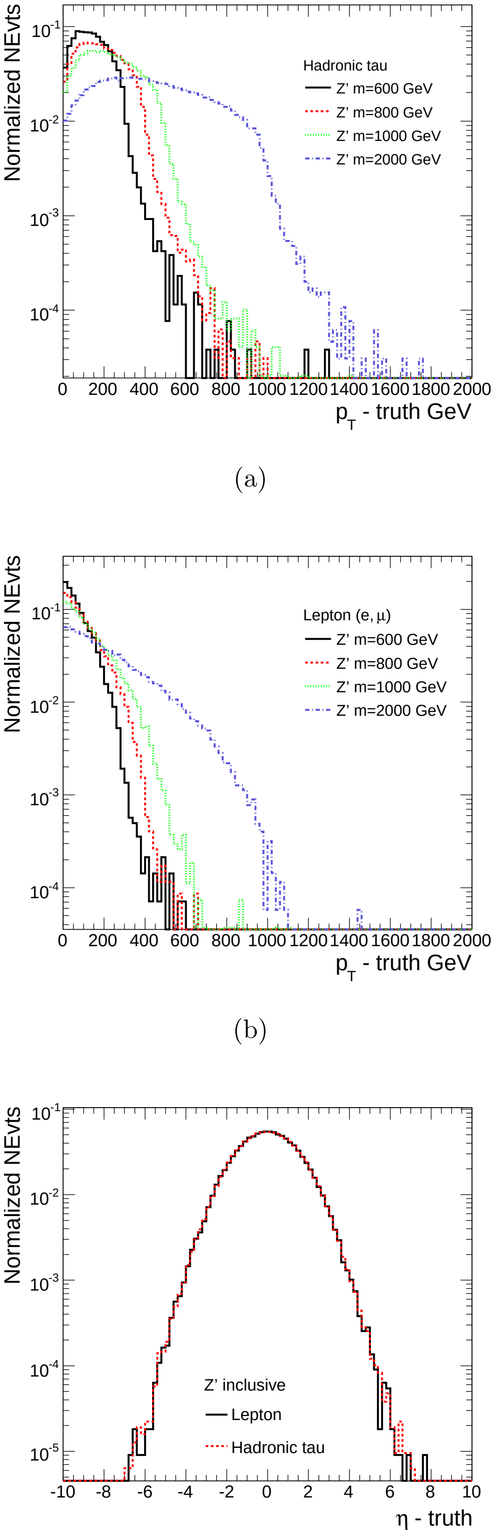

(a)

(b)

(c)

Figure 4: (a) The p_T distribution of the visible decay products of hadronic taus for various Z' masses, (b) the p_T distribution of leptons from tau decays for various Z' masses, and (c) the η distribution of leptons and hadronic taus evaluated inclusively on all Z' samples.

a reconstructed tau matching a reconstructed *tight* electron or muon in a cone of $\Delta\mathrm{R} < 0.2$ around the τ-jet central axis is not considered as a hadronic tau.[6]

Figure 5 shows the reconstruction efficiency, which is defined as the probability of the true hadronic tau to be reconstructed as a cluster, as a function of E_T,[7] η and ϕ. In the plots against E_T and ϕ only the true hadronic taus within $|\eta| \leq 2.5$ were considered. The efficiency for the e/μ-τ-jet overlap removal, defined as fraction of all reconstructed taus which pass overlap removal criteria, is also plotted in Fig. 5. The efficiencies from the four Z' samples are summarized in Tab. 2. The reconstruction efficiency is normalized to all true hadronic taus with $E_T > 15$ GeV inside of the η acceptance. Efficiencies for the electron and muon vetos are given w.r.t. all reconstructed taus. Electron and muon fake rates are normalized to all electrons or muons inside of the η acceptance, respectively.

For the reconstruction of the tau energy, all cells within $\Delta\mathrm{R} < 0.4$ around the barycenter are used. Cells are calibrated with an H1-style calibration, with cell weights optimized for the calibration of jets. This method overestimates the energy of the tau by roughly 4%. In the future, a scale factor should be applied to correct the overall τ energy. The current correction which is employed in ATLAS is optimal for low and intermediate E_T ranges where QCD di-jets cones are much broader than those originating from taus. Hence, the application of this scale factor would lead to an adversely large energy underestimation and introduce a significant bias for the reconstructed mass of the Z'. The relative energy resolution (the mean divided by σ) remains the same for the two calibration methods. It is for this reason that we only use the H1-style calibration, without any corrections, in the study presented here.

Figures 6a and 6b show the tau transverse energy resolution as a function of reconstructed E_T and η of the tau, respectively. We can see that at higher energies taus become more collimated and the resolution improves. Note that the energy is underestimated around $|\eta| = 1.5$, which corresponds to crack regions in the ECAL. Figure 6c shows the overall tau transverse energy resolution which is on the order of 7%.

	Z' Mass			
Efficiency %	600 GeV	800 GeV	1000 GeV	2000 GeV
Events in $|\eta| \leq 2.5$ (MC truth)	87.1±0.2	89.9±0.1	91.5±0.1	95.3±0.1
+$\mathrm{E_T}$ >15 GeV (MC truth)	85.5±0.2	88.7±0.1	90.6±0.1	94.8±0.1
Reconstruction	98.9±0.1	99.2±0.0	99.4±0.0	99.7±0.0
Electron veto	99.3±0.1	99.1±0.0	99.0±0.0	98.9±0.0
Muon veto	100.0±0.0	100.0±0.0	100.0±0.0	100.0±0.0
Electron -τ^{had} fake rate	46.0±0.6	46.4±0.4	47.7±0.4	58.5±0.4
Muon - τ^{had} fake rate	4.2±0.3	5.0±0.2	5.7±0.2	7.5±0.2

Table 2: For four Z' mass points the reconstruction efficiency, veto efficiency for e/μ-τ-jet overlap removal and e/μ fake rates for taus from Z' decays are shown. For completeness, the efficiencies for basic kinematic cuts are also shown.

---

[6] In later versions of the ATLAS software a dedicated tool has been implemented to provide efficient suppression of electrons while maintaining a high tau reconstruction efficiency.

[7] If not stated otherwise, E_T denotes the transverse energy of the visible decay products.

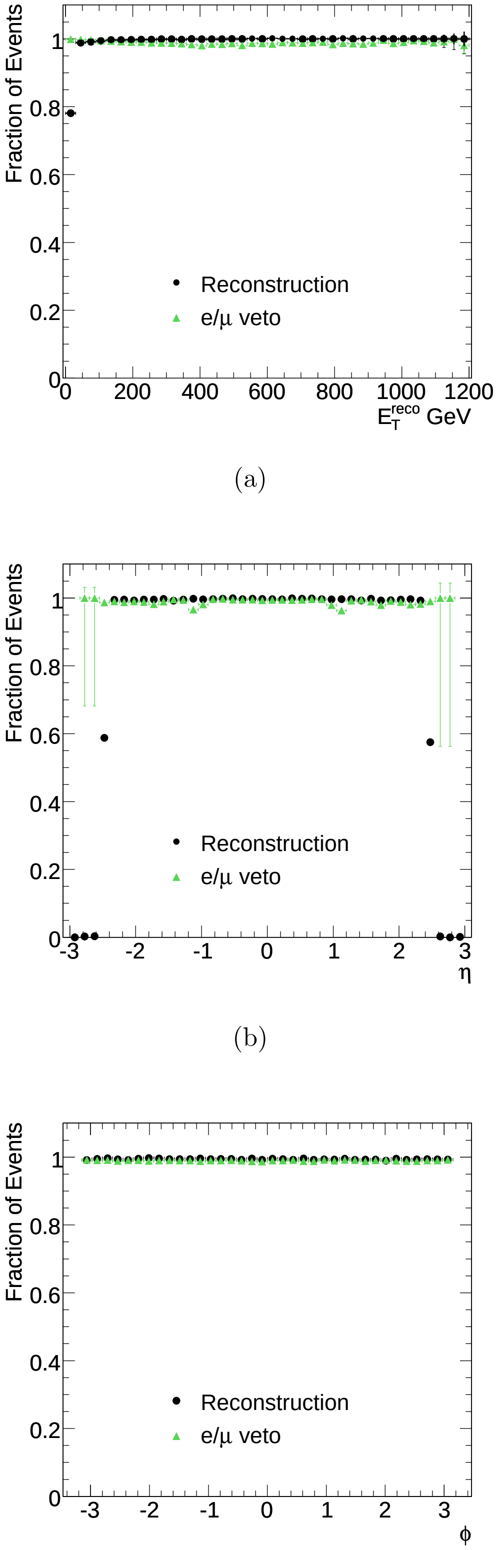

(a)

(b)

(c)

Figure 5: Reconstruction efficiency and overlap removal efficiency as a function of (a) $\mathrm{E_T}$, (b) η and (c) ϕ. These plots were made inclusively using all four Z' samples.

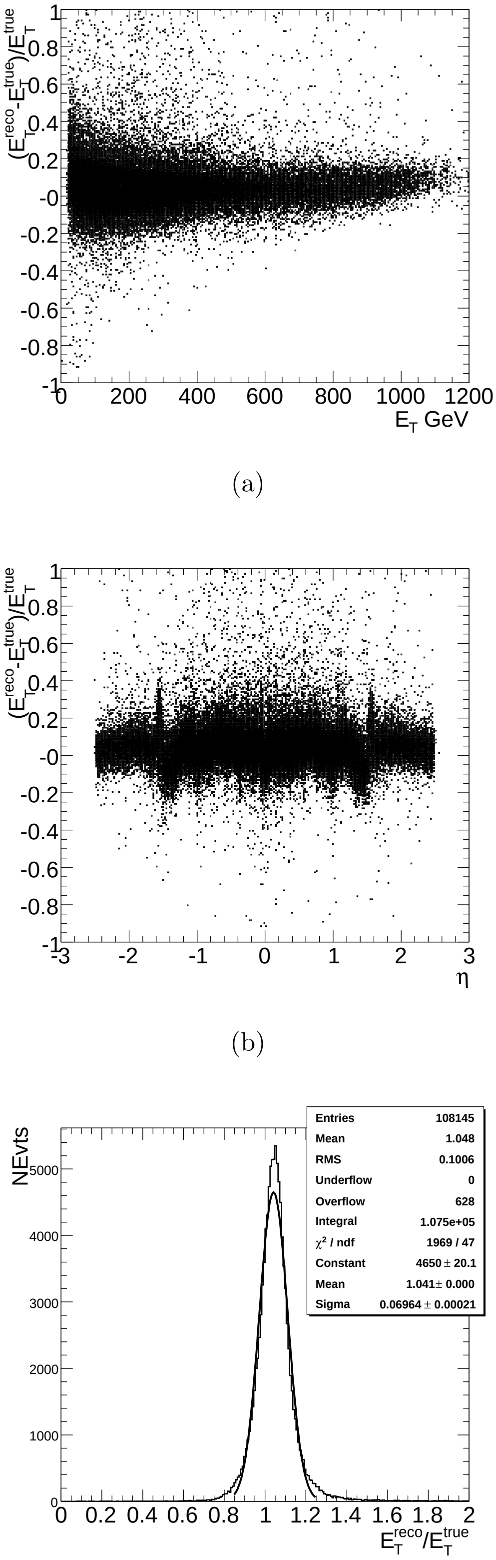

(a)

(b)

(c)

Figure 6: The tau energy resolution as a function of (a) E_T and (b) η. (c) The overall energy resolution together with a Gaussian fit performed in a range of two RMS values around the mean value. These plots were made inclusively using all four Z' samples.

3.2 Tau Identification: variables and performance

Several variables are considered in the `tauRec` package to exploit the well-collimated low-multiplicity character of tau jets; these are combined into one discriminant based on a likelihood method. A one-dimensional likelihood ratio is built based on 8 variables. Three of them are discrete:

(1) Number of associated tracks ($\mathrm{N_{trk}}$)

(2) Number of strips in η-strip layer ($\mathrm{N}_{\eta-\mathrm{hits}}$)

(3) τ-Charge

and five are continuous:

(4) EM-Radius — the radius of the cluster in the EM calorimeter.

(5) Isolation fraction ($\Delta\mathrm{E_T^{12}}$) — transverse energy deposited in a ring of $0.1 < \Delta$ R<0.2 around the cluster barycentre divided by transverse energy in cone Δ R<0.4.

(6) Transverse energy weighted width in the η strip layer ($\Delta\eta$)

(7) Energy over momentum of the leading track in the transverse plane ($\mathrm{E_T/p_T}$)

(8) Lifetime signed pseudo impact parameter significance (σ_{IP}) — ratio between impact parameter in x-y plane and the error on the impact parameter. σ_{IP} is designed in a way to have a positive (negative) sign if the decay happened in a flight (opposite to its flight) direction.

Nevertheless, an important correlation exists between the variables which is neglected within this approach. This method was proven to give the best hadronic tau identification versus QCD-jet rejection. A detailed description of the method can be found in [13]. At high E_T the $\mathrm{N_{trk}}$ variable, shown in Fig. 7a, provides the best discrimination against the QCD di-jet background. The discrimination power of $\Delta\mathrm{E_T^{12}}$, shown in Fig. 7b, is high at lower values of E_T and decreases with E_T when the QCD jets become very collimated due to the high Lorentz boost that they receive. It should be noted that the `tauRec` algorithm includes an intrinsic requirement on the number of tracks ($1 \leq N_{\mathrm{trk}} \leq 3$). Plots of the remaining six variables used in the calculation of the log(likelihood) are shown in Appendix B in Figures 26 and 27. Figure 7c shows the log(likelihood) discriminant (llh). Despite the fact that the log(likelihood) was tuned in 11 E_T bins, it shows a strong E_T dependence. A fixed cut on the log(likelihood) will not result in a flat efficiency, nor will it be optimal for jet rejection. Hence, an E_T-dependent cut should be applied as is also argued in [13].

Figures 8a and 8b summarize the performance of this approach in five different E_T bins. Plot 8a shows the ID efficiency for τ's from a Z' as a function of log(likelihood) cut. In Plot 8b the cross-section-weighted number of fake taus from QCD di-jets for 1 fb^{-1} of data as a function of the highest log(likelihood) jet in the event is shown. Plots of the QCD fake rate for six different p_T values of di-jets from the hard process and six different E_T bins as a function of the llh cut are shown in Appendix B (Figures 28 and 29).

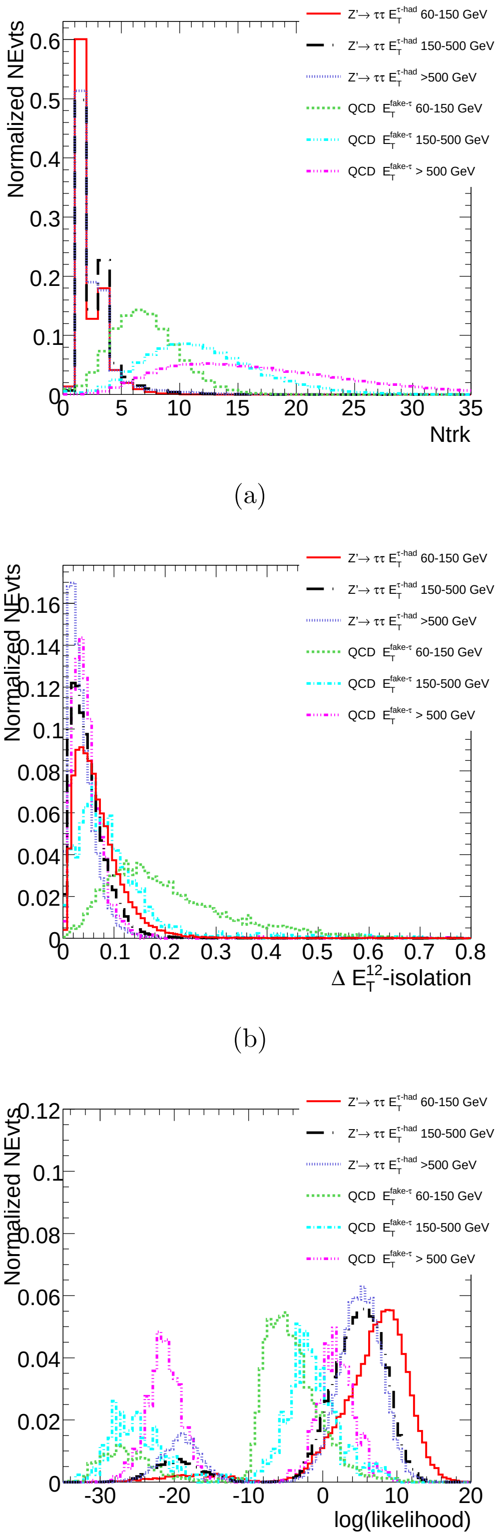

(a)

(b)

(c)

Figure 7: (a) $\mathrm{N_{trk}}$, (b) $\Delta \mathrm{E_T^{12}}$ and (c) Log(Likelihood). With the exception of (a), the distributions here are shown after requiring $1 \leq \mathrm{N_{trk}} \leq 3$. The QCD di-jet samples with a p_T of the hard process between 35 and 2240 GeV have been used.

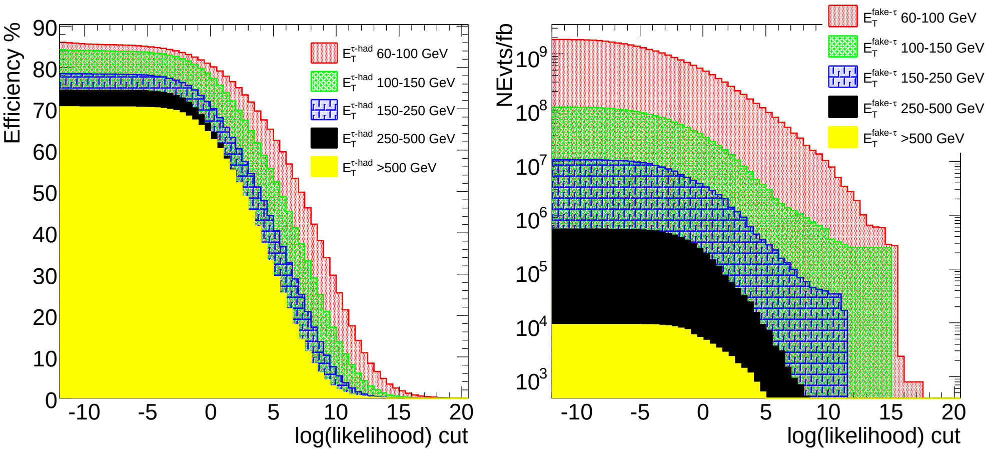

(a) (b)

Figure 8: For the five different E_T ranges: (a) The identification efficiency as a function of the llh cut for hadronic taus from Z' bosons. This plot was made inclusively using all four Z' samples. (b) The cross-section-weighted number of QCD events per 1 fb^{-1} of data as a function of the llh cut. For every event the highest llh fake tau is selected first. The QCD di-jet samples with a p_T of the hard process between 35 and 2240 GeV have been used.

3.3 Tau Identification: efficiency

To discriminate against backgrounds in this analysis, the hadronic tau needs to have $E_T > 60$ GeV, either 1 or 3 tracks, absolute value of the charge equal to 1 and fulfill an E_T-dependent llh cut as summarized in Tab. 3.

E_T range	60-100 GeV	100-150 GeV	150-250 GeV	250-500 GeV	>500 GeV
llh cut	6	4	2	0	-10

Table 3: The value of the log(likelihood) cut (llh) applied in different E_T ranges.

The efficiency of such pre-selection and identification requirements as a function of E_T, η and ϕ are shown in Fig. 5 and the exact values are summarized in Tab. 4. The efficiency is given w.r.t. reconstructed hadronic taus (after removal of the overlap with e or μ). The QCD fake rate, defined as the fraction of events having at least one fake tau at each step, is summarized in Tab. 5.

A clear drop in efficiency begins around $|\eta| = 1.3$ when requiring $1 \leq \mathrm{N_{trk}} \leq 3$. This reflects the non-uniform geometry of the ATLAS Inner Detector:

(i) The crack region in the Silicon strip (SCT) Detector at $|\eta| = 1.3$,

(ii) The crack region in the Pixel Detector at $|\eta| = 1.7$,

(iii) Lack of the coverage of the TRT Detector in the region $2.0 < |\eta| < 2.5$.

An additional drop in efficiency after applying cuts on the log(likelihood) variable is observed around $|\eta| = 1.5$. This corresponds to the crack regions in the ECAL, which of course adversely affects calorimeter-based identification variables.

	Z' Mass			
Efficiency %	600 GeV	800 GeV	1000 GeV	2000 GeV
$E_T > 60$ GeV	89.8±0.2	93.5±0.1	95.5±0.1	98.3±0.1
$+\mathrm{N}_{\mathrm{trk}}1{,}3$	66.9±0.3	69.1±0.2	70.3±0.2	70.3±0.2
$+\ \lvert\mathrm{charge}\rvert = 1$	66.0±0.3	68.2±0.2	69.2±0.2	69.1±0.2
$+llh$ cut	46.4±0.3	51.1±0.2	53.3±0.2	55.7±0.2

Table 4: For four Z' mass points the preselection and identification efficiency for taus from Z' decays are shown.

4 Triggers for High p_T Taus

The tau lepton decays to hadronic states in 65% of all cases, and the remaining fraction of the decays are to lighter leptons (e or μ, accompanied by neutrinos) leading to three different final states for a $Z' \to \tau\tau$ analysis: lepton-lepton, lepton-hadron and hadron-hadron. In this section we present the performance of the electron, muon and tau triggers based on a trigger decision at the level of the Event Filter (EF).[8]

4.1 Triggers for the lepton-lepton and lepton-hadron final states

In our studies of lepton-lepton and lepton-hadron final states we select events using a single lepton (e/μ) trigger.[9] Thus, we consider five true final states, which we denote $e\tau_h$, $\mu\tau_h$, ee, $\mu\mu$ and $e\mu$. For channels with electrons we consider two trigger menu items called `e25i` and `e60`, which are designed to select events that contain an electron with p_T above 25 GeV and 60 GeV, with and without isolation in the calorimeter required, respectively. Events with muons are selected using a trigger menu called μ`20`, appropriate for the selection of non-isolated muons with $p_T > 20$ GeV. For a true final state we define the trigger efficiency as the fraction of all events in a given final state which pass the relevant trigger item normalized to total number of event in this final state. Figures 10a and 10b show the efficiency of the triggers `e25i`, `e60` and μ`20` as a function of p_T and η for channels involving electrons and muons, respectively.

Since the trigger decision is stored per event, and back-navigation to trigger objects is not currently implemented in the ATLAS software, for true ee and $\mu\mu$ final states the efficiency is plotted as a function of the transverse momentum of the highest p_T lepton found in a sensitive region of the detector (i.e., $|\eta| < 2.5$). For all of the channels involving electrons we observe a drop of efficiency for the `e25i` menu item as a function of p_T as a result of the requirement of isolation in the calorimeter [10]. Due to the soft nature of the electrons from tau decays (as pointed out in Sect. 2) the `e60` trigger alone would results in unacceptably low efficiency. Hence we focus on events selected by either the `e25i` *or* the `e60` triggers. It is also worth noting that the electron triggers are also less efficient around $|\eta| = 1.5$ due to the End-Cap/Barrel transition in ATLAS.

---

[8] This of course is preceded by trigger decisions at both Level-1 and Level-2. The Event Filter is the third-level in the ATLAS trigger decision scheme.

[9] Combined electron-tau and muon-tau triggers were not yet implemented in the version of the ATLAS software used here.

[10] The isolation requirement (applied at Level-1) is based on the total energy deposited in the isolation ring rather than a fraction of the electron energy, therefore the high pT electrons are greatly affected by the e25i trigger. The same argument holds for isolated hadronic tau trigger items.

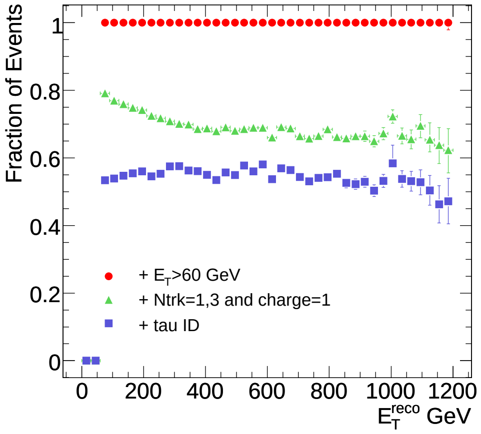

(a)

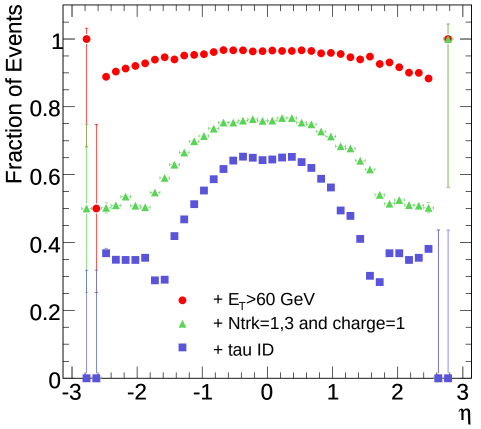

(b)

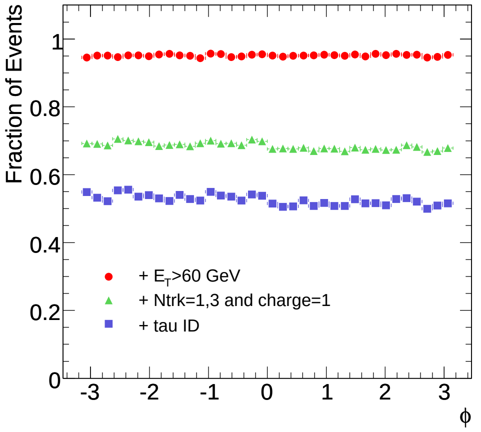

(c)

Figure 9: Preselection and identification efficiency as a function of (a) E_T, (b) η and (c) ϕ. These plots were made inclusively using all four Z' samples.

Fake rate %	35-70 GeV	70-140 GeV	140-280 GeV	280-560 GeV	560-1120 GeV	1120-2240 GeV
$E_T > 60$ GeV	8.06±0.05	80.18±0.07	99.30±0.01	99.97±0.00	100.00±0.00	100.00±0.00
+$\mathrm{N}_{\mathrm{trk}}$1,3	1.48±0.02	13.09±0.06	10.84±0.05	8.13±0.04	6.88±0.04	6.08±0.06
$+ \lvert\mathrm{charge}\rvert = 1$	1.39±0.02	12.19±0.05	10.12±0.05	7.58±0.04	6.40±0.04	5.64±0.06
$+llh$ cut	0.05±0.00	0.27±0.01	0.44±0.01	0.69±0.01	0.91±0.01	0.69±0.02
N Events for 1 fb^{-1}	$4{\cdot}10^7$	$4{\cdot}10^6$	$1{\cdot}10^6$	$9{\cdot}10^5$	$3{\cdot}10^3$	40

Table 5: Fake rate in percent after preselection and identification for QCD di-jet events for six different p_T ranges of the hard process. The last row gives the expected number of events having at least one jet identified as a hadronic tau.

The trigger for the muon channels is less efficient in the barrel region due to the designed support structure, in particular around $\eta = 0$ which corresponds to the crack region. Some loss in efficiency also appears between $\phi = -1.0$ and $\phi = -2.2$, corresponding to the 'feet' regions. Table 6 summarizes the efficiency of the trigger for each of the five true final states.

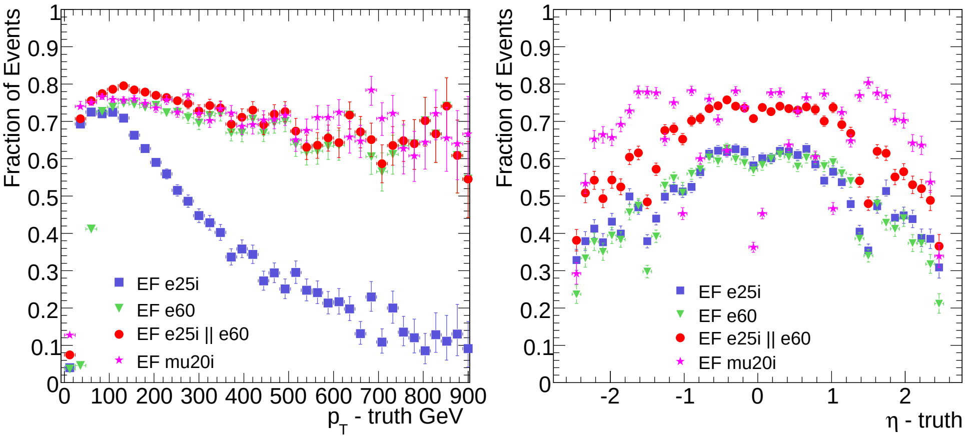

(a) (b)

Figure 10: The efficiency as a function of true (a) p_T and (b) η is shown for each trigger item relevant to channels involving electrons and muons. These plots were made inclusively using all four Z' samples.

	Z' Signal			
Efficiency %	600 GeV	800 GeV	1000 GeV	2000 GeV
e25i ($e\tau_h$)	48.0±0.7	51.3±0.5	50.4±0.5	42.3±0.5
e60 ($e\tau_h$)	34.0±0.7	43.6±0.5	48.5±0.5	56.2±0.5
e25i or e60 ($e\tau_h$)	52.9±0.7	59.2±0.5	61.4±0.5	64.3±0.5
mu20i ($\mu\tau_h$)	55.3±0.7	58.9±0.5	59.9±0.5	63.1±0.5
e25i (ee)	73.3±1.7	75.9±1.1	76.1±1.2	68.0±1.2
e60 (ee)	54.4±2.0	63.0±1.2	69.8±1.3	74.6±1.1
e25i or e60 (ee)	76.5±1.7	80.9±1.0	83.7±1.0	82.9±0.9
mu20i ($\mu\mu$)	80.1±1.7	81.9±1.0	84.5±1.1	87.3±0.9
e25i ($e\mu$)	46.0±1.4	49.8±0.9	51.3±1.0	42.8±0.9
e60 ($e\mu$)	30.8±1.3	41.1±0.9	45.8±1.0	52.9±0.9
e25i or e60 ($e\mu$)	49.8±1.4	56.7±0.9	60.6±1.0	61.3±0.9
mu20i ($e\mu$)	52.5±1.4	59.2±0.9	60.2±1.0	64.0±0.9

Table 6: For four Z' samples and the five true final states, the overall efficiency for each trigger menu item is given.

The real goal of the trigger is to select with high efficiency events of exceptional interest which are also expected to be found by the offline analysis. Due to the resolution of the p_T at different trigger levels, the efficiency of each trigger item is not a step function. Hence, the p_T threshold for offline selection should be set such that the efficiency becomes flat as a function of p_T. In our analyses we require p_T of electrons and muons to be 27 and 22 GeV, respectively; this corresponds to a 2 GeV shift above each of the trigger thresholds. Five final states: $e\tau_h$, $\mu\tau_h$, ee, $\mu\mu$ and $e\mu$ are selected by the aforementioned triggers and examined in the offline analyses presented here[11] and the efficiency is again defined as a fraction of all events in a given final state which pass relevant trigger item. Figures 11a and 11b show the efficiency of the triggers as a function of reconstructed p_T and η of the leptons. The exact numbers are summarized in Tab. 7 for the five different final states.

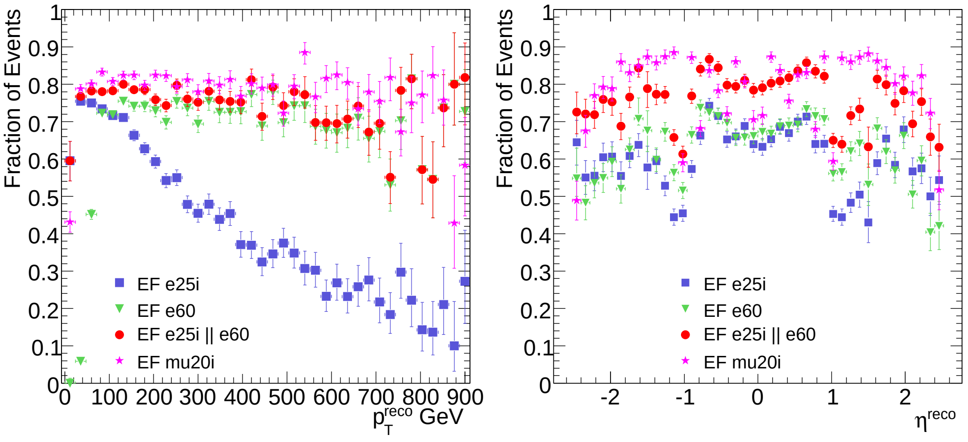

(a)

(b)

Figure 11: The efficiency as a function of offline (a) p_T and (b) η is shown for each trigger item relevant to channels involving electrons and muons. These plots were made inclusively using all four Z' samples.

	Z' Signal			
Efficiency %	600 GeV	800 GeV	1000 GeV	2000 GeV
e25i ($e\tau_h$)	65.1±1.3	64.3±0.8	60.3±0.9	49.0±0.8
e60 ($e\tau_h$)	55.5±1.4	61.8±0.8	63.6±0.9	69.1±0.7
e25i or e60 ($e\tau_h$)	73.0±1.2	75.8±0.7	74.9±0.8	75.6±0.7
mu20i ($\mu\tau_h$)	80.6±1.1	80.2±0.7	79.9±0.7	77.0±0.7
e25i (ee)	91.4±2.0	86.0±1.5	83.9±1.6	73.2±1.8
e60 (ee)	85.3±2.5	85.5±1.5	84.9±1.6	85.7±1.4
e25i or e60 (ee)	94.4±1.6	93.1±1.1	92.6±1.1	91.8±1.1
mu20i ($\mu\mu$)	97.9±1.0	96.1±0.8	96.4±0.8	94.1±0.9
e25i ($e\mu$)	67.3±2.4	62.6±1.4	62.0±1.5	47.5±1.4
e60 ($e\mu$)	55.0±2.5	61.8±1.4	62.8±1.5	66.3±1.3
e25i or e60 ($e\mu$)	75.1±2.2	75.4±1.2	76.3±1.3	72.8±1.2
mu20i ($e\mu$)	80.4±2.0	82.0±1.1	79.7±1.3	78.7±1.1

Table 7: For four Z' samples and for five final states as classified offline, the overall efficiency for each trigger menu item is given.

---

[11] Electrons were identified offline with the medium criteria whereas muons were required to pass a cut on $0 < \chi^2_{trk-match} < 20$. Both leptons were required to be isolated as explained in the next section. Hadronic taus were identified as described in Sec. 3.3.

4.2 Triggers for the hadron-hadron final states

Due to large QCD fake-rates at low energies, the soft p_T tau trigger menu items are designed to be used in combination with other trigger signatures, while very high p_T items could be used standalone. In our study of the hadron-hadron final state we select events using combined tau and missing E_T triggers, `tau35i` and `XE40`, which are designed to select events with an isolated hadronic tau with p_T above 35 GeV and missing transverse energy in the event above 40 GeV. Trigger efficiency is defined here in the same way as for lepton-lepton and lepton-hadron final states.

Figures 12a and 12b show the efficiency of the single and combined tau items as a function of p_T and η for true hadron-hadron final states, respectively. Here p_T denotes the transverse momentum of the leading hadronic tau found within $|\eta| < 2.5$. The efficiency of single `tau35i` drops significantly at high p_T due to isolation criteria applied at L1 for this signature[10]. Combining this hadronic tau trigger with the `XE40` menu item further degrades the efficiency in the low p_T region. These triggers are also less efficient around $|\eta|$=1.5 due to the End-Cap/Barrel transition in ATLAS. Table 8 summarizes the efficiency of the single and combined trigger for the true hadron-hadron final state.

It should be stressed that a single tau menu item such as `tau60`, designed to select events containing non-isolated hadronic tau with p_T above 60 GeV, would serve as a more optimal trigger for the selection of events for the double hadronic channel. Unfortunately this menu item was not yet implemented in the version of the ATLAS software used here, but does appear in newer releases that have been prepared for data taking [16].

For completeness, the performance of the trigger with respect to the offline selection has also been studied. The final state is marked as double hadronic if two hadronic taus, selected as outlined in Sect. 3.3, are found offline. Note that we require the hadronic tau to have p_T above 60 GeV which is far above the trigger threshold. Figures 13a and 13b show the efficiency of the single and combined tau trigger menu items as a function of p_T and η for a reconstructed hadronic tau in the hadron-hadron final states, respectively. Here again the p_T denotes the transverse momentum of the highest p_T hadronic tau found within $|\eta| < 2.5$. Table 9 summarizes the efficiency of the triggers for the offline-selected hadron-hadron final state.

	Z' Signal			
Efficiency %	$m = 600$ GeV	$m = 800$ GeV	$m = 1000$ GeV	$m = 2000$ GeV
tau35i	60.8±0.5	59.6±0.3	58.0±0.4	52.0±0.3
+ XE40	39.8±0.5	44.5±0.3	46.8±0.4	48.9±0.3

Table 8: For four Z' samples and the true hadron-hadron final state, the overall efficiency for single and combined tau trigger menu items is given.

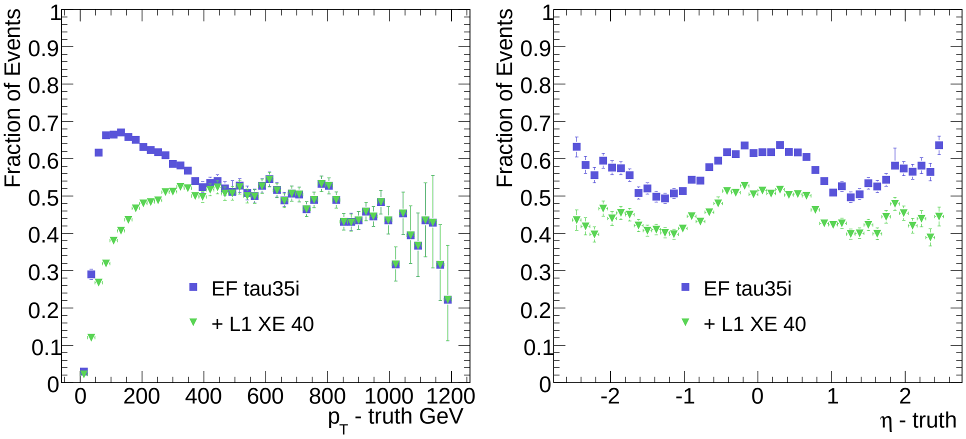

(a) (b)

Figure 12: Efficiency as a function of true (a) p_T and (b) η is shown for single and combined trigger items for the hadron-hadron channel. These plots were made inclusively using all four Z' samples.

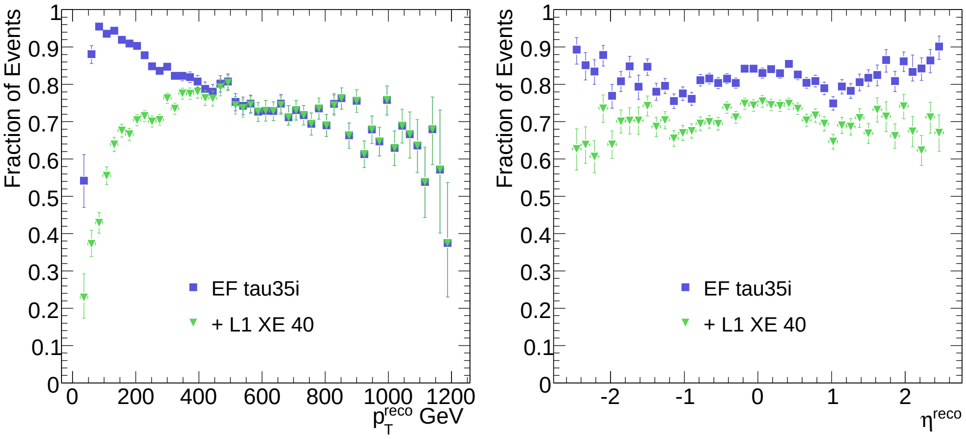

(a) (b)

Figure 13: Efficiency as a function of reconstructed (a) p_T and (b) η is shown for single and combined trigger items for the hadron-hadron channel. These plots were made inclusively using all four Z' samples.

	Z' Signal			
Efficiency %	$m = 600$ GeV	$m = 800$ GeV	$m = 1000$ GeV	$m = 2000$ GeV
tau35i	89.5±0.7	86.1±0.5	82.8±0.5	76.5±0.5
+ XE40	62.6±1.1	69.7±0.6	71.1±0.6	73.6±0.5

Table 9: For four Z' samples and the offline-selected hadron-hadron final state, the overall efficiency for single and combined tau trigger menu items is given.

5 The Di-Tau Final State Analyses

In this section we examine event selection criteria that have been tuned for each of the three di-tau final states: hadron-hadron, lepton-hadron and lepton-lepton. The final number of signal events, s, and background events, b, in the cutflow are then used in the calculation of the significance. We use a formula for the significance that is well-suited for small numbers of events and follows directly from the Poisson distribution [17]:

$$S = \sqrt{2((s+b)\ln(1+\frac{s}{b})-s)}$$

5.1 Common Selection Variables

The event selection variables that are common across each of the three final states are listed, motivated and detailed below. Detailed and itemized lists of the individual event selection criteria for each of the final states immediately follow in Sections 5.3, 5.4 and 5.5.

5.1.1 Opposite Charge

From charge conservation we know that the two taus coming from a Z' boson will have opposite charge. Hence, the product of the charges of the visible tau decay daughters must be less than zero. This requirement helps with the rejection of reducible backgrounds from W+jets, $t\bar{t}$ and QCD di-jets events, where we expect mis-identified hadronic tau jets and leptons to have like and opposite charges equally as often.

5.1.2 Missing Transverse Energy

The presence of neutrinos in the final state (four in the case of the lepton-lepton events, two in the case of the hadron-hadron decays) implies a significant missing E_T in the topology of the event. A cut on the missing transverse energy is efficient for rejecting backgrounds from QCD di-jet production within a relatively low p_T range. A cut on missing transverse energy also significantly reduces tails from Drell-Yan processes such as $Z \to ee$ ($\mu\mu$) which have very little or no true missing energy. Figures 14a and 14b show the missing transverse energy distribution for signal events with different masses, and a 600 GeV signal versus various backgrounds, respectively.

5.1.3 Transverse Mass

To further suppress backgrounds we cut on M_T, the transverse mass variable, calculated from the transverse momentum of one visible tau daughter (a charged lepton if available or a hadronically decaying tau in the case of the fully-hadronic final state) and the event missing E_T. The M_T is calculated as

$$M_T = \sqrt{2 \cdot p_{T,x} \cdot P_{MET}(1-\cos\Delta\phi_{x,MET})},$$

where $\Delta\phi_{x,MET}$ is the opening angle in the transverse plane between the visible tau daughter and the event missing energy. For the signal events, this transverse mass distribution reflects the mass of the τ and peaks at a low value, but displays a wide tail at higher values since the transverse missing momentum includes a contribution from the neutrinos of the two τ decays. Requiring the upper bound on M_T rejects most of

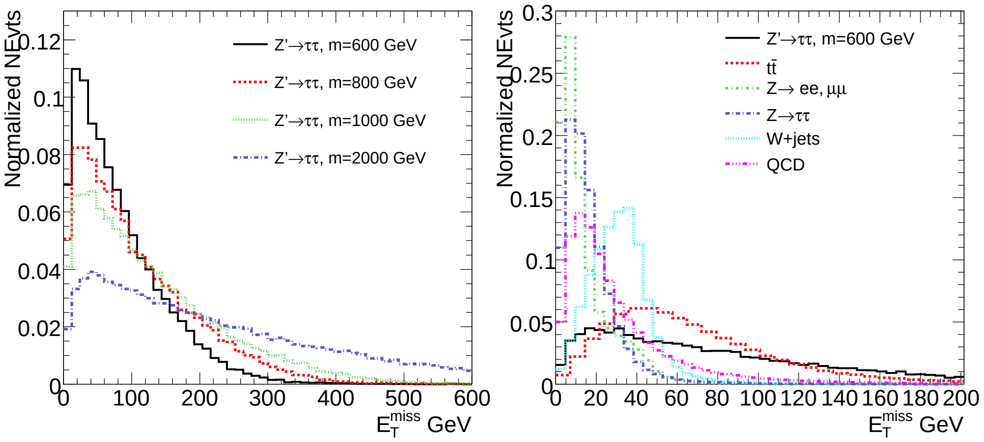

(a) (b)

Figure 14: The missing transverse energy distribution for signal events with different masses (a), and a 600 GeV signal versus various backgrounds (b).

the processes involving a W boson, for which the Jacobian peak of the M_T distribution lies much higher. Figures 15a and 15b show the transverse mass distribution for signal events with different masses, and a 600 GeV signal versus various backgrounds.

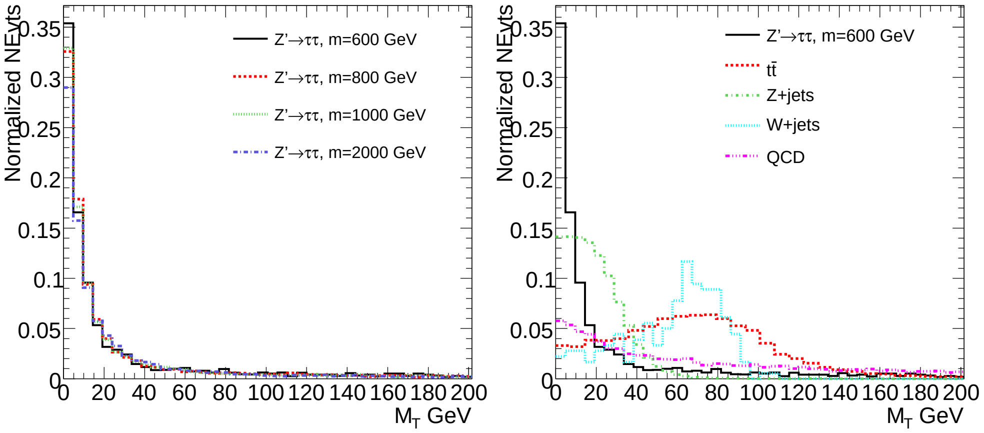

(a) (b)

Figure 15: The transverse mass distribution for signal events from various masses (a), and a 600 GeV signal versus various backgrounds (b).

5.1.4 Total Event p_T

The Z' boson is produced predominantly at rest or recoils againt jets from ISR radiation as discussed in Sect. 2. Therefore, a vector sum of the transverse missing energy with transverse momenta of the two tau visible daughters will result in a relatively low value. To properly balance an event, if it contains a jet with $p_T > 40$ GeV/c,[12] the four-vector for that jet is also added. We call such a vector sum the total p_T of an event and denote this quantity as $\mathrm{P_T}^{tot}$. A cut on high values of $\mathrm{P_T}^{tot}$ greatly aids in the rejection of $t\bar{t}$ backgrounds as well as QCD di-jets with high transverse momentum of the hard process. Figures 16a and 16b show the $\mathrm{P_T}^{tot}$ distribution for signal events with different masses, and a 600 GeV signal versus various backgrounds.

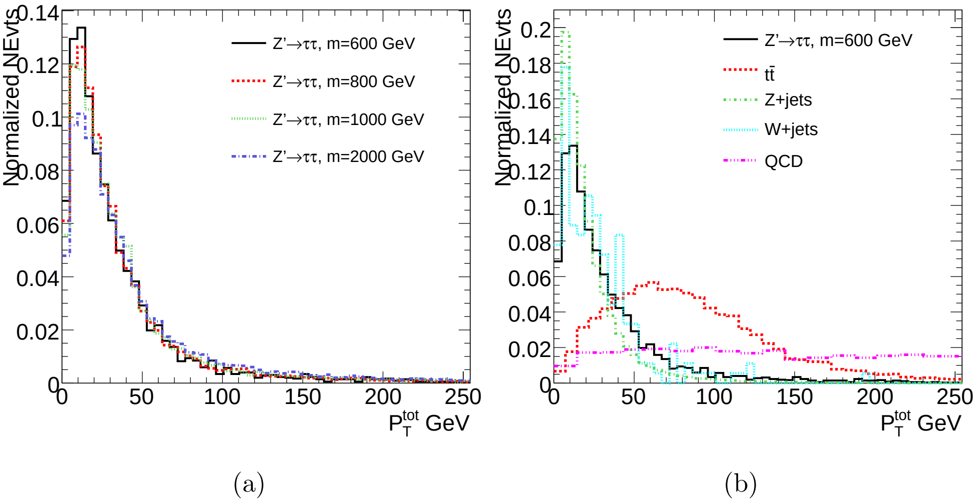

Figure 16: The event total transverse momentum distribution for signal events from various masses (a), and a 600 GeV signal versus various backgrounds (b).

5.1.5 Visible Mass

A visible mass variable, calculated as defined by CDF [12] by adding the measured four-momenta for both of the two visible tau daughters with the event missing transverse energy four-momentum (defined as: $\overline{p}_{\text{miss}} = (E_{T,x}^{\text{miss}}, E_{T,y}^{\text{miss}}, 0, |E_T^{\text{miss}}|)$), greatly helps with background rejection in each of the final states. Similar to the transverse mass variable, the visible mass offers partial mass reconstruction, hence the peak of the reconstructed mass appears lower than the true value but still allows us to make a coherent statement about the true Z' mass.

5.1.6 Collinear Mass Reconstruction

Although there are multiple nutrinos in the final state, event-by-event mass reconstruction is possible after making the assumption that the decay products of the τ lepton are collinear with the τ in the laboratory frame. This is a good approximation since $m_{Z'} \gg m_\tau$. The "collinear approximation" gives us two equations and two unknowns:

$$\frac{p_{x,l1}}{x_1} + \frac{p_x, l2}{x_2} = p_{x,l1} + p_{x,l2} + p_{x,\text{miss}}$$

$$\frac{p_{y,l1}}{x_1} + \frac{p_y, l2}{x_2} = p_{y,l1} + p_{y,l2} + p_{y,\text{miss}}.$$

---

[12] We have used a cone ΔR=0.4 algorithm using topological clusters seeds for jet reconstruction which is a standard ATLAS algorithm.

We can then solve for the fraction of the tau momentum carried by the visible decay daughters, x_1 and x_2, from the above formulas:

$$x_1 = \frac{p_{x,1} \cdot p_{y,2} - p_{x,2} \cdot p_{y,1}}{p_{y,2} \cdot p_{x,1} + p_{y,2} \cdot E_{T,x}^{\text{miss}} - p_{x,2} \cdot p_{y,1} - p_{x,2} \cdot E_{T,y}^{\text{miss}}}$$

$$x_2 = \frac{p_{x,1} \cdot p_{y,2} - p_{x,2} \cdot p_{y,1}}{p_{y,2} \cdot p_{x,1} + p_{x,1} \cdot E_{T,y}^{\text{miss}} - p_{x,2} \cdot p_{y,1} - p_{y,1} \cdot E_{T,x}^{\text{miss}}}$$

Using the invariant mass of the visible tau decay daughters, M_{12}, the reconstructed collinear mass for the Z' is then calculated as:

$$M_{\tau\tau} = \frac{M_{12}}{\sqrt{x_1 x_2}}.$$

Figures 17a, 17b and 18a, 18b show the distributions for signal events with different masses, and a 600 GeV signal versus various backgrounds for x_1 and x_2, respectively. The collinear approximation becomes singular and breaks down when the two taus are back-to-back, hence we impose the requirement that $\cos\Delta\phi_{12} > -0.99$, where $\Delta\phi_{12}$ is the opening angle in the transverse plane of the visible decay products of the two taus.

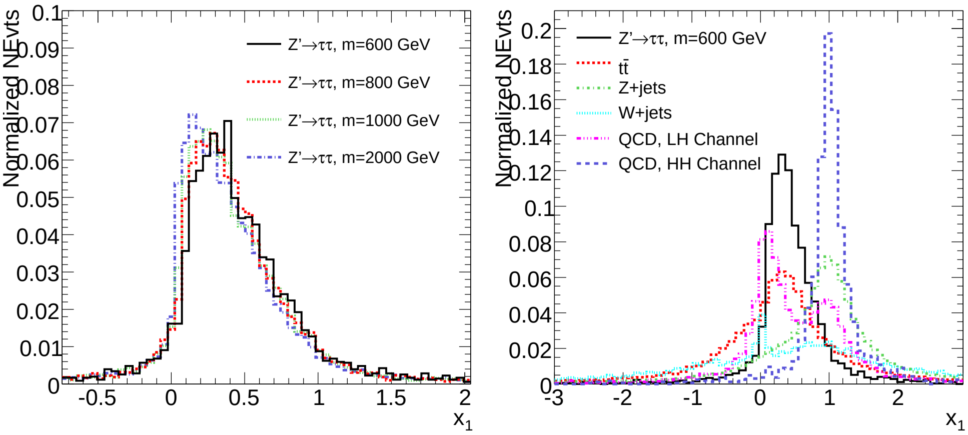

(a) (b)

Figure 17: The fraction of tau momentum carried away by the visible daughter (in this case from a leptonically-decaying tau) for signal events from various masses (a), and a 600 GeV signal versus various backgrounds (b).

Figures 19a and 19b show the integrated cosine of the opening angle between the decay daughters of the two taus for signal events from various masses and a 600 GeV signal versus various backgrounds. Since the Z' boson is produced predominantly at rest, most of events are back-to-back and although the cut on $\cos\Delta\phi_{12}$ is very loose[13] the acceptance which results is quite low. Figure 19b shows that a significant number of QCD events in the lepton-hadron channel have the two visible tau daughters pointing in the same direction. In those events the same jet has been misidentified as both a

---

[13] Cuts that are much stricter are applied in searches for relatively low-mass resonances such as $Z \to \tau\tau$ or VBF $H \to \tau\tau$.

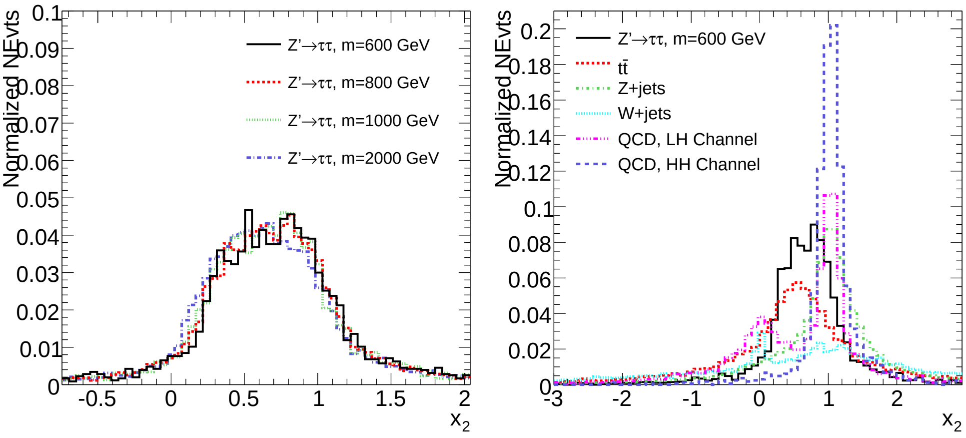

(a) (b)

Figure 18: The fraction of tau momentum carried away by the visible daughter (in this case from a hadronically-decaying tau) for signal events from various masses (a), and a 600 GeV signal versus various backgrounds (b).

hadronic tau and an electron of opposite charge.[14] This "double counting" also explains the double-peaked structure of the distributions in the x_1 and x_2 plots for QCD events classified in lepton-hadron channel.

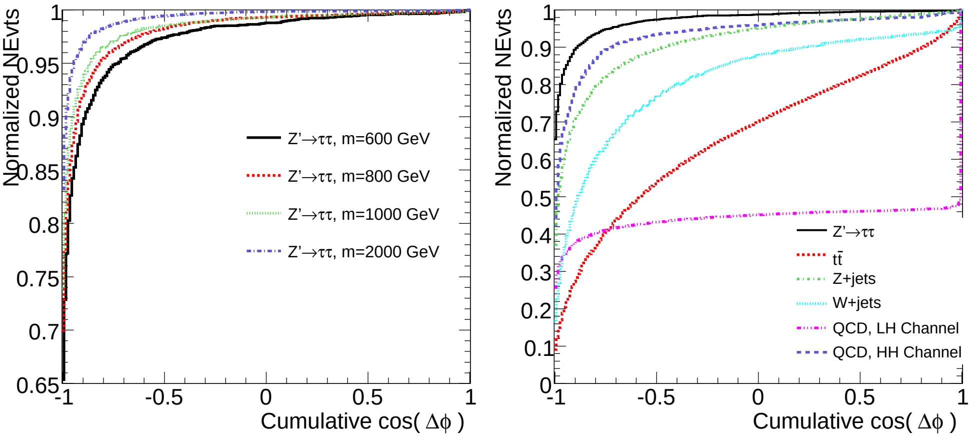

(a) (b)

Figure 19: The integrated cosine of the opening angle between the decay daughters of the two taus. Note that the collinear approximation breaks down when $\cos(\Delta\phi_{12}) = -1$ for signal events from various masses (a), and a 600 GeV signal versus various backgrounds (b).

It is worth noting that as the mass of the Z' increases, the more likely it is to have been created at rest in the lab-frame and the more likely the visible tau decay daughters

---

[14] Recall in Sec. 3 a discussion on the overlap removal between hadronic taus and electrons. There a *tight* electron was used whereas here in the event selection for the lepton-hadron channel we use electrons identified using the *medium* selection.

are to be back-to-back–in which case the collinear approximation is of limited use. This fact, considered together with the small SSM cross-section for a Z' above 1000 GeV, leads to our exclusive use of the visible mass for the 2000 GeV mass point. Of course if Nature delivered a 2000 GeV Z' to ATLAS with a cross-section significantly enhanced over that predicted by the SSM, one could afford to reject large numbers of events in exchange for a more precise determination of the mass of the resonance.

5.2 Background factorization

Although most of the backgrounds we consider here are common across many analyses in ATLAS, due to finite resources the Monte Carlo samples for these backgrounds have not been prepared with sufficiently large enough statistics. Particularly affected are the QCD and W+jets samples, where enormous rejection factors are required. It is for this reason that a cut factorization method was developed to predict the background rates. Assuming that the event selection cuts are uncorrelated with object identification cuts, the factorization of these backgrounds is performed in the following way:

(i) Evaluate the cutflow for each channel as described in Sections 5.3, 5.4 and 5.5. We call this the *tight* selection.

(ii) Evaluate the cutflow for each channel with the event selection cuts as described in Sections 5.3, 5.4 and 5.5 but without any object identification cuts.[15]

We call this the *loose* selection.

(iii) Beginning with the cut on missing transverse energy, the *loose* selection is scaled by a factor k, where for each channel k is defined as the ratio of the number of events after the opposite charge requirement obtained using both the *tight* and *loose* selections.

While this procedure has large uncertainties associated with it, these only affect our ability to estimate our discovery sensitivity and will not be used during the ATLAS data-taking era. Many efforts are currently underway to develop data-driven techniques for estimating the normalization and shape for several of our most dominant backgrounds.

5.3 Selection Criteria for the Hadron-Hadron Channel

The hadron-hadron final state is one of the most promising channels due to the large branching ratio as well as low amount of neutrinos in the event enabling more efficient mass reconstruction with better resolution. The selection criteria for this channel are summarized below. The cutflow for each contributing background and each Z' mass point in the hadron-hadron final state is summarized in Tab. 11. It is worth noting that to avoid double-counting Drell-Yan events present in the signal Monte Carlo sample, the Z+jets events passing the $\sqrt{\hat{s}}/2$ cut for each signal mass are subtracted from the signal column in the cutflow. For the fully-hadronic analysis, this amounts to a decrease of $\approx 7\%$ for each of the mass points—a conservative subtraction as it neglects interference effects. Table 10 gives the significance calculated for each Z' mass point as expected for 1 fb^{-1} of data for searches involving the visible and reconstructed masses, respectively.

---

[15] Note that p_T, η and isolation cuts are applied for electrons and muons. For taus neither preselection nor identification is required, only the p_T requirement.

(a) **Trigger**
For this analysis we only consider the use of tau triggers as outlined in Section 4.2 by selecting events which passed both `tau35i` and `XE_40` triggers.

(b) **Hadronic Tau Selection**
We require two hadronic taus passing the selection criteria described in Sec. 3.3.

(c) **Opposite Charge**
The contribution from the reducible background processes in the cutflow can be further suppressed by imposing the requirement that both hadronically-decaying tau candidates be of opposite charge.

(d) **Missing Transverse Energy**
As very little transverse missing energy is expected from QCD events, as well as most of the processes that contribute to the $Z+$ jets background, requiring $E_Tmiss > 40$ GeV here helps to reduce both of these backgrounds considerably.

(e) **Transverse Mass**
A cut on the transverse mass of the event, as defined in Sec. 5.1.3 above and constructed using the second-highest p_T hadronic tau [16] in the event along with the event transverse missing energy, helps to greatly reduce the background contributions from both $W+$ jets and $t\bar{t}$. Here we require $M_T < 35$ GeV.

(f) **Total Event p_T**
We require that the total event p_T, as defined in Sec. 5.1.4, be less than 50 GeV. This cut is especially helpful in suppression of contributions from both QCD di-jets and $t\bar{t}$.

(g) **Visible Mass**
For all events passing the event selection criteria up to this point, we construct a visible mass as defined in Sec. 5.1.5 using both of the hadronic tau four-vectors as well as the event missing energy. A cut on the M_{vis} variable is used as a kind of one-sided mass window that only possesses a lower bound. In the hadron-hadron analysis the lower bounds on M_{vis} are 400, 500, 600 and 800 GeV for Z' masses of 600, 800, 1000 and 2000 GeV, respectively. The reconstructed visible mass for this channel, for an 800 GeV Z' in 1 fb^{-1} of data, is shown in Fig. 21c.

(h) **Collinear Mass Reconstruction**
A reconstruction of the Z' collinear mass, as defined in Sec. 5.1.6 where x_1 and x_2 are the visible hadronically-decaying tau daughters, is attempted on those events that survive the M_{vis} cut. We require that $0 < x_1, x_2 < 1$. The reconstructed collinear mass for hadron-hadron events is exceptional, even with only 1 fb^{-1} of data. A Gaussian fit to the reconstructed signal peak for an 800 GeV Z' yields a mass resolution of $\sim 10\%$ (Figure 22a).

---

[16] The choice of using the second-highest p_T hadronic tau for the reconstruction of the transverse mass was motivated by the resulting discrimination power.

$m = 600$ GeV ($M_{vis} > 400$ GeV)	13.0
$m = 600$ GeV (M_{col})	6.8
$m = 800$ GeV ($M_{vis} > 500$ GeV)	8.4
$m = 800$ GeV (M_{col})	4.1
$m = 1000$ GeV ($M_{vis} > 600$ GeV)	5.4
$m = 1000$ GeV (M_{col})	3.8
$m = 2000$ GeV ($M_{vis} > 800$ GeV)	0.6

Table 10: Significance values for the hadron-hadron final state in 1 fb^{-1} of data.

5.4 Selection Criteria for the Lepton-Hadron Channel

The lepton-hadron final state is almost as powerful as the fully-hadronic channel. The selection criteria used for the analysis in the lepton-hadron channel can be found below. The cross-section for signal and backgrond processes after each selection cut, in fb, are listed in Tab. 13. It is worth noting that to avoid double-counting Drell-Yan events present in the signal Monte Carlo sample, the Z+jets events passing the $\sqrt{\hat{s}}/2$ cut for each signal mass are subtracted from the signal column in the cutflow. For the lepton-hadron analysis, this amounts to a decrease of $\approx 5\%$ for the lowest mass point—a conservative subtraction as it neglects interference effects. The remaining three mass points were not affected. Table 12 gives the significance calculated for each Z' mass point as expected for 1 fb^{-1} of data for searches involving the visible and reconstructed masses, respectively.

(a) **Trigger**
In the lepton-hadron analysis we only consider events that have been collected using high-p_T lepton triggers such as those already described in Sec. 4.1.

(b) **Lepton Selection**
For electron and muon selection we used the standard ATLAS electron and muon identification procedures. For electrons we require a track-match and impose the "medium" electron selection. For muon identification we require a χ^2 fit to lie between 0 and 20. We impose an isolation requirement: $\sum_i E_{T,EM<0.2}/p_T < 0.1$ where $\sum_i E_{T,EM<0.2}$ is the sum of the energy deposits in the electromagnetic calorimeter within a cone of $\Delta R = 0.2$ from the location of the lepton candidate in η-ϕ. To be considered by this analysis, isolated electrons and muons must have $p_T > 27$ GeV and $p_T > 22$ GeV, respectively, and $|\eta| < 2.5$. We require exactly one such lepton to be found in the event.

(c) **Hadronic Tau Selection**
We require exactly one hadronic tau passing the selection criteria described in Sec. 3.3 to be found in the event.

(d) **Opposite Charge**
The contributions from the reducible background in the cutflow can be significantly suppressed by imposing the requirement that the charged lepton daughter from the leptonically-decaying tau and the hadronically-decaying tau be of opposite charge.

	Z' Signal σ [fb]				Background σ [fb]			
Cut	$m = 600$ GeV	$m = 800$ GeV	$m = 1000$ GeV	$m = 2000$ GeV	$t\bar{t}$	$W+$ jets	$Z+$ jets	QCD
Trigger	1153.9	446.1	187.7	9.1	70531.8	1668621.5	404922.8	1833543.8
2 Taus	174.5	89.4	39.5	2.3	211.3	250.7	710.0	831.5
Charge	168.3	85.6	37.8	2.1	195.3	183.4	649.9	829.1
MET > 40 GeV	152.2	76.3	34.0	1.9	177.1	$128.6^{\dagger}$	73.2	$79.9^{\dagger}$
$M_T < 35$ GeV	132.1	63.5	28.6	1.4	42.3	$29.0^{\dagger}$	49.4	$38.8^{\dagger}$
$P_T^{tot} < 50$ GeV	115.5	55.9	24.3	1.0	12.6	$21.2^{\dagger}$	40.3	$27.6^{\dagger}$
$M_{vis} > 400$ GeV	109.1	–	–	–	1.1	$9.7^{\dagger}$	13.8	$16.8^{\dagger}$
M_{col}	17.8	–	–	–	$0.4^{\dagger}$	$0.0^{\dagger}$	0.8	$1.8^{\dagger}$
$M_{vis} > 500$ GeV	–	50.6	–	–	1.1	$4.6^{\dagger}$	10.8	$6.1^{\dagger}$
M_{col}	–	6.1	–	–	$0.1^{\dagger}$	$0.0^{\dagger}$	0.8	$0.0^{\dagger}$
$M_{vis} > 600$ GeV	–	–	22.3	–	$0.7^{\dagger}$	$3.0^{\dagger}$	3.0	$4.3^{\dagger}$
M_{col}	–	–	2.5	–	$0.02^{\dagger}$	$0.00^{\dagger}$	$0.04^{\dagger}$	$0.00^{\dagger}$
$M_{vis} > 800$ GeV	–	–	–	0.8	$0.2^{\dagger}$	$0.5^{\dagger}$	0.8	$0.3^{\dagger}$

Table 11: Cutflow for the hadron-hadron final state. Note that all cross-sections here are given in fb. †Cross-section determined by factorization.

(e) **Missing Transverse Energy**

As very little transverse missing energy is expected from QCD events, as well as most of the processes that contribute to the $Z+$ jets background, requiring $E_T miss > 30$ GeV helps to reduce both of these backgrounds considerably.

(f) **Transverse Mass**

A cut on the transverse mass of the event, as defined in Sec. 5.1.3 above and constructed using the charged lepton (e or μ) in the event with the event transverse missing energy, helps to reduce the background contributions from both $W+$ jets and ttbar by more than an order of magnitude. We require $M_T < 20$ GeV.

(g) **Total Event p_T**

We require that the total event p_T, as defined in Sec. 5.1.4, be less than 50 GeV. This cut is especially helpful in suppression of contributions from both QCD di-jets and $t\bar{t}$.

(h) **Visible Mass**

For all events passing the event selection criteria up to this point, we construct a visible mass as defined in Sec. 5.1.5 using the hadronic tau, leptonically-decaying tau daughter (e or μ) and missing energy four-vectors. A cut on the M_{vis} variable is used as a kind of mass window that only includes a lower bound. In the lepton-hadron analysis the lower bounds on M_{vis} are 300, 400, 500 and 700 GeV for Z' masses of 600, 800, 1000 and 2000 GeV, respectively. The reconstructed visible mass for this channel, for an 800 GeV Z' in 1 fb^{-1} of data, is shown in Fig. 21b.

(i) **Collinear Mass Reconstruction**

A reconstruction of the Z' collinear mass, as defined in Sec. 5.1.6 where x_1 is the charged lepton from a leptonically-decaying tau and x_2 is the hadronically-decaying tau, is attempted on those events that survive the M_{vis} cut. We require that $0 < x_1 < 0.75$ and $0 < x_2 < 1$. While the number of signal events in 1 fb^{-1} for SSM cross-sections is quite small, a Gaussian fit to the reconstructed signal peak for an 800 GeV Z', in 1 fb^{-1} of data, yields a mass resolution of $\sim 15\%$ (Figure 22b).

$m = 600$ GeV ($M_{vis} > 300$ GeV)	12.0
$m = 600$ GeV (M_{col})	4.0
$m = 800$ GeV ($M_{vis} > 400$ GeV)	8.2
$m = 800$ GeV (M_{col})	3.6
$m = 1000$ GeV ($M_{vis} > 500$ GeV)	5.2
$m = 1000$ GeV (M_{col})	3.0
$m = 2000$ GeV ($M_{vis} > 700$ GeV)	0.5

Table 12: Significance values for the lepton-hadron final state in 1 fb^{-1} of data.

	Z' Signal σ [fb]				Background σ [fb]			
Cut	$m = 600$ GeV	$m = 800$ GeV	$m = 1000$ GeV	$m = 2000$ GeV	$t\bar{t}$	$W+$ jets	$Z+$ jets	QCD
Trigger	1283.1	490.4	211.0	11.6	213494.2	12358210.0	2062080.5	3369127.5
Lepton	851.1	318.7	134.8	6.6	151010.4	9028033.0	1062146.4	121617.1
Tau	347.5	145.6	65.8	3.6	7808.2	74818.4	39573.5	3354.1
Charge	297.2	124.6	57.1	3.1	2487.0	3502.8	23097.7	831.4
MET > 30 GeV	254.6	108.2	52.2	2.9	2034.6	$2343.8^\dagger$	707.7	$181.8^\dagger$
$M_T < 20$ GeV	174.1	72.9	35.0	1.7	164.5	$182.6^\dagger$	245.4	$86.4^\dagger$
$P_T^{tot} < 50$ GeV	152.7	63.0	30.5	1.4	44.6	$149.7^\dagger$	175.7	$16.2^\dagger$
$M_{vis} > 300$ GeV	135.9	-	-	-	17.1	$44.5^\dagger$	18.8	$8.9^\dagger$
M_{col}	19.7	-	-	-	5.7	$5.8^\dagger$	5.0	$1.5^\dagger$
$M_{vis} > 400$ GeV	-	59.1	-	-	6.9	$20.1^\dagger$	5.0	$3.1^\dagger$
M_{col}	-	7.8	-	-	2.3	$0.0^\dagger$	$0.6^\dagger$	$0.0^\dagger$
$M_{vis} > 500$ GeV	-	-	25.4	-	3.4	$11.7^\dagger$	1.3	$0.1^\dagger$
M_{col}	-	-	2.4	-	$0.1^\dagger$	$0.0^\dagger$	$0.1^\dagger$	$0.0^\dagger$
$M_{vis} > 700$ GeV	-	-	-	1.2	2.3	$2.8^\dagger$	$0.6^\dagger$	$0.0^\dagger$

Table 13: Cutflow for the lepton-hadron final state. Note that all cross-sections here are given in fb. †Cross-section determined by factorization.

5.5 Selection Criteria for the Lepton-Lepton Channel

The lepton-lepton final state has a low branching ratio, which is on the order of 12%. As compared to the hadron-hadron and the lepton-hadron channels, the four neutrinos in the fully-leptonic final-state lead to a worse mass resolution from the collinear approximation. The cross-section for signal and backgrond processes after each selection cut, in fb, are listed in Tab. 15. It is worth noting that in the fully-leptonic final-state the subtraction of Drell-Yan events present in the signal Monte Carlo sample was not done due to the lack of the necessary information at the Monte Carlo truth-level in the samples used. The number of events in 1 fb^{-1} for $Z \to \tau\tau \to ll + \text{MET}$ with $M_{vis} > 300$ GeV is less than 1 and for $M_{vis} > 400$ GeV it was found that $Z \to \tau\tau$ does not contribute to the cutflow at all. Table 14 gives the significance calculated for each Z' mass point as expected for 1 fb^{-1} of data for searches involving the visible and reconstructed masses, respectively.

(a) **Trigger**
In this analysis we select events which pass either the `e25i`, `e60` or `mu20i` triggers as discussed in Section 4.1. We require that any one of these triggers be fired but do not reject an event if, for example, both the `e25i` and `mu20i` triggers were fired.

(b) **Lepton Selection**
We require two leptons selected using the same criteria as described above in Sec. 5.4 for the lepton-hadron channel.

(c) **Opposite Charge**
The contribution from the reducible backgrounds in the cutflow can be suppressed by imposing the requirement that the charged lepton daughters from the leptonically-decaying taus be of opposite charge.

(d) **Missing Transverse Energy**
As very little transverse missing energy is expected from most of the processes that contribute to the $Z+$ jets background, requiring $E_T miss > 30$ GeV helps to reduce these backgrounds considerably.

(e) **Transverse Mass**
A cut on the transverse mass of the event, as defined in Sec. 5.1.3 above and constructed using the highest p_T charged lepton (e or μ) in the event [17] with the event transverse missing energy, helps to reduce the background contributions from $W+$ jets by nearly an order of magnitude. We require $M_T < 35$ GeV.

(f) **Total Event p_T**
We require that the total event p_T, as defined in Sec. 5.1.4, be less than 70 GeV. This cut helps rejecting contributions from $t\bar{t}$ events.

(g) **b-Jet Veto**
The use of a b-jet veto is necessitated by the large number of $t\bar{t}$ background events that dominate over the Z' signal after both the transverse mass and total event p_T cuts. Significant numbers of $t\bar{t}$ events will have b-jets in the final state that have been tagged as such by the ATLAS offline reconstruction software (recall that

---

[17] The choice of using the highest p_T charged lepton for the reconstruction of the transverse mass was motivated by the resulting discrimination power.

$t \rightarrow Wb \sim 100\%$ of the time). To further suppress this background we employ a b-jet tagging method.

For jet reconstruction we have used a cone ΔR=0.4 algorithm [18]. Jets which overlap with identified leptons and taus within $\Delta R < 0.2$ were removed. A jet is tagged as a b-jet by applying a weight which is calculated using both a method of three-dimensional impact parameter and secondary vertex reconstruction [19]. Fig. 20 shows the distribution of the highest weight per event for a 600 GeV signal versus various background events. A cut at 4.0 provides roughly a factor of 4 rejection against this background. The reliability of b-jet tagging during early data-taking greatly depends on the inner detector alignment and the understanding of fake-rates.

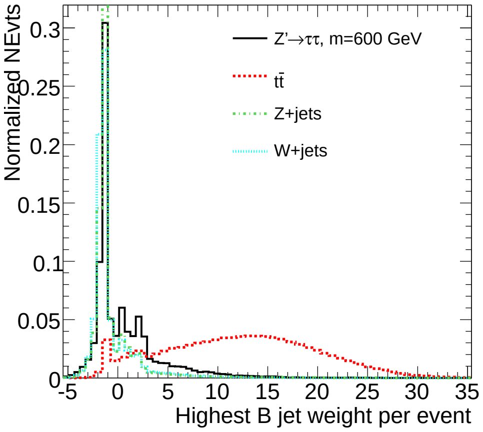

Figure 20: The distribution of the b-tagging weight variable for a 600 GeV signal versus various backgrounds.

(h) **Visible Mass**

For all events passing the event selection criteria up to this point, we construct a visible mass as defined in Sec. 5.1.5 using both of the charged leptonically-decaying tau daughter (e or μ) and missing energy four-vectors. A cut on the M_{vis} variable is used as a kind of mass window that only includes a lower bound. In the lepton-lepton analysis the lower bounds on M_{vis} are 300, 400, 500 and 700 GeV for Z' masses of 600, 800, 1000 and 2000 GeV, respectively. The reconstructed visible mass for this channel, for an 800 GeV Z' in 1 fb^{-1} of data, is shown in Fig. 21b.

(i) **Collinear Mass Reconstruction**

A reconstruction of the Z' collinear mass, as defined in Sec. 5.1.6 where x_1 and x_2 are the visible leptonically-decaying tau daughters, is attempted on those events that survive the M_{vis} cut. We require that $0 < x_1, x_2 < 0.75$. The resolution on the reconstructed collinear mass for the lepton-lepton final state suffers due to poor statistics and the presence of four neutrinos in the final state. Collinear mass reconstruction in this channel is really only helpful in the event of signal cross-sections that are significantly enhanced over those of the SSM (for 1 fb^{-1} of data).

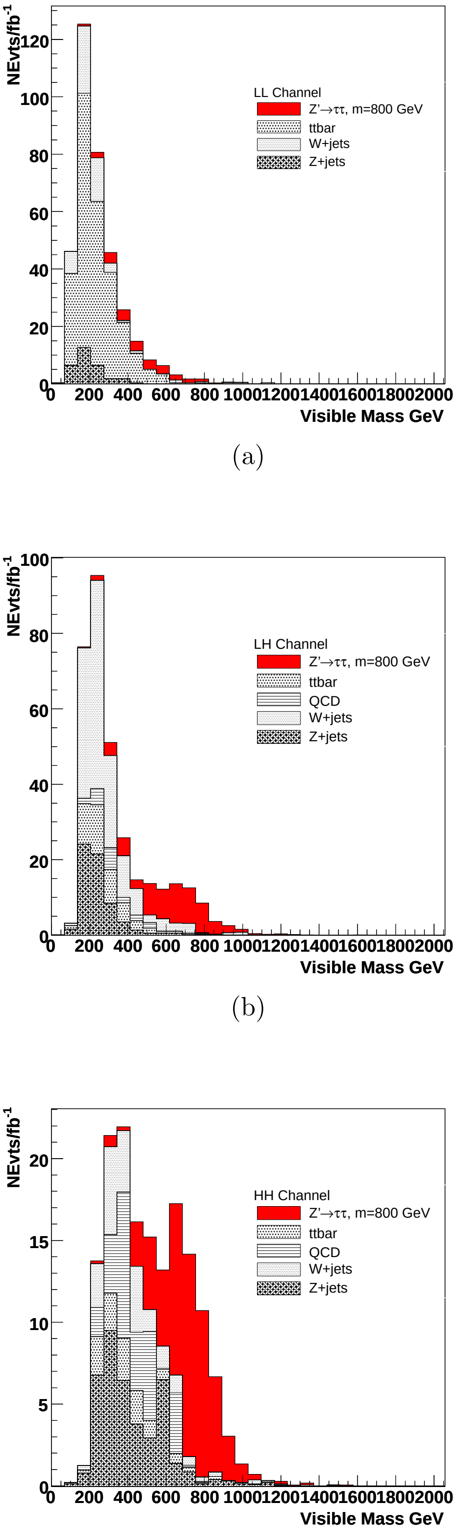

(a)

(b)

(c)

Figure 21: The reconstructed visible mass distribution obtained for the (a) lepton-lepton, (b) lepton-hadron and (c) hadron-hadron final states for a Z' signal mass of 800 GeV.

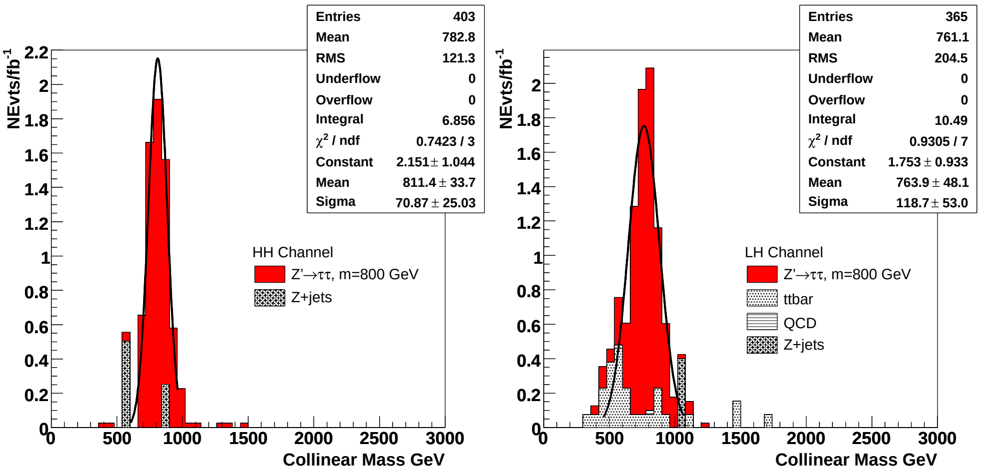

(a) (b)

Figure 22: (a) The collinear mass distribution obtained for the hadron-hadron final state and (b) the collinear mass distribution obtained for the lepton-hadron final state for a Z' signal mass of 800 GeV.

Signal Mass (Cut)	Z' Significance $[\sigma]$
$m = 600$ GeV ($M_{vis} > 300$ GeV)	4.8
$m = 600$ GeV (M_{col})	1.1
$m = 800$ GeV ($M_{vis} > 400$ GeV)	3.1
$m = 800$ GeV (M_{col})	0.4
$m = 1000$ GeV ($M_{vis} > 500$ GeV)	2.1
$m = 1000$ GeV (M_{col})	0.3
$m = 2000$ GeV ($M_{vis} > 700$ GeV)	0.1

Table 14: Significance values for the lepton-lepton final state in 1 fb^{-1}.

5.6 Di-tau Systematic Uncertainties

In this section we discuss various experimental systematic uncertainties which are specific for analyses involving τ leptons and their affect on the overall significance. Detailed studies of the theoretical uncertainties on heavy resonance production, common for both di-electron, di-muon and di-tau channels, and has been performed in [20].

The experimental systematic mis-measurements are as follows:

- The uncertainty on the efficiency of object identification is assumed to be 5% for muons, 1% for electrons, and 5% for tau leptons;
- The uncertainty on the energy scale is assumed to be 1% for muons, 0.5% for electrons, 5% for tau leptons and 7% for jets;
- The uncertainty on reconstructed p_T of the objects is as follows: $\sigma(E_T) = 0.012E_T$ for electrons, $\sigma(p_T) = 0.011p_T \oplus 1.710^{-4}p_T^2$ for muons, $\sigma(E) = 0.45\sqrt{E}$ for tau leptons and jets.

	Z' Signal σ [fb]				Background σ [fb]		
Cut	$m = 600$ GeV	$m = 800$ GeV	$m = 1000$ GeV	$m = 2000$ GeV	$t\bar{t}$	$W+$ jets	$Z+$ jets
Trigger	1355.9	516.8	223.7	11.6	213494.2	12365976.0	2050989.6
2 Leptons	132.3	55.2	25.7	1.1	13861.8	2250.3	640457.2
Charge	131.0	54.8	25.3	1.1	13219.4	1591.0	638777.9
MET $>$ 40 GeV	92.2	41.9	20.7	1.0	9964.5	$641.9^{\dagger}$	1205.9
M_T GeV < 35	69.3	31.9	16.0	0.7	1602.6	$82.5^{\dagger}$	331.9
$P_T^{tot} < 70$ GeV	52.2	24.5	12.3	0.5	551.6	$52.7^{\dagger}$	192.7
b Veto	52.0	24.2	12.0	0.5	130.1	$52.0^{\dagger}$	162.0
$M_{vis} > 300$ GeV	38.6	–	–	–	29.7	$5.0^{\dagger}$	18.4
M_{col}	2.5	–	–	–	0.9	$1.8^{\dagger}$	1.5
$M_{vis} > 400$ GeV	–	14.9	–	–	8.7	$1.8^{\dagger}$	7.7
M_{col}	–	0.6	–	–	$1.3^{\dagger}$	$0.9^{\dagger}$	$0.0^{\dagger}$
$M_{vis} > 500$ GeV	–	–	6.8	–	2.6	$0.9^{\dagger}$	4.6
M_{col}	–	–	0.2	–	$0.4^{\dagger}$	$0.0^{\dagger}$	$0.0^{\dagger}$
$M_{vis} > 700$ GeV	–	–	–	0.3	$1.7^{\dagger}$	$0.0^{\dagger}$	4.6

Table 15: Cutflow for the lepton-lepton final state. Note that all cross-sections here are given in fb. †Cross-section determined by factorization.

		Z' Mass			
Source	Relative uncertainty	600 GeV	800 GeV	1000 GeV	2000 GeV
Electron Energy Scale	±0.5%	0.4%	0.4%	0.3%	0.1%
Electron Energy Resolution	$\sigma(E_T) = 0.012E_T$	0.3%	0.2%	0.2%	0.2 %
Electron ID Efficiency	±1%	0.4%	0.4%	0.4%	0.3%
Muon Energy Scale	±1%	0.2%	0.2%	0.1%	0.1%
Muon Energy Resolution	$\sigma(p_T) = 0.011p_T \oplus 1.710^{-4}p_T^2$	0.4%	0.2%	0.1%	0.0%
Muon ID Efficiency	±5%	1.8%	1.8%	1.8%	1.6%
Tau Energy Scale	±5%	10.1%	6.0%	5.0%	3.0%
Tau Energy Resolution	$\sigma(E) = 0.45\sqrt{E}$	0.8%	0.2%	0.1%	0.1%
Tau ID Efficiency	±5%	6.4%	6.5%	6.5%	7.0%
Jet Energy Scale	±7%	1.2%	1.0%	1.1%	1.2%
Jet Energy Resolution	$\sigma(E) = 0.45\sqrt{E}$	0.3%	0.4%	0.5%	0.3%
Total		12.2%	9.1%	8.5%	7.8%

Table 16: Systematic uncertainties considered in the Z' analysis. The total systematic uncertainty is obtained by summing the individual contributions in quadrature.

- The uncertainty on the luminosity is assumed to be 20% with an integrated luminosity of 100 pb^{-1} of data and 3% for 10 fb^{-1}.

The uncertainties quoted on the resolution of muons, electrons, tau-leptons and jets are conservative estimates assuming sub-optimal performance of the corresponding algorithms at the beginning of ATLAS physics data-taking. In order to assess their impact, each of the variations is applied in turn and the affect on the result of the analysis is evaluated. Results are summarized in Tab. 16 for the four Z' mass points.

The most dominant systematic resulting in mis-measurement of the signal comes from the hadronic tau energy scale. The lowest mass signal is affected by 10%. The effect is less stringent for higher masses due to harder nature of taus coming from the Z' decay, which lie much further away from the p_T threshold used in the hadronic tau selection.

Given 1 fb^{-1} of data the dominant systematic source on the signal, on the order of 18%, comes from the uncertainty in the luminosity. Summing in quadrature the effect of all systematic mis-measurements on the signal Monte Carlo sample leads to a total systematic uncertainty of about ±20%. Given the insufficient statistics for the backgrounds, as discussed in Sec. 5.2, a rigorous evaluation of the systematics is not possible at this time. As a conservative estimate, we assume that the total systematic uncertainty on the backgrounds is identical to that observed in the signal Monte Carlo. This is a conservative estimate because the majority of the backgrounds in the data have very large cross-sections (di-jets, W+jets, ttbar) and the evaluation of systematic uncertainties there should be less sensitive to statistical fluctuations than for the signal events as also argued in [20]. Current studies on the evaluation of the $Z \to \tau\tau$ background using a control sample from data, estimate the systematic uncertainty of this sample to be around 10% [21].

5.7 Combined Significance

The discovery reach of resonance searches in the di-tau final state can be greatly enhanced by combining together each of the lepton-lepton, lepton-hadron and hadron-hadron final states. Table 17 shows the overall significance that can be obtained for 1 fb^{-1} of data by taking a quadrature sum of the individual significances. Figures 24a and 24b show the significance at the level of the M_{vis} and M_{col} selection cuts, respectively, in 1 fb^{-1} of data for the individual final states, as well as all combined. The grey region in each plot denotes the affect on the total significance assuming 20% systematic uncertainty on the background.

$m = 600$ GeV (M_{vis})	18.3
$m = 600$ GeV (M_{col})	8.0
$m = 800$ GeV (M_{vis})	12.1
$m = 800$ GeV (M_{col})	5.5
$m = 1000$ GeV (M_{vis})	7.8
$m = 1000$ GeV (M_{col})	4.9
$m = 2000$ GeV (M_{vis})	0.8

Table 17: Significance values for all final states combined, assuming 1 fb^{-1} of data.

Figures 23a and 23b show the reconstructed visible and collinear mass shapes obtained from the combination of all three final-states and assuming 1 fb^{-1} of data.

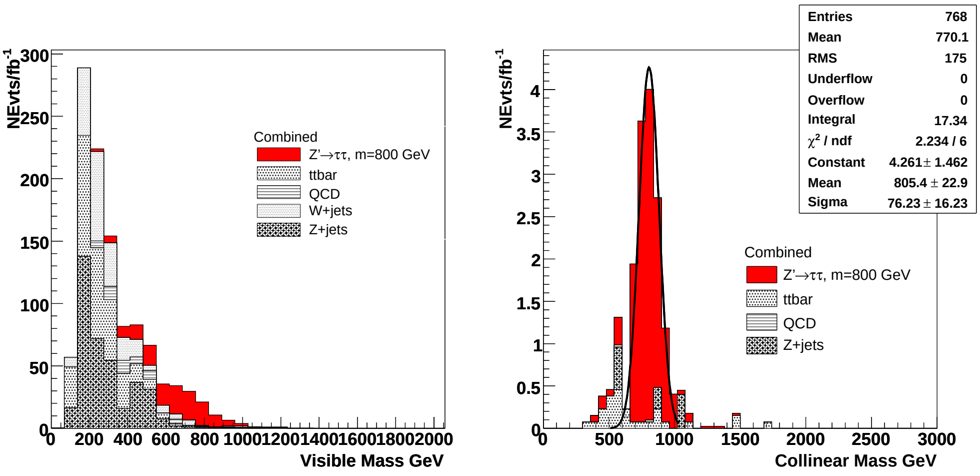

(a)

(b)

Figure 23: (a) The reconstructed visible mass distribution obtained for all final states and a Z' signal mass of 800 GeV, and (b) the collinear mass distribution obtained for all final states and a Z' signal mass of 800 GeV. In each case 1 fb^{-1} of data is assumed.

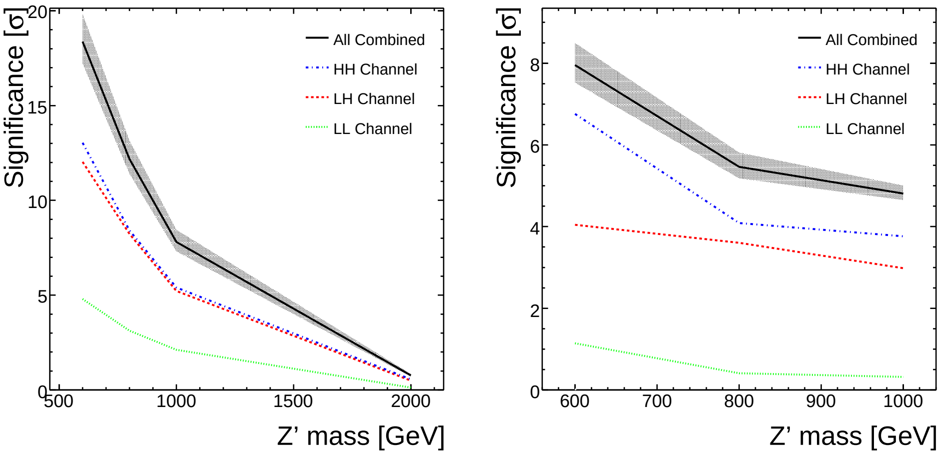

(a)

(b)

Figure 24: (a) The significance at the level of the M_{vis} selection in 1 fb^{-1} of data for the individual final states, as well as all combined. (b) The significance at the level of the M_{col} selection in 1 fb^{-1} of data for the individual final states, as well as all combined. The grey region in each plot denotes the effect on the total significance assuming 20% systematic uncertainty on the background.

6 Summary and Conclusion

Using the official ATLAS reconstruction package and ATLAS trigger system emulation we have studied the potential for discovering a Z' boson decaying into high p_T tau pairs. All di-tau final states (lepton-lepton, lepton-hadron and hadron-hadron) have been studied in a wide mass range extending from 600 to 2000 GeV.

The hadron-hadron and lepton-hadron final-states are the most promising channels due to the larger branching ratios and higher signal-to-background. In addition to suffering from the smallest total branching fraction, the lepton-lepton channel requires b-jet tagging to suppress backgrounds from ttbar events–it is not clear that this is a capability we will have during early ATLAS data-taking.

The best mass resolution comes from the hadron-hadron channel (via the collinear approximation) due to the fact that this final-state contains the fewest neutrinos. A total of four neutrinos from tau decays in the lepton-lepton final state adversely affects the mass resolution in this channel. It is worth noting that factorization of the QCD di-jet background was only conducted for those samples which had $p_T < 560$; for the higher p_T samples sufficently large statistics were available. It is also worthwhile to mention that the exact cross-sections for the QCD backgrounds at the LHC are not known, however scaling up the contribution from QCD di-jets by factors of 2 and 10 yield signifiances that are reduced by 10% and 45%, respectively. Even in the most pessimistic case, the fully-hadronic mode remains a discovery channel for the two lowest mass points that were considered in the analysis.

To gauge the discovery reach of these analyses, Figure 25a shows the amount of luminosity required for 3σ evidence or a 5σ discovery as a function of the true mass of the Z'. If a Z' exists with a relatively low mass, and is coupled to the third family, it could be discovered in the di-tau final state with only a few hundred pb^{-1} of data. Figure 25b shows the cross-section required for 3σ evidence or a 5σ discovery (all channels combined) as a function of a Z' mass given 1 fb^{-1} of data. The cross-section from the SSM, as a function of the true Z' mass, is superimposed. Assuming SSM couplings of the extra gauge boson to taus, we can reach a 5σ discovery limit if the Z' has a mass up to rougly 1200 GeV. However, such a discovery comes from a counting experiment using the visible mass as outlined in Sec. 5. As shown in Sec. 5 the invariant mass resolution is on the order of 10% in the hadron-hadron channel and 15% in the lepton-hadron final-state. Since the SSM Z' is very narrow, the intrinsic width of the resonance is completely dominated by the detector resolution. As discussed earlier, the collinear approximation reaches a limit of validity at a mass of around 1000 GeV, where almost all Z' signal events are back-to-back. If Nature presents ATLAS with a Z' heavier than $\sim$ 1000 GeV, the mass could be estimated from the data by using template and fitting methods, for example.

Although we assumed the SSM and it's branching fractions in our analysis, we did not consider possible contributions to the di-tau background from other Z' decays (e.g., e^+e^-, or $t\bar{t}$).

It should be stressed that ATLAS software is still very much under development and considerable improvements to a few areas have already appeared in newer releases. Regarding the hadronic tau trigger, a new high p_T single tau menu item has been added which is relevant for selecting events containing a non-isolated hadronic tau. This change will enhance the trigger efficiency for the hadron-hadron channel above that shown in Sec. 4.2 of this note. A few changes which could improve the analysis have also been implemented in the `tauRec` offline tau reconstruction package:

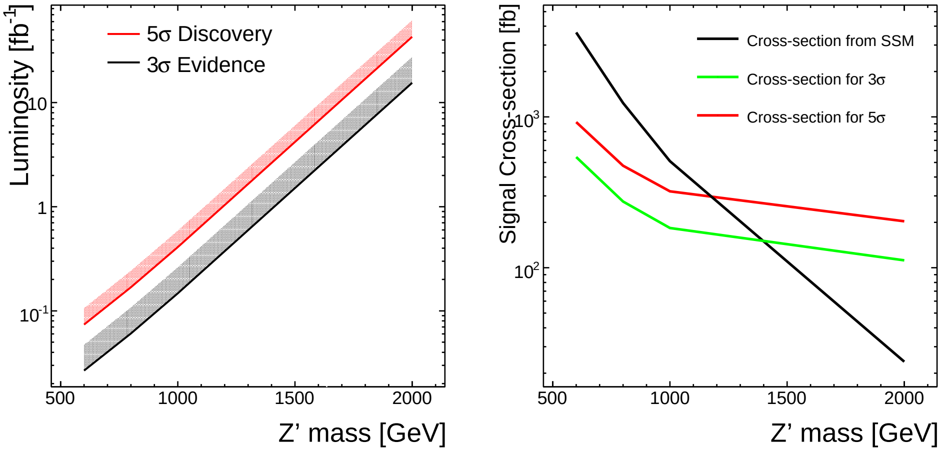

(a) (b)

Figure 25: (a) The luminosity required for 3σ evidence or a 5σ discovery (all channels combined) as a function of the true Z' mass. (b) The signal cross-section required for 3σ evidence or a 5σ discovery (all channels combined) as a function of the true Z' mass assuming 1 fb^{-1} of data. The signal cross-section from the SSM, as a function of Z' mass, is superimposed.

(1) The likelihood discriminant has been tuned to provide better separation of taus and QCD di-jets.

(2) Dedicated tools to veto electrons and muons have been added; these suppress fakes due to non-tau leptons and therefore increase the purity.

(3) Stricter track quality criteria have been employed to suppress tracks coming from conversions, which in turn diminish charge mis-identification and hence a higher efficiency of preselection is expected.

Although we have used a Z' from the Simple Extension to the Standard Model as a reference signal for the studies presented here, much of the discussion generalizes to a generic di-tau resonance search. The resulting cross-section needed for 3σ evidence or a 5σ discovery as a function of a mass (shown in Fig. 25b) is a general statement and holds for other types of resonances such as those from a very heavy MSSM Higgs or a graviton.

In the MSSM scenario, one observation can be crucial: At large values of $\tan\beta$ the coupling to down-type leptons and quarks is strongly enhanced. This means that the dominant Higgs production mechanism is no longer a direct gluon-gluon fusion ($gg \rightarrow H$) mode alone, but associated production with b quarks in a final state ($b\bar{b} \rightarrow H/A$, $bg \rightarrow bH/A$, $gg/q\bar{q} \rightarrow b\bar{b}H/A$) contribute as well. As the latter two production mechanisms are $2 \rightarrow 2$ and $2 \rightarrow 3$ processes, the Higgs boson acquires a large transverse momentum which in turn allows for a more efficient reconstruction of the invariant mass via the collinear approximation. As discussed in Sec. 5.1.6 most of the backgrounds peak around $\Delta\phi{=}-\pi/2$ and therefore searches using a reconstructed mass might become more sensitive.

In the event of a discovery of a new particle using generic searches, such as those outlined here, a natural question emerges regarding the exact nature of the observed resonance. Discrimination between different models can proceed by investigating the coupling of the resonance to τ-leptons and looking for the same resonance in other di-lepton final states. Conducting an exclusive analysis reliant on the number of b-tagged jets in a final-state could provide a clue as to whether the observed resonance is an MSSM Higgs or not.

Generic searches in di-tau final-states also provide a unique opportunity to determine the spin of the parent particle via correlations between the tau decay products [22, 23, 24]. Additionally, the spin-2 nature of a resonance can be determined by using the $\cos\theta^*$ variable–an angular distribution built directly from the decay products of the resonance [25]. The $\cos\theta^*$ method has broader applicability, as it can also be applied to di-electron and di-muon resonances.

Appendix A

For the studies presented in this note, the following Monte carlo samples were used:

Signal : Z' bosons of 600, 800, 1000 and 2000 GeV decaying to tau lepton pairs with all τ decay modes included. Details about the sample are summarized in Tab. 18. Events were generated with `PYTHIA` 6.403. TAUOLA [11] package for τ decays has not been used.

Backgrounds : Details about the samples are summarized in Tab. 19.

For analysis of tau performance and lepton-hadron and hadron-hadron final states AAN data format was used. For lepton-lepton analysis, due to lack of information on b-jet tagging in AAN, the AOD data format has been used.

Sample	Mass ($\sqrt{\hat{s}}/2$ cut)	Dataset ID	ATHENA	Cross-section [pb]	N Events
$Z' \to \tau\tau$	600 GeV (300 GeV)	5607	v12.0.6.1	3.64	20000
$Z' \to \tau\tau$	800 GeV (400 GeV)	5618	v12.0.6.5	1.24	49250
$Z' \to \tau\tau$	1000 GeV (500 GeV)	5619	v12.0.6.5	0.51	37950
$Z' \to \tau\tau$	2000 GeV (1000 GeV)	6683	v12.0.6.5	0.02	49650

Table 18: Signal samples used for the Z' lepton-lepton, lepton-hadron and hadron-hadron analyses. For each sample invariant mass, ATLAS CSC dataset IDs, offline reconstruction software version, cross-section and number of events is given.

Appendix B

Sample	Description	Generator	Dataset ID	ATHENA	Cross-section [pb]	N Events
QCD dijets	p_T cut: 35 - 70 GeV	`PYTHIA` 6.403	5011	v12.0.6.1	9.33×10^7	371k
QCD dijets	p_T cut: 70 - 140 GeV	`PYTHIA` 6.403	5012	v12.0.6.1	5.88×10^6	365.8k
QCD dijets	p_T cut: 140 - 280 GeV	`PYTHIA` 6.403	5013	v12.0.6.1	3.08×10^5	386.9k
QCD dijets	p_T cut: 280 - 560 GeV	`PYTHIA` 6.403	5014	v12.0.6.1	1.25×10^4	378.6k
QCD dijets	p_T cut: 560 - 1120 GeV	`PYTHIA` 6.403	5015	v12.0.6.1	360	476.2k
QCD dijets	p_T cut: 1120 - 2240 GeV	`PYTHIA` 6.403	5016	v12.0.6.4	5.71	137.8k
$t\bar{t}$	Single lepton filter	`MC@NLO` 3.1	5200	v12.0.6.5	833*0.54	438.6k
$t\bar{t}$	fully-hadronic	`MC@NLO` 3.1	5204†	v12.0.6.4	833*0.46	200k
$W(e\nu)$+jets	$\|\eta\| < 2.7$, $p_T > 10$ GeV	`PYTHIA` 6.403	5104	v12.0.6.5	10899	486.0k
$W(\mu\nu)$+jets	$\|\eta\| < 2.8$, $p_T > 5$ GeV	`PYTHIA` 6.403	5105	v12.0.6.5	11868	237.5k
$W(\tau_h\nu)$+jets	$\|\eta\| < 3.5$, $p_T > 10$ GeV	`PYTHIA` 6.403	5107	v12.0.6.5	5540	226.7k
$Z(ee)$+jets	$M_{ll} > 60$ GeV, 1e: $\|\eta\| < 2.7$, $p_T > 10$ GeV	`PYTHIA` 6.403	5144	v12.0.6.1	1436	302.6k
$Z(\mu\mu)$+jets	$M_{ll} > 60$ GeV, 1mu: $\|\eta\| < 2.8$, $p_T > 5$ GeV	`PYTHIA` 6.403	5145	v12.0.6.1	1495	396.6k
$Z(\tau_l\tau_l)$+jets	$M_{ll} > 60$ GeV, 2l: $\|\eta\| < 2.8$, $p_T > 5$ GeV/c	`PYTHIA` 6.403	5146†	v12.0.6.5	77	101.8k
$Z(\tau_{l,h}\tau_{h.h})$+jets	no $\Delta\phi$ cut	`PYTHIA` 6.403	5189‡	v12.0.6.5	458	481.5k

Table 19: Background samples used for the Z’ lepton-lepton, lepton-hadron and hadron-hadron analyses. The Monte Carlo generator, ATLAS CSC dataset IDs, offline reconstruction software version, cross-section times filter efficiency, number of events are listed. †Note that the contribution to the cutflow was found to be so small that it was neglected in Tables 15-11. ‡Note that no trigger simulation was available for this sample.

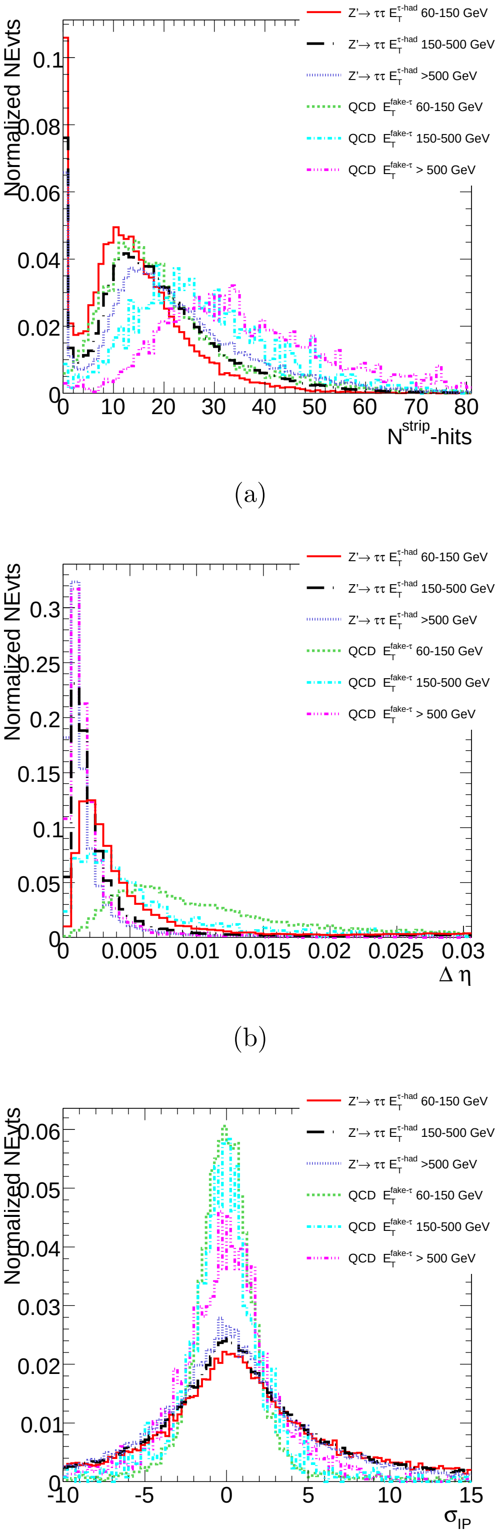

Figure 26: For three different E_T ranges (a) $N_{\eta-\text{hits}}$, (b) $\Delta\eta$ and (c) σ_{IP} are shown. All distributions here are shown after requiring $1 \leq N_{\text{trk}} \leq 3$. The QCD di-jet samples with a P_T of the hard process between 35 and 2240 GeV have been used.

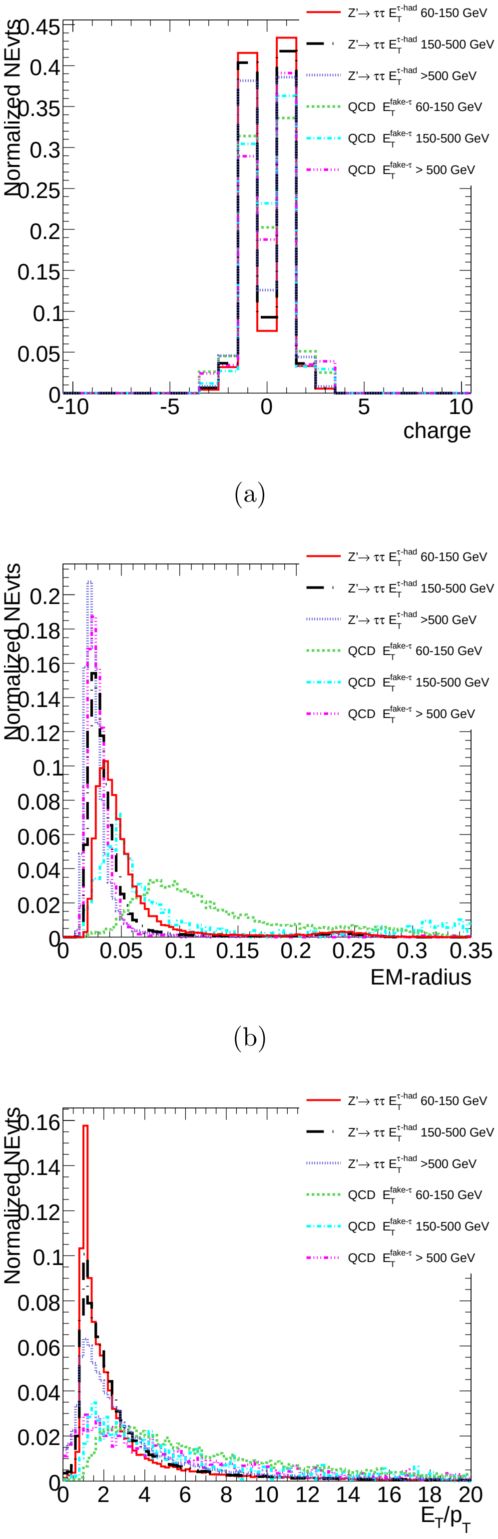

(a)

(b)

(c)

Figure 27: For three different E_T ranges (a) τ-Charge, (b) EM-Radius and (c) $\mathrm{E_T/P_T}$. All distributions here are shown after requiring $1 \leq \mathrm{N_{trk}} \leq 3$. The QCD di-jet samples with a P_T of the hard process between 35 and 2240 GeV have been used.

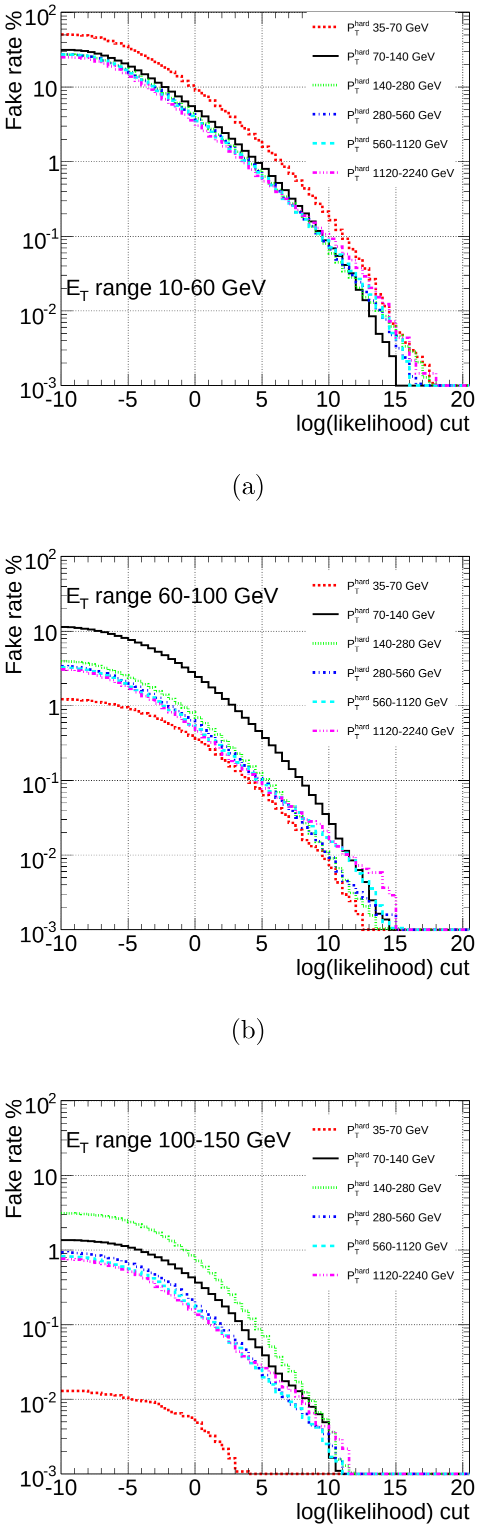

(a)

(b)

(c)

Figure 28: The QCD fake-rate as a function of the llh for three different E_T ranges as marked on each of (a), (b) and (c). The llh refers to the highest llh fake tau per event. p_T^{hard} denotes the p_T of the hard process used for the generation of the QCD di-jet events.

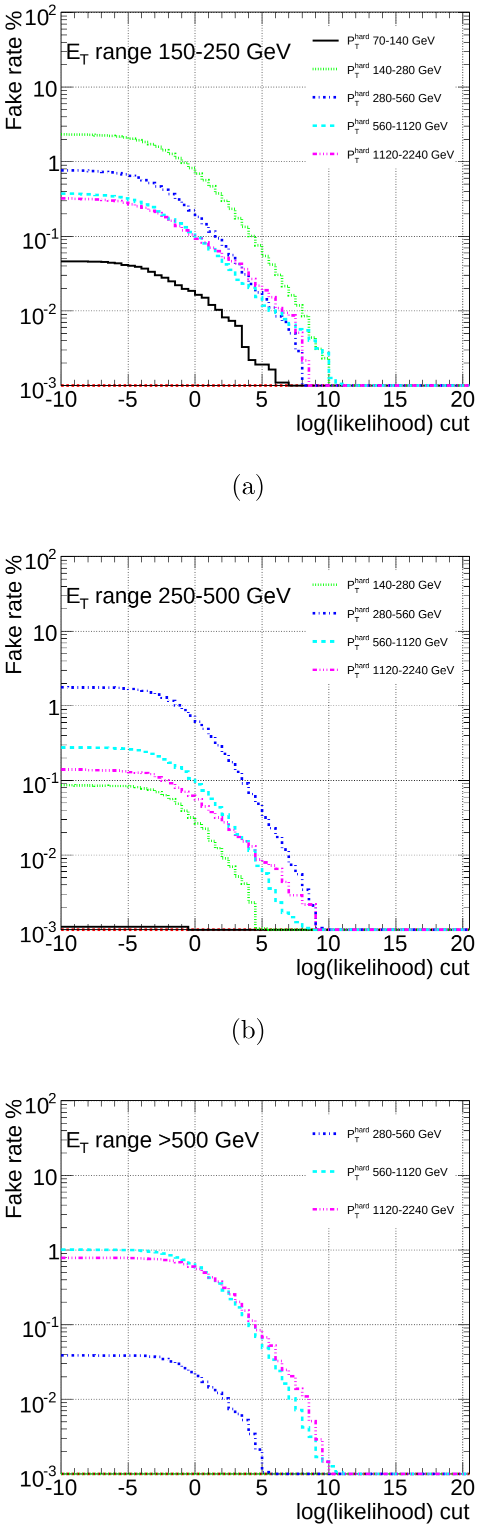

(a)

(b)

(c)

Figure 29: The QCD fake-rate as a function of the llh cut for three different E_T ranges as marked on each (a), (b) and (c) plot. The llh refers to the highest llh fake tau per event. p_T^{hard} denotes the p_T of the hard process used for the generation of the QCD di-jet events.

References

[1] H. Georgi and S.L. Glashow, Phys. Rev. Lett. 32 (1974).

[2] L. Randall and R.Sundrum, Phys. Rev. Lett. 83 (1999).

[3] N. Arkani-Hamed, A.G.Cohen and H.Georgi, Phys Letters B 513 (2001).

[4] M. Carena *et al.*, Phys. Rev. D70 093009 (2004).

[5] A. A. Andrianov, P. Osland, A. A. Pankov, N. V. Romanenko and J. Sirkka, "On the phenomenology of a Z-prime coupling only to third family fermions", Phys. Rev. D58 (1998).

[6] K. R. Lynch, S. Mrenna, M. Narain and E. H. Simmons, "Finding Z' bosons coupled preferentially to the third family at CERN LEP and the Fermilab Tevatron", Phys. Rev. D63 035006 (2001).

[7] K. Lane and E. Eichten, Phys. Lett. B 222 (1989).

[8] K. Lane and E. Eichten, "Natural topcolor-assisted technicolor", Phys. Lett. B 352 (1995).

[9] R.S. Chivukula, A.G. Cohen and E.H. Simmons, Phys. Lett. B 380 (1996).

[10] T. Sjöstrand *et al.*, Comput. Phys. Commun. **135**, 238 (2001); T. Sjöstrand *et al.*, J. High Energy Phys. JHEP05 026 (2006).

[11] S. Jadach *et al.*, The tau decay library, TAUOLA: version 2.4, Comp. Phys.Commun. 76 (1993).

[12] D. Acosta *et al.*, "Search for New Physics Using High Mass Tau Pairs from 1.96-TeV $p\bar{p}$ Collisions", Phys. Rev. Lett. 95, 131801 (2005).

[13] M.Heldmann and D. Cavalli, "An Improved τ-Identification For The ATLAS Experiment", ATLAS-PHYS-PUB-2006-008.

[14] A. Kaczmarska, E. Richter-Was, M. Wolter, L. Janyst, "Performance of the tau1p3p algorithm for hadronic tau decays identification with release 12.0.6", ATL-COM-PHYS-2007-039.

[15] E. Richter-Was and T. Szymocha, Hadronic tau identification with track based approach : the Z→tautau, W→tau nu and dijet events from DC1 data samples, ATL-PUB-PHYS-2005-005

[16] ATLAS Collaboration, "ATLAS Tau Trigger: Performance and Menus for Early Running", CSC Note in preparation.

[17] CMS Physics TDR, CERN-LHCC 2006-021.

[18] ATLAS Collaboration, "Jet Algorithm Performance in ATLAS", CSC Note in preparation.

[19] ATLAS Collaboration, "b-Tagging Performance in ATLAS", CSC Note in preparation.

[20] ATLAS Collaboration, “Dilepton Resonances at High Masses,” CSC Note in preparation.

[21] T. Vickey, *et al.*, “A Data-driven Control Sample for $Z \rightarrow \tau\tau + \text{jets}$ Backgrounds to Higgs Searches,” In Preparation.

[22] T.Pierzchala, E.Richter-Was, Z.Was and M.Worek, “Spin Effects in tau lepton pair production at LHC”, Acta Physica Polonica B, Vol 32 (2001).

[23] G.R.Bower, T.Pierzchala, Z.Was and M.Worek, “Measuring the Higgs boson’s parity using tau→rho nu”, Physics Letter B 543 (2002) 227-234.

[24] B.K. Bullock, K. Hagiwara and A.D. Martin, “Tau Polarization ans its corrections as a probe of new physics”, Physics Letter B 395 (1993) 499-533.

[25] B.C. Allanach, K. Odagiri, M.A. Parker and B.R. Webber, “Searching for Narrow Graviton Resonances with the ATLAS Detector at the Large Hadron Collider”, hep-ph/0006114.

B

Z.Czyczula, M.Dam

Electron veto in the τ identification package tau1p3p

Electron veto in the τ identification package tau1p3p

Z. Czyczula, M. Dam
Niels Bohr Institute, University of Copenhagen,
DK-2100 Copenhagen, Blegdamsvej 17, Denmark

Abstract

A track based algorithm for suppression of electrons in an efficient identification of hadronic τ decays is described. The algorithm is seeded by the leading track of a τ candidate reconstructed by the TAU1P3P algorithm. Information on energy depositions in the hadronic and electromagnetic calorimeters close to the track extrapolation are used for the separation. In addition, the transition radiation in the TRT is used. The analysis covers the full detector region, $|\eta| < 2.5$, relevant for τ reconstruction. Results of the algorithm are presented and a significant improvement is observed relative to the standard ATLAS electron identification procedure (the IsEM flag).

1 Introduction

Two algorithms are currently implemented in ATLAS for the reconstruction of hadronic τ decays: The calorimeter seeded TAURec algorithm [1], and the track based TAU1P3P algorithm [2]. The first one starts from a calorimeter cluster and builds identification variables based on information from the electromagnetic (ECAL) and hadronic (HCAL) calorimeters as well as from the Inner Detector (ID). The latter one starts from a reconstructed track and collects calorimeter energy deposited in a fixed cone seeded by the track direction at the vertex. Neither of these methods, making use of the narrowness and isolation of calorimeter showers and low track multiplicity, intrinsically provides discrimination against electrons, and without further rejection the major part of electrons would be reconstructed as hadronic τ decays. In the TAURec algorithm, electron rejection is provided using a Neural Network discriminant [3]. Here we present an algorithm for electron suppression in the TAU1P3P package. The algorithm is track based and uses a fixed cut method to discriminate hadronic τ decays from electrons.

The note is organized as follows. First, the track quality cuts applied in TAU1P3P are revisited and new improved quality cuts suggested. These improved cuts have been now implemented as default in TAU1P3P. Next, the electron rejection procedure is discussed. Last, the efficiency is presented together with comparison to the standard ATLAS electron identification procedure (IsEM flag). Appendix A presents details about the used data samples. Appendix B describes an implementation of the algorithm in TAU1P3P together with the status in different releases.

2 Track selection and removal of electrons from conversions

In TAU1P3P, a tau candidate is seeded by the presence of a track with transverse momentum above a certain threshold (default $p_{\mathrm{T}} > 9\,\mathrm{GeV}$). Other nearby tracks are recognized if their transverse momentum exceeds a lower threshold (default $p_{\mathrm{T}} > 2\,\mathrm{GeV}$). To ensure that tracks are of good quality, they were required to fulfill the following set of criteria:

1. transverse impact parameter, $A_0 < 1$ mm;
2. number of pixel plus SCT hits ≥ 8;
3. good quality of the track fit, i.e. χ^2/d.o.f. < 1.7;
4. number of TRT hits ≥ 10 (η range up to 1.9);
5. number of high threshold TRT hits < 5.

For an improved efficiency for three-prong decays, one of three tracks is allowed to fulfill only the first two of these criteria. It is then required that a maximum of three good tracks be found in the region considered as the core of the tau decay, and subsequently an isolation cut on tracks is applied. The track with the highest momentum is called the leading track, the other tracks are called additional.

Reconstructed tau decays are categorized as one-prong (1P), two-prong (2P), or three-prong (3P) decays based on the number of reconstructed good quality tracks. In the material of the ID, some fraction of photons from π^0 decays undergo conversion into e^+e^- pairs. Another source of additional tracks is the underlying event. As a consequence, true one-prong decays may migrate to higher topologies, typically two- or three-prong. Due to inefficiencies in the reconstruction of good quality tracks, downwards migration is also observed.

In order to minimize upwards migration, rejection against electrons from conversions is needed at the reconstruction level. In TAU1P3P, once a tau decay is built and categorized as 1P, 2P, or 3P it cannot be moved from one category to the other. Therefore, suppression of conversion electrons has to be performed already at the same stage as the selection of good quality tracks.

The track selection variables are the following:

$\mathrm{N_B}$: Number of hits in the innermost layer of the Pixel Detector, the B-layer. Since most conversions happen at larger radii, at least one hit in this layer ensure that the track is a primary one. Requiring B-layer hits for the additional tracks rejects a significant number of tracks from photon conversions (Fig. 1a and b). The leading track, however, with very high probability (more than 99% in W→ $\tau\nu$) is a primary one, why this cut, which would lead to an additional 3-4% efficiency loss, is unnecessary.

$\mathrm{N_{LT}}$: Number of TRT hits. A track is required to have at least ten TRT hits. For an improved efficiency, *outlier hits* (i.e. hits associated with the track, but not used in the track fit) are included. Adding outlier hits improves the efficiency by 5-10% (Fig. 1c). A significant number of additional tracks have no TRT hits (Fig. 1c). These are predominantly soft tracks, $p_{\mathrm{T}} < 10$ GeV, (Fig. 1e) which are likely lost due to inefficiencies in the reconstruction and/or interaction in the ID material. Thus, this cut is applied only for primary tracks.

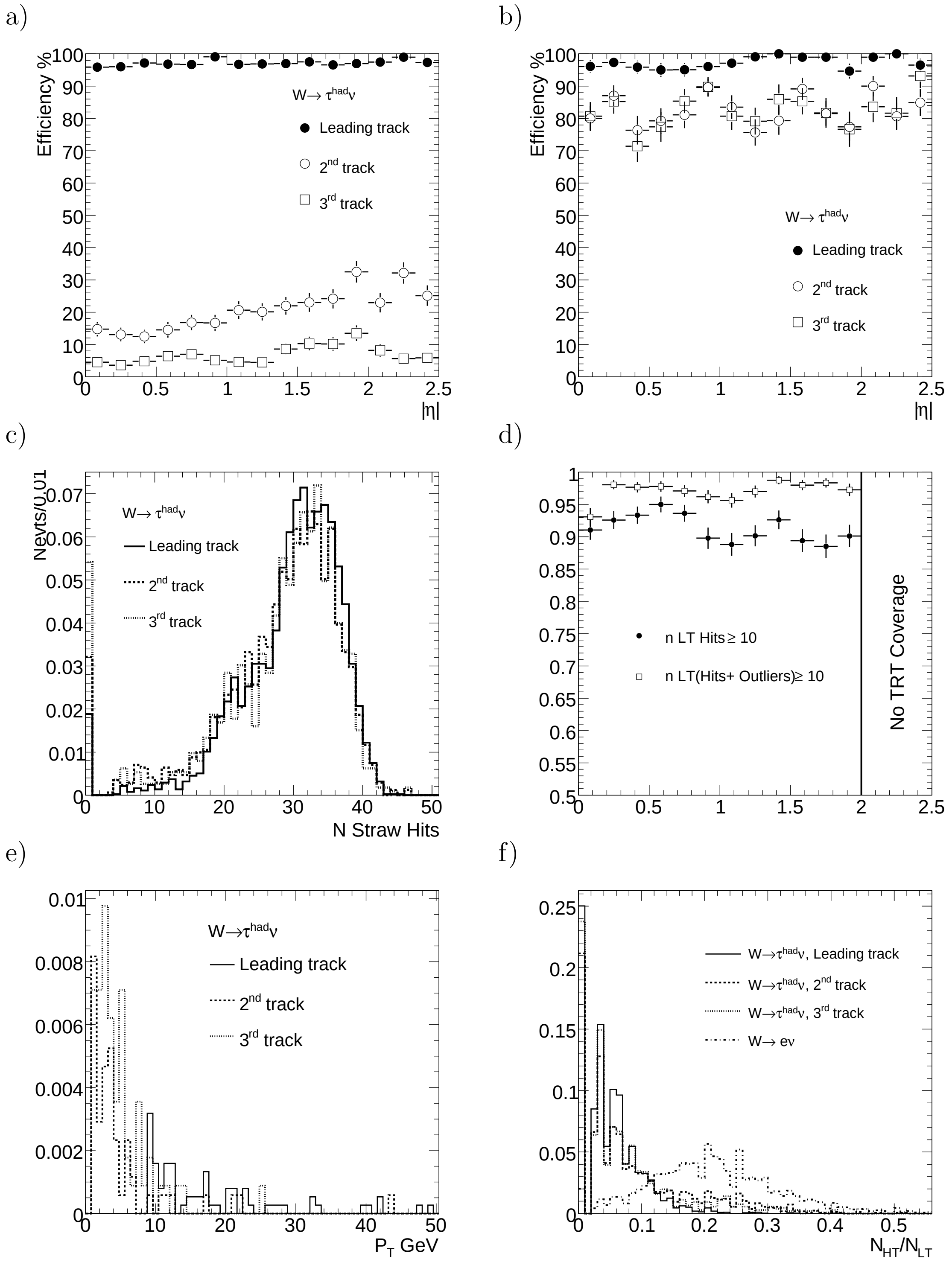

Figure 1: Top: Fraction of tracks from true one-prong (a) and three-prong (b) tau decays having at least one hit in the B layer. Middle: c) Distribution of number of TRT hits including outliers; d) Fraction of leading tracks having at least ten TRT hits. Bottom: e) Transverse momentum of tracks with no TRT hits (distributions normalized to number of leading, $2^{\rm nd}$ and $3^{\rm rd}$ tracks respectively). f) Tracking variable $\rm N_{HT}/N_{LT}$.

	W $\rightarrow \tau\nu$ old selection	W $\rightarrow \tau\nu$ new selection
Reconstruction efficiency	55.2 %	57.2 %
1P $\rightarrow$ 3P migration	3.8 %	3.4 %
3P $\rightarrow$ 1P migration	5.0 %	3.6 %
Charge Mis-identification 1P	2.0 %	1.8 %
Charge Mis-identification 3P	2.4 %	3.0 %

Table 1: Reconstruction efficiency and probabilities for 1P → 3P and 3P → 1P migration and charge mis-identification (in %), for new and old track selection criteria.

$\mathbf{N}_{\mathrm{HT}}/\mathbf{N}_{\mathrm{LT}}$: Fraction of TRT hits (including outliers) with response exceeding high threshold (Fig. 1f). High threshold hits indicate transition radiation and are therefore sensitive to electrons.

The revised criteria to define good quality tracks are the following:

1. transverse impact parameter, $A_0 < 1$ mm;
2. number of pixel plus SCT hits ≥ 8;
3. good quality of the track fit: χ^2/d.o.f. < 1.7;
4. number of TRT hits (including outliers) ≥ 10 for leading track
5. fraction of TRT hits exceeding high threshold < 0.2;
6. for additional tracks, at least one B layer hit

The TRT cuts (cuts 4 and 5) are only applied in the range $|\eta| < 1.9$, and again, for three prong candidates, one track is allowed to fulfill only the first two criteria. These criteria have been implemented in TAU1P3P since release 13.0.20. We refer to them as “new selection” as opposed to the “old selection” used previously. If not otherwise stated, the new criteria are used.

The reconstruction efficiency and the probabilities for 1P → 3P and 3P → 1P migration and charge misidentification are summarized in Tab. 1, for the old and new selections. Here, the reconstruction efficiency is defined as the ratio between the number of reconstructed tau candidates and all true tau decays with $p_{\mathrm{T}} > 9$ GeV. The probability for 1P → 3P (3P → 1P) migration is the fraction of true 1P (3P) decays being reconstructed as 3P (1P). Finally, the charge mis-identification probability is the fraction of tau decays being reconstructed with a wrong charge.

3 Electron rejection

The rejection of electrons is based on the following variables:

E_{HCAL}: The energy deposit in the first layer of the HCAL in a window $\Delta\phi \leq 0.2$ and $\Delta\eta \leq 0.2$ around the track extrapolation (Fig. 2a). Cutting in E_{HCAL} at 0.4 GeV (or alternatively at 0.2 GeV) already gives a good separation of electrons from hadrons (Fig. 2c). In the barrel HCAL transition region at $|\eta| \sim 1$, the first HCAL layer is partly missing, as visible from Fig. 2c. To compensate for this, the energy in the full HCAL depth is collected in the region $0.8 \leq |\eta| < 1.2$. The E_{HCAL} variable is plotted for electrons and pions in the left hand column of Fig. 2. Note from Fig. 2c, the step in efficiency around $|\eta| \simeq 1.7$. This coincides with the transition in technology of the HCAL going from the tile calorimeter in the central part to LAr in the forward parts [4].

$E_{\text{strip}}^{\text{max}}$: This variable has been designed to be sensitive to secondary energy deposits in the ECAL not associated to the leading track. The energy in the strip compartment is summed over three cells in ϕ, and local maxima are searched for in 101 cell sums in η centered around the impact point of the leading track (excluding a region $1.475 \leq |\eta| \leq 1.5$ corresponding to the ECAL crack). Excluding the energy associated with the leading track, the variable measures the maximum strip energy sum within the searched range. The variable is used only in the region of $|\eta| \leq 1.7$, where discrimination power is provided by the TRT.

E_{ECAL}/p: The ratio between the ECAL energy and the momentum of the track. The energy is calculated in the following windows ($\Delta\eta \times \Delta\phi$) around the impact cell: 0.075×0.3 in presampler, 0.0475×0.3 in strips, 0.075×0.075 in middle, and 1.5×0.075 in back compartment.

$\mathbf{N}_{\text{HT}}/\mathbf{N}_{\text{LT}}$: The ratio of high threshold to low threshold hits in the TRT including outliers.

In the region where the TRT provides efficient discrimination between electrons and hadrons ($|\eta| \leq 1.7$), the separation procedure is as follows:

1. As a first step, candidates with $E_{\text{HCAL}} > 0.4\,\text{GeV}$ are selected as hadrons. Very few electrons leak through the ECAL to deposit energy in the HCAL, as seen from Fig. 2a. Thus, the electron contamination in this sample is already very low. As seen from Fig. 2e, the efficiency for hadronic decays to pass this cut varies from about 70% at low momenta to about 95% at high momenta and is decreasing with pseudorapidity.

2. We concentrate next on candidates with $E_{\text{HCAL}} < 0.4\,\text{GeV}$. For this sample, the plots in the right hand column of Fig. 2 show the variable $E_{\text{strip}}^{\text{max}}$. The decay $\tau \to \rho\nu$ tends to have a rather energetic secondary shower from the π^0 photons. Also for the $\tau \to \pi\nu$ decay, a tendency towards secondary showers is observed. This is likely caused by hadronic interactions in front of and inside the ECAL. We apply the cut $E_{\text{strip}}^{\text{max}} > 0.3\,\text{GeV}$, to select hadrons. In the selected sample, the electron contamination is larger than above, so we apply a cut on the TRT, $\text{N}_{\text{HT}}/\text{N}_{\text{LT}} \leq 0.11$, in order to suppress this background.

3. The remaining candidates which have neither a significant HCAL energy ($E_{\text{HCAL}} < 0.4\,\text{GeV}$) nor a secondary electromagnetic shower ($E_{\text{strip}}^{\text{max}} < 0.3\,\text{GeV}$) are very rich in electrons. Fig. 3a shows E_{ECAL}/p for this sample with the electrons tending to peak at unity as expected. A cut, $E_{\text{ECAL}}/p < 0.85$, in combination with the TRT requirement, $\text{N}_{\text{HT}}/\text{N}_{\text{LT}} \leq 0.12$, is applied to suppress electrons.

In the region $|\eta| > 1.7$, where the TRT provides no efficient electron/hadron separation, a much simplified rejection procedure is applied. Any candidate with $E_{\text{HCAL}} > 0.2\,\text{GeV}$ is accepted as a hadronic τ decay. For candidates with $E_{\text{HCAL}} \leq 0.2\,\text{GeV}$, it is required that $E_{\text{ECAL}}/p < 0.8$ and that $\text{N}_{\text{HT}}/\text{N}_{\text{LT}} \leq 0.12$. The lower requirement on the HCAL energy as compared to the more central detector region improves the selection efficiency significantly.

The electron rejection procedure is summarized in Tab. 2 and the efficiency at each step is given in Tab. 3.

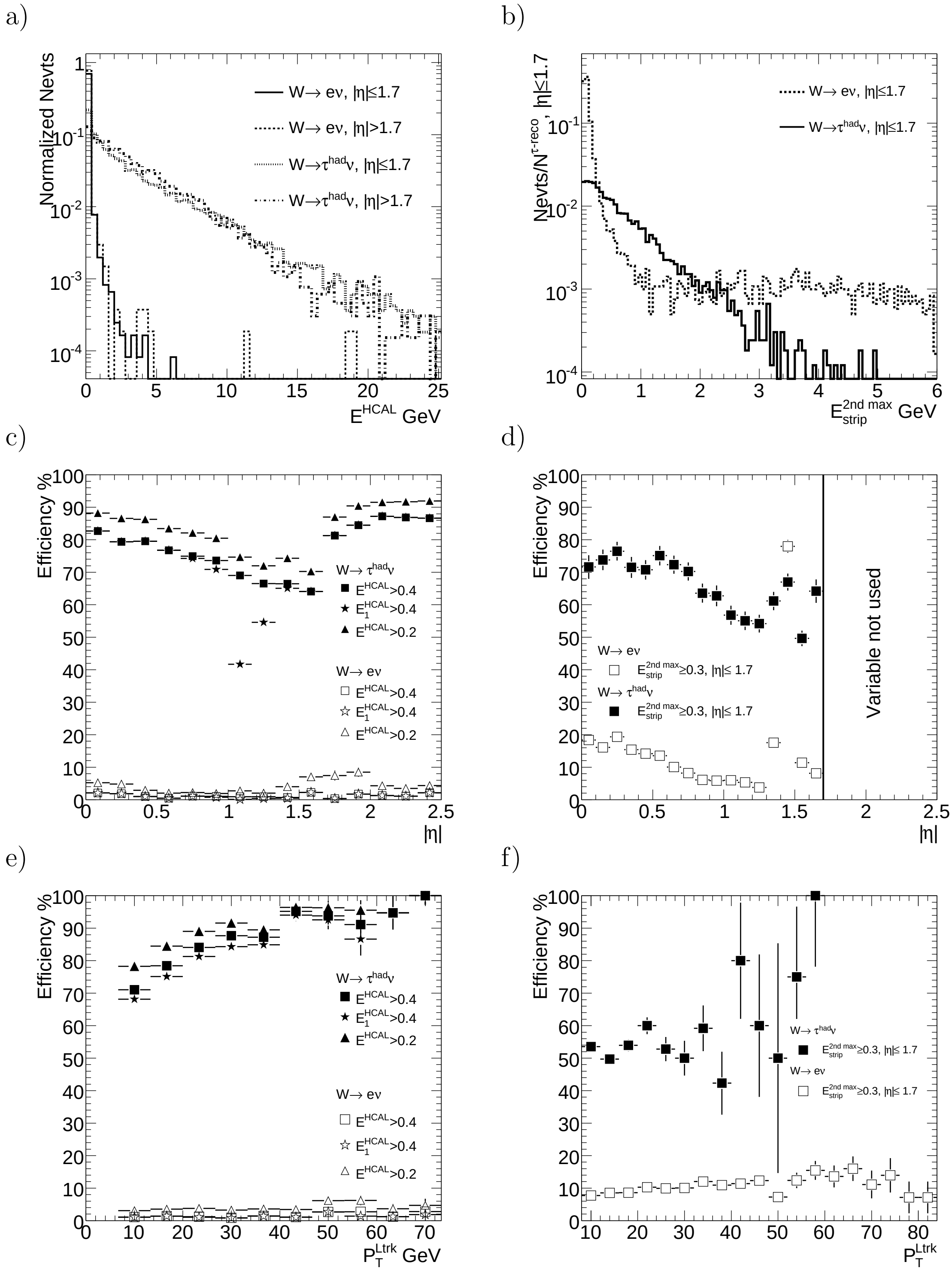

Figure 2: Separation variables for hadronic tau decays and electrons. Left column: The $E_{\rm HCAL}$ variable. a) $E_{\rm HCAL}$ for taus and electrons. c) fraction of taus/electrons passing the $E_{\rm HCAL}$ cut as function of $|\eta|$; e) same as function of p_T. Right column: The $E^{\rm max}_{\rm strip}$ variable for candidates passing the $E_{\rm HCAL}$ cut; b) $E^{\rm max}_{\rm strip}$ for taus/electrons; d) fraction of taus/electrons with $E^{\rm max}_{\rm strip} > 0.3\,{\rm GeV}$ as function of $|\eta|$; f) same as function of p_T.

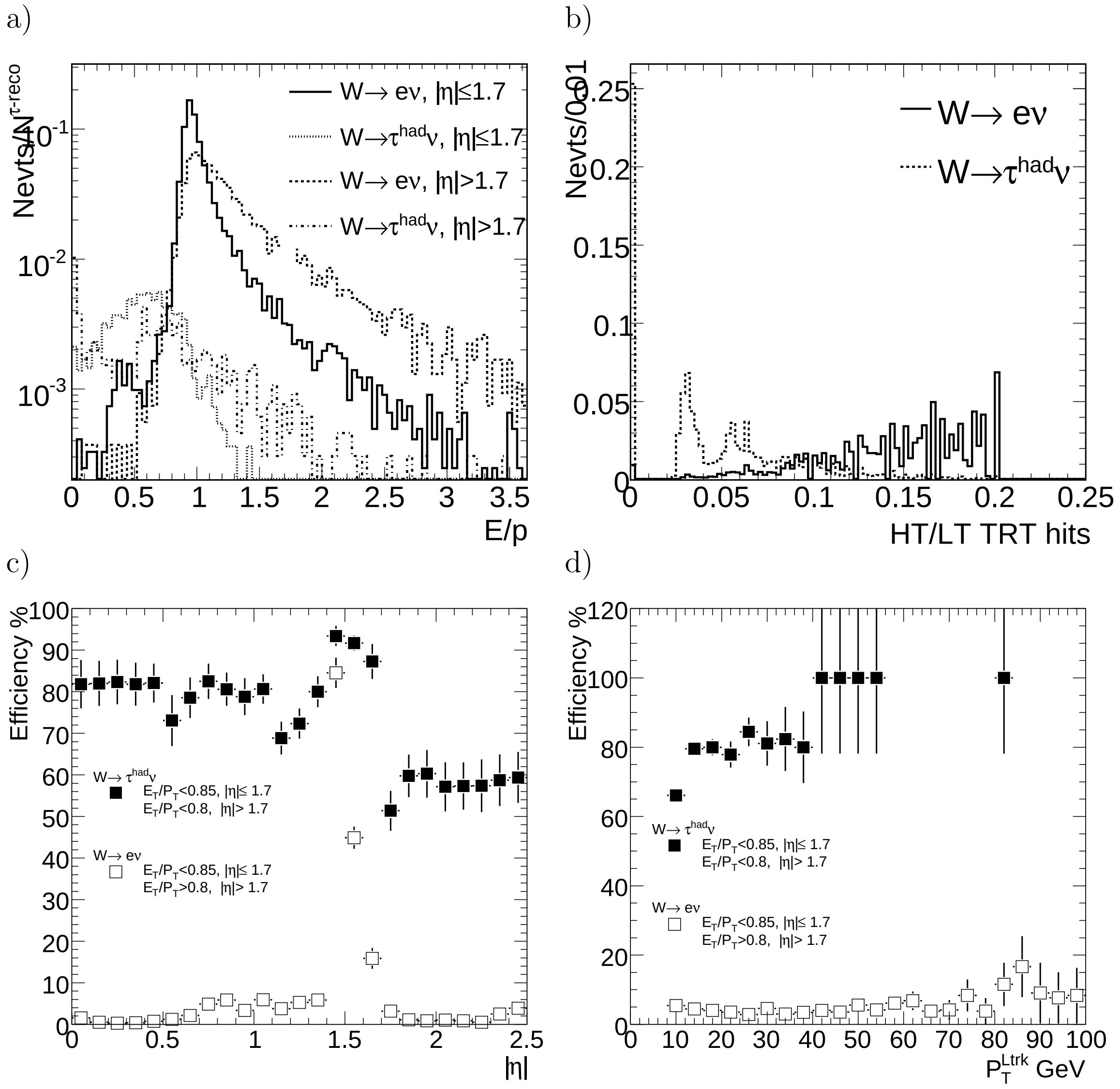

Figure 3: Separation variables and efficiencies for events that passed E_{HCAL} and $E_{\mathrm{strip}}^{\mathrm{max}}$ cuts. Top: E_{ECAL}/p (a) and $N_{\mathrm{HT}}/N_{\mathrm{LT}}$ (b). Bottom: Efficiency for electrons and hadronic tau decays to pass the applied cut on E_{ECAL}/p plotted versus $|\eta|$ (c) and p_{T} (d).

Rejection cuts for $|\eta| < 1.7$

	$E_{\mathrm{HCAL}} < 0.4\,\mathrm{GeV}$	$\mathrm{E}_{\mathrm{HCAL}} \geq 0.4\,\mathrm{GeV}$
$E_{\mathrm{strip}}^{\mathrm{max}} \geq 0.3\,\mathrm{GeV}$	$\mathrm{N}_{\mathrm{HT}}/\mathrm{N}_{\mathrm{LT}} < 0.12$	$\mathrm{N}_{\mathrm{HT}}/\mathrm{N}_{\mathrm{LT}} < 0.2$
$E_{\mathrm{strip}}^{\mathrm{max}} < 0.3\,\mathrm{GeV}$	$E_{\mathrm{ECAL}}/p < 0.85$ $\mathrm{N}_{\mathrm{HT}}/\mathrm{N}_{\mathrm{LT}} < 0.11$	

Rejection cuts for $|\eta| < 1.7$

$E_{\mathrm{HCAL}} < 0.2\,\mathrm{GeV}$	$E_{\mathrm{HCAL}} \geq 0.2\,\mathrm{GeV}$
E/p <0.8 $\mathrm{N}_{\mathrm{HT}}/\mathrm{N}_{\mathrm{LT}}$ <0.13	no cut

Table 2: Cuts for electron veto. At the top, for $|\eta| < 1.7$: Tracks are divided into three categories based on the variables E_{HCAL} and $E_{\mathrm{strip}}^{\mathrm{max}}$. For each category, cuts are applied on the variables E_{ECAL}/p and $\mathrm{N}_{\mathrm{HT}}/\mathrm{N}_{\mathrm{LT}}$ as indicated. At the bottom, for $|\eta| > 1.7$.

$|\eta| \leq 1.7$

Physics event	$W \to \tau\nu$	$W \to e\nu$
$E_{\mathrm{HCAL}} \geq 0.4\,\mathrm{GeV}$ a)	73.6	1.9
$E_{\mathrm{HCAL}} < 0.4\,\mathrm{GeV}$	26.4	98.1
$+ E_{\mathrm{strip}}^{\mathrm{max}} \geq 0.3\,\mathrm{GeV}$	16.9	14.0
$+ \mathrm{N}_{\mathrm{HT}}/\mathrm{N}_{\mathrm{LT}} < 0.11$ b)	15.3	2.1
$E_{\mathrm{HCAL}} < 0.4\,\mathrm{GeV}$	26.4	98.1
$+ E_{\mathrm{strip}}^{\mathrm{max}} < 0.2$	9.5	84.1
$+ E_{\mathrm{ECAL}}/p < 0.85$	7.7	4.3
$+ \mathrm{N}_{\mathrm{HT}}/\mathrm{N}_{\mathrm{LT}} < 0.12$ c)	7.4	1.2
Full selection: a)+b)+c)	96.3	5.2

$|\eta| > 1.7$

Physics event	$W \to \tau\nu$	$W \to e\nu$
$E_{\mathrm{HCAL}} \geq 0.2\,\mathrm{GeV}$ a)	90.7	4.4
$E_{\mathrm{HCAL}} < 0.2\,\mathrm{GeV}$	9.3	95.6
$+ E_{\mathrm{ECAL}}/p < 0.8$	5.3	1.8
$+ \mathrm{N}_{\mathrm{HT}}/\mathrm{N}_{\mathrm{LT}} < 0.13$ b)	5.1	1.6
Full selection: a)+b)	95.8	6.0

Table 3: Efficiency w.r.t all tau candidates (in %) given at each step of the selection procedure, for $|\eta| \leq 1.7$ (top) and $|\eta| > 1.7$ (bottom)

	reconstructed as single-prong	reconstructed as two-prong	reconstructed as three-prong	Overall
This algorithm:				
$W \to e\nu$ w.r.t. true	2.0	0.1	0.0	2.1
$W \to e\nu$ w.r.t. reco	5.2	13.5	9.0	5.4
$W \to \tau\nu$ w.r.t. reco	95.6	96.8	97.2	96.1
ISEM (tight):				
$W \to e\nu$ w.r.t. true	13.0	13.2	24.1	13.1
$W \to e\nu$ w.r.t. reco	34.1	34.6	65.2	34.2
$W \to \tau\nu$ w.r.t. reco	99.9	99.9	99.9	99.9

Table 4: Selection efficiencies (in %) of the presented algorithm within $|\eta| <2.5$ and $p_T > 9$ GeV for electrons ($W \to e\nu$) and hadronic tau decays ($W \to \tau\nu$). Efficiencies are given separately for candidates reconstructed as 1-, 2- and 3-prongs. The overall efficiency is the weighted average of the 1-, 2-, and 3-prong numbers. For comparison, the corresponding efficiencies of the ISEM algorithm is also shown.

4 Algorithm efficiency and comparison with IsEM

Selection efficiencies of the presented algorithm within $|\eta| <2.5$ and $p_T > 9$ GeV are summarized in Tab. 4. The efficiencies, which have been deduced from samples of electrons from $W \to e\nu$ and hadronic tau decays from $W \to \tau\nu$, are given both separately for candidates reconstructed as one, two and, three prongs, and overall defined as the weighted average of the former. Here, efficiencies are defined as the fraction of selected candidates with respect to all reconstructed candidates in the given category. As described in Sec. 2, some electron veto based on transition radiation in the TRT is applied already at the level of track selection. As a result the probability to reconstruct a $W \to e\nu$ as a (fake) hadronic tau decay without any further veto decreases from about 90% to 38%. For reference, therefore also given are efficiencies defined as the ratio between the number of selected candidates and all true electrons.

For comparison, the corresponding efficiencies for the ISEM flag are also given. Notice, that we are here using the tight electron identification criterium (ISEM = 0) for vetoing of electrons. Since, however, the ISEM flag has not been optimized for electron vetoing but for electron identification, it is not surprising, that this method works less optimal for our purpose than the dedicated electron rejection method.

Fig. 4a–d shows selection efficiencies as function of transverse momentum and pseudorapidity of the leading track. Overall the selection is rather stable against momentum. At the lowest momenta, however, the efficiency for hadronic tau decays falls somewhat off. This is mainly caused by the lower tendency of soft hadrons to penetrate the ECAL and leave energy in the HCAL. As a result, lowering the p_T threshold of the leading track from 9 GeV, as studied here, to 6 GeV, which is the new default in TAU1P3P, results in an overall drop of efficiency for hadonic tau decays from $W \to \tau\nu$ by 1.5%. The selection efficiency for electrons changes very little. Some variation of efficiency with pseudorapidity reflects the non-uniform geometry of the ATLAS detector: i) lack of the TRT coverage for $|\eta| > 2$; ii) crack region in the ECAL around $|\eta| \simeq 1.5$; iii) crack region in HCAL around $|\eta| \simeq 1$; and iv) change in HCAL technology at $|\eta| \simeq 1.7$. In Fig. 4e–f, the selection efficiencies for hadronic tau decays are shown separately for candidates with 1, 2, and 3 reconstructed tracks. One prong tau

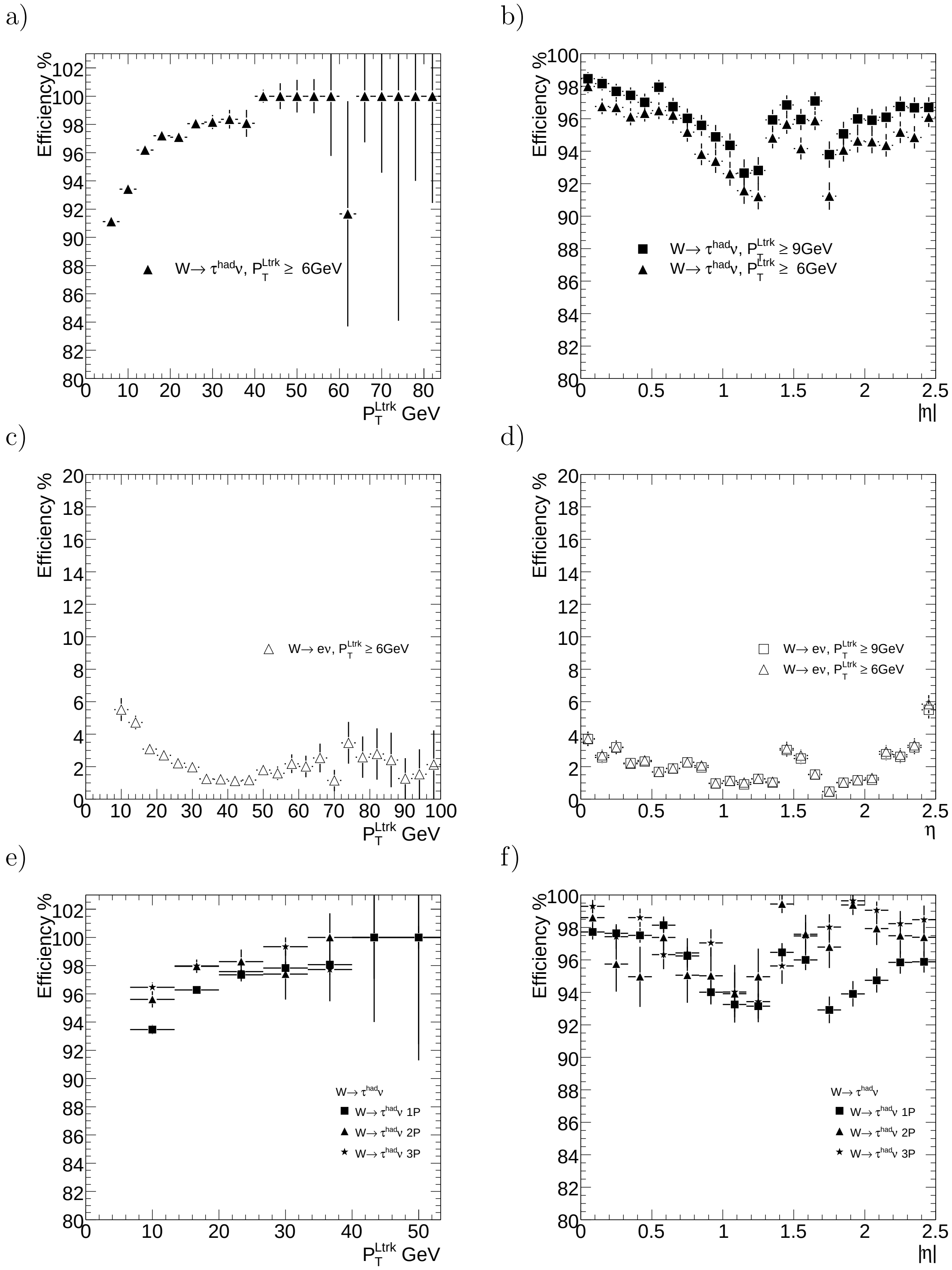

Figure 4: Top: Selection efficiency for hadronic tau decays as function of p_{T} of the leading track (a), and $|\eta|$ (b). Selection efficiency is shown for two thresholds for the leading track, 6 and 9 GeV respectively. Middle: Same for electrons. Bottom: e) Selection efficiency for hadronic tau decays reconstructed as 1P, 2P and 3P as function of p_{T} of the leading track (e), and $|\eta|$ (f).

decays, are predominantly associated with one or more neutral pions, which deposit significant amount of energy in ECAL. In the region $|\eta| > 1.7$, where the algorithm is much simplified, the E_{ECAL}/p cut brings down the selection efficiency for 1P tau decays.

5 Summary

A dedicated algorithm for electron suppression in a track based reconstruction of hadronic tau decays has been developed. It covers the full detector region relevant for tau reconstruction ($|\eta| \leq 2.5$). Track selection criteria have been revisited and optimized to achieve a higher reconstruction efficiency for hadronic tau decays and at the same time lowering the 1P → 3P and 3P → 1P migration. Compared to using the standard electron identification tool, ISEM, for electron vetoing, the developed algorithm performs considerably better, achieving a much higher rejection factor for electrons for a relatively small loss of efficiency for hadronic tau decays.

6 Ackowlegements

The authors would like to thank Anna Kaczmarska for her help with implementation of the presented algorithm in TAU1P3P package. We would also like to thank S. Xella, E. Richter-Was for very useful discussions and A.C le Bihan for important suggestion concerning track selection for hadronically decaying taus.

Appendix

A. Algorithm implementation in tau1p3p

The electron veto algorithm is implemented in ATHENA since release 12.0.5 as the tool `tau1p3pEleVeto` in TAU1P3P.

Release 12: `tau1p3pEleVeto` is executed at the level of reconstruction, after track selection criteria are applied. It is switched off by default. In order to use it, the user needs to produce her own ATHENA aware ntuples from ESD setting in the jobOptions: `doCaloCluster = True` and `doTauRec = True` to rerun TAUREC on ESD and `tau1p3pAlg.EleVeto.doEleVeto = 1` to switch on the tool.

Note, that before release 13, the algorithm does not have the optimal performance presented in this note. In particular it does not provide any discrimination against electrons in the region of $|\eta| \geq 1.7$.

Release 13: `tau1p3pEleVeto` is switched on by default. It provides a two-bit flag for tau objects, returning 1 or 0 depending on whether the object was identified as an electron or not. One bit is reserved for identification based on the presented algorithm, the other corresponds to identification based on the tight selection for electrons provided by the ISEM flag (ISEM = 0.)

Note, that in ATLAS software version 13.0.20 and later, the new selection criteria described in Sec. 2 are set by default in the `selecGQTracks` tool, without, however, a cut on $\mathrm{N_{HT}}/\mathrm{N_{LT}}$ applied on the leading track. This cut has been moved to the `tau1p3pEleVeto` tool, which in release 13.0.2 does not include outlier hits in the TRT and thus performance is not optimal. The complete version of the algorithm is implemented since release verion 13.0.30.

B. Technical details

Data samples from the ATLAS CSC production have been used as detailed in the table below. From the ESD samples, ATHENA Aware Ntuples (AAN) were produced using release 12.0.6 of the ATLAS software with the TAU1P3P algorithm integrated inside the TAUREC package. AAN's were produced using TAUREC `tag 02-04-43` and TAUEVENT `tag 00-02-09`, with the following modifications: In TAUREC newer versions of `selecGQTracks` and `tau1p3pEleVeto` tools were used as implemented in TAUREC `post branch 02-04-43-09`. The AAN samples can be made available on request.

Events	Dataset	Nevts
$W \rightarrow e\nu$	`trig1_misal1_csc11.005104.PythiaWenu.recon.ESD.v12000601`	50,000
$W \rightarrow \tau_{\text{had}}\nu$	`trig1_misal1_csc11.005107.pythia_Wtauhad.recon.ESD.v12000601`	50,000

References

[1] An improved tau-Identification for the ATLAS experiment. M.Heldmann, D.Cavalli. ATL-PHYS-PUB-2006-008

[2] Performance of the TAU1P3P algorithm for hadronic tau decays identification with release 12.0.6. A.Kaczmarska, E. Richter-Was, L. Janyst. ATL-COM-PHYS-2007-039.

[3] http://maria-laach.physik.uni-siegen.de/2006/participants/files/E-07_Christov.pdf

[4] ATLAS Technical Desin Report (TDR) vol.I

[5] https://twiki.cern.ch/twiki/bin/view/Atlas/ElectronGammaIsEM

C

Z.Czyczula, M.Dam

Cut-based electron veto algorithm for the track-seeded part of `tauRec`

Cut-based electron veto algorithm for the track-seeded part of tauRec

Z. Czyczula, M. Dam
Niels Bohr Institute, University of Copenhagen,
DK-2100 Copenhagen, Blegdamsvej 17, Denmark

Abstract

A cut-based method of electron rejection for the track-seeded identification of hadronic τ decays in the `tauRec` package is described. The analysis covers the full detector region, $|\eta| < 2.5$, relevant for τ reconstruction and the p_{T} range from 10 to 1000 GeV. Three selection flags are introduced *loose*, *medium* and *tight*.

1 Introduction

For the reconstruction of hadronic decays of τ-leptons, two algorithms are currently implemented in the ATLAS `tauRec` package [1]: the calorimeter-seeded and the track-seeded algorithms. The calorimeter-seeded algorithm starts from a TopoJet [1] with $E_{\mathrm{T}} > 10\,\mathrm{GeV}$, which is labelled a *reconstructed* τ candidate, and builds identification variables based on information from the electromagnetic (ECAL) and hadronic (HCAL) calorimeters as well as from the Inner Detector (ID). The track-seeded algorithm starts from a leading track of good quality with $p_{\mathrm{T}} > 6\,\mathrm{GeV}$ and collects secondary tracks and calorimeter energy depositions in a cone around the track direction at the vertex. Tight track selection criteria applied in the track-seeded approach, enables efficient suppression of fake tracks from conversion and therefore assures precise charge determination, minimising confusion between one and three-prong decays [1, 2]. The calorimeter-seeded method, being almost 100% efficient at the level of reconstruction, uses a looser track selection, hence results in higher charge misidentification and one- and three-prong migration.

An efficient suppression of electrons is important for analyses involving τ-leptons. Neither the track-seeded nor the calorimeter-seeded algorithm, making use of the narrowness and isolation of calorimeter showers and low track multiplicity, intrinsically provides discrimination against electrons. Without further rejection the majority of electrons would be identified as, predominantly one-prong, hadronic τ decays. In `tauRec`, electron rejection is provided by dedicated methods. In the calorimeter-seeded part, this is enabled by a discriminant variable built using a likelihood method [1]. In the track-seeded approach, a cut based method (e-veto tool) is implemented [2]. In this note, we discuss a new optimisation of this method. The algorithm has been extended to provide three flags for the user, *loose*, *medium* and *tight*, corresponding to different levels of electron suppression.

2 Sample and method

The tuning of the electron veto algorithm was based on simulated samples of hadronic τ decays and electrons from various physics processes. Tau decays with a visible transverse momentum in the intermediate range from 20 to 80 GeV were from $W \to \tau\nu$ and $Z \to \tau\tau$. As a source of high p_T tau decays a sample of MSSM Higgs boson decays, $b\bar{b}A \to b\bar{b}\tau\tau$, with a Higgs mass of 800 GeV and a samples of Z′ boson decays, $Z' \to \tau\tau$, with Z′ mass of 2 TeV, respectively, were used. The samples of electrons included $W \to e\nu$ and $Z \to ee$ as well as electrons from $\tau \to e\nu$ decays from $Z \to \tau\tau$, $b\bar{b}A \to b\bar{b}\tau\tau$, and $Z' \to \tau\tau$ processes. All samples were generated using the Pythia 6.403 [3] Monte Carlo event generator and passed through the full detector simulation and reconstruction. More details about the MC samples can be found in Appendix A.

For the performance study, in the current analysis, tau candidates were matched to true electrons or hadronic tau decays, respectively. A candidate was labelled a hadronic tau decay, τ^{hadr}, if the leading track matched a charged pion from a τ decay at the truth level. Similarly, a candidate was labelled an electron if the leading track matched a true, primary electron from a W, Z or τ decay[1].

Reconstruction of hadronic tau decays, particularly the track multiplicity, can depend on the event topology. Migration, of true one-prong tau decays from $b\bar{b}A \to b\bar{b}\tau\tau$ events, to higher track multiplicity categories, was observed to be larger than in case of taus from Z′ decays. This was traced to overlaps of tracks from b-jets and the tau jet. Hence, in this study, efficiencies are given for each sample separately.

Table 1 shows the fraction of electrons reconstructed as hadronic tau decays by the track seeded algorithm, when no rejection of electrons is attempted.

Candidate	$\langle p_T \rangle$	Overall	1P	2P	3P
Electron from $W \to e\nu$	34 GeV	73.8±0.1	70.9±0.2	2.5±0.1	0.4±0.0
Electron from $Z \to ee$	38 GeV	74.6±0.2	71.5±0.2	2.6±0.1	0.4±0.0
Electron from $Z \to \tau\tau$	25 GeV	73.1±0.3	70.3±0.3	2.5±0.1	0.3±0.0
Electron from $b\bar{b}A \to b\bar{b}\tau\tau$	109 GeV	80.9±0.2	75.9±0.3	3.5±0.1	1.0±0.1
Electron from $Z' \to \tau\tau$	244 GeV	79.3±0.3	76.0±0.3	2.6±0.1	0.6±0.1

Table 1: Fraction of electrons, in %, reconstructed as hadronic tau decays by the track-seeded part of `tauRec` when no electron rejection is attempted. Numbers are normalised to all true electrons with $p_T > 6\,\mathrm{GeV}$ within $|\eta| < 2.5$, and are given separately for candidates reconstructed as one (1P), two (2P) and three (3P) prongs. The overall efficiency is the sum of the one- to six-prong numbers.

3 Electron veto algorithm

The electron veto algorithm has three levels of severity, *loose*, *medium*, and *tight*. Of these the first is based on the use of the `IsEM` of the electron identification package [5], whereas the two latter are provided by the dedicated cut-based algorithm.

---

[1] Electrons originating from conversion and semi-leptonic decays in b- and c-jets have not been considered in the present studies.

3.1 *loose* veto

For the *loose* electron veto, use is made of the `IsEM` flag from the ATLAS electron identification procedure [5]. If a reconstructed tau candidate is matched within a cone of $\Delta R < 0.2$ by an electron candidate identified using the tight `IsEM` flag, the candidate is vetoed. This method, being almost 100% efficient for hadronic tau decays, provides a rejection factor of five against electrons from $\mathrm{W} \rightarrow \mathrm{e}\nu$ decays. It should be stressed that the `IsEM` flag has been optimised for electron identification and not for electron vetoing. Hence a dedicated vetoing procedure naturally is more performant.

3.2 *medium* and *tight* veto

The electron vetoing algorithm is seeded by the leading track and uses a cut based method to discriminate hadronic τ-leptons from electrons. It is based on the following variables:

$E_{\mathrm{HCAL}}/p^{\mathrm{Ltrk}}$: The ratio between the energy deposit in the first layer of the HCAL in a window $|\Delta\phi| \leq 0.2$ and $|\Delta\eta| \leq 0.2$ around the track extrapolation[2] and the track momentum. In the barrel HCAL transition region at $|\eta| \sim 1$, the first HCAL layer is partly missing. To compensate for this, the energy in the full HCAL depth is collected in the region $0.8 \leq |\eta| < 1.2$ [2]. The $E_{\mathrm{HCAL}}/p^{\mathrm{Ltrk}}$ variable is illustrated in Fig. 1. Here as elsewhere, distributions were derived from unweighted samples of $\mathrm{W} \rightarrow \tau\nu$, $\mathrm{W} \rightarrow \mathrm{e}\nu$, $\mathrm{Z} \rightarrow \tau\tau$, $\mathrm{Z} \rightarrow \mathrm{ee}$, $\mathrm{A} \rightarrow \tau\tau$, and $\mathrm{Z}' \rightarrow \tau\tau$. Note the, higher separation power at $|\eta| > 1.7$ as compared to $|\eta| \leq 1.7$. This coincides with the transition in technology of the HCAL going from the tile calorimeter in the central part to LAr in the forward parts [4].

$E^{\mathrm{max}}_{\mathrm{strip}}$: This variable was designed to be sensitive to secondary energy deposits in the ECAL not associated to the leading track. The energy in the strip compartment is summed over three cells[1] in ϕ, and local maxima are searched for in 101 cell sums in η centred around the impact point of the leading track (excluding a region $1.475 \leq |\eta| \leq 1.5$ corresponding to the ECAL crack). Excluding the energy associated with the leading track, the variable measures the maximum strip energy sum within the searched range. More detailed description of the variable is presented in Appendix B. The variable is used only in the region of $|\eta| \leq 1.7$ and $p_{\mathrm{T}}^{\mathrm{Ltrk}} \leq 50\,\mathrm{GeV}$, where the TRT provides efficient discrimination between pions and electrons. The $E^{\mathrm{max}}_{\mathrm{strip}}$ variable is illustrated in Fig. 2.

$E_{\mathrm{ECAL}}/p^{\mathrm{Ltrk}}$: The ratio between the ECAL energy and the momentum of the leading track. The energy is calculated in the following $\Delta\eta \times \Delta\phi$ windows around the impact cell[1]: 0.075×0.3 in presampler, 0.0475×0.3 in strips, 0.075×0.075 in middle, and 1.5×0.075 in back compartment. The variable is used only for $p_{\mathrm{T}}^{\mathrm{Ltrk}} < 50$ GeV. The $E_{\mathrm{ECAL}}/p^{\mathrm{Ltrk}}$ variable is illustrated in Fig. 3. Electrons tend to peak at unity as expected. A large fraction of electrons is accepted around $|\eta| \sim 1.5$ corresponding to the ECAL barrel/end-cap transition region. The resulting lower overall separation power in the $|\eta| \leq 1.7$ region can be observed from Fig. 3b.

$\mathrm{N}_{\mathrm{HT}}/\mathrm{N}_{\mathrm{LT}}$: The ratio of high threshold to low threshold hits in the TRT including *outlier hits* (i.e. hits associated with the track, but not used in the track fit). High

---

[2] Only cells with $|E_T| > 2\sigma$ noise threshold are considered.

threshold hits indicate transition radiation (TR) and are therefore sensitive to electrons. The probability for a pion to emit TR, increases with its momentum. The $\mathrm{N}_{\mathrm{HT}}/\mathrm{N}_{\mathrm{LT}}$ variable is illustrated in Fig. 4. To minimise loss of hadronic tau decays this variable is only used in low momentum region, i.e. for $p_{\mathrm{T}}^{\mathrm{Ltrk}} < 50\,\mathrm{GeV}$. Given the lack of the coverage of the TRT for $|\eta| > 2$, efficient electron/hadron discrimination from this variable has been limited to within $|\eta| \leq 1.7$.

As indicated above, not all variables are used in the whole kinematic region. Table 2 summarises the usage of the variables within different ranges of $|\eta|$ and $p_{\mathrm{T}}^{\mathrm{Ltrk}}$.

$p_{\mathrm{T}}^{\mathrm{Ltrk}}$ $\lvert\eta\rvert$	$\leq 50\,\mathrm{GeV}$	$> 50\,\mathrm{GeV}$
≤ 1.7	$E_{\mathrm{HCAL}}/p^{\mathrm{Ltrk}}$,$E_{\mathrm{strip}}^{\mathrm{max}}$ $E_{\mathrm{ECAL}}/p^{\mathrm{Ltrk}}$, $\mathrm{N}_{\mathrm{HT}}/\mathrm{N}_{\mathrm{LT}}$	$E_{\mathrm{HCAL}}/p^{\mathrm{Ltrk}}$
> 1.7	$E_{\mathrm{HCAL}}/p^{\mathrm{Ltrk}}$, $E_{\mathrm{ECAL}}/p^{\mathrm{Ltrk}}$	$E_{\mathrm{HCAL}}/p^{\mathrm{Ltrk}}$

Table 2: Usage of the e-veto variables in different kinematical regions.

In the region where the TRT provides efficient discrimination between electrons and hadrons ($|\eta| \leq 1.7$, $p_{\mathrm{T}}^{\mathrm{Ltrk}} < 50\,\mathrm{GeV}$), the separation procedure is the following for the *medium* (*tight*) selection:

1. As a first step, candidates with $E_{\mathrm{HCAL}}/p^{\mathrm{Ltrk}} > 0.03$ are selected as hadrons. Very few electrons leak through the ECAL to deposit energy in the HCAL, as seen from Fig.1a. Thus, the electron contamination in this sample is already very low. As seen from Fig.1e, the efficiency for hadronic decays to pass this cut varies from about 75% at low momenta to about 95% at high momenta and is decreasing with pseudorapidity as seen from Fig. 1e. The remaining electrons are suppressed requiring that $\mathrm{N}_{\mathrm{HT}}/\mathrm{N}_{\mathrm{LT}} < 0.2$ (0.17).

2. The next step concentrates on candidates with $E_{\mathrm{HCAL}}/p^{\mathrm{Ltrk}} < 0.03$. The decay $\tau \longrightarrow \rho\nu$ tends to have one or two rather energetic secondary showers from the π^0 photons. Also for the $\tau \longrightarrow \pi\nu$ decay, a tendency towards secondary showers is observed. This is likely caused by hadronic interactions in front of and inside the ECAL. We apply the cut $E_{\mathrm{strip}}^{\mathrm{max}} > 0.25$ (0.5) GeV to select hadrons. In the selected sample, the electron contamination is larger than above, so we apply a stricter cut on the TRT, $\mathrm{N}_{\mathrm{HT}}/\mathrm{N}_{\mathrm{LT}} < 0.11$ (0.09), in order to suppress this background.

3. The remaining candidates which have neither a significant fraction of HCAL energy nor a secondary electromagnetic shower are very rich in electrons. A cut on $E_{\mathrm{ECAL}}/p^{\mathrm{Ltrk}} < 0.85$ (0.6) in combination with the TRT requirement $\mathrm{N}_{\mathrm{HT}}/\mathrm{N}_{\mathrm{LT}} < 0.12$ (0.09) is applied to suppress electrons.

In the region $|\eta| > 1.7$ and $p_T^{\mathrm{Ltrk}} < 50$ GeV, where the TRT provides no efficient electron/hadron separation, a simplified rejection procedure is applied. Any candidate with $E_{\mathrm{HCAL}}/p^{\mathrm{Ltrk}}$ exceeding 0.02 for the *medium* (0.05 for the *tight*) selection is accepted as a hadronic τ decay. For candidates with $E_{\mathrm{HCAL}}/p^{\mathrm{Ltrk}}$ below this value, it is required that $E_{\mathrm{ECAL}}/p^{\mathrm{Ltrk}} < 0.85$ for the *medium* (< 0.6 for the *tight*) selection, respectively.

The lower requirement on HCAL energy for the *medium* selection as compared to the more central detector region improves the efficiency significantly.

In the higher momentum region, $p_{\mathrm{T}}^{\mathrm{Ltrk}} > 50$ GeV, separation based on the $E_{\mathrm{HCAL}}/p^{\mathrm{Ltrk}}$ variable alone improves significantly as seen from Fig. 1b. Hence a cut on $E_{\mathrm{HCAL}}/p^{\mathrm{Ltrk}}$ is sufficient to efficiently discriminate electrons from hadronic tau decays. In order to preserve a flatter signal efficiency, the cuts applied on $E_{\mathrm{HCAL}}/p^{\mathrm{Ltrk}}$ were optimised in two η and two $p_{\mathrm{T}}^{\mathrm{Ltrk}}$ bins. The electron rejection procedure is summarised in Table 3.

Given the very small fraction of electrons reconstructed as three-prong candidates (see Table 1), for *medium* selection the above procedure is only applied to one- and two-prong candidates. Candidates with three or more tracks with $p_T^{\mathrm{Ltrk}} > 50$ GeV are recognised as hadronic tau decays. For $p_T^{\mathrm{Ltrk}} < 50$ GeV, a cut on the TRT, $\mathrm{N_{HT}}/\mathrm{N_{LT}} < 0.2$, is applied to provides protection against non-isolated electrons in jets. Since the *tight* selection is aiming at very high electron suppression, the separation procedure is here applied to all candidates disregarding the number of tracks.

Rejection cuts for $|\eta| \leq 1.7$ and $p_T^{\mathrm{Ltrk}} \leq 50$ GeV

	$E_{\mathrm{HCAL}}/p^{\mathrm{Ltrk}} \leq 0.03$	$E_{\mathrm{HCAL}}/p^{\mathrm{Ltrk}} > 0.03$
$E_{\mathrm{strip}}^{\mathrm{max}} > 0.25\ (0.5)$ GeV	$\mathrm{N_{HT}}/\mathrm{N_{LT}} \leq 0.11\ (0.09)$	$\mathrm{N_{HT}}/\mathrm{N_{LT}} \leq 0.2$
$E_{\mathrm{strip}}^{\mathrm{max}} \leq 0.25\ (0.5)$ GeV	$E_{\mathrm{ECAL}}/p < 0.85\ (0.6)$ $\mathrm{N_{HT}}/\mathrm{N_{LT}} \leq 0.12\ (0.09)$	

Rejection cuts for $|\eta| > 1.7$ and $p_T^{\mathrm{Ltrk}} \leq 50$ GeV

$E_{\mathrm{HCAL}}/p^{\mathrm{Ltrk}} \leq 0.02\ (0.05)$	$E_{\mathrm{HCAL}}/p^{\mathrm{Ltrk}} > 0.02\ (0.05)$
$E_{\mathrm{ECAL}}/p^{\mathrm{Ltrk}} < 0.8\ (0.6)$	no cut

Rejection cuts for $p_T^{\mathrm{Ltrk}} > 50$ GeV

$|\eta|$ \ $p_{\mathrm{T}}^{\mathrm{Ltrk}}$	≤ 200 GeV	> 200 GeV
≤ 1.7	$E_{\mathrm{HCAL}}/p^{\mathrm{Ltrk}} > 0.005\ (0.04)$	$E_{\mathrm{HCAL}}/p^{\mathrm{Ltrk}} > 0.008\ (0.07)$
> 1.7	$E_{\mathrm{HCAL}}/p^{\mathrm{Ltrk}} > 0.005\ (0.04)$	$E_{\mathrm{HCAL}}/p^{\mathrm{Ltrk}} > 0.015\ (0.05)$

Table 3: Cuts for electron veto. Cut values are given for the *medium* (*tight*) selection. At the top, for $|\eta| \leq 1.7$ and $p_T^{\mathrm{Ltrk}} < 50$ GeV: Tracks are divided into three categories based on the variables $E_{\mathrm{HCAL}}/p^{\mathrm{Ltrk}}$ and $E_{\mathrm{strip}}^{\mathrm{max}}$. For each category, cuts are applied on the variables $E_{\mathrm{ECAL}}/p^{\mathrm{Ltrk}}$ and $\mathrm{N_{HT}}/\mathrm{N_{LT}}$ as indicated. In the middle, for $|\eta| > 1.7$ and $p_T^{\mathrm{Ltrk}} < 50$ GeV: Tracks are divided into two categories based on the variable $E_{\mathrm{HCAL}}/p^{\mathrm{Ltrk}}$. For low values of $E_{\mathrm{HCAL}}/p^{\mathrm{Ltrk}}$, a cut on $E_{\mathrm{ECAL}}/p^{\mathrm{Ltrk}}$ is applied to suppress electrons. At the bottom, for $p_T^{\mathrm{Ltrk}} > 50$ GeV: A cut on $E_{\mathrm{HCAL}}/p^{\mathrm{Ltrk}}$ is applied.

4 Algorithm Performance

The performance of the algorithm for the three different criteria, *loose*, *medium*, and *tight*, are summarised in Table 4. The efficiencies deduced from different physics samples, $\mathrm{W} \rightarrow \tau\nu$, $\mathrm{W} \rightarrow \mathrm{e}\nu$, $\mathrm{Z} \rightarrow \tau\tau$, $\mathrm{Z} \rightarrow \mathrm{ee}$, $\mathrm{A} \rightarrow \tau\tau$, and $\mathrm{Z}' \rightarrow \tau\tau$, are shown separately

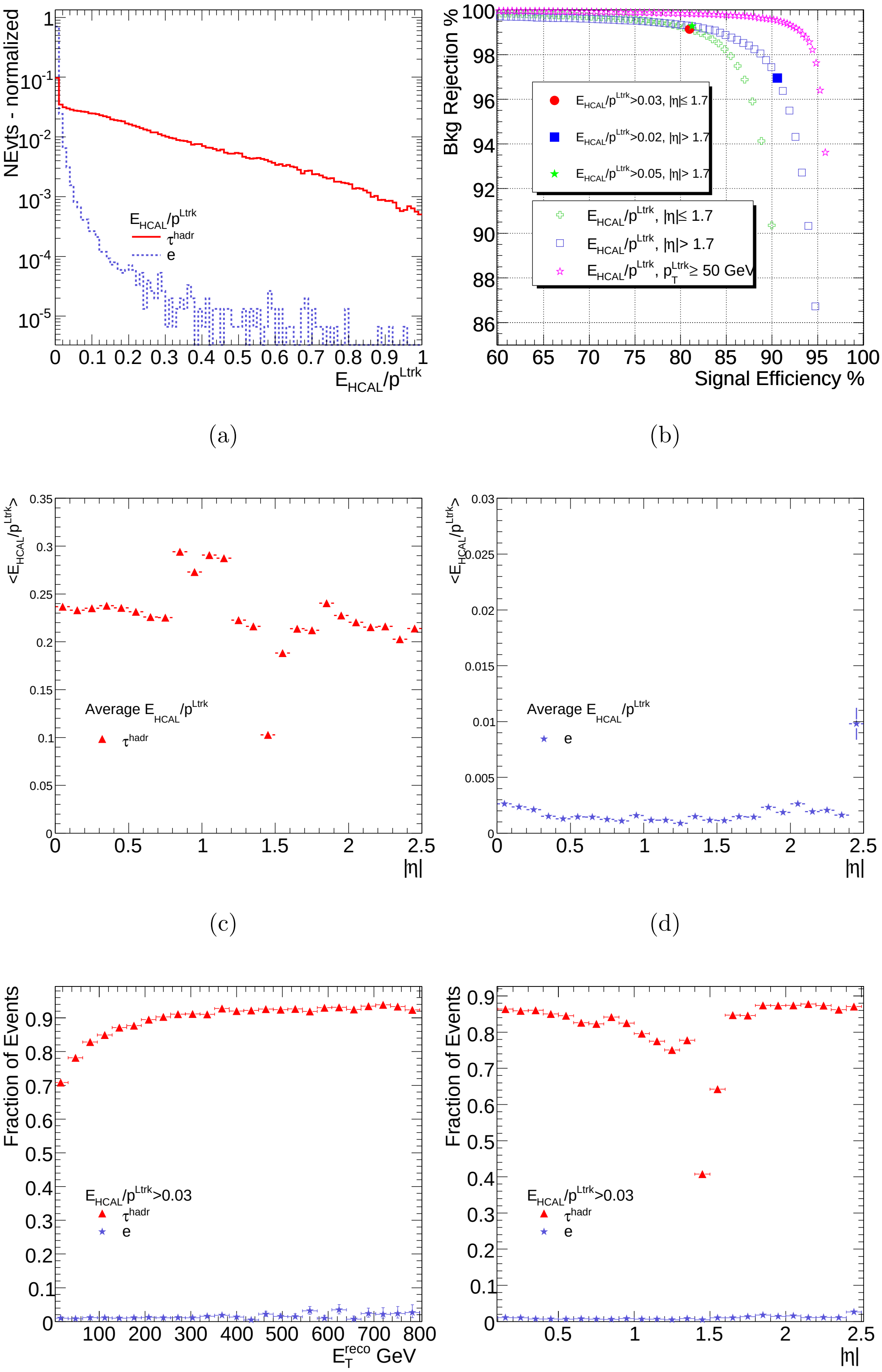

(a) (b)

(c) (d)

(e) (f)

Figure 1: The $E_{\mathrm{HCAL}}/p^{\mathrm{Ltrk}}$ variable: (a) distribution for hadronic tau decays and electrons, (b) background rejection versus signal efficiency, (c) average $E_{\mathrm{HCAL}}/p^{\mathrm{Ltrk}}$ as a function of $|\eta|$ for hadronic tau decays, and (d) for electrons, (e) fraction of taus/electrons passing the $E_{\mathrm{HCAL}}/p^{\mathrm{Ltrk}} > 0.03$ cut as a function of reconstructed E_{T}, and (f) as a function of $|\eta|$.

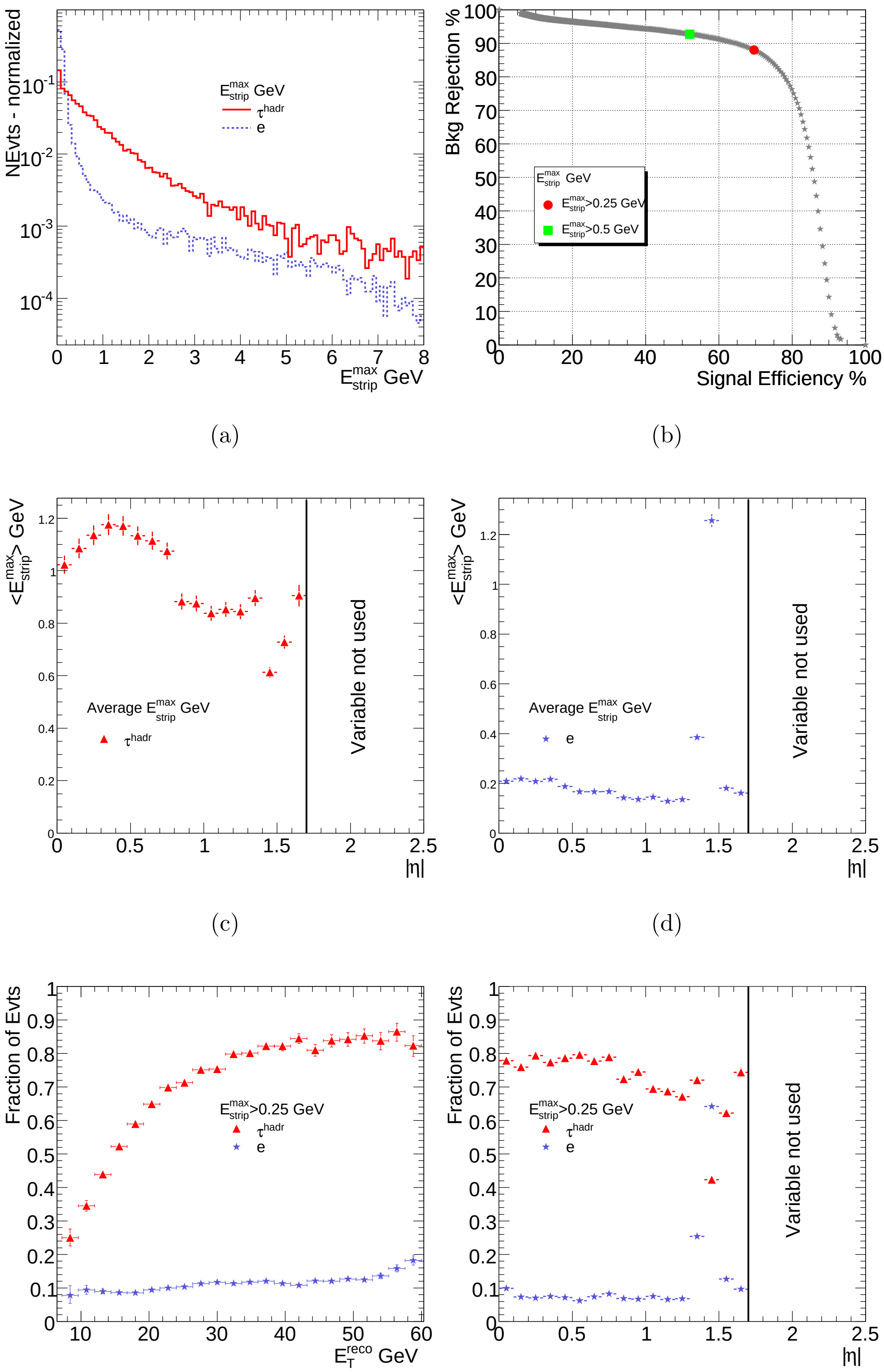

(a) (b)

(c) (d)

(e) (f)

Figure 2: The $E^{\rm max}_{\rm strip}$ variable for candidates within $|\eta| < 1.7$ and with $p_{\rm T}^{\rm Ltrk} < 50\,{\rm GeV}$ and $E_{\rm HCAL}/p^{\rm Ltrk} < 0.03$: (a) distribution for hadronic tau decays and electrons, (b) background rejection versus signal efficiency, (c) average $E^{\rm max}_{\rm strip}$ as a function of $|\eta|$ for hadronic tau decays, and (d) for electrons, (e) fraction of taus/electrons passing the $E^{\rm max}_{\rm strip} > 0.25$ GeV cut as a function of reconstructed $E_{\rm T}$, and (f) as a function of $|\eta|$.

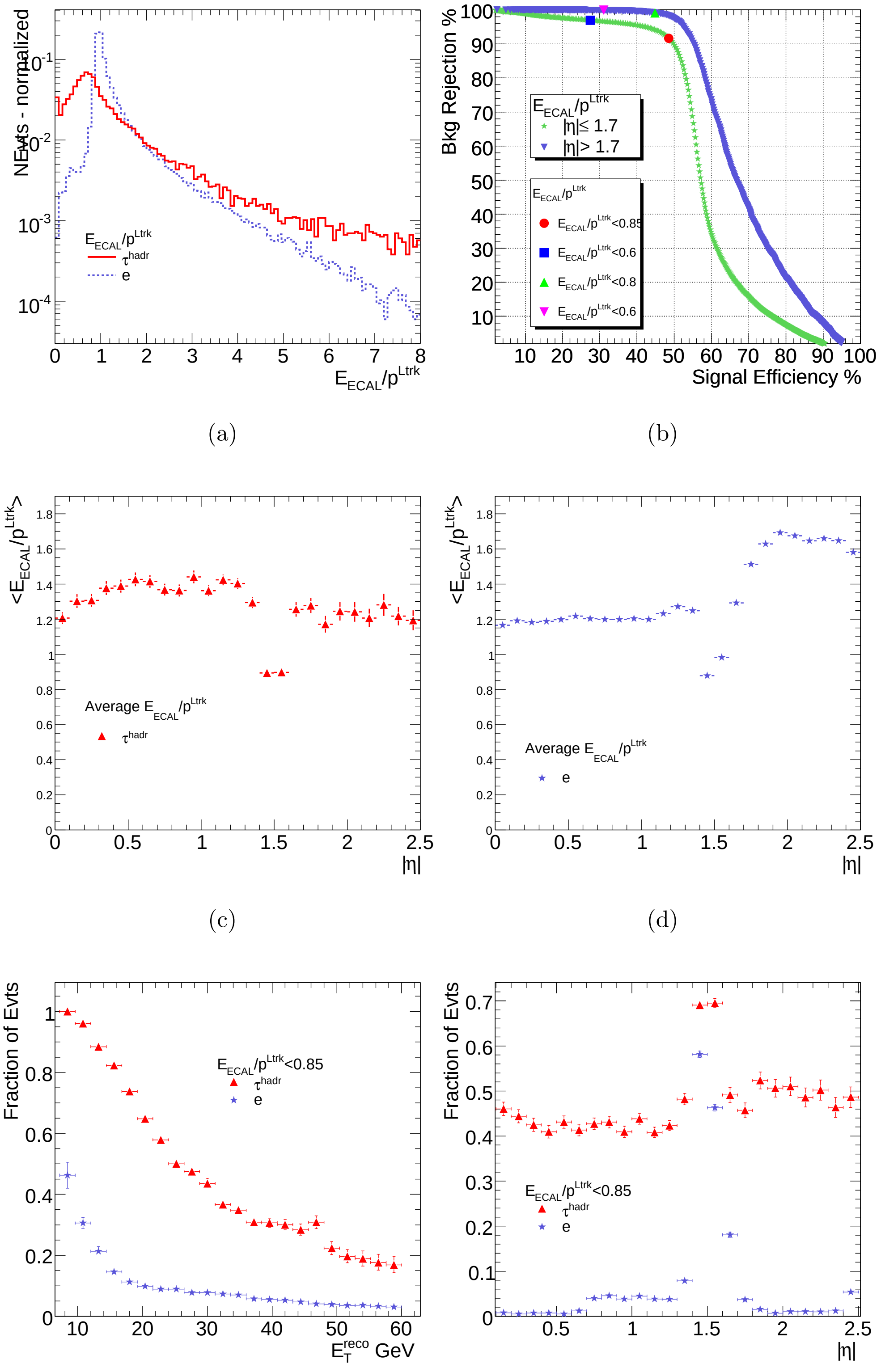

(a)

(b)

(c)

(d)

(e)

(f)

Figure 3: The $E_{\mathrm{ECAL}}/p^{\mathrm{Ltrk}}$ variable for candidates with $p_{\mathrm{T}}^{\mathrm{Ltrk}} < 50\,\mathrm{GeV}$, $E_{\mathrm{HCAL}}/p^{\mathrm{Ltrk}} < 0.03$, and $E_{\mathrm{strip}}^{\mathrm{max}} < 0.25\,\mathrm{GeV}$: (a) distribution for tau decays and electrons, (b) background rejection versus signal efficiency for two $|\eta|$ regions as marked on the plot, (c) average $E_{\mathrm{ECAL}}/p^{\mathrm{Ltrk}}$ as a function of $|\eta|$ for hadronic tau decays, and (d) for electrons, (e) fraction of taus/electrons passing the $E_{\mathrm{HCAL}}/p^{\mathrm{Ltrk}} < 0.85$ cut as a function of reconstructed E_{T}, and (e) as function of $|\eta|$.

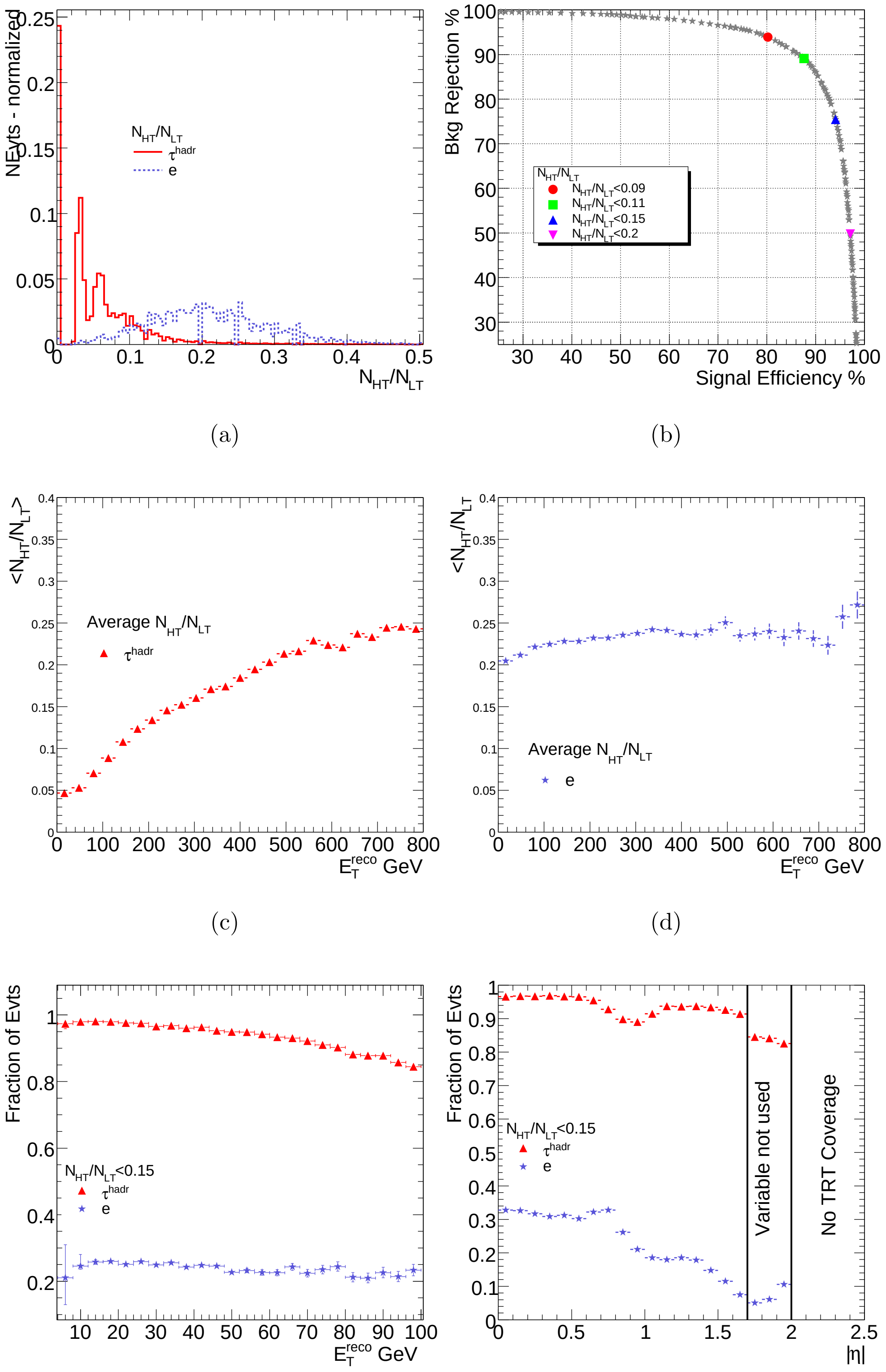

(a) (b)

(c) (d)

(e) (f)

Figure 4: The N_{HT}/N_{LT} variable for candidates within $|\eta| < 1.7$ with $p_T^{Ltrk} < 50$ GeV: (a) distribution for hadronic tau decays and electrons, (b) background rejection versus signal efficiency, (c) average N_{HT}/N_{LT} as a function of E_T for hadronic tau decays, and (d) for electrons, (e) fraction of taus/electrons passing the $N_{HT}/N_{LT} < 0.15$ cut as a function of reconstructed E_T, and (f) as a function of $|\eta|$.

for candidates reconstructed as one and three prongs and overall. Both for hadronic taus and electrons the efficiencies are given with respect to reconstructed candidates. Tables 6–9 in Appendix C show a breakdown of the efficiencies of the *medium* and *tight* criteria for each step of the selection procedure in the different kinematical regions.

It should be noted that by construction, tau candidates selected by *tight* requirement will also pass the *medium* selection. This is, however, not true for the *loose* flag, which is based on a different method. Therefore it might happen that a candidate which is selected by a *medium* or a *tight* requirement does not pass the *loose* selection.

Figure 5 shows the selection efficiency as function of the pseudorapidity and the reconstructed transverse energy of the tau candidate. The selection is rather stable against E_{T}, however for the *loose* selection, the electron contamination increases significantly with energy. Some variation of efficiency with pseudorapidity reflects the non-uniform geometry of the ATLAS detector:

(i) Lack of the TRT coverage for $|\eta| > 2$.

(ii) Crack region in the ECAL around $|\eta| \simeq 1.5$.

(iii) Crack region in HCAL around $|\eta| \simeq 1$.

(iv) Change in HCAL technology at $|\eta| \simeq 1.7$.

In Fig. 6 the selection efficiencies for hadronic tau decays are shown separately for candidates with 1 and 3 reconstructed tracks. One prong tau decays, are predominantly associated with one or more neutral pions. An experimental overlaps between photon showers from π^0 decays and the charge track will occur, potentially leading to misidentification for electrons. Hence higher selection efficiency for three-prong hadronic taus as compared to one-prong events.

5 Summary and Outlook

A dedicated algorithm for electron suppression in a track based reconstruction of hadronic tau decays has been developed and optimised. It covers the full detector region relevant for tau reconstruction, $|\eta| \leq 2.5$, and a wide range of transverse momenta from 10 to 1000 GeV. It provides three flags corresponding to different levels of electron suppression. The *loose* veto rejects tracks identified as *tight* electron by the `IsEM` flag of the standard ATLAS electron identification algorithm [5]. Being almost 100% efficient, it provides a factor of five rejection against isolated electrons from $\mathrm{W} \rightarrow e\nu$. More stringent suppression has been achieved by the dedicated algorithm. The *medium* flag provides a factor of 50 rejection at the expense of losing about 5% of the reconstructed hadronic taus. To match a requirement of the $\mathrm{W} \rightarrow \tau\nu$ analysis the *tight* criterion has been introduced enabling suppression of electrons down to the per mill level with 15% loss of signal. Appendix C describes an implementation of the algorithm together with the status in different ATLAS software releases.

In the current studies we concentrated on tau candidates reconstructed by the track-seeded version of `tauRec`. Moreover we focused on rejection of isolated electrons from W, Z and τ decays. Further studies should involve the following steps.

(i) Extension of the algorithm to perform on both track-seeded and calorimeter-seeded candidates.

Efficiency %	*tight*			*medium*			*loose*		
Candidate	Overall	1P	3P	Overall	1P	3P	Overall	1P	3P
τ from W $\rightarrow \tau\nu$	85.3±0.2	83.3±0.3	89.5±0.4	95.7±0.2	94.1±0.3	99.5±0.4	99.9±0.2	99.9±0.3	99.9±0.4
τ from Z $\rightarrow \tau\tau$	85.8±0.1	84.3±0.1	89.7±0.2	95.7±0.1	94.4±0.1	99.4±0.2	99.9±0.1	99.8±0.1	99.9±0.2
τ from A $\rightarrow \tau\tau$	85.3±0.1	83.2±0.1	92.7±0.2	93.7±0.1	92.3±0.1	99.1±0.2	99.0±0.1	98.8±0.1	99.7±0.2
τ from Z$'$ $\rightarrow \tau\tau$	85.5±0.2	84.8±0.2	90.9±0.5	93.9±0.2	93.2±0.2	99.2±0.5	98.3±0.2	98.2±0.2	99.2±0.5
Electron from W $\rightarrow$ eν	0.6±0.0	0.5±0.0	5.0±1.1	2.8±0.0	2.3±0.0	69.6±1.1	27.3±0.0	26.6±0.0	59.4±1.1
Electron from Z $\rightarrow$ ee	0.6±0.0	0.5±0.0	3.1±1.2	2.9±0.0	2.3±0.0	73.7±1.2	26.7±0.0	26.0±0.0	59.8±1.2
Electron from Z $\rightarrow \tau\tau$	0.7±0.1	0.6±0.1	7.4±3.6	3.1±0.1	2.7±0.1	63.0±3.6	29.4±0.1	28.9±0.1	53.7±3.6
Electron from A $\rightarrow \tau\tau$	0.8±0.1	0.5±0.0	6.7±1.5	5.0±0.1	3.4±0.0	84.4±1.5	27.8±0.1	26.7±0.0	61.9±1.5
Electron from Z$'$ $\rightarrow \tau\tau$	0.6±0.1	0.5±0.1	2.9±1.7	5.2±0.1	4.3±0.1	90.3±1.7	40.4±0.1	40.1±0.1	65.0±1.7

Table 4: Selection efficiencies of the presented algorithm within $|\eta| < 2.5$. Numbers are given for one-prong (1P) and three-prong (3P) candidates separately, as well as overall. Efficiencies for taus are given relative to reconstructed candidates. Efficiencies for electrons are given relative to all true electrons.

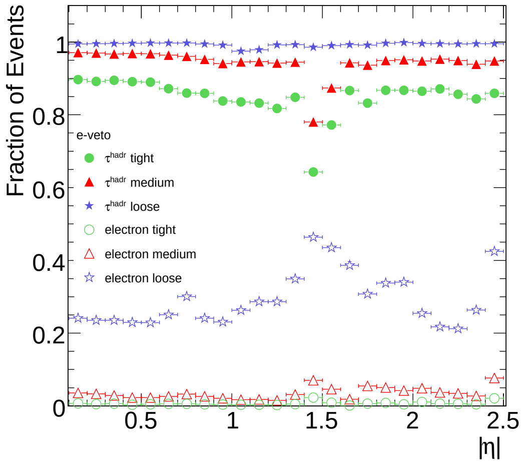

(a)

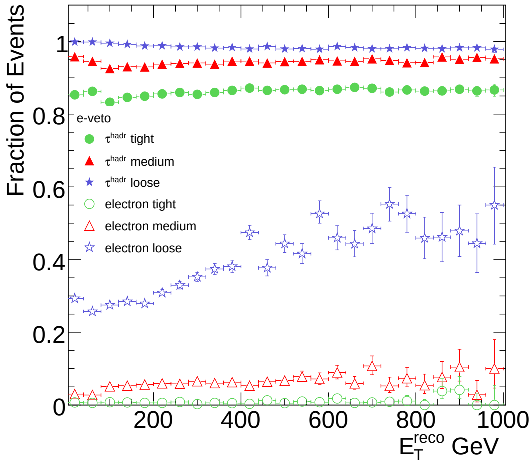

(b)

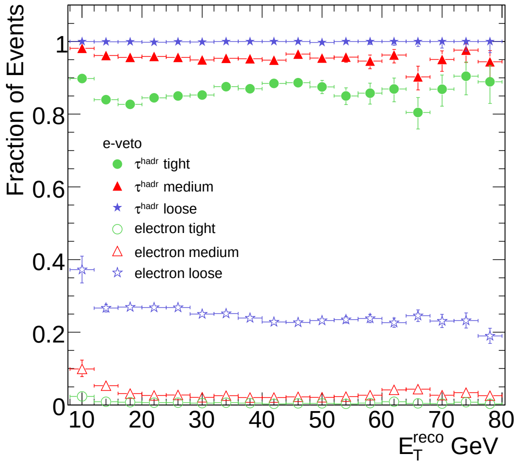

(c)

Figure 5: Selection efficiency for taus and electrons (a) as a function of $|\eta|$, (b) as function of the reconstructed E_T, and (c) as a function of E_T in the low E_T range.

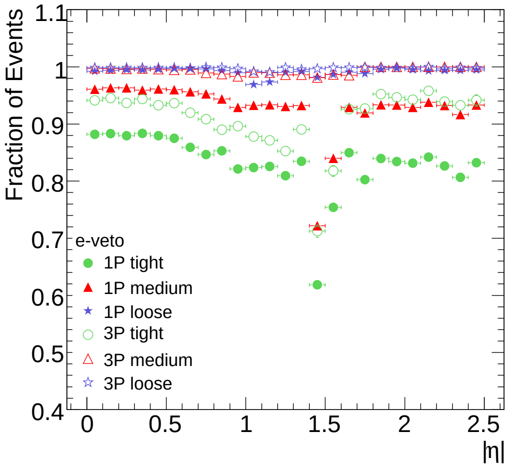

(a)

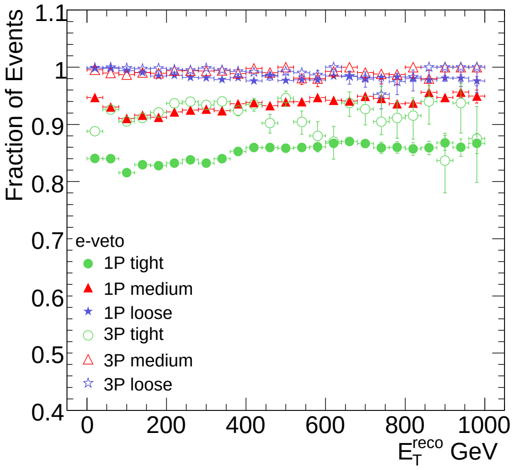

(b)

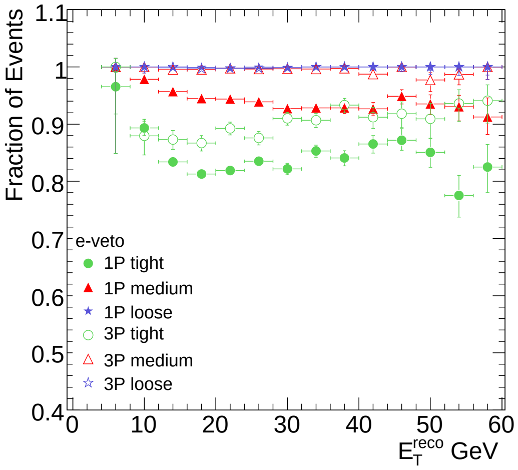

(c)

Figure 6: Selection efficiency for one-prong (1P) and three-prong (3P) taus separately (a) as a function of $|\eta|$, (b) as function of the reconstructed E_{T}, and (c) as a function of E_{T} in the low E_{T} range.

(ii) Study of performance of the algorithm on non-isolated electrons coming from semi-leptonic decays in b- and c-jets.

(iii) Tuning of performance of the algorithm with different pile-up scenarios foreseen for higher luminosities of ATLAS operation.

Appendix A

All fully simulated samples used for the analysis presented in this note have been reconstructed using release 14.2.10. Additional tags used which were not included in release: TauDPDMaker-00-02-34, EventViewInserters-14-02-05, EventViewUserData-14-02-12. Details about the samples are summarised in Tab. 5.

Sample	Dataset ID	N Events
W$\rightarrow e\nu$	5104	98k
W$\rightarrow \tau\nu$	5107	34k
Z$\rightarrow ee$	5144	27 k
Z$\rightarrow \tau\tau$	5188	99 k
A/H$\rightarrow \tau\tau$	5862	83 k
Z'$\rightarrow \tau\tau$	6683	49 k

Table 5: Samples used for the analysis. For each sample ATLAS CSC dataset IDs and number of events is given.

All samples include misaligned geometry with material distortions, simulated with 30 μm displacement.

Appendix B

The $E_{\text{strip}}^{\text{max}}$ variable is calculated in the following way. First the energy in the strip compartment around the impact point of the leading track is summed over three cells in ϕ. Only cells with $|E_T| > 2\sigma$ noise threshold are considered. Subsequently local maxima are searched for in 101 cell sums in η around the impact point excluding a region $1.475 \leq |\eta| \leq 1.5$ corresponding to the ECAL crack. It is assumed that the most energetic strip is associated with the energy carried by the leading track. The second highest energy local maximum, which is the $E_{\text{strip}}^{\text{max}}$ variable, is on the other hand sensitive to the photon shower from π^0 decays. This variable is only calculated in the region of $|\eta| \leq 1.7$ and $p_{\text{T}}^{\text{Ltrk}} \leq 50\,\text{GeV}$, where the TRT provides efficient discrimination between pions and electrons.

Appendix C

e-veto *medium*: selection efficiency %		1P hadronic τ	1P electron
$E_{\mathrm{HCAL}}/p > 0.03$		63.7±0.5	0.5±0.0
$+ \mathrm{N}_{\mathrm{HT}}/\mathrm{N}_{\mathrm{LT}} < 0.2$	a)	63.2±0.5	0.2±0.0
$E_{\mathrm{HCAL}}/p < 0.03 + E_{\mathrm{strip}}^{\mathrm{max}} > 0.25$		24.4±0.4	9.5±0.1
$+ \mathrm{N}_{\mathrm{HT}}/\mathrm{N}_{\mathrm{LT}} < 0.11$	b)	22.4±0.4	1.0±0.0
$E_{\mathrm{HCAL}}/p < 0.03 + E_{\mathrm{strip}}^{\mathrm{max}} < 0.25$		11.9±0.3	90.1±0.1
$+ \mathrm{N}_{\mathrm{HT}}/\mathrm{N}_{\mathrm{LT}} < 0.11 + E_{\mathrm{ECAL}}/p < 0.85$	c)	9.2±0.3	0.7±0.0
Full selection a)+b)+c)		94.9±0.2	1.9±0.1

e-veto *tight*: selection efficiency %		hadronic τ			electron		
		Overall	1P	3P	Overall	1P	3P
$E_{\mathrm{HCAL}}/p > 0.03$		68.5±0.4	63.7±0.5	78.9±0.7	0.6±0.0	0.5±0.0	10.4±2.0
$+ \mathrm{N}_{\mathrm{HT}}/\mathrm{N}_{\mathrm{LT}} < 0.15$	a)	66.7±0.4	62.0±0.5	76.8±0.7	0.1±0.0	0.1±0.0	3.5±1.2
$E_{\mathrm{HCAL}}/p < 0.03 + E_{\mathrm{strip}}^{\mathrm{max}} > 0.5$		14.4±0.3	18.9±0.4	6.0±0.0	6.7±0.1	6.7±0.1	13.0±0.0
$+\mathrm{N}_{\mathrm{HT}}/\mathrm{N}_{\mathrm{LT}} < 0.09$	b)	17.1±0.3	17.4±0.4	15.1±0.6	0.3±0.0	0.3±0.0	0.3±0.0
$E_{\mathrm{HCAL}}/p < 0.03 + E_{\mathrm{strip}}^{\mathrm{max}} < 0.5$		17.1±0.3	17.4±0.4	15.1±0.6	92.7±0.1	92.8±0.1	76.6±2.8
$+ \mathrm{N}_{\mathrm{HT}}/\mathrm{N}_{\mathrm{LT}} < 0.09 + E_{\mathrm{ECAL}}/p < 0.6$	c)	7.0±0.2	6.9±0.3	6.8±0.4	0.1±0.0	0.1±0.0	0.1±0.0
Full selection a)+b)+c)		85.5±0.3	84.3±0.4	88.3±0.5	0.5±0.0	0.5±0.0	3.9±1.3

Table 6: Efficiency at each step of the selection procedure, for $|\eta| < 1.7$ and $p_{\mathrm{T}}^{\mathrm{Ltrk}} < 50$ GeV of the *medium* (top) and *tight* (bottom) selection.

e-veto *medium*: selection efficiency %		1P hadronic τ	1P electron
$E_{\mathrm{HCAL}}/p > 0.02$	a)	85.4±0.6	2.2±0.1
$E_{\mathrm{HCAL}}/p < 0.02 + E_{\mathrm{ECAL}}/p < 0.8$	b)	6.9±0.4	1.0±0.1
Full selection a)+b)		92.3±0.4	3.2±0.1

e-veto *tight*: efficiency %	hadronic τ			electron		
	Overall	1P	3P	Overall	1P	3P
$E_{\mathrm{HCAL}}/p > 0.05$ a)	78.2±0.5	73.0±0.7	90.6±0.8	0.6±0.1	0.5±0.1	6.2±2.1
$E_{\mathrm{HCAL}}/p < 0.05$ $+E_{\mathrm{ECAL}}/p < 0.6$ b)	6.6±0.3	7.8±0.4	2.8±0.5	0.1±0.0	0.1±0.0	0.8±0.8
Full selection a)+b)	84.8±0.5	80.8±0.6	93.4±0.7	0.7±0.1	0.6±0.1	7.0±2.2

Table 7: Efficiency at each step of the selection procedure, for $|\eta| > 1.7$ and $p_{\mathrm{T}}^{\mathrm{Ltrk}} < 50\,\mathrm{GeV}$ of the *medium* (top) and the *tight* selection.

e-veto *medium*: efficiency %	1P hadronic τ	1P electron
E_{HCAL}/p cut	95.3±0.1	4.1±0.2

e-veto *tight*: efficiency	hadronic τ			electron		
	Overall	1P	3P	Overall	1P	3P
E_{HCAL}/p cut	87.0±0.2	86.4±0.2	91.2±0.5	0.3±0.1	0.3±0.1	1.6±1.6

Table 8: Efficiency at each step of the selection procedure, for $|\eta| < 1.7$ and $p_{\mathrm{T}}^{\mathrm{Ltrk}} > 50\,\mathrm{GeV}$ of the *medium* (top) and the *tight* selection.

e-veto *medium*: efficiency	1P hadronic τ	1P electron
E_{HCAL}/p cut	95.0±0.4	7.1±0.9

e-veto *tight*: efficiency %	hadronic τ			electron		
	Overall	1P	3P	Overall	1P	3P
E_{HCAL}/p cut	89.3±0.5	87.8±0.6	95.3±0.8	0.4±0.2	0.5±0.2	0.1±0.0

Table 9: Efficiency at each step of the selection procedure, for $|\eta| > 1.7$ and $p_{\mathrm{T}}^{\mathrm{Ltrk}} > 50\,\mathrm{GeV}$ of the *medium* (top) and *tight* selection.

Appendix D

The electron veto algorithm is implemented in ATHENA since release 12.0.5 as the tool `tau1p3pEleVeto` in the track-seeded version of `tauRec`[3].

Release 12: `tau1p3pEleVeto` is executed at the level of reconstruction, after track selection criteria are applied. It is switched off by default. In order to use it, the user needs to produce her own ATHENA aware ntuples from ESD setting in the jobOptions: `doCaloCluster = True` and `doTauRec = True` to rerun TAUREC on ESD and `tau1p3pAlg.EleVeto.doEleVeto = 1` to switch on the tool. Before release 13, the algorithm does not provide any discrimination against electrons in the region of $|\eta| \geq 1.7$.

Release 13: `tau1p3pEleVeto` is switched on by default. It provides a two-bit flag for tau objects, returning 1 or 0 depending on whether the object was identified as an electron or not. One bit, the *IsEle* flag, is reserved for identification based on the presented algorithm, the other, the *IsEle_eg* flag, corresponds to identification based on the tight selection for electrons provided by the ISEM flag (ISEM = 0.). The algorithm covers full detector region $|\eta| < 2.5$ however is not optimal for high p_T (> 100 GeV) taus.

Release 14: Since release 14.1.0 some improvement in performance in high P_T region is included [1]. The complete version of the algorithm presented in this note is available since release 14.4.0.

References

[1] A.Christov et al., *Performance of the tau reconstruction and identification algorithm with release 14.2.10*, ATL-COM-PHYS-2008-196.

[2] Z. Czyczula and M. Dam, *Electron Veto in the τ identification package TAU1P3P* , ATL-PHYS-INT-2008-007.

[3] T. Sjöstrand *et al.*, Comput. Phys. Commun. **135**, 238 (2001); T. Sjöstrand *et al.*, J. High Energy Phys. JHEP05 026 (2006).

[4] ATLAS Technical Desin Report (TDR) vol.I

[5] The ATLAS Collaboration, *Reconstruction and Identification of Electrons in ATLAS*, CSC Book, ATL-PUB-2008-0XX.

---

[3] In releases prior to 14 the track seeded part of `tauRec` was called `tau1p3p`

D

Z.Czyczula, M.Dam

Feasibility Study of Tau Polarisation Measurement in $Z' \rightarrow \tau^+\tau^-$ events in ATLAS

Prospects of Measuring the Tau Polarisation in $Z' \longrightarrow \tau^-\tau^+$ events in ATLAS

Z. Czyczula[*], M. Dam[†]
Niels Bohr Institute, Copenhagen, Denmark

Should a Z′ boson be observed at the LHC with decays to tau pairs, measurement of the longitudinal tau polarisation can provide valuable information on the Z′ couplings and hence help to discriminate between various models. By analysing the kinematics of the final state pions in the $\tau^\pm \to \pi^\pm\pi^0\nu$ decay mode, the tau polarisation can be extracted without reconstructing the energy of the decaying tau. Based on fully simulated data at $\sqrt{s} = 14\,\text{TeV}$, the sensitivity of the measurement is investigated in a benchmark scenario, where a 600 GeV mass Z′ has couplings according to the *sequential model.*

1 Introduction

The existence of a new heavy neutral boson decaying to fermion pairs is predicted by several models. Within the Standard Model, this could be the Higgs boson, although current estimates indicate a mass lower than 200 GeV. In models going beyond the Standard Model, a new heavy resonance could be a heavier Higgs boson—most notably predicted by SUSY theories—or it could be a new heavy gauge boson; a Z′. Following the possible discovery of a heavy resonance at the LHC, the next step would be to establish its properties. The first properties to be determined are its production cross section, its mass and width, and its branching fractions. Furthermore, measurement of the forward-backward charge asymmetry, A_{FB}, in leptonic decay modes can provide valuable information on its couplings [1]. Additional information on the nature of its couplings can be acquired from the longitudinal polarisation of tau leptons in the $\tau^-\tau^+$ decay channel. A non-zero polarisation, which arises from parity violation in the decay, is expected in most Z′ models. No polarisation should arise if the resonance would be a Higgs. The measurement of tau polarisation was successfully exploited at LEP, where very precise information on the Z boson couplings was obtained from $Z \to \tau^-\tau^+$ decays [2].

In this note, we study the prospects of measuring the tau polarisation in the decay of a heavy resonance to tau pairs. As a concrete model for the resonance, we consider a

---

[*] `czyczula(AT)nbi.dk`

[†] `dam(AT)nbi.dk`

Channel	Dominant decay mode	BR [%]
$e^- \bar{\nu}\nu$	$e^- \bar{\nu}_e \nu_\tau$	17.9
$\mu^- \bar{\nu}\nu$	$\mu^- \bar{\nu}_\mu \nu_\tau$	17.4
$h^- \nu$	$\pi^- \nu_\tau$	11.6
$h^- \pi^0 \nu$	$\rho^- \nu_\tau \rightarrow \pi^- \pi^0 \nu_\tau$	26.0
$h^- \pi^0 \pi^0 (\pi^0) \nu$	$a_1^- \nu_\tau \rightarrow \pi^- \pi^0 \pi^0 \nu_\tau$	10.8
$h^- h^- h^+ (\pi^0) \nu$	$a_1^- \nu_\tau \rightarrow \pi^- \pi^- \pi^+ \nu_\tau$	14.6

Table 1: *Tau lepton branching fractions [3] classified according to leading decay modes. h^- stands for π^- or K^-. The Cabibbo suppressed kaon modes amount to 0.5% in the case of $h^-\nu$ and 0.4% in the case of $h^-\pi^0\nu$.*

Z′ boson. Due to angular momentum conservation, fermions produced in Z′ decays have opposite helicities: $\mathrm{Z}' \rightarrow \tau^-_\mathrm{L}\tau^+_\mathrm{R}$ or $\mathrm{Z}' \rightarrow \tau^-_\mathrm{R}\tau^+_\mathrm{L}$. The polarisation of τ^- and τ^+ therefore have opposite signs. In this work, we define P_τ as the polarisation of τ^-. In terms of the cross sections, σ_R and σ_L, for production of a right and a left handed τ^-, respectively, the tau polarisation is

$$P_\tau = \frac{\sigma_\mathrm{R} - \sigma_\mathrm{L}}{\sigma_\mathrm{R} + \sigma_\mathrm{L}}. \tag{1}$$

Averaging over the tau production angle (inside any reasonably defined acceptance), the tau polarisation depends on the Z′ couplings to the final state taus only.

Since parity is maximally violated in the charged-current weak decay of the tau lepton, the angular distributions of its decay products depend strongly on the spin orientation of the tau. Tau decays can therefore be used as spin analysers. In particular the hadronic decay modes, having only one neutrino in the final state, are powerful analysers of the tau polarisation. For the fully leptonic modes, with two final state neutrinos, the sensitivity is somewhat reduced. The main tau branching fractions are summarised in Table 1.

Powerful methods to extract the tau polarisation from data were developed at the time of the LEP experiments [4, 5, 6]. The variables used to extract the polarisation relied on knowledge of the energy of the decaying taus from the beam energy constraint. No such luxury is available at hadron colliders, where the tau energies can be only reconstructed in some fraction of events via the so-called *collinear approximation* (see Sec. 3.2). Without knowledge of the tau energy, the polarisation can be only extracted from a helicity analysis in decays going via a vector meson. In this note, we will demonstrate how the tau polarisation can be extracted from the energy sharing between the two pions in the $\pi^-\pi^0\nu$ channel. A further complication at hadron colliders is the experimental isolation of pure samples of taus. Strict event selection criteria are necessary to suppress the overwhelming background from QCD [7, 8]. Such criteria can be expected to influence the polarisation observables in intricate ways and may obscure the tau polarisation measurement.

Many models exist describing a possible Z′ (for a recent review, see Ref. [9]). Most of the theories predict the Z′ boson to couple equally to all fermion generations [10]. There are, however, models which extend the Standard Model gauge structure in such a way that coupling to third generation is enhanced [11, 12]. For this study, we have assumed the so-called *sequential model* (SSM), where the Z′ couplings are the same as those of the Z boson. The current experimental limit on the mass of a SSM Z′ boson, derived from searches using high-mass tau pairs at the Tevatron, is 399 GeV [13]. Here we have assumed a Z′ mass of 600 GeV.

The study aims to explore the prospects of the tau polarisation measurement in a realistic experimental scenario with all detector effects included. For this, fully simulated data produced at a 14 TeV centre-of-mass energy have been employed.

2 Data Samples

Samples of Z′ bosons were generated with the general purpose event generator `PYTHIA` [14]. The Z′ bosons were forced to decay to tau lepton pairs. The tau leptons were then made to decay using the `TAUOLA` package [15]. The interface between `PYTHIA` and `TAUOLA` was modified in such way that the Z′ coupling constants from `PYTHIA` were propagated to `TAUOLA` and correctly used for the generation of the longitudinal polarisation of the tau leptons. The modification was performed at the level of amplitudes, hence taking into account the interference with the Standard Model γ/Z [16]. The ATLAS detector was fully simulated using the `GEANT4` package [17], implemented inside the ATLAS software framework, `ATHENA`. No pile-up effects were included. Remaining technical issues related to the data samples can be found in Appendix A.

As default, the `PYTHIA` input parameters were adjusted so that the Z′ couplings were in accord with the *sequential model*, i.e. identical to those of the Z boson. Then, by modifying the coupling of the Z′ to tau leptons only, it was possible to control the longitudinal polarisation of the tau leptons, with everything else being the same. This way two large data samples were produced: one where the Z′ coupled to $\tau_{\mathrm{L}}^{-}\tau_{\mathrm{R}}^{+}$ pairs only (the τ_{L} sample) and the other where it coupled to $\tau_{\mathrm{R}}^{-}\tau_{\mathrm{L}}^{+}$ pairs only (the τ_{R} sample). For enhanced statistics in the sensitive hadronic channels, all taus were forced to decay hadronically.

For the production, an invariant tau pair mass of at least 300 GeV was requested. The invariant mass distribution is shown in Figure 1. Due to interference between the Z′ and the γ/Z, a small fraction (∼2%) of the τ_{L} (τ_{R}) sample had the “wrong” helicity combination, i.e. $\tau_{\mathrm{R}}^{-}\tau_{\mathrm{L}}^{+}$ ($\tau_{\mathrm{L}}^{-}\tau_{\mathrm{R}}^{+}$). As expected, these events were concentrated at the lower end of the mass distribution. Hence, to obtain cleaner τ_{L} and τ_{R} samples, a mass window of ±100 GeV around the peak was applied, reducing this problem significantly.

3 Tau Polarisation Measurement

As already stated, in Z′ decays, the helicities of the τ^{-} and τ^{+} are opposite. Since, however, also the helicities of the ν_τ and $\bar{\nu}_\tau$ are opposite, the angular distributions in τ^{-} and τ^{+} decays will be identical. We can therefore simply add up the decay distributions of τ^{-}

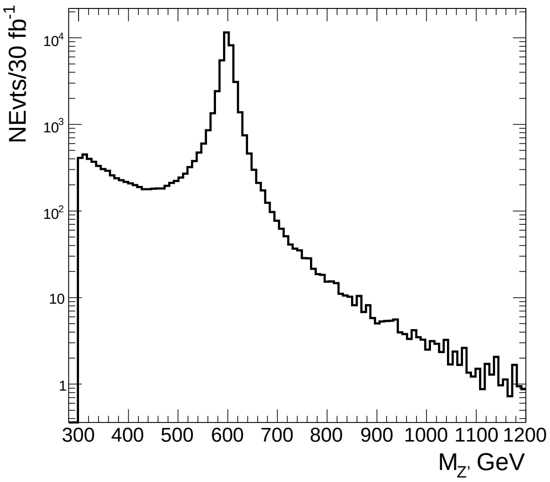

Figure 1: *Invariant mass of the generated $\tau^+\tau^-$ pairs.*

and τ^+. In the following, we will be discussing the decay of the τ^-. However, the charged conjugate decay of the τ^+ would everywhere display the same characteristics.

3.1 Polarisation Observables

Here we introduce the tau polarisation variables following largely Ref. [4].

For all tau decay modes, the main observable being sensitive to the tau polarisation is the angle, θ, in the tau rest frame between the tau line of flight and the direction of the visible decay products. With P_τ being the longitudinal polarisation of the tau, the decay distribution in the $h^-\nu$ channel ($h^- = \pi^-/K^-$) is

$$\frac{1}{\Gamma_h}\frac{\mathrm{d}\Gamma_h}{\mathrm{d}\cos\theta} = \frac{1}{2}\left[1 + P_\tau \cos\theta\right]. \tag{2}$$

For decays involving vector mesons (ρ^-, a_1^-, K^{*-}), the hadronic system can be either transversely (T) or longitudinally (L) polarised. The two possibilities give rise to the two decay distributions

$$\frac{1}{\Gamma_v}\frac{\mathrm{d}\Gamma_v^{\mathrm{L}}}{\mathrm{d}\cos\theta} = \frac{\frac{1}{2}m_\tau^2}{m_\tau^2 + 2m_v^2}\left[1 + P_\tau \cos\theta\right], \tag{3}$$

and

$$\frac{1}{\Gamma_v}\frac{\mathrm{d}\Gamma_v^{\mathrm{T}}}{\mathrm{d}\cos\theta} = \frac{m_v^2}{m_\tau^2 + 2m_v^2}\left[1 - P_\tau \cos\theta\right], \tag{4}$$

respectively, where v indicates the vector meson state.

Since the ν_τ is not observed, the τ^- direction and thus the decay angle θ cannot be directly measured. In the relativistic limit ($E_\tau \gg m_\tau$), θ is related to the energy fraction

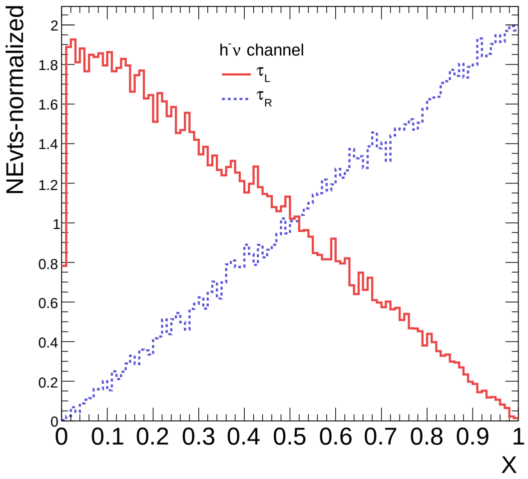

Figure 2: *For the $h^-\nu$ channel, fraction of the tau energy taken by the h^- in the τ_{L} and τ_{R} samples. Plots based on Monte Carlo generator-level information.*

carried by the hadronic system in the laboratory frame, $x = E/E_\tau$, through the relation

$$\cos\theta = \frac{2x - 1 - m^2/m_\tau^2}{1 - m^2/m_\tau^2}, \tag{5}$$

where m is the mass of the hadronic system.

Figure 2 shows, for the $h^-\nu$ channel, the x distribution for the τ_{L} and τ_{R} samples separately. A clear difference between the two samples can be observed.

For vector meson modes, if no attempt is made to analyse the vector meson polarisation, one must average over Eqs. (3) and (4). As a result, the sensitivity to P_τ is reduced by a factor $\alpha = (m_\tau^2 - 2m^2)/(m_\tau^2 + 2m^2)$, that takes a value of 0.46 for ρ^- and 0.12 for a_1^-.

Most of the lost sensitivity can be regained if information on the helicity of the hadronic final state is incorporated. For the $\rho^-\nu \to \pi^-\pi^0\nu$ channel, the decay angle ψ in the ρ^- rest frame between the ρ^- and π^- directions is sensitive to the polarisation of the hadronic state. In terms of laboratory observables, ψ is given by

$$\cos\psi = \frac{m_v}{\sqrt{m_v^2 - 4m_\pi^2}} \frac{E_{\pi^-} - E_{\pi^0}}{|\mathbf{p}_{\pi^-} + \mathbf{p}_{\pi^0}|}, \tag{6}$$

where E_{π^-} and E_{π^0} ($\mathbf{p}_{\pi^-}$ and $\mathbf{p}_{\pi^0}$) are the energies (momenta) of the charged and neutral pions, respectively.

Figures 3a and 3b show the $\cos\theta$ and $\cos\psi$ distributions for the $h^-\pi^0\nu$ channel. The clear difference in the $\cos\psi$ distribution between the τ_{L} and τ_{R} samples reflects that the ρ^- in the decay of left-handed (right-handed) taus is predominantly transversely (longitudinally) polarised in the laboratory frame. As a consequence, for left-handed taus the two pions from the ρ^- decay tend to share the energy equally, whereas for right-handed taus one pion tend to be harder that the other.

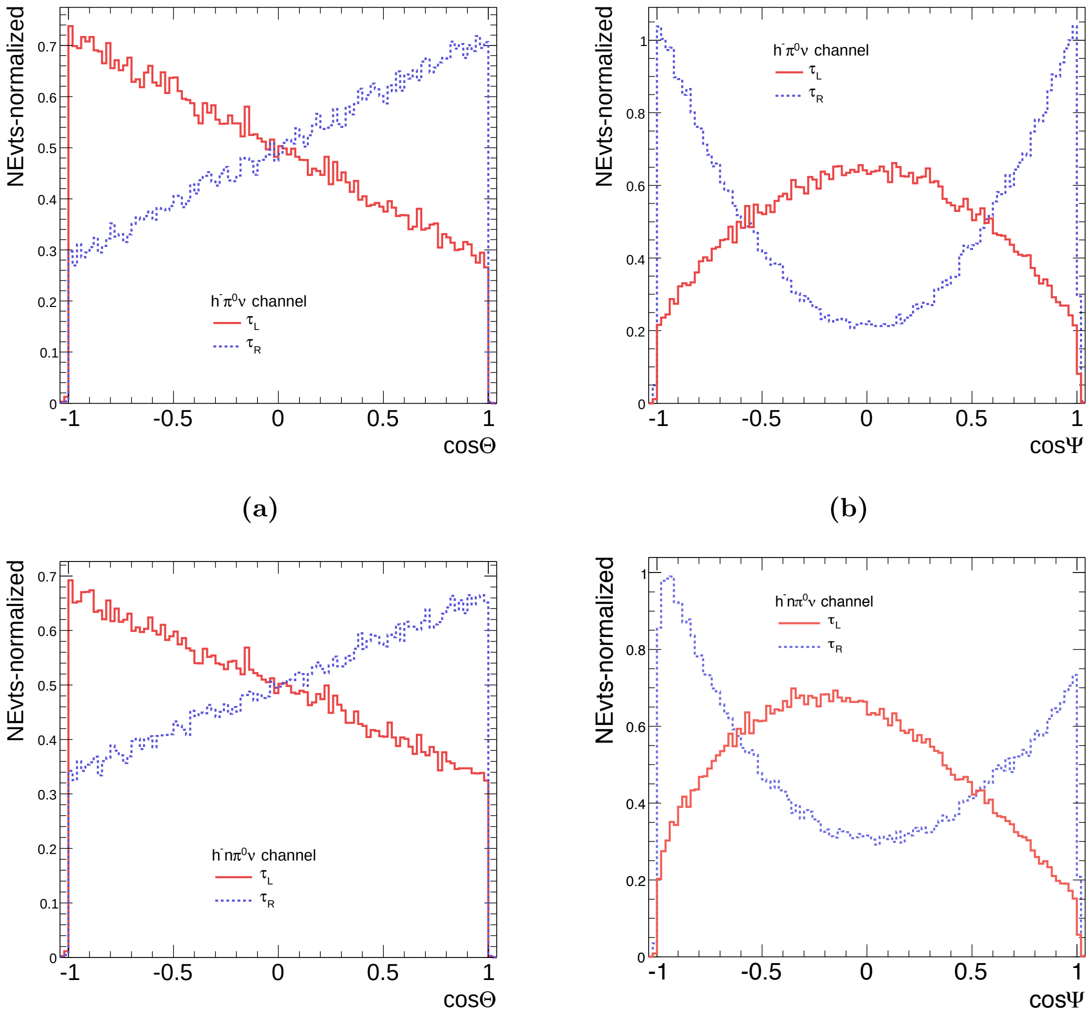

(a) **(b)**

(c) **(d)**

Figure 3: *The* $\cos\theta$ *(left) and* $\cos\psi$ *(right) distributions for the pure* $h^-\pi^0\nu$ *channel (top), and for the inclusive* $h^-\mathrm{n}\pi^0\nu$ *channel (bottom). The inclusive channel includes* $h^-\pi^0\nu$ *and* $h^-\pi^0\pi^0(\pi^0)\nu$*. Plots based on Monte Carlo generator-level information.*

3.2 Observables at the LHC

At LHC energies, tau leptons are strongly boosted and their decay products tightly collimated. Experimentally, the determination of the number of final state π^0 s is therefore difficult. Hence, in the current study, no attempt has been made to separate the $h^-\pi^0\nu$ state from states with additional π^0 s. All decays in the inclusive sample with one or more π^0 s—denoted $h^-\mathrm{n}\pi^0\nu$— are treated in the same way as $h^-\pi^0\nu$ decays. For the multi-π^0 states, Eq. (6) is still being used, however, E_{π^0} ($\mathbf{p}_{\pi^0}$) now designates the sum of all π^0 ener-

	$h^-\nu$	$h^-\pi^0\nu$	$h^-\pi^0\pi^0(\pi^0)\nu$	$h^-\mathrm{n}\pi^0\nu$
$\cos\theta$	0.57	0.26	0.06	0.21
$\cos\psi$	–	0.37	0.19	0.31
$\cos\theta$ and $\cos\psi$	–	0.48	0.18	0.39

Table 2: *For one-prong τ decay modes, generator-level sensitivities of the two polarisation variables. The $h^-\mathrm{n}\pi^0\nu$ inclusive mode comprises $h^-\pi^0\nu$ and $h^-\pi^0\pi^0(\pi^0)\nu$.*

gies (momenta). Figures 3c and 3d show the $\cos\theta$ and $\cos\psi$ distributions for the inclusive $h^-\mathrm{n}\pi^0\nu$ channel.

Table 2 summarises the sensitivities (for definition, see [5]) of the $\cos\theta$ and $\cos\psi$ observables for the one-prong hadronic decay modes. As expected the $h^-\nu$ channel is the most sensitive. For the $h^-\pi^0\nu$ channel, the sensitivity is increased considerably by inclusion of the $\cos\psi$ variable. In fact, the $\cos\psi$ alone carries nearly 50% more information than the $\cos\theta$ variable alone. The addition of multi-π^0 final states to the $h^-\pi^0\nu$ channel results in a dilution reducing the sensitivity by about one fifth.

Since $\cos\theta$ is extracted from the energy fraction $x = E/E_\tau$, its definition relies on knowledge of the tau energy. As energy is carried away by neutrinos, this is experimentally accessible only via the *collinear approximation* [20] in which the tau direction is assumed to be identical to the direction of the visible decay products, and the total missing momentum in the event is assumed to arise from the neutrinos from the tau decays. The collinear approximation reaches its limit when the two tau decays are back-to-back. Thus, for a heavy Z′, it leads to a considerable loss of statistics with an acceptance only at the 10% level.

The $\cos\psi$ variable, on the other hand, does not depend on the tau energy. Apart from the preceding mass factor, $\cos\psi$ depends only on the sharing of energy between the charged and the neutral pions from the $\rho^-\nu$ decay. Experimentally, measurement of the mass of the hadronic state, m_v, is difficult, so instead of $\cos\psi$ we use the variable Υ being identical to $\cos\psi$ except that the mass factor is left out. Observing that $|\mathbf{p}_{\pi^-} + \mathbf{p}_{\pi^0}| = E_{\pi^-} + E_{\pi^0}$, Υ is therefore defined as

$$\Upsilon = \frac{E_{h^-} - E_{\pi^0}}{E_{h^-} + E_{\pi^0}}. \tag{7}$$

A Monte Carlo generator-level study has shown, that the sensitivity of the Υ variable is practically identical to that of $\cos\psi$.

4 Analysis Procedure

4.1 Tau Identification

As a first step of the event selection, hadronic tau candidates are reconstructed. The reconstruction is done using the calorimeter-seeded version of `tauRec` [21, 22]. The algorithm starts from a jet within $|\eta| < 2.5$ with transverse energy exceeding 10 GeV. Identification variables are then built based on information from the electromagnetic and hadronic calorimeters and the Inner Detector. For the purpose of performance studies, the candidate is labelled a *matched* tau if a generated tau is found inside a cone of $\Delta R = \sqrt{(\Delta\eta)^2 + (\Delta\phi)^2} < 0.2$ around the reconstructed tau. Reconstructed candidates are categorised as one-prong or multi-prong (typically two- or three-prong) decays based on the number of reconstructed tracks with $p_{\mathrm{T}}^{\mathrm{trk}} > 2\,\mathrm{GeV}$ satisfying a set of quality criteria. Due to detector effects and reconstruction inefficiencies both upwards and downwards migration in the track multiplicity relative to the true number of tracks are observed.

As a second step, reconstructed candidates are subjected to a set of tau identification criteria as developed for an earlier study of high-p_{T} tau pairs from Z' decays [8]. Candidates are required to have $E_{\mathrm{T}} > 60\,\mathrm{GeV}$, to have either one or three tracks, and to fulfil an E_{T} dependent cut on the `tauRec` log-likelihood variable (*llh*).

As discussed below, $\mathrm{Z}' \to \tau^+\tau^-$ events are required to have two identified taus according to these criteria. On top of this, the candidate for which the polarisation is to be measured is required to have exactly one track.

In Figure 4, efficiencies of the tau identification cuts, including the one-track requirement, are shown as a function of E_{T}, $|\eta|$, and Υ for the τ_{L} and τ_{R} samples separately. Here, as in the rest of the document, efficiencies are defined with respect to all true taus inside the acceptance of $|\eta| < 2.5$. A clear structure can be observed in the $|\eta|$ dependence. The drop in efficiency from the track multiplicity requirement at forward rapidities reflects the higher material budget in the forward region of the tracking detectors, making precise tracking more difficult. For the *llh* variable, the dip around $|\eta| \sim 1.5$ reflects the transition region between the barrel and end-cap electromagnetic calorimeters.

The structure in the Υ dependence is more intricate. The differences between the τ_{L} and τ_{R} samples reflect the influence of the tau polarisation on the kinematics of the tau decay products. As an example, in candidates with Υ close to -1, the charged pion carries only a small fraction of the total energy. As, at the same time, the τ_{L} sample tends to be softer than the τ_{R} sample, the requirement that there be a track with $p_{\mathrm{T}}^{\mathrm{trk}} > 2\,\mathrm{GeV}$ leads to a larger loss in the τ_{L} sample than in the τ_{R} sample in this region.

Table 3a summaries the reconstruction and identification efficiencies for the τ_{L} and τ_{R} samples. Again the efficiencies are given with respect to all true taus inside the acceptance.

4.2 Selection of $h^-\mathrm{n}\pi^0\nu$ Decays

As already discussed, the tau polarisation will be extracted using the Υ variable from an inclusive sample of one-prong hadronic tau decays with a single or multiple π^0 s. Inclusion also of the $h^-\nu$ channel, which has no physically meaningful definition of Υ, would dilute the sensitivity, and is therefore avoided. No attempt will be made to reconstruct the individual π^0 energies. Instead, the total transverse energy deposited by π^0 s is estimated as the difference between the transverse energy of the tau visible decay products, as measured by the calorimeters, and the transverse momentum of the charged pion, as measured by

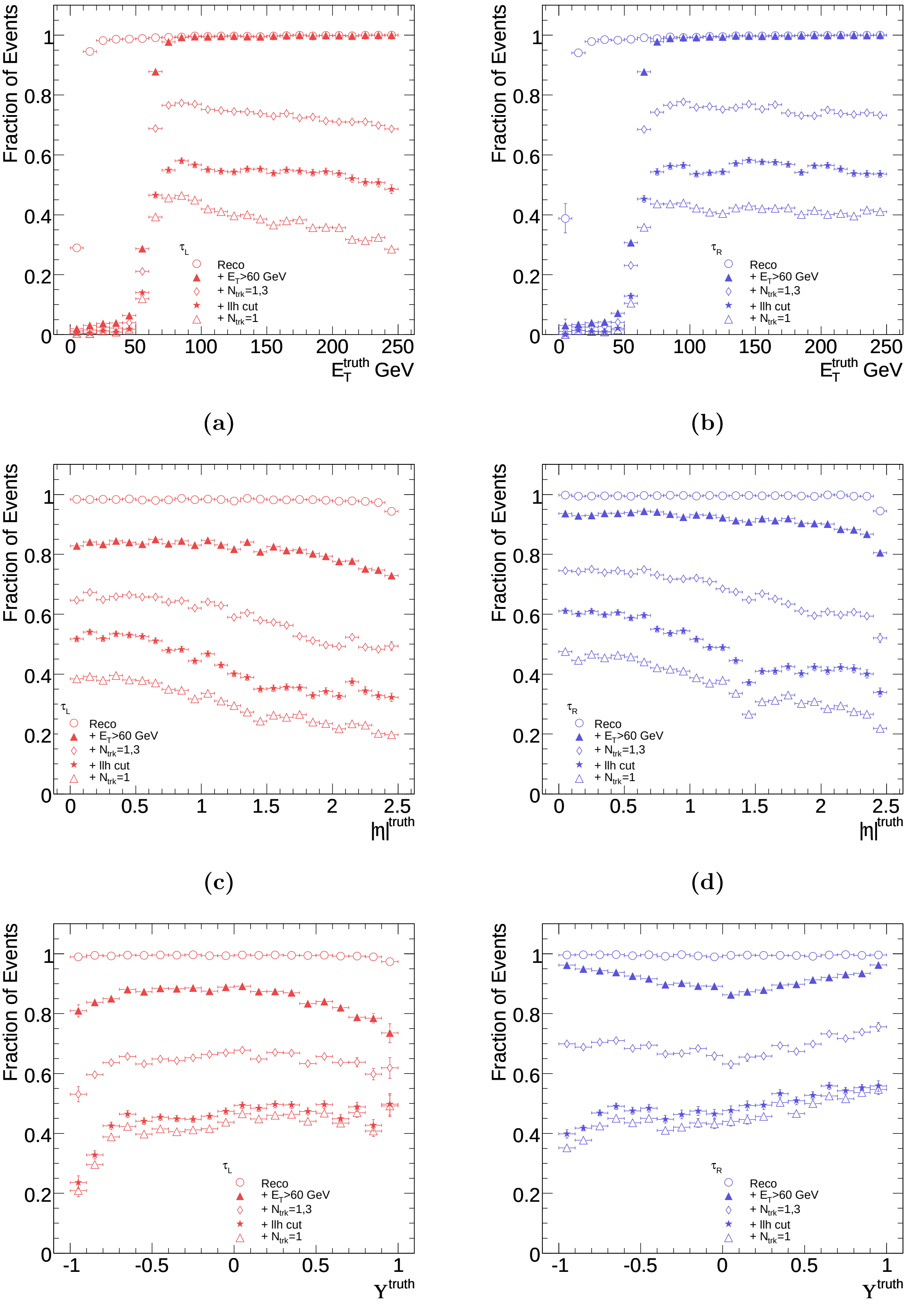

(a)

(b)

(c)

(d)

(e)

(f)

Figure 4: *Efficincies of the tau identification criteria as function of true* $E_{\rm T}$ *(top),* $|\eta|$ *(middle), and* Υ *(bottom) for the* $\tau_{\rm L}$ *(left) and* $\tau_{\rm R}$ *(right) samples.*

Efficiency [%]	τ_{L} sample			τ_{R} sample		
	$h^-\nu$	$h^-\pi^0\nu$	$h^-\pi^0\pi^0(\pi^0)\nu$	$h^-\nu$	$h^-\pi^0\nu$	$h^-\pi^0\pi^0(\pi^0)\nu$
(a) Tau identification						
- reconstruction	92.6	99.4	99.7	99.2	99.5	99.5
- $E_{\mathrm{T}} > 60\,\mathrm{GeV}$	54.1	83.3	94.6	88.9	90.6	95.3
- $\mathrm{N}_{\mathrm{ntrk}} = 1, 3$	47.0	64.1	66.8	78.7	70.2	67.4
- *llh* cut	36.5	46.3	44.8	62.2	50.4	45.4
(b) $h^-\mathrm{n}\pi^0\nu$ selection						
- $\mathrm{N}_{\mathrm{ntrk}} = 1$	36.3	43.4	40.1	61.8	47.3	40.7
- $E_{\mathrm{T}}^0/E_{\mathrm{T}} > 0.2$	3.6	38.3	38.7	5.9	34.8	38.3
(c) Event selection						
- two identified taus	1.4	15.3	15.9	2.8	15.9	17.8
- other selection cuts	0.6	6.5	7.2	1.4	7.3	7.9

Table 3: *Cumulative efficiencies for the three parts of the overall tau selection: (a) tau identification, (b) selection of $h^-\mathrm{n}\pi^0\nu$ decays, and (c) event selection. (For discussion of the three parts of the selection, see Sections 4.1, 4.2, and 4.3.) All efficiencies are given at the tau level with respect to all generated taus inside the acceptance.*

the Inner Detector, i.e.

$$E_{\mathrm{T}}^0 = E_{\mathrm{T}} - p_{\mathrm{T}}^{\mathrm{trk}}. \tag{8}$$

Figure 5 illustrates the resolution of E_{T} for identified one-prong hadronic tau decays. On average, the reconstructed E_{T} is higher than its true value, as defined from the visible decay products of the matched tau decay, by about 2.5%. This is a calibration effect, which could be easily removed if sufficient attention was paid to the calibration of high momentum taus. The possible effect on the tau polarisation measurement of such a scale error is discussed below. The resolution on E_{T} is found to be about 6%.

Figure 6 illustrates the resolution on E_{T}^0 for identified one-prong tau decays with a total true π^0 energy exceeding 12 GeV. The distribution is clearly non-Gaussian, reflecting the composed nature of the E_{T}^0 variable. On average, the reconstructed E_{T}^0 is higher than its true value by 7%. This is a reflection of the scale error on E_{T}.

For an identified one-prong hadronic tau candidate to be selected as a $h^-\mathrm{n}\pi^0\nu$, that is as having one or more π^0 s, it is required that the ratio between its reconstructed neutral and total energy, $E_{\mathrm{T}}^0/E_{\mathrm{T}}$, be at least 0.2. Figure 7 shows the $E_{\mathrm{T}}^0/E_{\mathrm{T}}$ distributions, for the $h^-\nu$, $h^-\pi^0\nu$, and $h^-\pi^0\pi^0(\pi^0)\nu$ channels. The clear difference between the τ_{L} and τ_{R} samples for $h^-\pi^0\nu$ is directly reflecting the polarisation. For left-handed taus, the two pions tend to share the energy equally, whereas for right-handed taus, one pion tends to be harder than the other leading to the observed double peaking structure. From this it is clear, that the selection will be less efficient for right-handed taus, since these have more candidates in the region of the $E_{\mathrm{T}}^0/E_{\mathrm{T}}$ cut. The efficiencies of the selection are summarised in Table 3b.

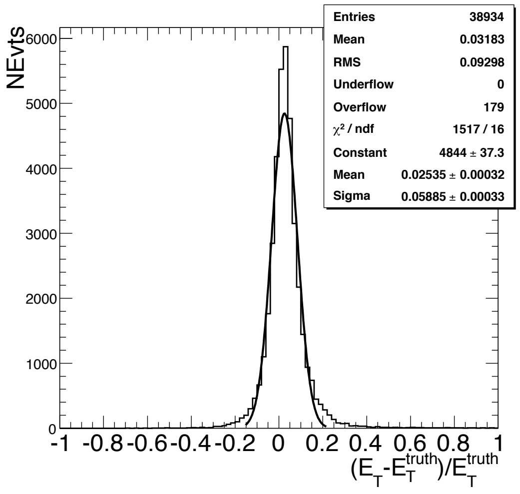

__Figure 5:__ E_{T} resolution of the identified one-prong tau decays.

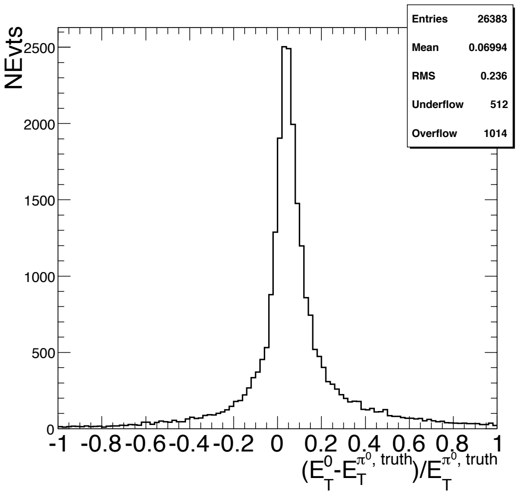

__Figure 6:__ E_{T}^{0} resolution for identified one-prong tau decays with true transverse energy of π^0 s above 12 GeV.

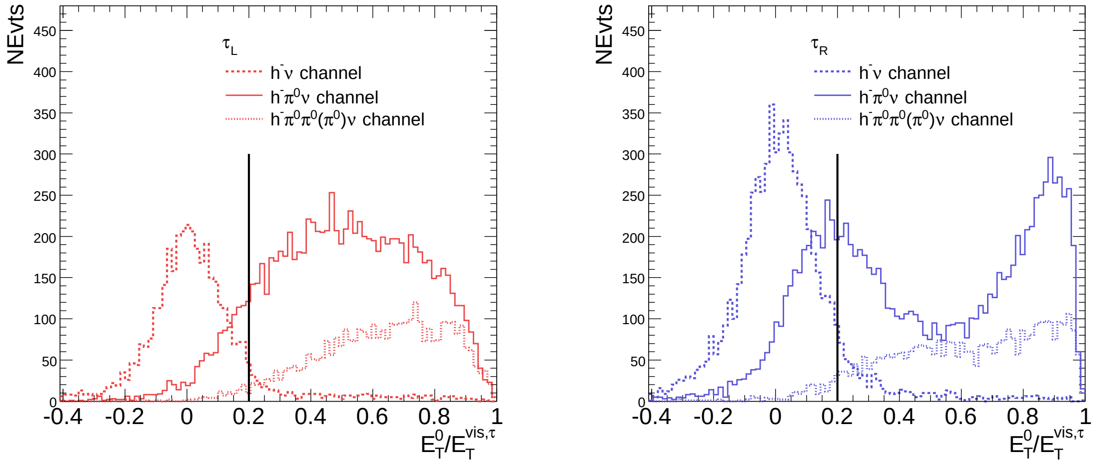

(a) **(b)**

__Figure 7:__ Ratio between neutral and total energy for $h^-\nu$, $h^-\pi^0\nu$, and $h^-\pi^0\pi^0(\pi^0)\nu$ decays passing the tau identification requirements. The vertical line denotes the cut.

At this level, the dominant internal background from other tau decay modes comes from the $h^-\nu$ channel with 3% (5%) in the τ_{L} (τ_{R}) sample. Another sizable contribution of 1.8% comes from decays with a final state K_{L}^{0}. Three-prong decays contribute with about 1%. Backgrounds from the leptonic modes have not been addressed in the current study. However, their contribution can be reduced to the per mille level by dedicated lepton veto

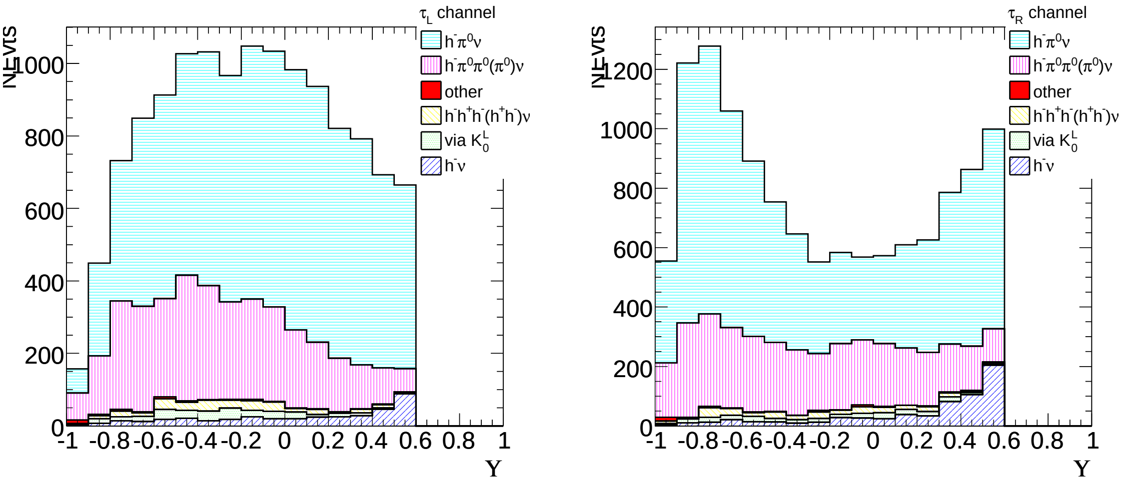

(a) **(b)**

Figure 8: *The Υ distributions for the signal samples after full selection. Leptonic decay modes not included.*

algorithms [22]. Further work should assess this point.

Figure 8 shows the reconstructed Υ distributions for the selected decays including internal backgrounds. No candidates appear with $\Upsilon > 0.6$ due to the $E_{\mathrm{T}}^{0}/E_{\mathrm{T}} > 0.2$ cut. Figure 9 shows true versus reconstructed Υ values. The band at $\Upsilon^{\mathrm{truth}} = 1$ is due to the background from $h^{-}\nu$.

4.3 Event selection

At the LHC, discovery of a Z′ boson decaying to tau pairs is a challenging task. Harsh selection criteria must be applied to suppress the large backgrounds from QCD jet production, W+jet, $t\bar{t}$, and Z+jets events [7, 8]. A further complication is, that the resonance mass can be only reconstructed via the *collinear approximation*, leading to a considerable loss of efficiency. For the current study, where knowledge of the Z′ energy is not required, use of the collinear approximation is avoided. It has been shown in Refs.[8, 24] that it is possible this way to extract a sample of $\mathrm{Z}' \to \tau^{+}\tau^{-}$, with a signal to background ratio (S:B) of 3:1. The main requirements for the event selection were:

i) Two hadronic tau decays of opposite charge be identified, both with one or three tracks and $E_{\mathrm{T}} > 60\,\mathrm{GeV}$;

ii) The missing transverse energy, $E_{\mathrm{T}}^{\mathrm{miss}}$, be below 40 GeV;

iii) The transverse mass, m_{T}, as constructed from the lower p_{T} tau candidate and the missing momentum, be below 35 GeV;

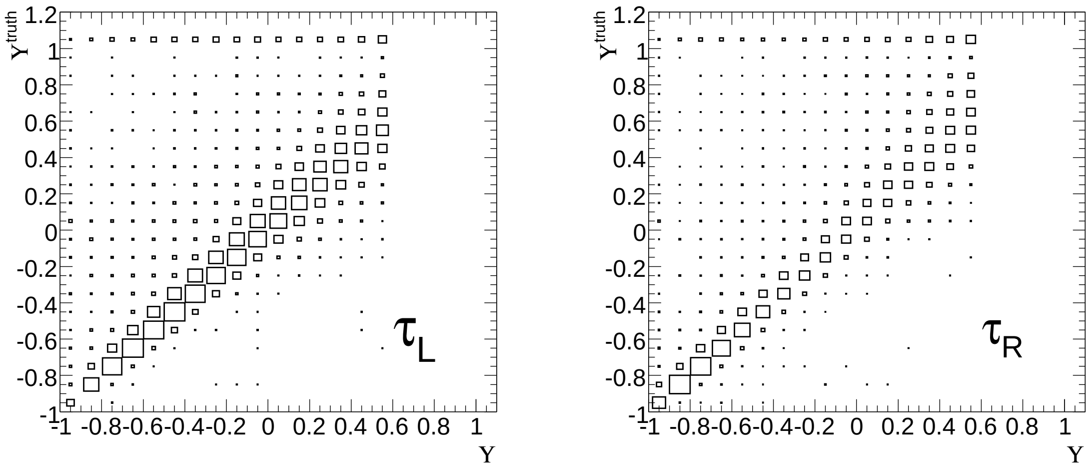

(a) **(b)**

Figure 9: *True value of* Υ *versus the reconstructed value for the selected tau decays.*

iv) The magnitude, $p_{\mathrm{T}}^{\mathrm{TOT}}$, of the vector sum of the transverse momenta of the two tau candidates and the missing momentum be smaller than 50 GeV. (In case a jet with $p_{\mathrm{T}} > 40\,\mathrm{GeV}$ was found, this was included in the sum).

v) The visible mass, m_{vis}, constructed from the visible decay products of the two tau candidates and the missing momentum be above 400 GeV.

Figure 10 displays the discriminating variables for the τ_{L} and τ_{R} samples. Except for the m_{vis} variable, good agreement between the two samples is observed. The clear difference between the two m_{vis} distributions, which reflects the harder nature of the decay products from right-handed taus, results in a overall difference in selection efficiency between the two samples.

To gauge the impact of the event selection, Figure 11 shows the selection efficiency as function of Υ. Two steps are illustrated: after cut i), and after cut v). As seen, the acceptance is rather flat in Υ, however, lower for the τ_{L} than for the τ_{R} sample.

The final selection efficiencies are summarised in Table 3c. At the event selection level, the efficiency for the τ_{R} sample is somewhat higher than for the τ_{L} sample. This is again due to the harder nature of the decay products from right-handed taus, leading to a higher probability for the event to pass the $E_{\mathrm{T}} > 60\,\mathrm{GeV}$ cut on the other tau and for the event to pass the $m_{\mathrm{vis}} > 400\,\mathrm{GeV}$ cut. It should be noticed, that this effect depends on the spin correlation of the two taus, and thus on the assumed spin-1 nature of the decaying resonance. Had we been dealing with a spin-0 resonance, these effects would have been different.

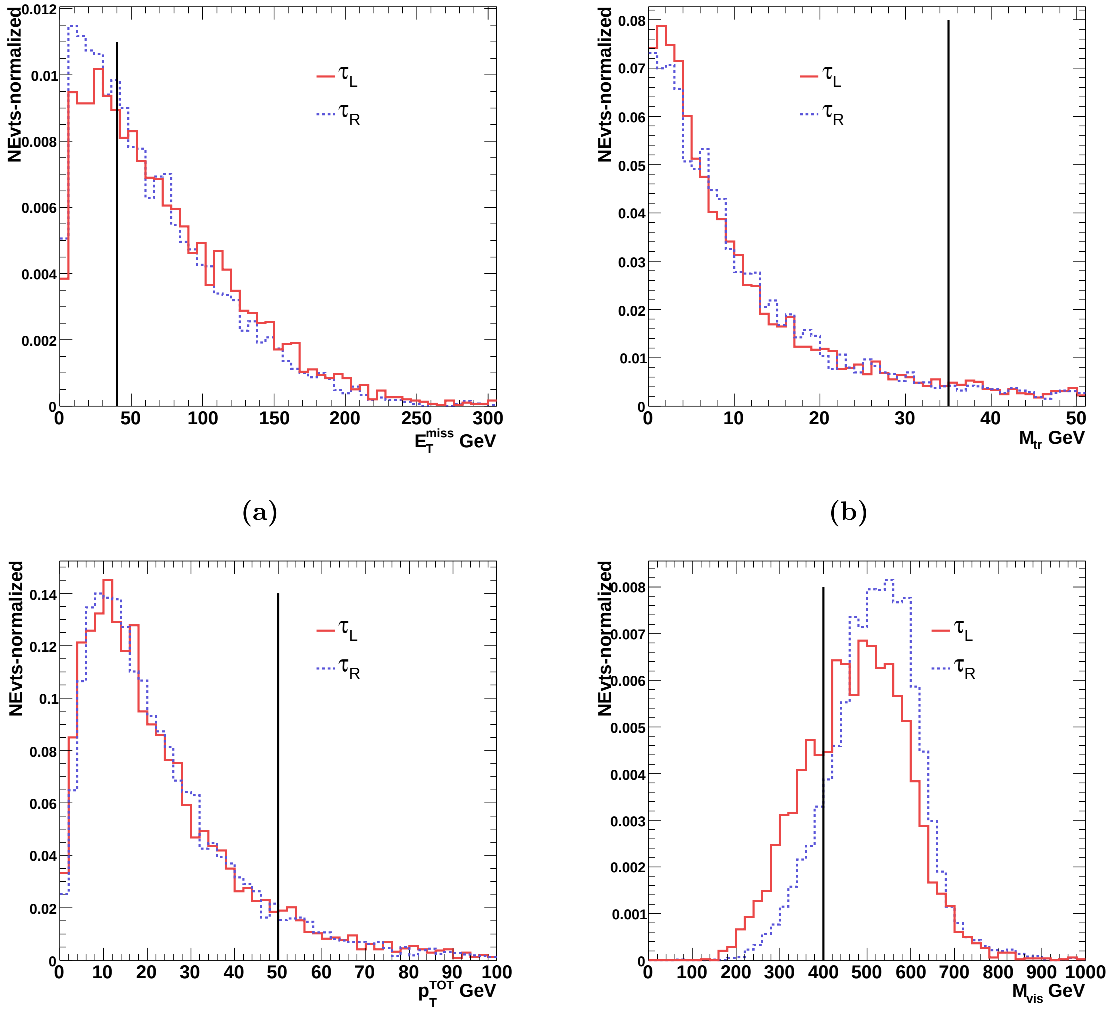

(a) **(b)**

(c) **(d)**

Figure 10: *Event selection variables for the τ_L and τ_R samples. The vertical lines correspond to the cut values.*

4.4 Method to extract the Tau Polarisation

The method to measure the tau polarisation takes advantage of the linear dependence on P_τ of the shape of the Υ distribution. In the presence of real data, P_τ would be extracted from the best fit to the observed Υ distribution of a linear combination of the the two Υ distributions corresponding to simulated right- and left-handed taus. Since real data are not available, simulated data has to be used instead. Thus, each of the samples, τ_L and τ_R, were divided into two approximately equally large subsamples. The idea being, that half of the data would emulate real data, while the other half would be simulated data used to

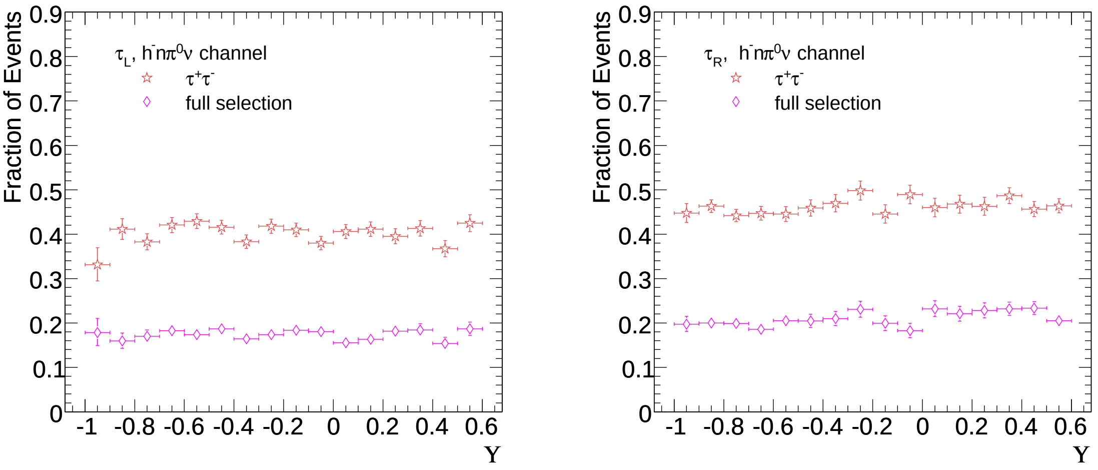

(a) **(b)**

Figure 11: *Event selection efficiency as function of* Υ.

extract the polarisation from the "real data". By adjusting the relative admixture of the $\tau_{\rm L}$ and $\tau_{\rm R}$ samples, a resulting "real data" sample, denoted $\tau_{\rm SSM}$, with a polarisation of $P_\tau = -0.15$ was established, in accordance with the expectation from the *sequential model.*

To extract the polarisation, a binned log likelihood relating the "observed" and predicted Υ distributions is maximised with respect to P_τ. The predicted number, M_i, of tau candidates from Monte Carlo in a given bin, i, is the sum

$$M_i = C_i + W_i + B_i, \tag{9}$$

where C_i is the number of correctly identified tau decays, W_i is the number of incorrectly identified taus from some other decay mode, and B_i is non-tau background. All the dependence on P_τ is carried in C_i and W_i. Letting $S_i \equiv C_i + W_i$, we have

$$M_i = S_i + B_i, \tag{10}$$

where, assuming equally many decays have been generated of both helicities, S_i can be written as

$$S_i = N\left(\frac{1+P_\tau}{2}\cdot S_i^{\rm R} + \frac{1-P_\tau}{2}\cdot S_i^{\rm L}\right). \tag{11}$$

Here the superscripts R and L refer to the particular τ^- helicity. The normalisation factor, N, is such that the predicted number of taus in the Monte Carlo equals the total number of tau candidates in the "data", minus the predicted non-tau background.

4.5 Result

Here we present the result of the tau polarisation measurement on the “real data” sample, τ_{SSM}. At this stage, we ignore external backgrounds, which are deferred to the discussion below.

Before carrying out the actual measurement, it is interesting to investigate the remaining sensitivity of the Υ variable to the tau polarisation after all selection cuts. Relative to the generator-level sensitivity of 0.31 reported in Table 2 ($\cos\psi$), the sensitivity after all cuts is found to be reduced to 0.24, where the main reason for the drop is the truncation of the Υ distribution at 0.6.

From each of the two samples, τ_{L} and τ_{R}, 32,000 events were used to construct the Monte Carlo S_i^{L} and S_i^{R} spectra. The initial number of events in the τ_{SSM} sample was 38,700 corresponding to an integrated luminosity of $30\,\mathrm{fb}^{-1}$. Hence, by construction, the normalisation factor, N, should be 1.21.

The results of the fit are

$$P_\tau = -0.173 \pm 0.073 \text{ (stat.)},$$

and

$$N = 1.214 \pm 0.023 \text{ (stat.)},$$

in good agreement with the true values. Figure 12 shows the fit result graphically.

4.6 External Backgrounds

To investigate the effect of external backgrounds, one would ideally perform a Monte Carlo study generating large samples and subjecting these to the same selection criteria as the signal events. Due, however, to limited resources and the enormous rejection factors for the backgrounds, this strategy could not be pursued. Instead, an alternate path is followed.

In accordance with the above discussion, a signal to background ratio of 3:1 is assumed. This is likely to be a conservative estimate, since the background, being dominated by QCD jets, was evaluated in Ref. [10] for an inclusive sample of one- and three-prong tau decays. Concentrating here on one-prong decays only, a somewhat lower background level can be expected. As a model for the shape of the background it is assumed that the Υ distribution be the same as that of the τ_{R} sample. This can have the following justification. If, on the one hand, the source of the misidentified taus is QCD jets, the single charged track will likely be accompanied by a sizable amount of neutral energy, resulting in Υ values close to -1. If, on the other hand, the source is an electron or a muon from W+jets, Z+jets, or $t\bar{t}$, the background will likely be concentrated on the positive side of the Υ distribution.

First, the fit procedure to extract the tau polarisation was repeated assuming a perfect modelling of the background level and shape in the Monte Carlo. This was done by adding the background contribution to the “real data” sample as well as to the Monte Carlo samples, as represented by the term B_i in Eq. (9). This way it was confirmed, that the assumed external background, as long as it is well modelled in the Monte Carlo, has no appreciable

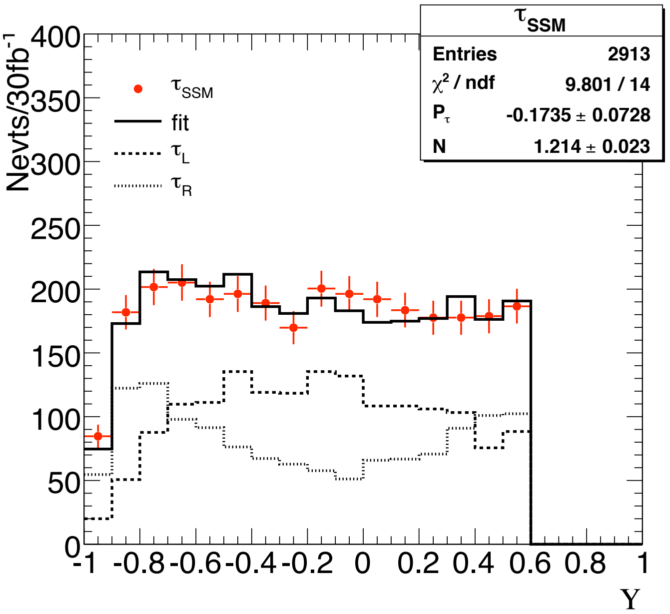

Figure 12: *Fit result. The points with error bars are the observed spectrum. The dashed (dotted) histograms is the Monte Carlo contribution from left- (right-) handed taus. The solid-line histogram indicates the sum of the Monte Carlo contributions.*

effect on the central value of the polarisation measurement. The background leads, however, to a dilution of the sample reflected in an increase in the statistical uncertainty from 0.073 to 0.087.

Second, the influence of a wrong Monte Carlo modelling of the background was investigated. For this, the background level was varied by ±10% in the “real data” sample, keeping the Monte Carlo samples unchanged. The size of the variation was inspired by current studies of the evaluation of the backgrounds in $Z \rightarrow \tau^+\tau^-$ using control samples from real data [26]. By following this procedure variations in the extracted P_τ values of the order of ±0.049 were observed.

In conclusion, it is important for the tau polarisation measurement to understand well the level and shape of the external backgrounds. To control the measurement to the few percent level, the external backgrounds have to be understood to the same level of accuracy. When real data will be available, the study of like-sign candidates could potentially be a handle to understand in particular the background of QCD events.

4.7 Other Systematic Effects

Besides the external backgrounds, other contributions which may have a sizable systematic effect on the tau polarisation measurement is the energy response of the calorimetry. Two effects have been studied:

- A variation of the calorimetric energy scale ($E_{\mathrm{T}}^{\pm}$) by ±5%.
- An increase of the energy resolution ($E_{\mathrm{T}}^{\mathrm{res}}$) on top of what is already provided by the detector simulation by the term $(0.45\,\mathrm{GeV}) \times \sqrt{E[\mathrm{GeV}]}$. This amounts to an relative increase of the resolution by about 25% at the lower end of the E_{T} scale falling to about 15% at the higher end.

The systematic effects were evaluated by applying each of the variations to the "real data" sample, keeping the Monte Carlo samples unchanged. The tau polarisation measurement was influenced in two ways: *i)* by a direct shift in the Υ values for the selected events, and *ii)* by a change in the selection efficiencies. Table 4 summarises, for the τ_{L} and τ_{R} samples, the selection efficiencies with and without the systematic variations. Sizable shifts in the acceptance can be observed.

Efficiency [%]	τ_{L} sample			τ_{R} sample		
	$h^-\nu$	$h^-\pi^0\nu$	$h^-\pi^0\pi^0(\pi^0)\nu$	$h^-\nu$	$h^-\pi^0\nu$	$h^-\pi^0\pi^0(\pi^0)\nu$
No variation	0.6	6.5	7.2	1.4	7.3	7.9
E_{T}^{+}	0.9	7.3	7.8	2.2	8.5	8.5
E_{T}^{-}	0.4	5.5	6.4	1.0	6.3	7.2
$E_{\mathrm{T}}^{\mathrm{res}}$	0.7	6.5	7.2	1.5	7.3	7.9

Table 4: *Overall tau selection efficiencies without and with the systematic variations in the calorimeter response.*

Table 5 summarises the observed effects on the tau polarisation measurement of the studied variations. It should be noted, that the statistical precision of our studies is such, that a rigorous evaluation of the systematics effects cannot be carried out. Hence the reported numbers should be merely seen as indicative.

Variation considered	ΔP_τ
E_{T}^{+}: shift of calorimeter scale by +5%	0.071
E_{T}^{-}: shift of calorimeter scale by −5%	−0.023
$E_{\mathrm{T}}^{\mathrm{res}}$: smear calorimeter response by $\sigma(E) \oplus 0.45\sqrt{E}$	0.031

Table 5: *Systematic uncertainties from experimental mis-measurements.*

5 Summary and Discussion

Using fully simulated data samples, the prospects of measuring the tau polarisation in $\mathrm{Z}' \to \tau^+\tau^-$ events, with both taus decaying hadronically, have been studied. For the sake of definiteness, the mass of the Z′ was set to 600 GeV and the *sequential model* was chosen as a benchmark scenario. Although necessary to make such specific assumptions for a concrete study, it should be stressed that this work illustrates, in general, the possibility of measuring the tau polarisation in the decay of a heavy resonance.

The investigated method is making use of the inclusive sample of $h^- \mathrm{n}\pi^0\nu$ final states with one or more π^0 s, corresponding to more than one third of all tau decays. The main sensitivity comes from the $\pi^-\pi^0\nu$ channel, whereas decays with multiple π^0 s are included mainly to avoid the experimental difficulty of having to separate these from the $\pi^-\pi^0\nu$ decays. The polarisation is extracted from the energy sharing between the charged and the neutral pions, and, thus, does not require knowledge of the energy of the decaying tau. This avoids the use of the *collinear approximation*, which would have otherwise resulted in a significant loss of statistics.

Assuming the Z′ production cross section of the *sequential model*, the amount of data used corresponds to an integrated luminosity of $30\,\mathrm{fb}^{-1}$. From this, about 3,000 $\tau^\pm \rightarrow h^\pm \mathrm{n}\pi^0\nu$ decays were selected, resulting is a statistical precision on the tau polarisation measurement of 0.09. By extending the study to also include events, where the other tau decays leptonically, it should be possible to increase the statistics by nearly a factor two.

Various systematic effects which may influence the measurement have been investigated. Important effects are the level of non-tau backgrounds and the calorimetric energy scale. The necessary control of external backgrounds to the few percent level may turn out to be a challenging task requiring detailed studies on real data control samples. To match the statistical precision, the calorimetric energy scale has to be understood to the 5% level which would seem a realistic goal. If a heavy resonance will be indeed observed in all three leptonic channels, consistency of the mass measurements may give an important handle on the calorimetric scale.

In conclusion, within the chosen scenario, a measurement of the tau polarisation in $\mathrm{Z}' \rightarrow \tau^+\tau^-$ events to a statistical precision of 0.09 has been demonstrated using $30\,\mathrm{fb}^{-1}$ of data. Control of the systematics to the same level of precision seems plausible, resulting in a overall precision at the 0.12 level. This would already constitute an interesting constraint on the Z′ couplings. The statistical precision can be improved by including events where the other tau decays leptonically and, beyond that, by collecting more data. Whether or not the systematic precision can be made to match this improved statistical precision can probably be only answered with certainty when real data will be actually available.

Appendix A

Samples of Z′ boson was generated with `PYTHIA` [14] in `ATHENA` version 14.2.10. The Z′ boson was forced to decay to tau lepton pairs. The tau leptons were then made to decay using the `TAUOLA` package [15] version 00-01-49. Details related to the generated samples are summarised in Table 6. Validation plots, jobOption files used for the events generation and the sample location can be found in Ref. [28].

The ATLAS detector was fully simulated using the `GEANT4` package [17], implemented

Sample	`PYTHIA` parameters	`TAUOLA` parameters	Mass ($\sqrt{\hat{s}}/2$ cut)	NEvts
τ_{L}	`pydat1 parj 192 1` `pydat1 parj 193 1`	`dmode 2`	600 (300)	200,000
τ_{R}	`pydat1 parj 192 1` `pydat1 parj 193 −1`	`dmode 2`	600 (300)	205,000

Table 6: *For each generated sample set the (non-default)* `PYTHIA` *and* `TAUOLA` *parameters, the invariant mass and number of events are given.*

inside the `ATHENA`. Simulation and digitalisation was performed in one step using the official transformation `csc_simul_trf.py` and the `ATHENA` version 14.2.23.1. These data were saved in the Raw Data Object (RDO) format. Offline reconstruction was performed with the official `csc_reco_trf.py` transformation and `ATHENA` version 14.2.25.2. These data were stored in the Athena Aware Ntuple (AAN) format. Transformation parameters can be found in [28]. Available statistics are summarised in Table 7.

NEvts	RDO	AAN
τ_{L}	90,000	84,000
τ_{R}	90,000	83,000

Table 7: *Number of events for each sample and data format*

References

[1] J.D. Anderson, M.H. Austern, R.N. Cahn, *Measurement of Z' couplings at future hadron colliders through decays to τ leptons*, Phys. Rev. D46 (1992) 290–302.

[2] The ALEPH Collaboration, The DELPHI Collaboration, The L3 Collaboration, The OPAL Collaboration, The SLD Collaboration, The LEP Electroweak Working Group and The SLD Electroweak and Heavy Flavour Groups, *Precision electroweak measurements on the Z resonance* and references therein, Phys. Rep. 427 (2006) 257–454.

[3] Particle Data Group, C. Amsler et al., Phys. Lett. B 667 (2008) 1.

[4] K. Hagiwara, A.D. Martin and D. Zeppenfeld, *τ Polarization measurement at LEP and SLC*, Phys Lett B235 (1989) 198–202.

[5] M. Davier, L. Duflot, F. Le Diberder and A. Rougé, *The optimal method for the measurement of tau polarization*, Phys. Lett. B306 (1993) 411–417.

[6] A. Rougé, *Polarization observables in the $3\pi\nu$ decay mode of the τ*, Z.Phys C48 (1990) 75–77.

[7] The ATLAS Collaboration, *Exotic Processes* in *Expected Performance of the ATLAS Experiment, Detector, Trigger and Physics*, CERN-OPEN-2008-020, `arXiv:0901.0512`.

[8] Z. Czyczula (ATLAS Collaboration), *Tau Physics with First Data in ATLAS*, Nucl. Phys. B (Proceedings Supplements) 2009, pp. 344-349.

[9] P. Langacker, *The Physics of Heavy Z' Gauge Bosons*, `arXiv:0801.1345v2`.

[10] M. Carena, A. Daleo, B.A. Dobrescu, T.M.Tait, *Z' gauge bosons at the Fermilab Tevatron*, Phys. Rev. D70 (2004) 093009.

[11] A.A. Andrianov, P. Osland, A.A. Pankov, N.V. Romanenko and J. Sirkka, *Phenomenology of a Z' coupling only to third family fermions*, Phys. Rev. D58 (1998) 075001.

[12] K.R. Lynch, S. Mrenna, M. Narain and E.H. Simmons, *Finding Z' bosons coupled preferentially to the third family at CERN LEP and the Fermilab Tevatron*, Phys. Rev. D63 (2001) 035006.

[13] D. Acosta *et al.*, *Search for New Physics Using High-Mass Tau Pairs from 1.96 TeV $p\bar{p}$ Collisions*, Phys. Rev. Lett. 95 (2005) 131801.

[14] T. Sjöstrand *et al.*, *High-energy-physics event generation with Pythia 6.1*, Comp. Phys. Comm. 135 (2001) 238; T. Sjöstrand *et al.*, *PYTHIA 6.4 physics and manual*, J. High Energy Phys. JHEP05 (2006) 026.

[15] S. Jadach, Z. Was, R. Decker and, J.H. Kühn, *The τ decay library TAUOLA, version 2.4*, Comp. Phys. Comm. 76 (1993) 361.

[16] G. Azuelos *et al.*, *Polarization and spin correlation effects in third family resonances*, in *Les Houches "Physics at TeV colliders 2005". Beyond the Standard Model working group: Summary report*, arXiv:hep-ph/0602198v1

[17] The Geant4 Collaboration (S. Agostinelli *et al.*), *Geant4 - A Simulation Toolkit*, NIM A506 (2003) 250-303.

[18] ATLAS collaboration, *ATLAS Computing Technical Design Report*; and Refs. therein, ATLAS-TDR-017; CERN-LHCC-2005-022.

[19] C.Ciobanu *et al.*, *Z' generation with PYTHIA*, CDF/PHYS/EXOTIC, PUBLIC/7755.

[20] J. Campbell, R.K. Ellis, F. Maltoni, and S. Willenbrock, *Higgs boson production in association with a single bottom quark*, Phys. Rev. D67 (2003) 095002.

[21] The ATLAS Collaboration, *Tau Leptons* in *Expected Performance of the ATLAS Experiment, Detector, Trigger and Physics*, CERN-OPEN-2008-020, `arXiv:0901.0512`.

[22] A.Christov *et al.*, *Performance of the tau reconstruction and identification algorithm with release 14.2.10*, ATL-PUB-PHYS-2009-xxx

[23] Z. Czyczula, M. Dam, *Cut-based electron veto algorithm for the track-seeded part of tauRec*, ATL-PHYS-INT-2009-023.

[24] Z. Czyczula *et al.*, *Searching for New Physics using High-p_T Tau Pairs in ATLAS*, ATL-PHYS-INT-2008-038.

[25] R. Brun, F. Rademakers, *ROOT - An Object Oriented Data Analysis Framework*, `http://root.cern.ch/`

[26] T. Vickey *et al.*, *A Data-driven Control Sample for $Z \rightarrow \tau\tau$ + jets Backgrounds to Higgs Searches*, ATL-COM-PHYS-2008-144.

[27] The ATLAS Collaboration, *Trigger* in *Expected Performance of the ATLAS Experiment, Detector, Trigger and Physics*, CERN-OPEN-2008-020, `arXiv:0901.0512`.

[28] `https://twiki.cern.ch/twiki/bin/view/AtlasProtected/ZprimeTauTau`, "Exotics Validation Plots"